Faraday Rotation of Pulsed and Continuous-wave Light in Atomic Vapour

PAUL SIDDONS

Faraday Rotation of Pulsed and Continuous-wave Light in Atomic Vapour

Paul Siddons

Abstract

The absorptive and dispersive properties of a Doppler-broadened vapour of rubidium atoms is investigated. A detailed model of the atom-light interaction is developed and found to be in excellent agreement with experiment in the regime where the interacting light field is sufficiently weak such that it does not significantly alter the medium through which it propagates. The importance of using a weak beam to probe atomic systems is discussed, and a method of characterising how weak such a beam has to be is provided. The theoretical model is applied to both situations of illumination by continuous-wave and pulsed light, the latter situation providing a demonstration of the slow light effect. This phenomenon is a manifestation of the dispersive properties of the medium and is shown to exist over a particularly large frequency range, compared to the absorption spectrum, in thermal vapours. Off-resonant interactions are studied, in which incident laser-light is detuned from resonance to such a degree that Doppler-broadening can be neglected. We quantify the extent to which the light needs to be detuned to be in this regime, and provide approximations to the line-shape function developed in earlier parts of the thesis. The approximate line-shapes are much easier to manipulate and allow a more intuitive understanding of the atom-light interaction. In the second part of the thesis we study the Faraday effect and related phenomena which are an expression of the birefringent properties of the atom-light system. Beginning with a theoretical and experimental investigation of the Faraday rotation of a weak continuous-wave beam, we move on to the consideration of pulsed light. Optically-induced birefringence via the application of an intense continuous-wave pumping field is demonstrated experimentally, and the theoretical plausibility of controlling the polarisation state of a weak pulsed field mediated via intense pulsed light is shown.

Faraday Rotation of Pulsed and Continuous-wave Light in Atomic Vapour

Paul Siddons

A thesis submitted in partial fulfilment
of the requirements for the degree of
Doctor of Philosophy

Department of Physics
Durham University

October 3, 2011

Contents

List of Figures

List of Tables

Declaration

I confirm that no part of the material offered has previously been submitted by myself for a degree in this or any other University. Where material has been generated through joint work, the work of others has been indicated.

Paul Siddons
Durham, October 3, 2011

I dedicate this work to you,
Dear reader[1]*,*
without whom this thesis would
forever languish upon a dusty bookshelf
(or in this digital age more than likely end up on the wrong side of a 404)

[1]On the proviso that you read the whole thesis, *including* the appendices. I presume you're not the kind of casual reader who just dips into a thesis, otherwise you wouldn't be reading a footnote to a dedication.

Acknowledgements

First and foremost I'd like to thank my supervisors Dr Ifan Hughes and Prof Charles Adams. There enthusiasm for the subject encouraged me to keep going in the face of adversity i.e. dealing with temperamental lab equipment (though to be fair it was on occasion due to incompetence on my part: its hard to stay upbeat with the knowledge that both the laser and oscilloscope are more valuable than I am - and seem to know it). Our weekly meets ensured that our project kept on the straight and narrow. The future of the slow-light project is now in the capable hands of Lee, who is discovering that the unexpected observations we see in our experiment are usually more interesting than the expected. I'd also like to acknowledge the dept to my supervisors in the writing of the articles we worked on together. Their valuable insights have informed my writing style and have hopefully propagated through to this *magnum opus* you see before you. Thanks also go to Ifan for his tireless proof reading of this thesis - if there are any split infinitives surviving in the final manuscript it is a reflection upon my willful malevolence rather than his diligence.

Thank you to Sylvi and the many other people who kept me in practice with Mathematica after I was appointed as the go-to guy for such things in the AtMol collective unconsciousness, a status conferred not through actual expertise but rather due to my having the longest continuous service on the Wolfram coal-face.

I am grateful to the people with whom I shared an office. Of particular note were Mark, James and Josh whose banter made the day more enjoyable/bearable, which included the invaluable hypothesis that everything just boils down to an energy argument, invariably provoking the question "Why am I wasting my energy having this argument?" I'm especially grateful to Monsit not just for fruitful physics-based discussion but also for his continued friendship. I am also grateful to my family whom I do not acknowledge enough.

Chapter 1

Introduction

1.1 Motivation

The aim of this investigation is to study the interaction of laser light with an atomic vapour, both from a theoretical and an experimental stand point. Of particular interest is the Faraday effect, in which the polarisation state of a transmitted probe beam is altered in a controlled manner by either an applied magnetic field or by an additional optical beam.

1.2 Atom-light interactions in an atomic vapour

We begin by offering a holistic description of the atom-light interaction and explain why approximations to the complete picture are often necessary, and more than likely unavoidable. Nevertheless, these approximations lead to theoretical predictions which agree well with experimental measurements. A complete description of the interaction between light and atoms treats both entities using quantum mechanical formalism, namely the theory of quantum electrodynamics [1]. Light is represented as a discrete set of travelling-wave modes propagating through space-time, containing an integer number of quanta, the photons. Atoms contain charge carriers in a set of quantised energy states. Interactions proceed via the exchange of quanta between the

states of the light field and atoms. The problem at hand is the interaction of one or more laser beams with a multi-species atomic vapour contained within a cell.

We deal not with a single photon interacting with a single atom, but with a vast number of photons in numerous modes interacting with a large collection of atoms in various states of excitation. If we consider the conditions of a typical experiment with a room temperature vapour of rubidium, we have an atomic density of 10^{15} m^{-3}. Inside an interaction volume of 1 cm^3 we have 10^9 atoms. For a 1 mW beam of photons with energy 1.5 eV, and assuming its intensity is uniform over the interaction volume, 10^{11} photons enter the medium every second. Treating such a system by following the trajectory of every single photon as it interacts with every single atom in every possible way is unfeasible. It is advisable to look at the bigger picture and consider the collective dynamics of the macroscopic system, by considering the statistical behaviour of the atom-light interaction. Thus we make an important approximation: treating the laser light as a classical electromagnetic wave and not as a field containing photons. This is an acceptable approximation and gives accurate results in the limit that the number of photons in the field is large. We then make a complementary approximation to the atomic system, by considering the collection of atoms as a statistical ensemble. The atomic ensemble takes the various degrees of freedom associated with individual particles, such as velocity, position, energy state, and averages them to produce distribution functions of these quantities. As with the light field, the vast number of particles involved in the averaging process leads to predictions with a high degree of reliability. Hence we shall consider classical electromagnetic fields, not photons, and atomic ensembles, not individual atoms. There are some situations when it is necessary to have recourse to the quantum theory of light, namely in dealing with spontaneous emission. In this process, the vacuum field is a continuum of empty modes into which a single photon is randomly emitted by an atom. The average behaviour can, however, be described in a classical frame work by treating the process of decay statistically. Hence we are free to use a classical field description at the expense of information about individual emissive events.

Starting from the well-known Maxwell-Bloch equations [2, 3] which describe

the interaction of macroscopic electric fields with an ensemble of atoms, we develop a theoretical model able to handle the complexities of realistic atomic systems. There are two broad classes of interaction we consider in this thesis. The first is the attenuation and dispersion experienced by a weak beam as it propagates through a medium. In this case the atoms, to a high degree of accuracy, remain unperturbed during the interaction. The second class of interaction we consider is the limit of strong excitation, where a beam has a major effect on the state of the atoms. A medium prepared in such a way can have a dramatic effect on the state of a weak beam which propagates through the medium subsequently.

1.3 Weak-beam transmission spectra

We study the Doppler-broadened absorption of a weak monochromatic probe beam in a thermal rubidium vapour cell on the D lines. A detailed model of the susceptibility is developed which takes into account the absolute line-strengths of the allowed electric dipole transitions and the motion of the atoms parallel to the probe beam. All transitions from both hyperfine levels of the ground term of both isotopes are incorporated. The absorption and refractive index as a function of frequency are expressed in terms of the complementary error function. The absolute absorption profiles are compared with experiment, and are found to be in excellent agreement provided a sufficiently weak probe beam with an intensity under one thousandth of the saturation intensity is used. The importance of hyperfine pumping for open transitions is discussed in the context of achieving the weak-probe limit. Theory and experiment are shown to be in excellent agreement.

In alkali-metal atoms the D lines couple strongly to light, and from an experimental perspective rubidium and cesium are ideal species as they have sufficient room temperature vapour pressure to yield large absorption (10-50%) in cells of modest length (50-70 mm). In addition, for these atoms the D lines occur at wavelengths where inexpensive and reliable diode laser sources exist. These transitions are frequently studied in atomic physics; the D_2 transition is used extensively in laser-cooling experiments [4–7], whereas nonlinear optical processes such as electromagnetically induced transparency [8]

and chip-scale atomic magnetometers [9] are realised with the D_1 transition.

Controlling the propagation of light through a medium by modifying its absorptive and dispersive properties is a flourishing area of research [10–12]. Having a model which calculates the absorption and refractive index of a Doppler-broadened medium is useful for predicting the magnitude of relevant pulse propagation properties. Such a model has a number of applications. For example, in analysing EIT spectra [13, 14]. Absolute absorption spectroscopy can yield the number density of the sample being studied and has many applications in physics, chemistry, metallurgy and industry [15, 16]; when applied to the measurement of different spectral lines the populations of occupied levels are revealed, from which a temperature can be deduced [17]. In addition, Rb and Cs spectroscopy is frequently used for generating a signal used for frequency reference ("locking") of a laser. Understanding the evolution of the absorption profile aids in the decision of, for example, which temperature to use to maximise the signal [18]. The importance of using a weak probe in order to maximise the absorption will be highlighted. Many laser-lock schemes have signals which have a non-trivial dependence of signal amplitude on absorption, such as polarisation spectroscopy [19–21] or the dichroic atomic vapour laser lock (DAVLL) [22–24]. The choice of which probe power to use is a trade-off between two competing effects: a weak probe beam ensures that the largest absorption is obtained, whereas higher probe power gives a better signal-to-noise ratio.

1.4 The slow light effect

The phenomenon of reduced optical group velocity (slow light) is a topic of burgeoning interest [25, 26]. In a slow-light medium, the group refractive index, n_g, (the ratio of the speed of light *in vacuo* to the pulse velocity) is many orders of magnitude larger than the phase index, n. Hence an optical pulse propagates much more slowly than a monochromatic light beam. Large group indices of $\sim 10^7$ are achievable in resonant optical processes, such as electromagnetically induced transparency (EIT), accompanied by a refractive index that is of the order of unity [27]. The slow light effect relies on the interaction between light and a suitable dispersive material such as

optical fibres, photonic crystals, or hot atomic vapour cells. High temperature atomic vapours are correspondingly highly Doppler-broadened, which is usually an undesirable effect. However, there is particular interest in off-resonant schemes as high dispersion is combined with low absorption and low group velocity dispersion over a large bandwidth. The large group refractive index associated with Doppler-broadened media has been utilised to control the propagation of broadband optical pulses in experimental [28–30] and theoretical studies [31]. In such systems, group indices of $\sim 10^3$ are achievable, with gigahertz pulse bandwidths. This broad bandwidth allows large fractional pulse delays of up to 80 [29]. Delaying pulses by more than their widths has applications in data synchronisation and qubit operations for quantum computing [32]. Additional interesting applications of slow light include light storage [33–35] and interferometry. Slow-light interferometry has been demonstrated using both monochromatic light sources [36, 37], where the large dispersion associated with a slow-light medium results in greater phase sensitivity; and polychromatic light, where the large pulse delays can increase the resolution of a Fourier transform interferometer by orders of magnitude [38].

1.5 The Faraday effect

The ability to probe quantum systems on fast timescales is central to the advancement of quantum technology. In this thesis we show that this is possible using an off-resonant dispersive probe. By applying a magnetic field to an atomic vapour the spectra of the group index for left and right circularly polarised light become displaced leading to a slow-light Faraday effect which results in large dispersion and high transmission over tens of gigahertz. This large frequency range opens up the possibility of probing dynamics on a nanosecond timescale. In addition we show that the group index enhances the spectral sensitivity of the polarisation rotation giving large rotations of up to 15π rad for continuous-wave light. With respect to pulsed light, we demonstrate dynamic broadband pulse switching, by rotating a linearly polarised nanosecond pulse by $\pi/2$ rad with negligible distortion and transmission close to unity.

For the case of off-resonant atomic systems (where detuning from resonance is more than two times the resonance linewidth, including inhomogeneous broadening) dispersive effects dominate over absorption. This arises because the real part of the susceptibility is inversely proportional to detuning, whereas the imaginary part is inversely proportional to detuning squared. The frequency dependence of the dispersion also means that, in general, a large bandwidth is available for dispersive effects, and consequently off-resonance dispersive probes can achieve a fast time response. The off-resonant Faraday effect can be used to separate the components of Raman light with high fidelity [39], and can be used as a dispersive probe with continuous-wave or pulsed light [40]. The non-invasive nature of off-resonant dispersive probing could also be used as a read-out tool for quantum information [41].

1.6 Optical control

In the latter chapters of this thesis we demonstrate controlled polarisation rotation of an optical field conditional on the presence of a second field, inducing large rotations with high transmission of the probing field. This combination of large, controlled rotation and low loss is well-suited for the manipulation of light pulses. The ability to manipulate optical pulses is central to the advancement of information and communications technology [42]. All-optical switching [43] has the advantage that the optical information can be processed without conversion to an electrical signal. An all-optical switch is produced by using an optical control field to modify the refractive index or the absorption of the medium. For example, in electromagnetically induced transparency (EIT) [44, 45] or off-resonance Raman resonances [46–48] a strong control field is employed to reduce the absorption at a particular frequency. Reducing the intensity of the control field to the single photon level is of interest for certain quantum information protocols [49]. All-optical switching at low light levels has been demonstrated using EIT [50], and also using transverse optical pattern formation [51].

Polarisation rotation of a linearly polarised optical field has been studied extensively in atomic systems. Such rotations may be induced by an applied

magnetic field, i.e., the Faraday effect [40, 52, 53], by an applied electric field [54], or by spin polarising the medium, i.e., the paramagnetic Faraday effect [19, 55–57]. For optical switching, a rotation angle of $\pi/2$ rad is required such that two orthogonal linear polarisation modes can be exchanged. An EIT scheme reported by Li *et al.* provides rotations in the region of $\pi/4$ rad, with $\sim 50\%$ loss [58]. In this thesis we demonstrate larger rotations with lower loss.

1.7 Thesis summary

The structure of the thesis is as follows:

Chapter 2 The Maxwell-Bloch equations which govern the interaction of electromagnetic radiation with atomic media are introduced. Numerical solutions are shown for an ensemble of two-level atoms illuminated by a continuous-wave and pulsed light.

Chapter 3 Approximations to the Maxwell-Bloch equations are discussed with a view to solving atom-light interactions with realistic media, in which case a more computationally-efficient approach is required to cope with the complexity added by moving beyond the two-level atom.

Chapter 4 We apply the methods described in chapter 2 to develop a theoretical model of weak-beam transmission through a vapour cell containing atomic rubidium. Calculations are then compared to experimental measurements. This chapter is based on the article [59].

Chapter 5 With the theoretical model developed in chapter 3 we investigate the dispersive and absorptive properties of a rubidium vapour interacting with off-resonant light. We note that in this regime Doppler broadening can be neglected, and go on to validate this claim by comparing our calculations with experimental data. This chapter is based on the article [60].

Chapter 6 The phenomena of slow light is considered in this chapter, an effect in which the velocity of light pulses traversing dispersive

media can be substantially slower than the speed of light *in vacuo*. We take measurements of a nanosecond-duration pulse propagating through rubidium vapour and compare our measurements with theory. This chapter is based on the article [40].

Chapter 7 We introduce the Faraday effect, by which a magnetic field applied to a medium changes the material's response to the different polarisation components of interacting light. The Faraday effect is shown to be particularly strong in a hot atomic vapour, where we demonstrate the rotation of the plain of polarisation of a beam of many π radians. This chapter is based on the article [40].

Chapter 8 The phenomena of the previous two chapters are combined as we apply the Faraday effect to pulsed-light propagation. We demonstrate experimentally that large rotations over a broad frequency range (and thus a short time scale) are possible with the use of atomic vapours. We also contrast the behaviour of continuous-wave and pulsed light, showing that under certain conditions rather than under going polarisation rotation pulsed light can be temporally separated into its constituent polarisation components.

Chapter 9 In this chapter we demonstrate control of the Faraday effect with the application of an intense optical field. Through preparation of the atomic vapour by a pumping field, the Faraday rotation experienced by another, weaker beam is altered. We show this experimentally and leave it until chapter 9 to investigate optical control from a theoretical perspective. This chapter is based on the article [61].

Chapter 10 We return to the theoretical consideration of the Maxwell-Bloch equations, this time investigating the regime where interacting light of sufficiently high intensity can have a profound effect upon the medium through which it propagates. We also demonstrate the feasibility of inducing birefringence with an optical field, in analogy to the Faraday effect.

Chapter 11 We draw our conclusions and give an outlook on the future of the work presented in this thesis.

1.8 Publications

During the preparation of work for this thesis the following papers have been published:

P. Siddons, C. S. Adams, C. Ge, and I. G. Hughes, *Absolute absorption on rubidium D lines: comparison between theory and experiment*, J. Phys. B: At. Mol. Opt. Phys. **41**, 155004 (2008), 10.1088/0953-4075/41/15/155004.

P. Siddons, N. C. Bell, Y. Cai, C. S. Adams, and I. G. Hughes, *A gigahertz-bandwidth atomic probe based on the slow-light Faraday effect*, Nature Photon. **3**, 225 (2009), 10.1038/nphoton.2009.27.

P. Siddons, C. S. Adams, and I. G. Hughes, *Off-resonance absorption and dispersion in vapours of hot alkali-metal atoms*, J. Phys. B: At. Mol. Opt. Phys. **42**, 175004 (2009), 10.1088/0953-4075/42/17/175004.

R. P. Abel, U. Krohn, P. Siddons, I. G. Hughes, and C. S. Adams, *Faraday dichroic beam splitter for Raman light using an isotopically pure alkali-metal-vapor cell*, Opt. Lett. **34**, 3071 (2009), 10.1364/OL.34.003071.

P. Siddons, C. S. Adams, and I. G. Hughes, *Optical control of Faraday rotation in hot Rb vapor*, Phys. Rev. A **81**, 043838 (2010), 10.1103/PhysRevA.81.043838.

L. Weller, R. J. Bettles, P. Siddons, C. S. Adams, and I. G. Hughes, *Absolute absorption on the rubidium D_1 line including resonant dipole-dipole interactions*, J. Phys. B: At. Mol. Opt. Phys. **44**, 195006 (2011), 10.1088/0953-4075/44/19/195006

Part I

Atom-light interactions

Chapter 2

The Maxwell-Bloch equations

We require a set of equations which describe the light-atom interaction, and by extension, the coupled evolution of the electromagnetic field and atomic ensemble. As this problem is well known (see for example [2, 3]), it is sufficient to provide the equations before proceeding to describe them. They consist of the four Maxwell equations [62] governing the propagation and creation of electromagnetic fields (represented by the electric and magnetic fields $\mathbf{E}$ and $\mathbf{B}$), and the optical Bloch equations of the atomic ensemble [63] (represented by the density operator $\hat{\rho}$). In a non-magnetic medium with no free charges,

$$\nabla \cdot \mathbf{E} = -\frac{1}{\epsilon_0}\nabla \cdot \mathbf{P}, \tag{I}$$

$$\nabla \cdot \mathbf{B} = 0, \tag{II}$$

$$\nabla \times \mathbf{E} = -\partial_t \mathbf{B}, \tag{III}$$

$$\nabla \times \mathbf{B} = \mu_0 \partial_t (\mathbf{P} + \epsilon_0 \mathbf{E}), \tag{IV}$$

$$\partial_t \hat{\rho} = \frac{\mathrm{i}}{\hbar}[\hat{\rho}, \mathscr{H}] + \hat{\Gamma}. \tag{V}$$

We refer to this set of expressions as the Maxwell-Bloch equations. Here, ∇ is the vector differential operator, and ∂_t is the temporal differential operator; ϵ_0 and μ_0 are, respectively, the permittivity and permeability of free-space; $\mathscr{H}$ is the Hamiltonian of the system and $\hat{\Gamma}$ the operator accounting for spontaneous decay. The polarisation density $\mathbf{P}$ provides the coupling between the dynamics of the electromagnetic field and atomic ensemble. An isolated particle interacts with an external electromagnetic field via its bound charges.

Subjected to such a field, the charge distribution of the particle is distorted, creating a multipole moment. If the wavelength of light is much larger than the distance of the electron from the nucleus, this moment is dominated by the electric dipole $\mathbf{d}$: neglecting all other terms of the multipole is known as the *electric-dipole approximation*[1]. The dipole can be taken to be a classical quantity or quantum mechanical operator. This provides a rather convenient link between the behaviour of the classical electric and magnetic fields, and the operator-based formalism underpinning the quantum mechanical Bloch equations. Treated classically, a medium composed of $\mathcal{N}_\mathrm{a}$ particles per unit volume has a macroscopic polarisation density $\mathbf{P} = \mathcal{N}_\mathrm{a}\langle\mathbf{d}\rangle$, i.e., the average dipole per unit volume. As an operator, the expectation value shows its relation to matrix elements of the density operator:

$$\langle\mathbf{d}\rangle = \sum_{m,n} \rho_{mn}\mathbf{d}_{nm}. \tag{2.1}$$

Under the dipole approximation, a medium interacts via the electric field only, so it is prudent to eliminate the magnetic field from the Maxwell-Bloch equations. This allows us to combine the four Maxwell equations into a single electromagnetic wave equation, along with an equation describing the source of these waves. Taking the curl of (III) and inserting the partial time derivative of (IV) gives

$$\nabla(\nabla\cdot\mathbf{E}) - \nabla^2\mathbf{E} = -\mu_0\partial_{tt}(\mathbf{P} + \epsilon_0\mathbf{E}), \tag{2.2}$$

where the vector identity $\nabla\times(\nabla\times\mathbf{E}) \equiv \nabla(\nabla\cdot\mathbf{E}) - \nabla^2\mathbf{E}$ has been used. Substituting (I) and rearranging

$$(\partial_{tt} - c^2\nabla^2)\mathbf{E} = -\frac{1}{\epsilon_0}(\partial_{tt}\mathbf{P} - c^2\nabla(\nabla\cdot\mathbf{P})), \tag{2.3}$$

where $c = 1/\sqrt{\mu_0\epsilon_0}$.

[1]The next most significant interaction terms are due to the electric quadrupole and the magnetic dipole moments. Assuming the electron-nucleus distance is equal to the Bohr radius ($\sim 5\times10^{-11}$ m), and the light is in the visible region of the spectrum (wavelength $\sim 5\times10^{-7}$ m), these terms are smaller than the electric dipole interaction by a factor known as the fine-structure constant $\alpha \sim 1/137$. Thus the electric dipole dominates unless the transition is dipole-forbidden. See reference [1].

Throughout this work we are considering only the propagation of plane waves in one dimension. A plane wave is defined as one in which points of constant phase are confined to a plane perpendicular to the direction of the phase velocity (see section 2.1.1). A realistic beam can be decomposed into plane-wave components with individual propagation directions. A full three-dimensional simulation of plane waves is required to account for diffraction and multiple beams which are not co-propagating. However, this can be computationally intensive and is not required to model many problems which can be accurately simulated with a simpler, faster one-dimensional method. For propagation in the z-direction, $\partial_x \mathbf{E} = \partial_y \mathbf{E} = 0$, and $E_z = P_z = 0$, hence we arrive at the Maxwell Wave Equation (MWE)

$$(\partial_{tt} - c^2 \partial_{zz})\mathbf{E} = -\frac{1}{\epsilon_0}\partial_{tt}\mathbf{P}. \qquad \text{MWE}$$

The left-hand side describes wave propagation of the electric field, with the right-hand side showing a source which is proportional to the second time derivative of the polarisation, i.e. accelerating charge creates electromagnetic fields.

The atom-light interaction can be understood in the following manner. A field enters a region of space containing an atomic medium. Energy is transfered from the field to the medium, creating dipoles. In turn, these dipoles radiate energy, creating new electric fields. Some of the energy may be transfered back into the field which created the dipoles, in which case there is interference between the newly created and original field. The modified field then travels on to another region of space where it is able to interact with the medium in a similar manner. The remainder of the energy may radiate as a new field distinct from the original, or dissipate non-radiatively e.g. by heating the medium.

2.1 Solving the Maxwell-Bloch equations

A natural starting point for finding solutions of the coupled atom-light system is to examine the individual systems. Literature abounds in solutions to Maxwell's equations, in the presence and absence of source terms, and in various media. There also exists extensive research into solutions of the

Bloch equations (and related formalism) describing the evolution of material systems under applied electric and magnetic fields. We will look first at analytic solutions to the Maxwell equations. We then look at the Bloch equations in more detail, but postpone solving them until we have chosen a specific atomic system to model.

2.1.1 *Maxwell's equations*

We seek classical plane-wave solutions to Maxwell's equations in the absence of sources ($\mathbf{P} = 0$). We have already come some way by deriving the Maxwell wave equation (MWE). The source-free MWE is a one-dimensional second-order partial differential equation which can be solved analytically by a variety of methods, among them d'Alembert's solution, via a Fourier transform, or by separation of variables. Plane-wave solutions can be found of the form

$$\mathbf{E}(z,t) = \mathbf{E}_0 \mathrm{e}^{\mathrm{i}(\mathbf{k}\cdot\mathbf{z}-\omega t)}. \tag{2.4}$$

This expression represents a travelling complex sinusoidal plane wave oscillating temporally at angular frequency ω and spatially at angular frequency $\mathbf{k}$ (usually referred to as the wavevector). The wave has a complex amplitude $\mathbf{E}_0$, its magnitude determining the peak of the oscillation whilst its phase determines the spatiotemporal point at which the oscillation begins. The wave propagates at the phase velocity $v_\mathrm{p} = \omega/k$ in the direction of the wavevector[2]. Inserting (2.4) into MWE gives a relationship between the angular frequency and wavevector (the dispersion relation):

$$\omega^2 = c^2(\mathbf{k}\cdot\hat{\mathbf{z}})^2, \tag{2.5}$$

where $\hat{\mathbf{z}}$ is a unit vector along the z-axis. This allows two values of the wavevector: either $\mathbf{k}$ is $k\hat{\mathbf{z}}$ (a forward-travelling wave) or $-k\hat{\mathbf{z}}$ (a backward-travelling wave). The speed of the wave is a constant c for all frequencies,

[2]The direction of wave propagation is more formally in the direction of energy transportation, given by the Poynting vector. The wavevector points in a direction normal to surfaces of constant phase, which travel at the phase velocity. In certain optical phenomena the phase and energy velocities are not parallel; in isotropic media and free-space, the wavevector and Poynting vector always point in the same direction. See reference [64] for further discussion.

and there is no attenuation, hence electromagnetic plane waves *in vacuo* are self-regenerating and dispersionless[3].

Note that as a physical quantity the electric field is a real-valued function, obtained by taking the real part of the complex function given by equation (2.4). Manipulating complex functions has certain mathematical advantages, such as summing waves of different phase, so we will tend to keep the electric field complex unless absolutely necessary. In typical experiments we measure the light not by its electric field, but rather by the energy it transfers to a detector. This is characterised by the intensity of the light, I, the average incident energy per unit area per unit time during an optical cycle $2\pi/\omega$. The intensity of travelling plane-wave electromagnetic radiation is [65]

$$I = nc\epsilon_0\langle E^2\rangle, \tag{2.6}$$

where the angular brackets denote a time-averaged quantity, and n is the refractive index of light (described in the next chapter). The phase of the light can be measured by various phase-sensitive detection methods, for example homodyne detection [66].

For wave propagation in interacting media, where $\mathbf{P}$ is non-zero, solutions to Maxwell's equations depend heavily on the form of the polarisation density, and exact analytic expressions are difficult to obtain. As $\mathbf{P}$ is inextricably tied to the evolution of the atomic system, we will go no further in our discussion of the electromagnetic field, and shift focus to the source polarisation density, the Bloch equations.

2.1.2 *Bloch equations*

The Bloch equations (V) are a set of linear first-order ordinary differential equations which, in a limited number of cases, can be solved analytically, e.g., for an AC electric field of constant amplitude applied to an ensemble of two-level atoms [67, 68]. Later on in this investigation, more complex

[3]The traditional use of the term 'dispersion' in optics denotes the phenomenon in which phase velocity is dependent on frequency. More generally, the term encompasses a wide range of phenomena related to phase irrespective of any frequency dependence, for which see 3.2.

forms of the field are considered, which require the use of numerical methods to arrive at a solution of ensemble evolution. As such we will concentrate our efforts on numerical analysis, and for the sake of brevity only solve the full Maxwell-Bloch equations. In this section we expand upon the Bloch equations and the source of the atom-light coupling.

The optical Bloch description of atom-light interaction is a semi-classical theory, in which the atomic system is treated using quantum formalism of wavefunctions and operators, and the field is treated classically. One limitation of the semi-classical theory is that it cannot give a complete description of spontaneous emission, but the treatment provided here is perfectly adequate for the macroscopic systems which are considered in this work.

There are three basic ways in which the state of an isolated atom in an external electromagnetic field can change: by absorption of a photon from the field, and by either stimulated or spontaneous emission of a photon. The first two processes involve the interaction of the atom with a photon in the applied field; the third is the atom interacting with virtual photons in the vacuum field. This relapse into quantum electrodynamics is necessary to describe the fundamental processes that are happening at the quantum level. To return to the regime in which the classical theory of light is valid, the following heuristic argument can be used. When the number of photons involved in an interaction is large then classical electrodynamics gives an acceptable description of the process. Such is the case of an intense field interacting with an atom. However, this is not the case for spontaneous emission, where the vacuum field is a continuum of empty modes into which a single photon is randomly emitted by an atom. The average behaviour can, however, be described in a semi-classical frame-work by treating the process of decay statistically. Hence we are free to use classical fields and atomic ensembles at the expense of information about individual emissive events.

Momentarily excluding spontaneous emission, the evolution of an ensemble of atoms which do not interact with each other is described by the master equation [63]

$$\frac{\partial \hat{\rho}}{\partial t} = \frac{\mathrm{i}}{\hbar}[\hat{\rho}, \mathscr{H}]. \tag{2.7}$$

Here, the right-hand side is the Liouvillian operator, being the commutator

of the density operator and the system Hamiltonian $\mathscr{H}$. The Hamiltonian is the sum of the bare-state atomic Hamiltonian $\mathscr{H}_{\mathrm{a}}$, and $\mathscr{H}_{\mathrm{int}}$, which describes the interaction between the atomic states and external fields. The form of the interaction Hamiltonian will be provided later (equation (2.12)); the atomic Hamiltonian is given by

$$\mathscr{H}_{\mathrm{a}} = \sum_{m} \hbar\omega_m |m\rangle\langle m|. \tag{2.8}$$

Here ω_m is the angular frequency of the state $|m\rangle$, which is related to the state's energy $\mathcal{E}_m = \hbar\omega_m$. Equation (2.7) is the density-matrix picture equivalent of the time-dependent Schrödinger equation. The master equation describes the population dynamics of a quantum state. With the specific Hamiltonian given above, the effects of absorption and stimulated emission on the atomic state are accounted for. To cover the effects of spontaneous emission it is necessary to include the interaction between the atomic system and the vacuum field, which results in decay from excited states to lower-lying states. This is achieved by adding the Lindblad operator to the right-hand side of (2.7), which is given by [69]

$$\hat{\Gamma} = \sum_{n,m<n} \sigma_{mn}\hat{\rho}\sigma_{mn}^{\dagger} - \tfrac{1}{2}\{\hat{\rho}, \sigma_{mn}^{\dagger}\sigma_{mn}\}, \tag{2.9}$$

where the double summation represents the fact that an excited state $|n\rangle$ can in general decay to any lower energy state $|m\rangle$, the curly brackets $\{\}$ denote the anticommutator, and $\sigma_{mn}/\sigma_{mn}^{\dagger}$ is the lowering/raising operator. As the name suggests, the lowering operator mediates the transition from state $|n\rangle \rightarrow |m\rangle$, given by

$$\sigma_{mn} = c_{mn}\sqrt{\Gamma_n}|m\rangle\langle n|, \tag{2.10}$$

$$\sigma_{mn}^{\dagger} = \sigma_{mn}^{*}. \tag{2.11}$$

These transitions happen at a rate given by the product of Γ_n, the total decay rate out of state $|n\rangle$, and $|c_{mn}|^2$, the branching ratio. The branching ratio expresses the fact that there is, in general, more than one state the atom can decay to. The sum of transition probabilities out of a state $|n\rangle$ is $\sum_m |c_{mn}|^2 = 1$.

The first term of the Lindblad operator is diagonal and describes repopulation of lower-lying energy states via spontaneous emission from excited states.

The second term describes two types of decay: decay of diagonal terms of the density operator (providing the mechanism for the process of repopulation); and decay of the off-diagonal terms, which results in decoherence.

For an atomic ensemble initially found in a pure state, there is maximum phase coherence between the atomic states (see appendix A). The interaction of the ensemble with a coherent electric field preserves this phase coherence. However, random processes on particles within the ensemble, such as collisions and spontaneous decay, can alter an individual particle's wavefunction such that it is no longer in phase with other members of the ensemble. These incoherent processes result in an ensemble which can no longer be described by a pure state.

The electric multipole moment provides a means by which atomic states evolve in response to an external electric field. Under the assumption that the spatial variation of the field is sufficiently small such that field can be taken to be constant over the extent of the atom, and that the multipole moment is dominated by the dipole, then the interaction Hamiltonian is

$$\mathscr{H}_{\text{int}} = -\mathbf{d} \cdot \mathbf{E}, \tag{2.12}$$

$$\mathbf{d} = \sum_{n,m<n} \mathbf{d}_{mn}|m\rangle\langle n| + \mathbf{d}_{nm}|n\rangle\langle m|, \tag{2.13}$$

where $\mathbf{d}$ is the dipole operator. The dipole operator has matrix elements $\langle m|\mathbf{d}|m\rangle = 0$, $\langle m|\mathbf{d}|n\rangle = \mathbf{d}_{mn}$, and as a hermitian operator the elements $\mathbf{d}_{mn} = \mathbf{d}^*_{nm}$. The diagonal elements evaluate to zero since $\mathbf{d}$ has odd parity due to its vectorial nature. The left-hand side of (2.13) acts to lower the atomic state from $|n\rangle$ to $|m\rangle$ i.e. stimulated emission, whilst the right-hand side raises the state i.e. absorption.

2.2 Time-scale approximations

Before solving the Maxwell-Bloch equations, an important point must be addressed. The frequency of light in the visible region of the electromagnetic spectrum is of the order of hundreds of terahertz, thus having a peak-to-peak duration of a few femtoseconds. In this thesis we are interested in observing gigahertz phenomena lasting up to a few microseconds. This large disparity

in magnitude warrants a simplification to the Maxwell equations known as the *slowly-varying envelope approximation*, and a related simplification to the Bloch equations, the *rotating-wave approximation*. We make these approximations for two reasons. Firstly, the rapid oscillations in field average to zero over the observation time-scale considered and so are justifiably neglected. Secondly, without factoring out the high-frequency components our numerical model would require petahertz sampling frequency and sub-femtosecond time resolution, leading to unfeasibly large computational memory allocation and calculation time.

2.2.1 *Slowly-varying envelope approximation*

The electric field can be written as the product of a carrier wave and an envelope function. The carrier takes the form of a single-frequency solution to the MWE equation, with an angular frequency and wavevector of ω_c and $\mathbf{k}_\mathrm{c}$ respectively. The envelope, $\tilde{\mathbf{E}}(z,t)$, is a much more slowly-varying quantity which acts to modulate the amplitude and phase of the carrier. The intention behind factorising the electric field is that we are much more interested in the slow time dependence, and by factoring out the rapidly-varying carrier from the field we are also able to factor it out of the system of equations we are required to solve.

Writing the electric field in terms of a forward-travelling carrier wave, with angular frequency ω_c and wavevector k_c,

$$\mathbf{E} = \mathrm{Re}[\tilde{\mathbf{E}}\mathrm{e}^{\mathrm{i}(k_\mathrm{c}z-\omega_\mathrm{c}t)}] = \tfrac{1}{2}\tilde{\mathbf{E}}\mathrm{e}^{\mathrm{i}(k_\mathrm{c}z-\omega_\mathrm{c}t)} + \tfrac{1}{2}\tilde{\mathbf{E}}^*\mathrm{e}^{-\mathrm{i}(k_\mathrm{c}z-\omega_\mathrm{c}t)}, \tag{2.14}$$

where the field is the sum of positive and negative frequencies waves. Both the negative and positive wave is fully determined by the other, so that it is possible to consider the propagation of one wave in isolation. Henceforth the negative wave is neglected from further consideration. Given that the polarisation has its origins in the electric field, a similar decomposition can be made:

$$\mathbf{P} = \tilde{\mathbf{P}}\mathrm{e}^{\mathrm{i}(k_\mathrm{c}z-\omega_\mathrm{c}t)} + \tilde{\mathbf{P}}^*\mathrm{e}^{-\mathrm{i}(k_\mathrm{c}z-\omega_\mathrm{c}t)}. \tag{2.15}$$

Substituting for the field and polarisation into MWE gives

$$\left[(\partial_{tt} - \mathrm{i}2\omega_\mathrm{c}\partial_t) - c^2(\partial_{zz} + \mathrm{i}2k_\mathrm{c}\partial_z) - (\omega_\mathrm{c}^2 - c^2k_\mathrm{c}^2)\right]\tilde{\mathbf{E}} = \\ -\frac{2}{\epsilon_0}\left[\partial_{tt} - \mathrm{i}2\omega_\mathrm{c}\partial_t - \omega_\mathrm{c}^2\right]\tilde{\mathbf{P}}. \quad (2.16)$$

The last term of the left-hand side evaluates to zero since the usual dispersion relation applies to the carrier i.e. $\omega_\mathrm{c}^2 = c^2k_\mathrm{c}^2$. If the change of the envelope is small over a distance of the order of the wavelength, then

$$|\partial_{zz}\tilde{\mathbf{E}}| \ll |k_\mathrm{c}\partial_z\tilde{\mathbf{E}}|. \quad (2.17)$$

Similarly, if the envelope doesn't change significantly in a optical cycle

$$|\partial_{tt}\tilde{\mathbf{E}}| \ll |\omega_\mathrm{c}\partial_t\tilde{\mathbf{E}}|. \quad (2.18)$$

Similar arguments can be made for the polarisation density, in which we can also neglect the first-order time derivative. Making use of these inequalities is known as the slowly-varying envelope approximation (SVEA) [70], and reduces the second-order MWE to a first-order equation

$$(\partial_t + c\partial_z)\tilde{\mathbf{E}} = \mathrm{i}\frac{\omega_\mathrm{c}}{\epsilon_0}\tilde{\mathbf{P}}, \quad (2.19)$$

which has solutions, *in vacuo*, of the form

$$\tilde{\mathbf{E}} = \mathbf{E}_0\mathrm{e}^{\mathrm{i}(\Delta_k z - \Delta_\omega t)}, \quad (2.20)$$

$$\Delta_\omega = \omega - \omega_\mathrm{c}, \quad (2.21)$$

$$\Delta_k = k - k_\mathrm{c}, \quad (2.22)$$

where $\mathbf{E}_0$ is constant, and Δ_ω and Δ_k are the detunings from the carrier angular frequency and wavevector, respectively. These solutions are the monochromatic frequency elements of the envelope. With the definition of the phase element (2.20), the expressions (2.17) and (2.18) shows that the equalities $|\Delta_k| \ll k_\mathrm{c}, |\Delta_\omega| \ll \omega_\mathrm{c}$ must be met for the envelope wave equation to be valid. For an envelope composed of many monochromatic waves, this condition amounts to the maximum frequency extent of the envelope (the bandwidth) being much less than the frequency of the carrier.

The free-space dispersion relation obtained from (2.19) with envelope (2.20) is $\Delta_\omega = c\Delta_k$, hence $\omega - ck = \omega_\mathrm{c} - ck_\mathrm{c}$. The right-hand side is equal to zero

(by definition), and therefore $\omega = ck$ which is consistent with the forward travelling wave solution. If instead a backward moving carrier wave was substituted into (2.19), by replacing $k_c \to -k_c$ in (2.22), the dispersion relation no longer holds: the equation derived is valid for forward moving waves only. This is in contrast to the MWE, which is valid for both forward and backward moving waves. It is not surprising that only forward motion is possible, since it was necessary to constrain the motion to one particular direction and in this case a forward travelling carrier was chosen. This situation is illustrated in figure 2.1, where for small detunings only the positive solution to the dispersion relation is represented. Repeating the above analysis for backward motion gives the envelope equation

$$(\partial_t - c\partial_z)\tilde{\mathbf{E}} = \mathrm{i}\frac{\omega_c}{\epsilon_0}\tilde{\mathbf{P}}, \tag{2.23}$$

which is simply the replacement $\partial_z \to -\partial_z$ in the forward wave equation. The loss of the backward travelling wave solution is only of significance in high density media where reflections are important [71] or if counter-propagating fields are created due to the nonlinear polarisation [72].

The light intensity under the slowly-varying envelope approximation can be found from (2.6) by integrating over an optical cycle $2\pi/\omega_c$, the duration of which is sufficiently small that the magnitude and phase of the envelope are effectively constant. This gives an intensity

$$I = \tfrac{1}{2}nc\epsilon_0|\tilde{E}|^2. \tag{2.24}$$

2.2.2 *Rotating-wave approximation*

The slowly-varying envelope equation was made based on the fact that for a small bandwidth envelope it is possible to separate the electric field into the product of a slowly-varying envelope and a rapidly-varying carrier wave. In this section a similar analysis is undertaken for the Bloch equations, which is exactly equivalent to the approximation made upon Maxwell's equations. In this way, it is possible to follow the ensemble evolution due to the slow dynamics of the envelope, ignoring the effects of the envelope's carrier frequency.

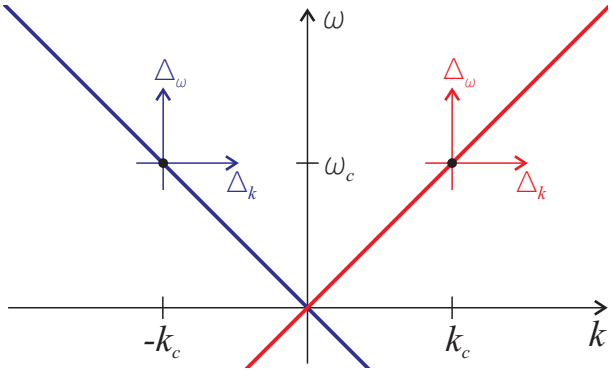

Figure 2.1: The dispersion relation for light propagation *in vacuo*. The red line (of gradient $+c$) denotes the forward-travelling branch, whilst the blue line (of gradient $-c$) denotes the backward-travelling branch. The red(blue) inset axes gives the detuning around the forward(backward)-travelling, positive-frequency carrier wave.

Assuming for clarity a single atomic resonance, the carrier wave is detuned by $\Delta = \omega_c - \omega_0$ from resonance (here ω_0 is the resonant frequency of the atom). Introducing the slowly-varying electric field into the dipole interaction (2.13) produces

$$\mathbf{d}\cdot\mathbf{E} = \tfrac{1}{2}\mathbf{d}_{21}\cdot\tilde{\mathbf{E}}e^{-i\omega_c t}|2\rangle\langle 1| + \tfrac{1}{2}\mathbf{d}_{12}\cdot\tilde{\mathbf{E}}^* e^{i\omega_c t}|1\rangle\langle 2| + \tag{2.25}$$

$$\tfrac{1}{2}\mathbf{d}_{12}\cdot\tilde{\mathbf{E}}e^{-i\omega_c t}|1\rangle\langle 2| + \tfrac{1}{2}\mathbf{d}_{21}\cdot\tilde{\mathbf{E}}^* e^{i\omega_c t}|2\rangle\langle 1|. \tag{2.26}$$

The first two terms represent, respectively, the excitation of an atom along with absorption of light, and the de-excitation of an atom along with emission of light. The last two terms are energy non-conserving processes, respectively the de-excitation of an atom and simultaneous absorption of light, and atomic excitation with emission of light. For light at a frequency close to resonance the energy non-conserving processes have little effect on the ensemble dynamics. Thus we can neglect these terms in the Bloch equations. This is known as the rotating-wave approximation. Further discussion can be found in references [1, 2].

In addition to the rapidly-varying electric field, we saw in section 2.2.1 that the polarisation density, and by implication the density matrix, also contains

high-frequency components. Via the relations $\mathbf{P} = \mathcal{N}_\mathrm{a}\langle\mathbf{d}\rangle$, (2.1), and (2.15)

$$\mathbf{P} = \mathcal{N}_\mathrm{a} \sum_{n,m<n} \left(\rho_{nm}\mathbf{d}_{mn} + \rho_{mn}\mathbf{d}_{nm}\right), \tag{2.27}$$

$$= \tilde{\mathbf{P}}\mathrm{e}^{-\mathrm{i}\omega_\mathrm{c}t} + \tilde{\mathbf{P}}^*\mathrm{e}^{\mathrm{i}\omega_\mathrm{c}t}, \tag{2.28}$$

implying that the coherence term ρ_{nm} is the product of a slowly-varying envelope $\tilde{\rho}_{nm}$ and carrier $\mathrm{e}^{-\mathrm{i}\omega_\mathrm{c}t}$. Care needs to be taken when multiple fields exist as there is no single carrier frequency ω_c at which all coherence terms oscillate.

2.3 A two-level atom ensemble subjected to an electromagnetic field

We are now in a position to solve the Maxwell-Bloch equations. Consider the following atom-light system [2]. The atom consists of two energy states: the ground state $|1\rangle$ and the higher-energy excited state $|2\rangle$, separated in energy by $\hbar\omega_0$. Decay out of the excited state happens at a rate Γ, and all excited state population lost by this process returns to the ground state. There are thus four density matrix elements: the populations of the ground and excited states ρ_{11} and ρ_{22}, respectively, and the coherence terms ρ_{12} and ρ_{12}. Due to conservation of population $\rho_{11} + \rho_{22} = 1$. An external electric field is applied with angular frequency ω_c, which is blue-detuned from resonance by $\Delta = \omega_\mathrm{c} - \omega_0$. The atom-light coupling is expressed via the dipole operator $\mathbf{d} = \mathbf{d}_0(|1\rangle\langle 2| + |2\rangle\langle 1|)$. With this information inserted into the master equation of (V), the following set of coupled differential equations are obtained:

$$\dot{\rho}_{22} = -\Gamma\rho_{22} - \mathrm{i}\frac{1}{\hbar}(\mathbf{d}_0 \cdot \mathbf{E}^*\rho_{21} - \mathbf{d}_0 \cdot \mathbf{E}\rho_{12}) = -\Gamma\rho_{22} - \frac{2}{\hbar}\mathrm{Im}[\mathbf{d}_0 \cdot \mathbf{E}\rho_{21}^*], \tag{2.29}$$

$$\dot{\rho}_{11} = -\dot{\rho}_{22}, \tag{2.30}$$

$$\dot{\rho}_{21} = -(\tfrac{1}{2}\Gamma + \mathrm{i}\omega_0)\rho_{21} - \mathrm{i}\frac{1}{\hbar}\mathbf{d}_0 \cdot \mathbf{E}(\rho_{22} - \rho_{11}), \tag{2.31}$$

$$\dot{\rho}_{12} = \dot{\rho}_{21}^*. \tag{2.32}$$

We then make the slowly-varying envelope and rotating-wave approximations, replace $\rho_{21} \to \tilde{\rho}_{21}\mathrm{e}^{-i\omega_\mathrm{c}t}$ and note that slowly-varying polarisation den-

sity of the system is $\tilde{\mathbf{P}} = \mathcal{N}_\mathrm{a}\mathbf{d}_0\tilde{\rho}_{21}$. Hence the Maxwell-Bloch equations can be formed by combining the above equations with (2.19):

$$(\partial_t + c\partial_z)\tilde{\mathbf{E}} = \mathrm{i}\frac{\mathcal{N}_\mathrm{a}\mathbf{d}_0\omega_\mathrm{c}}{\epsilon_0}\tilde{\rho}_{21}, \tag{2.33}$$

$$\dot{\rho}_{22} = -\Gamma\rho_{22} - \mathrm{Im}[\Omega\tilde{\rho}^*_{21}], \tag{2.34}$$

$$\dot{\tilde{\rho}}_{21} = -(\tfrac{1}{2}\Gamma - \mathrm{i}\Delta)\tilde{\rho}_{21} - \mathrm{i}\tfrac{1}{2}\Omega(2\rho_{22} - 1), \tag{2.35}$$

where $\Omega = \mathbf{d}_0 \cdot \tilde{\mathbf{E}}/\hbar$ is known as the Rabi angular frequency of the transition (after I.I.Rabi [73]), and is the rate at which transitions are coherently induced between atomic levels. Its significance is briefly dealt with in section 2.3.2.

The numerical model used to solves the Maxwell-Bloch equations is described in appendix B.

2.3.1 *Results of continuous-wave propagation*

We will begin by solving the Maxwell-Bloch equations for an electromagnetic field designed to mimic the output of a laser operating in continuous-wave mode, and observe the atom-light system as it achieves an equilibrium state. Ideally, this would involve light of a single frequency instantaneously switching from zero to a constant amplitude and phase. Quite apart from the impossibility of this situation from an experimental perspective, the numerical scheme we use cannot model discontinuities in field[4]. To avoid this problem we will consider a Gaussian switch-on so that the field begins at an infinitesimally small value before smoothly reaching a constant peak amplitude. Consider a real-valued electric field envelope at $z = 0$ linearly polarised orthogonal to the z axis, of the form

$$\begin{aligned} \tilde{E} &= A_0 \exp\left[-2\ln 2\left(\frac{t - t_0}{\Delta t}\right)^2\right] && \text{for } t \leq t_0, \\ &= A_0 && \text{for } t > t_0. \end{aligned} \tag{2.36}$$

[4]This is due to the so-called *Gibbs phenomenon*, in which attempts to interpolate a function involving a discontinuity causes spurious oscillations, or 'ringing' around the discontinuity.

The turning-on stage of the envelope is governed by Δt, which is twice the time it takes for the intensity ($I \propto |\tilde{E}|^2$) to rise from half of its maximum value to its peak. We will see later when we talk about pulsed light that Δt is the full-width at half-maximum of the Gaussian intensity profile. We refer to the point t_0 as the envelope front.

We use the following parameters (see appendix C) to represent light resonant with the Rb D_1 transition (in the absence of hyperfine structure): $\omega_c = \omega_0 = 2\pi(377\text{ THz})$, $\mathbf{d}_0 = 5.182ea_0\hat{\mathbf{x}}$ (with the Bohr radius $a_0 = 5.292 \times 10^{-11}$ m and electronic charge $e = 1.602 \times 10^{-19}$ C), $k_c = k_0 = 2\pi(795\text{ nm})^{-1}$, $\Gamma = 2\pi(5.75\text{ MHz})$ (hence excited state lifetime $1/\Gamma = 27.7$ ns). The medium, of length $L = 32$ m has a number density of $\mathcal{N}_a = 10^{11}$ m^{-3}. The reason for the medium being unrealistically long is that we are observing the atom-light interaction over such a long duration (hundreds of nanoseconds). This issue is solely due to the numerical scheme we use: see appendix B for discussion.

Results for the propagation of resonant (i.e. $\Delta = 0$), low-intensity light are shown in figures 2.2 and 2.3. The incident intensity of light $I_0 \propto A_0^2$ is equal to $10^{-3}I_{\text{sat}}$; the significance of the saturation intensity, I_{sat}, will be elaborated in section 2.3.2. The electric field has the temporal profile (2.36) with $\Delta t = 0.55/\Gamma$ (15.3 ns). The normalised intensity $I/I_0 = |\tilde{E}|^2/A_0^2$ is shown in figures 2.2(a), 2.3(a). At $t = 0$ the envelope front enters the medium and begins to interact with the ensemble. The front of the envelope passes through the medium (at a speed close to that *in vacuo*) and re-enters free-space at a small loss of amplitude; the main body is attenuated to a larger degree. Eventually, after several excited state lifetimes, the intensity reaches a time-independent state at each position inside the medium. The evolution of the medium is shown in figures 2.2 and 2.3: part (b) shows the excited state population whilst (c) shows the imaginary component of the coherence (NB: the real part of the coherence is zero on resonance). It can be seen that there is a small delay between the front of the envelope entering the medium and the onset of transfer of population to the excited state, resulting in little absorption of the envelope front. This is because the medium cannot respond instantaneously to the electric field. As with the light, the ensemble tends towards a steady-state.

The physical argument behind the atom-light interaction is as follows. As the

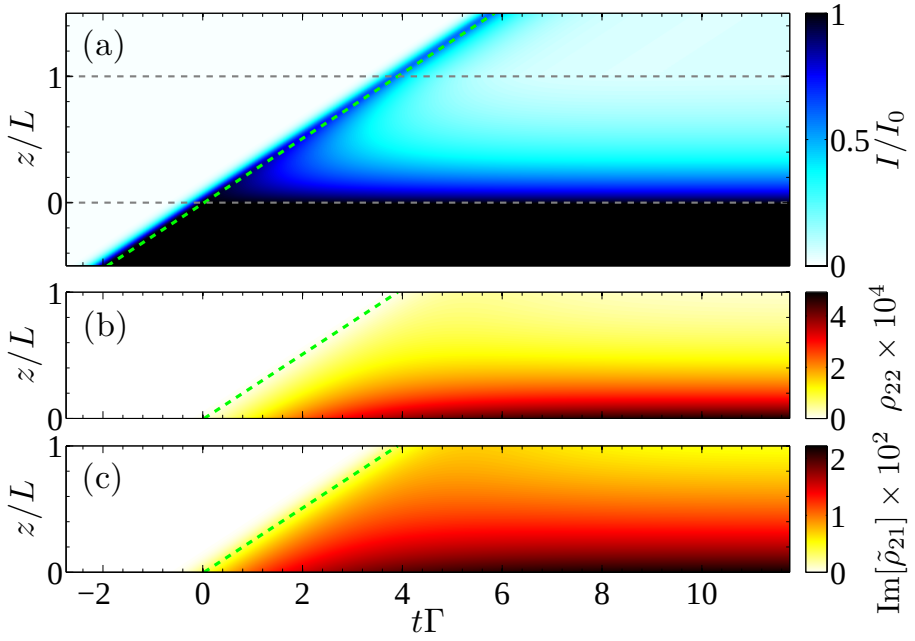

Figure 2.2: Numerical solutions to the Maxwell-Bloch equations, shown versus z in units of medium length L and t in units of the excited state lifetime $1/\Gamma$. (a) The normalised intensity of light I/I_0, (b) the excited state population $\rho_{22} \times 10^4$, (c) the imaginary part of the coherence $\mathrm{Im}[\tilde{\rho}_{21}] \times 10^2$. The horizontal dashed lines delineate the extent of the medium; the dashed green line represents the trajectory a wave travelling in free-space would take.

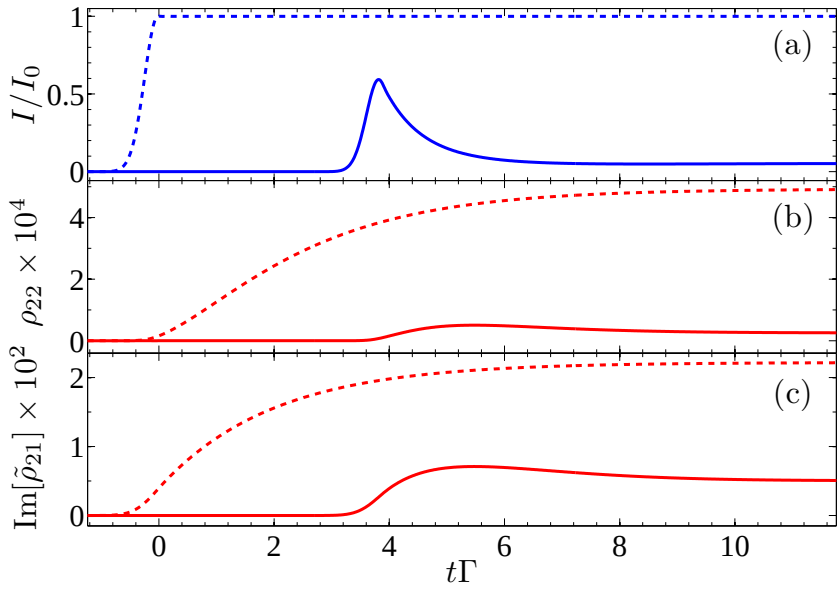

Figure 2.3: Data shown in figure 2.2(a)-(c) versus t only. Dashed curves show the data at the entrance to the medium ($z = 0$), solid curves at the exit ($z = L$).

envelope enters the medium, its leading edge excites a polarisation (represented by the coherence ρ_{21}) in a thin slice at the entrance. This polarisation radiates an electric field π rad out of phase with the input electric field. The π rad phase shift is a combination of two factors: the first $\pi/2$ lag is due to a resonant wave driving oscillations of a single absorbing dipole; the second $\pi/2$ lag comes from interference between all of the contributions from a plane of dipoles. The summing of these contributions to reach the total phase shift is essentially buried in the formalism of Maxwell's equations: see reference [74] for further discussion. As the dipole-radiated field is coherent with the applied field they interfere destructively, and as such the field incident upon the next slice of the medium is attenuated. The energy lost by the pulse is transfered to the medium in the form of an atomic excitation ρ_{22}. This excitation is not stable, and decay back to the ground state releases this energy in the form of spontaneously emitted light, which is incoherent with respect to the excitation field. Spontaneous emission also reduces the degree of coherence between the ensemble and applied electric field. Eventually the rate at which electromagnetic energy is absorbed is balanced by the rate at which light is spontaneously emitted, and at this point equilibrium is achieved between the field and ensemble, which is the subject of the next section.

2.3.2 *Steady-state solutions of the Maxwell-Bloch equations*

We saw in the last section that under constant illumination the atomic system reaches a steady-state. This is a well known situation epitomised by the Rabi problem [73] (with the inclusion of decay mechanisms), a solution to the Bloch equations. In brief, the atoms cycle between the ground and excited state at the Rabi angular frequency Ω, represented by the populations ρ_{11} and ρ_{22}. The rate at which photons are absorbed by the medium is $-\mathrm{Im}[\Omega\tilde{\rho}_{21}^{*}]$ (see chapter 10), where $\tilde{\rho}_{21}$ represents the atomic coherence. Decay from the excited state removes photons from the system via spontaneous emission, happening at the rate $-\Gamma\rho_{22}$; decay also serves to damp the Rabi oscillations by dephasing the coherence[5] which happens at the rate $-\frac{\Gamma}{2}\tilde{\rho}_{21}$. Eventually a

[5] Additional dephasing mechanisms e.g. collisions can increase the coherence decay rate; here the decay rate is simply the average decay rate of the excited and ground state

time is reached at which the rate of absorption is equal to the rate of decay, at which point the matrix elements of $\hat{\rho}$ cease to change.

The equilibrium state of the Maxwell-Bloch equations differs from the steady-state of the Rabi problem with respect to the electromagnetic field. In the Bloch equations the magnitude of the electric field is time-independent and thus begins in a steady state. In the Maxwell-Bloch equations the electromagnetic field propagates through space, so for a given slice of medium the incident field is modified due to atom-light interaction. If absorption is significant over a slice of medium the field seen by the next slice is different to that of the first, and thus the medium sees a field varying in both space and time. An equilibrium between the light and atoms is reached when the rate at which energy is lost from the field is equal to the rate at which energy is lost from the medium through spontaneous emission.

Steady-state solutions can be found by setting the time derivatives to zero in equations (2.33)-(2.35). Then, rearranging the equations we arrive at

$$\partial_z \tilde{\mathbf{E}} = \mathrm{i}\frac{\mathcal{N}_\mathrm{a}\mathbf{d}_0\omega_\mathrm{c}}{c\epsilon_0}\tilde{\rho}_{21}^{\mathrm{st}}, \tag{2.37}$$

$$\rho_{22}^{\mathrm{st}} = \tfrac{1}{2}\frac{s}{1+s}, \tag{2.38}$$

$$\tilde{\rho}_{21}^{\mathrm{st}} = \frac{\mathrm{i}\Gamma - 2\Delta}{\Omega^*}\rho_{22}^{\mathrm{st}}. \tag{2.39}$$

Here the saturation parameter s has been introduced, where

$$s = \frac{I/I_{\mathrm{sat}}}{1+4(\Delta/\Gamma)^2}, \tag{2.40}$$

$$I/I_{\mathrm{sat}} = 2(|\Omega|/\Gamma)^2, \tag{2.41}$$

$$I_{\mathrm{sat}} = \tfrac{1}{4}c\epsilon_0(\hbar\Gamma/\mathrm{d})^2, \tag{2.42}$$

where the constant I_{sat} is the saturation intensity of resonant light, the significance of which is given below. We now have a set of coupled equations dependent on z, though the situation is complicated by the fact the equations now depend on the Rabi angular frequency $\Omega^* \propto \tilde{E}^*$ and the intensity $I \propto |\tilde{E}|^2$. Since we seek analytic solutions, we can simplify matters by looking at the intensity rather than the electric field. From equations (2.24) and (2.37) we

$\frac{1}{2}\times\Gamma + \frac{1}{2}\times 0 = \frac{1}{2}\Gamma$. See reference [63].

can obtain the gradient in intensity using $\partial_z I = \frac{1}{2}c\epsilon_0\partial_z|\tilde{E}|^2 = c\epsilon_0\mathrm{Re}[\tilde{E}^*\partial_z\tilde{E}]$. Thus

$$\partial_z I = -\mathcal{N}_\mathrm{a}\hbar\omega_\mathrm{c}\Gamma\rho_{22}^\mathrm{st}, \tag{2.43}$$

$$\rho_{22}^\mathrm{st} = \tfrac{1}{2}\frac{s}{1+s}, \tag{2.44}$$

$$|\tilde{\rho}_{21}^\mathrm{st}| = \tfrac{1}{\sqrt{2}}\frac{\sqrt{s}}{1+s}, \tag{2.45}$$

where we have taken the magnitude of the coherence to get an equation dependent on s.

Consider a thin slice of medium, of thickness $\mathrm{d}z$, upon which light of intensity I falls. Assuming the fraction of light leaving the slab, $\mathrm{d}I$, is proportional to its thickness,

$$\mathrm{d}I = -\beta I\mathrm{d}z, \tag{2.46}$$

where

$$\beta = \frac{\alpha_0}{\alpha_0/\alpha + I/I_\mathrm{sat}}, \tag{2.47}$$

$$\alpha = \frac{\alpha_0}{1+4(\Delta/\Gamma)^2}. \tag{2.48}$$

The factor β is intensity dependent, except for low light intensities in which case α, which is known as the absorption coefficient, dominates the attenuation of light. The constant $\alpha_0 = \mathcal{N}_\mathrm{a}\hbar\omega_\mathrm{c}\Gamma/2I_\mathrm{sat}$ is the resonant absorption coefficient. The transmission through an extended medium is given by the solution of the differential equation (2.46), which can be solved exactly in the regimes of low and high saturation, respectively

$$I = \begin{cases} I_0\exp[-\alpha z] & \text{for } s \ll 1, \quad (2.49) \\ I_0 - \alpha_0 I_\mathrm{sat} z & \text{for } s \gg 1. \quad (2.50) \end{cases}$$

We have assumed that α_0 is independent of displacement inside the medium, z, which is true for a homogeneous material. Equation (2.49) is the well-known Beer-Lambert law [16], demonstrating an exponential attenuation of light with distance. The linear decrease of light expressed by equation (2.50) is less familiar and leads to significantly higher transmission than the Beer-Lambert law. It is a result of intense light saturating the absorbing material, in which case the medium is said to be 'bleached'.

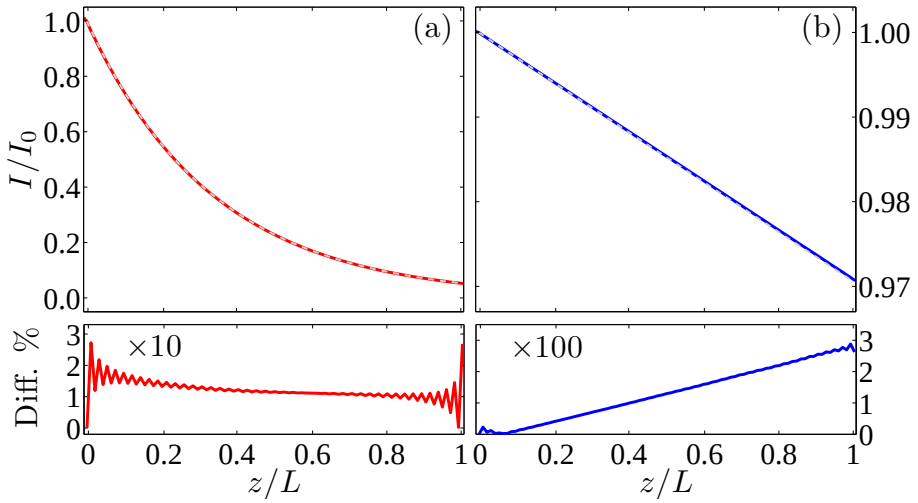

Figure 2.4: Steady-state of the light as a function of displacement through the medium, for (a) a weak field of $I_0 = 10^{-3} I_{\text{sat}}$ and (b) a strong field of $I_0 = 100 I_{\text{sat}}$. The top panels show the numerical solution as a solid curve, with the dashed grey curve showing the analytic prediction. The bottom panels shows the percentage difference between the numerical and analytical curves.

The intensity profile of figure 2.2 as a function of displacement through the medium, at equilibrium, is shown in figure 2.4(a). The exponential attenuation with distance expected by the Beer-Lambert law is in good agreement with the numerical solution, with a resonant absorption coefficient of $\alpha_0 = 0.09$ m^{-1}. We also show the numerical solution at equilibrium for a high intensity light field in figure 2.4(b). In contrast to the exponential decrease of weak light, strong light follows a linear decrease with distance, with a characteristic absorption coefficient $\alpha_0 I_{\text{sat}}/I_0 = 0.0009$ m^{-1}. Discrepancy between the numerical and analytic solutions is low, the most significant deviation being at the boundary of the medium. This is due to a discontinuity in the gradient of the field between the medium and free-space, an artifact of the numerical model (for which see appendix B).

With regards to the material properties in the steady-state, we see in equations (2.38) and (2.39) that the density matrix elements depend on light intensity via the saturation parameter s. Using the fact that I and the matrix elements of $\hat{\rho}$ are functions of displacement, it is possible to map the numerical solutions we have calculated for ρ_{22}^{st} and $\tilde{\rho}_{21}^{\text{st}}$ to a function of s. For a number of different incident light intensities, a composite plot of the matrix

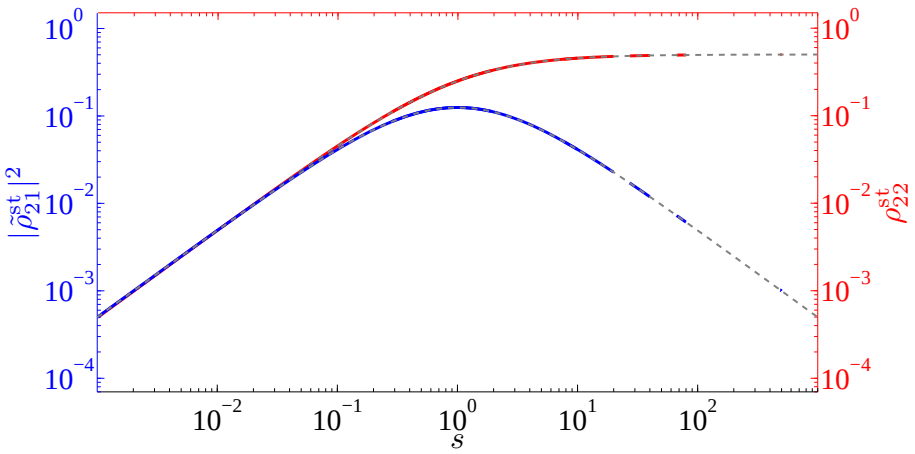

Figure 2.5: Steady-state dependence of the excited state population (red curve) and coherence (blue) on the saturation parameter s. Solid curves show numerical solutions, dashed curves show the analytic solutions.

elements of $\hat{\rho}$ versus s can be produced, giving figure 2.5. At $s = 1$ the excited state population is $\rho_{22}^{\rm st} = 1/4$, and the coherence reaches a peak value of $|\tilde{\rho}_{21}^{\rm st}| = 1/\sqrt{8}$. As $s \to \infty$, the excited state population tends to one half, whilst the coherence tends to zero: the incident field therefore saturates the transition. The physical explanation for the saturation phenomenon is dealt with in reference [63], we only give a cursory treatment of it here. Close to resonance, the electric field emitted by an atom is proportional its dipole moment $\mathbf{d}$. The average intensity $\langle I \rangle$ of this electric field is proportional to the excited state population $\rho_{22}^{\rm st}$. We can make a distinction between the fraction of the light which is coherent with the driving field $\langle I_{\rm coh} \rangle \propto |\tilde{\rho}_{21}^{\rm st}|^2$, and the fraction due to spontaneous emission which is incoherent $\langle I_{\rm incoh} \rangle \propto \rho_{22}^{\rm st} - |\tilde{\rho}_{21}^{\rm st}|^2$, illustrated in figure 2.6. The coherent fraction is due to the radiation of the mean dipole moment; the incoherent fraction is due to fluctuations around this mean. For $s \ll 1$, scattering is dominated by coherent light. At $s = 1$ the coherent fraction reaches a peak, and is equal to the incoherent fraction. As $s \to \infty$ the coherent fraction becomes negligible, whilst the incoherent fraction tends to one half, becoming independent of the incident field. This expresses the fact that the atom cannot emit more than $\Gamma/2$ photons per unit time, because the atom spends on average half its time in the excited state.

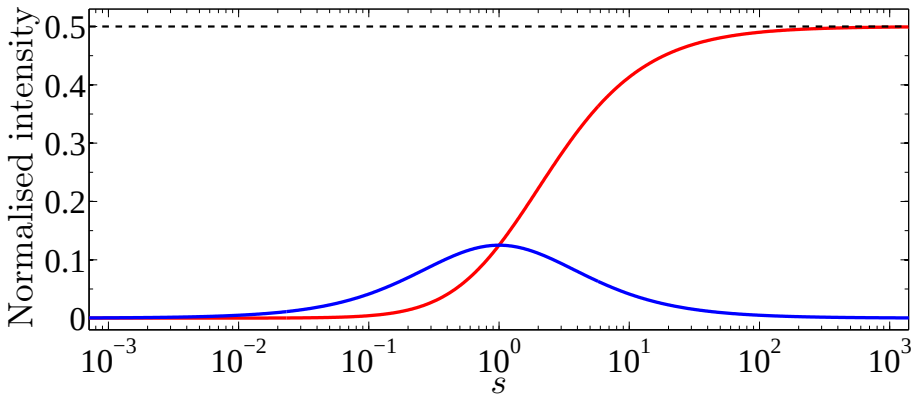

Figure 2.6: Steady-state dependence of the emitted light intensity, showing the coherent fraction (blue curve) and incoherent fraction (red) versus the saturation parameter s. The dashed line at 0.5 marks the asymptotic limit of the incoherent scattering process.

2.3.3 *Results of pulse propagation*

In this section we consider the propagation of electromagnetic fields which have finite duration, switching from zero to a finite amplitude before returning to zero. In contrast to the pseudo-continuous field we saw in the last section, the atoms do not have enough time in which to reach equilibrium with the applied field. However, we shall see in section 2.4 that for low-intensity fields there exists a quasi-static regime akin to the steady-state achieved via constant illumination.

We use the same conditions as per the continuous-wave propagation in section 2.3.1, the exceptions being the length ($L = 16$ m) and density ($\mathcal{N}_a = 1.7\times10^{11}$ m^{-3}) of the medium, and of course the envelope of the electric field. The envelope takes the form of a Gaussian, $\tilde{E} = A_0 \exp[-2\ln2((t-t_0)/\Delta t)^2]$, with an amplitude such that the initial intensity $I_0 = 10^{-3} I_{\text{sat}}$ and full-width at half-maximum (FWHM) $\Delta t = 0.74\Gamma$ (20.4 ns). From figures 2.7(a) and 2.8(a) we see the pulse traverses the medium in a similar manner to the front of the continuous-wave envelope (of section 2.3.1), suffering moderate absorption. A 'tail' is seen to emerge from the main peak, which is a well-known consequence of a resonant pulse having a duration comparable to or smaller than the excited state lifetime [75, 76]. In figure 2.7(b) (and 2.8(b)) we see transfer of population to the excited state, peaking after the main

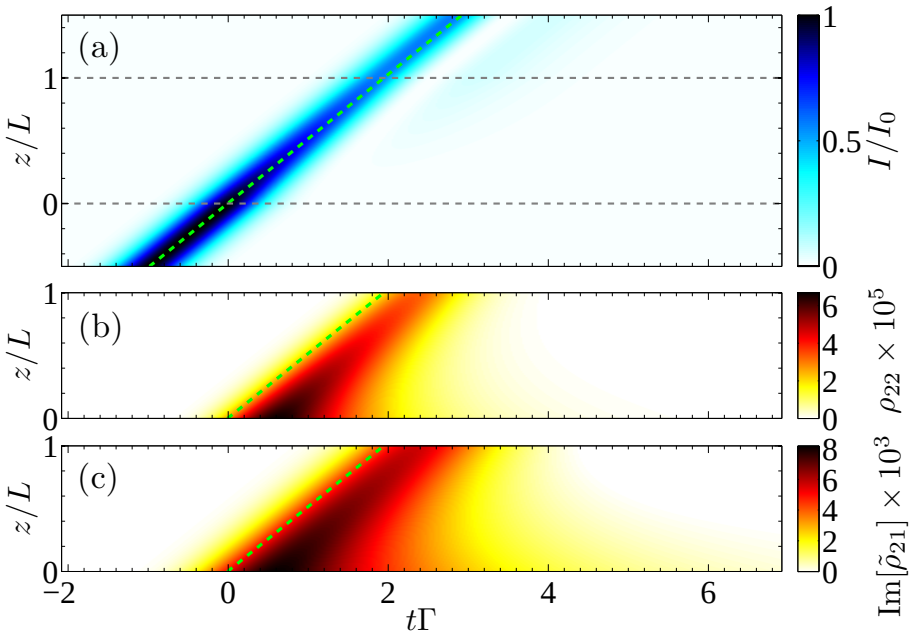

Figure 2.7: Numerical solutions to the Maxwell-Bloch equations, for pulsed light. (a) The normalised intensity of light I/I_0, (b) the excited state population $\rho_{22} \times 10^5$, (c) the imaginary part of the coherence $\mathrm{Im}[\tilde{\rho}_{21}] \times 10^3$. The horizontal dashed lines delineate the extent of the medium; the dashed green line represents the trajectory a wave travelling in free-space would take.

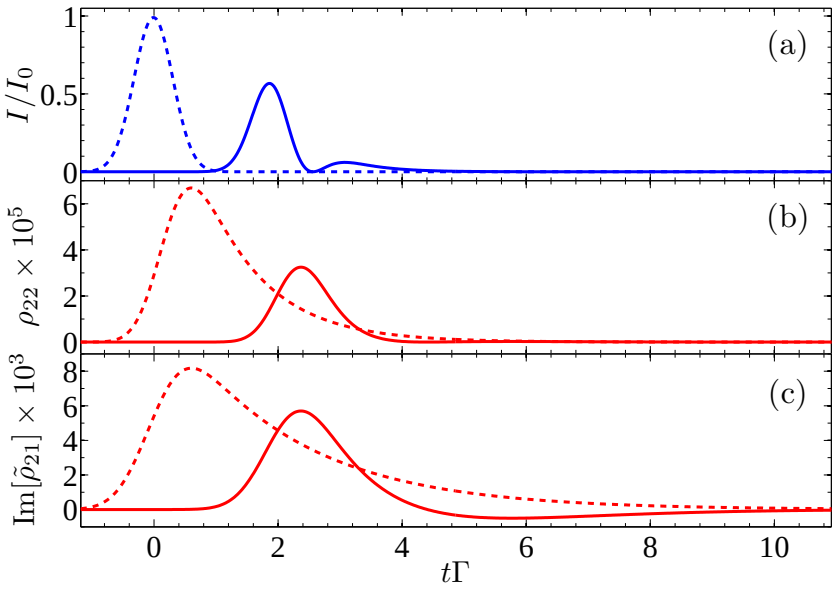

Figure 2.8: Data shown in figure 2.2(a)-(c) versus t only. Dashed curves show the data at the entrance to the medium ($z = 0$), solid curves at the exit ($z = L$).

body of the pulse has passed through. After peaking, the excited state population decays away exponentially at a rate Γ. The coherence (figures 2.7(c) and 2.8(c)) shows similar time dependence to the excited state population, decaying away at a rate $\Gamma/2$. Towards the exit of the medium the coherence becomes negative in response to the tail of the distorted pulse (for reasons described below).

The physical interpretation of the pulsed atom-light interaction is slightly different to that of continuous-wave light. The leading edge of the pulse enters a slice at the medium's entrance, creating a polarisation which radiates a field π rad out of phase with respect to the input field. The dipoles excited by the front of the pulse radiate for a time of order $1/\Gamma$. If the trailing edge of the incident pulse drops off faster than the coherence lifetime, then the envelope of the pulse leaving the slice will drop to zero (due to destructive interference) until the exiting pulse is solely due to the radiated field. The resultant tail thus differs in phase by π rad with respect to the main body of the pulse. The next slice of the medium will see a pulse whose main body drops off faster than before and hence the tail will be added to. Over significant distances, the π rad phased tail can beget further tails, leading to several bands of field alternating between zero and π rad phase with respect to the original pulse. Although energy is lost by the front of the pulse, a fraction of the energy is returned to the trailing edge, the rest being lost from the system during spontaneous emission of incoherent light.

2.4 Spectral dependence of the Maxwell-Bloch equations

So far we have dealt with the Maxwell-Bloch equations exclusively in the time domain, i.e. we have found solutions by looking at the time-dependence of the atom-light interaction with no reference to their frequency-dependence. This is in contrast to Fourier optics [77] where the equations are solved via Fourier analysis, the essence of which is a transformation into the frequency domain (spatial and/or temporal). We produce the electric field angular-frequency

spectrum $E(z,\omega)$ via the transform

$$E(z,\omega) = \frac{1}{\sqrt{2\pi}} \int_{-\infty}^{+\infty} E(z,t) \mathrm{e}^{\mathrm{i}\omega t} \mathrm{d}t, \tag{2.51}$$

and recover the time domain field $E(z,t)$ via the inverse transform

$$E(z,t) = \frac{1}{\sqrt{2\pi}} \int_{-\infty}^{+\infty} E(z,\omega) \mathrm{e}^{-\mathrm{i}\omega t} \mathrm{d}\omega. \tag{2.52}$$

The angular-frequency spectrum is a measure of how much each angular frequency contributes to the pulse. The electric field at a point in space is thus essentially the superposition of monochromatic wave elements, with amplitude and phase given by $E(z,\omega)$.

As we did in section 2.2.1 we can make the slowly-varying envelope approximation. The Gaussian temporal envelope has the property that its angular-frequency spectrum is also Gaussian. For an envelope at the entrance to the medium $\tilde{E}(z=0,t)$, of constant zero phase, the initial spectrum $\tilde{E}(0,\omega)$ is

$$\tilde{E}(0,\omega) = \frac{A_0 \Delta t}{2\sqrt{\ln 2}} \exp\left[-\frac{1}{8\ln 2} \Delta t^2 (\omega - \omega_\mathrm{c})^2\right], \tag{2.53}$$

where the spectrum is centred at the carrier angular frequency ω_c. The relationship between the FWHM of the profile and spectrum is $\Delta t \Delta\nu = 2\ln 2/\pi \approx 0.441$, where $\Delta\omega = 2\pi\Delta\nu$.

By taking the Fourier transform (2.51) of the pulse envelope $\tilde{E}(z,t)$ in section 2.3.3, we obtain the angular-frequency spectrum $\tilde{E}(z,\omega)$ as a function of propagation distance inside the medium. Figure 2.9 shows the intensity spectrum $I(z,\omega) \propto |\tilde{E}(z,\omega)|^2$. It can be seen that the incident Gaussian spectrum (of FHWM $\Delta\omega = 3.8\Gamma$) becomes attenuated heavily around its peak (coincident with the resonant frequency of the medium). Fourier analysis provides another explanation of the tail seen to develop in the pulse envelope, explained in section 2.3.3 to be the result of re-radiated light of a pulse whose duration is shorter than the coherence lifetime. The spectrum of such a pulse contains significant angular-frequency components outside of the range of the absorptive response of the medium. The incident singular peak of the spectrum evolves into twin peaks, due to greater attenuation close to resonance. This causes an additional amplitude modulation in the temporal envelope (cf. the phenomenon of acoustic beats).

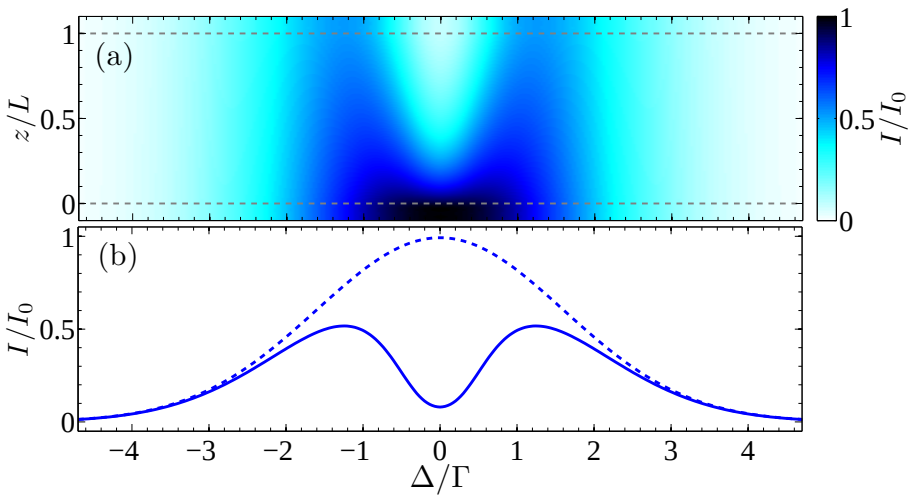

Figure 2.9: Normalised intensity spectrum of the pulse in figure 2.7. (a) Spectrum throughout the medium, delineated by the grey dashed lines. (b) Spectrum at the entrance (dashed curve) and exit (solid) of the medium.

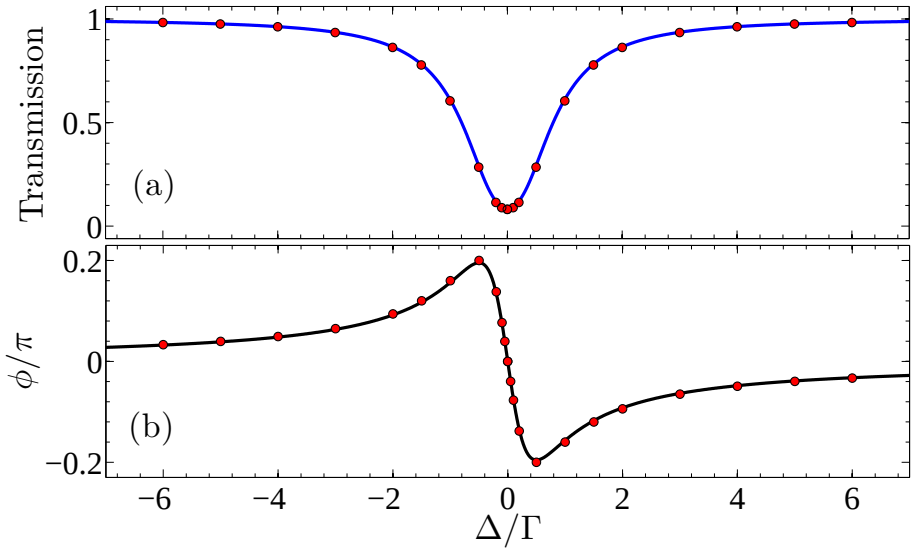

Figure 2.10: Frequency response of a single atomic resonance to low-intensity light. (a) Transmission and (b) phase at the exit of the medium. Curves show the numerical solution of a single pulse centred at $\Delta = 0$, and markers show the numerical solutions of many continuous-wave envelopes at various detunings (see text). The pulse and continuous-wave envelopes all have incident intensity $I = 10^{-3} I_{\text{sat}}$.

The spectrum of the pulse experiences the same exponential decay with distance as was observed for the steady-state solution of section 2.3.1. In figure 2.10 we compare the transmission and phase shift experienced by the pulse of figure 2.9 to that of many individual monochromatic waves of different frequencies. The monochromatic waves are separate numerical simulations of the continuous-wave envelope as performed in section 2.3.1, with different detunings. After reaching equilibrium the Fourier transforms of each wave are Dirac delta functions in the frequency domain, resulting in the individual points (represented by markers) in figure 2.10. The agreement between the pulse simulation and the monochromatic simulations show that the pulse behaves as though it is composed of many frequency components simultaneously interacting with the medium independently and unaffected by each other. The reason for this is as follows. For low-intensity waves the Maxwell-Bloch equations can be reduced to a set of linear equations. In systems described using linear operators a linear combination of individual solutions to the system is itself a solution: this is known as the *superposition principle*.

The situation we observe for low-intensity light is what we call the *quasi-static regime*: the state of the medium changes sufficiently slowly such that, to a good approximation, the medium can be assumed to remain in equilibrium with the interacting electromagnetic field. As the electromagnetic field in this regime is by necessity weak, the medium can also be assumed to remain in its initial state[6]. Thus the steady-state solutions of the Maxwell-Bloch equations (section 2.3.2) provide a good approximation of the atom-light interaction.

[6]Of course for the atom-light interaction to proceed the state of the medium must change, but for low-intensity light the change is negligible.

2.5 Discussion

In this chapter we have derived the Maxwell-Bloch equations which govern the propagation of light through an atomic medium. Numerical solutions were found, both for continuous-wave light in the steady state and for pulsed light. At sufficiently low light intensities, the interaction with the medium is linear with respect to the electric field. It is this 'weak probe' or quasi-static regime which we will develop further over the next few chapters, during which time we shall see that the simple, analytic solutions exist. By obviating the need to solve light propagation with a computationally-intensive numerical scheme we are able to model more complicated (and, conveniently from an experimental view point, more realistic) atomic systems. In the final chapter we shall make a return to the Maxwell-Bloch equations as we investigate nonlinear atom-light interactions.

Chapter 3

Applying the Maxwell-Bloch equations to realistic media

In the last chapter we found numerical solutions of the Maxwell-Bloch equations for a medium comprised of non-interacting, stationary, two-level atoms illuminated by a plane-wave electromagnetic field. Our goal is to develop a theoretical model able to handle the complexities of realistic atomic systems. Including all of the necessary factors, such as multiple energy states, particle motion and interaction, additional atomic species and additional light fields would result in a computationally-intensive numerical scheme. Fortuitously, a full treatment of the atom-light interaction is not always required. On some occasions, for example, one is more concerned with the attenuation a light beam suffers during its passage through a medium than how the atoms are affected during this interaction. In this instance it may be possible to simplify the problem by subsuming the medium parameters into the light propagation equations. This is indeed the approach taken in considering the dynamics of weak beam propagation. In counterpoint, there are situations where one's goal is to prepare a medium in a specific atomic state, in which case certain circumstances allow the propagation of light to be ignored. These cases can arise when considering a dilute medium which has only a minor effect on the light beam. In this chapter we derive a set of equations applicable for a low-intensity light field propagating through a medium close to a state of equilibrium.

3.1 Towards analytic propagation equations

The polarisation density $\mathbf{P}$ represents a source (or sink) of electric fields. If we limit our discussion to the case where an electromagnetic wave is incident upon an initially unpolarised medium[1], then any subsequent polarisation of the medium is solely due to the applied electromagnetic field. The polarisation at a given instant in time t is related to the electric field via the medium's electric susceptibility χ, expressed by the relation

$$\mathbf{P}(t) = \epsilon_0 \int_{-\infty}^{\infty} \chi(t')\mathbf{E}(t-t')\mathrm{d}t'. \tag{3.1}$$

This has the form of a convolution, expressing the fact that the polarisation at time t may depend upon the electric field at times other than t. The electric susceptibility is generally field-dependent, leading to many interesting nonlinear optical phenomena [78]. We will see later in this chapter that in the field-independent case (the domain of linear optics), relation (3.1) can be used to provide analytic solutions to the Maxwell wave equation (MWE).

It should be noted that in general the susceptibility is a tensor, so that vector components of the polarisation can be induced that are not parallel to the applied electric field. Also, the different polarisation states of the electric field are able to interact with one another. The medium in this instance is said to be *anisotropic*, that is to say it responds differently to the polarisation states of an applied field [79]. We will investigate anisotropic media in the second part of this thesis.

We can simplify the wave dynamics by working in the frequency domain. We looked at this domain in section 2.4 in order to calculate the electric field spectrum $E(z,\omega)$ of the numerical solutions to the Maxwell wave equation. Here we do so in order to find solutions to the wave dynamics via other means. Working in the frequency domain allows us to utilise the convolution property of Fourier transforms, namely *the Fourier transform of a convolution is equal to the product of the Fourier transforms of its component functions.* Expressed mathematically, if $\mathbf{P}(t) = \epsilon_0\chi(t) \otimes \mathbf{E}(t)$, then $\mathbf{P}(\omega) = \epsilon_0\chi(\omega)\mathbf{E}(\omega)$. Here ω, the angular frequency, is the Fourier conjugate of the time variable. If we take the temporal Fourier transform of the

[1] We will meet situations where this is not true in chapter 10.

Maxwell wave equation (MWE) (using the definition of the transform from section 2.4) and substitute for the polarisation density, we obtain the one-dimensional inhomogeneous Helmholtz equation

$$\left(\omega^2 + c^2\partial_{zz}\right)\mathbf{E}(z,\omega) = -\omega^2\chi(z,\omega)\mathbf{E}(z,\omega), \tag{3.2}$$

where we have used the fact that the Fourier transform of the nth derivative of a function is $(-\mathrm{i}\omega)^n$ times the Fourier transform of the function. We will make an assumption on the nature of the susceptibility (and implicitly on the form of the medium) in order to arrive at simple solutions to equation (3.2). We assume that the medium is such that the polarisation states of the applied electric field do not affect each other, in which case the susceptibility tensor is proportional to the identity matrix. With the aforementioned assumption we can take the factor on the right-hand side of the equation to the left to give

$$\left(n^2\left(z,\omega\right)\omega^2 + c^2\partial_{zz}\right)\mathbf{E}\left(z,\omega\right) = 0, \tag{3.3}$$

where $n = \sqrt{1+\chi}$ is the refractive (or phase) index of the medium. This equation has solutions of the form

$$\mathbf{E}(z,\omega) = \mathbf{E}(0,\omega)\mathrm{e}^{\mathrm{i}\int \mathbf{k}\cdot\mathrm{d}\mathbf{z}}. \tag{3.4}$$

Hence we have an equation relating the angular-frequency spectrum at a point z in space to the spectrum at $z = 0$. Substituting this solution back into equation (3.3) leads to a relation between the wavevector $\mathbf{k}$ and angular frequency of the electromagnetic wave

$$n(z,\omega)^2\omega^2 = c^2(\mathbf{k}\cdot\hat{\mathbf{z}})^2, \tag{3.5}$$

This equation bears a distinct resemblance to the dispersion relation of the free-space plane-waves seen in chapter 2. The wavenumber $k = n\omega/c$ differs from the free-space wavenumber ω/c by the the refractive index n. This angular-frequency dependent function governs the propagation of light in dispersive media, describing both the propagation speed and attenuation a monochromatic wave experiences upon interacting with the medium.

We saw in section 2.4 that in general the electric field of a pulse contains many frequency elements. We return to the time domain by taking the

inverse Fourier transform of the angular-frequency spectrum, and arrive at the solutions to the electric field of the form

$$\mathbf{E}(z,t) = \frac{1}{\sqrt{2\pi}} \int_{-\infty}^{+\infty} \mathbf{E}(0,\omega) \mathrm{e}^{\mathrm{i}\left(\int \mathbf{k}\cdot \mathrm{d}\mathbf{z} - \omega t\right)} \mathrm{d}\omega. \tag{3.6}$$

Note that in general $\mathbf{k}$ is a function of field and thus equation 3.6 is transcendental, which by all appearances has taken us farther away from finding a solution than the numerical method used in chapter 2. We will however concentrate on atom-light interactions in which the wavevector is field-independent.

3.1.1 *Propagation of monochromatic light*

The angular-frequency spectrum of a monochromatic wave is given by the Dirac delta function of amplitude $\mathbf{E}_0$, centred at angular frequency ω i.e. $\mathbf{E}(0,\omega') = \mathbf{E}_0 \delta(\omega' - \omega)$. Sustituting this into equation (3.6), we find solutions in the time-domain of the form

$$\mathbf{E}(z,t) = \mathbf{E}_0 \mathrm{e}^{\mathrm{i}\left(\int \mathbf{k}\cdot \mathrm{d}\mathbf{z} - \omega t\right)}. \tag{3.7}$$

This reduces to the free-space solutions found in section 2.1.1 for a displacement- and frequency-independent refractive index of $n \equiv 1$.

To illustrate the propagation of a monochromatic wave, we take the forward-moving solution ($\mathbf{k} \cdot \mathrm{d}\mathbf{z} > 0$) and substitute for the wavenumber $k = (n_\mathrm{R} + \mathrm{i}n_\mathrm{I})\, k_0$, where n_R and n_I are, respectively, the real and imaginary parts of the refractive index, and $k_0 = \omega/c$ is the free-space wavenumber. Thus

$$\begin{aligned} \mathbf{E}(z,t) &= \mathbf{E}_0 \mathrm{e}^{\mathrm{i}\left(k_0 \int (n_\mathrm{R} + \mathrm{i}n_\mathrm{I})\mathrm{d}z - \omega t\right)}, \\ &= \mathbf{E}_0 \mathrm{e}^{-k_0 \int n_\mathrm{I} \mathrm{d}z} \mathrm{e}^{\mathrm{i}\left(k_0 \int n_\mathrm{R} \mathrm{d}z - \omega t\right)}. \end{aligned} \tag{3.8}$$

The real-valued exponential term shows that the amplitude of the electric field decreases with distance for positive n_I, and the imaginary-valued exponential term shows that the wave has an instantaneous phase velocity of $v_\mathrm{p} = c/n_\mathrm{R}$.

Two important parameters characterising the transmitted wave are the optical depth L_depth and phase shift $\Delta\phi$ measured on a detector at a position $z = L$ from the light source at $z = 0$. The optical depth is defined via

$I/I_0 = \exp[-L_{\text{depth}}]$, where I and I_0 are the transmitted and incident intensity, respectively. The phase shift is the difference between the phase accrued by the wave on its journey from source to detector and the phase experienced by an equivalent wave travelling through free-space. The optical depth and phase shift are

$$L_{\text{depth}} = k_0 \int_0^L 2n_{\text{I}} \mathrm{d}z \tag{3.9}$$

$$\Delta\phi = k_0 \int_0^L (n_{\text{R}} - 1)\mathrm{d}z. \tag{3.10}$$

3.2 Electric susceptibility

We saw in the last section that the real part of the refractive index describes the dispersive effects of the medium (phase shift, propagation velocity etc.), whilst the imaginary part describes the absorptive properties. The real and imaginary components of the refractive index are in fact inextricably linked: knowledge of one implies knowledge of the other. This is a direct result of the principle of causality, that no cause should be preceded by its effect. We can illustrate the connection between causality and dispersion using the following argument [80]. Suppose the input field $\mathbf{E}(t)$ in equation (3.1) is zero for times $t < t'$. The angular-frequency spectrum of the input field is such that its frequency elements destructively interfere to produce the zero signal for times less than t'. Suppose we have a system which absorbs just the single angular-frequency component ω, producing an output polarisation $\mathbf{P}(t) \propto \mathbf{E}(t) - \mathbf{E}_0 \cos(\omega t)$. This signal does not vanish for $t < t'$, a contradiction of the principle of causality. Thus causality requires that absorption of one frequency component must be accompanied by a phase shift in other frequencies to produce the destructive interference necessary such that no output precedes the input. The frequency-dependent phase shifts are provided by dispersion relations. A more detailed discussion on the connection between dispersion and causality can be found in reference [81].

The condition that there be no polarisation before the applied electric field means that $\chi(t') = 0$ for $t' < 0$ and therefore the inverse Fourier transform

of the susceptibility need be performed for positive t' only:

$$\chi(\omega) = \int_0^\infty \chi(t')\mathrm{e}^{\mathrm{i}\omega t'}\mathrm{d}t'. \tag{3.11}$$

Independently of each other, Kramers [82] and Kronig [83] found that this form of $\chi(\omega)$ implies a relationship between the real and imaginary parts of the susceptibilty. These are the Kramers-Kronig relations [62]

$$\mathrm{Re}[\chi(\omega)] = \frac{2}{\pi}\mathcal{P}\int_0^\infty \frac{\omega'\mathrm{Im}[\chi(\omega')]}{\omega'^2-\omega^2}\mathrm{d}\omega' \tag{3.12}$$

$$\mathrm{Im}[\chi(\omega)] = -\frac{2}{\pi}\mathcal{P}\int_0^\infty \frac{\omega\mathrm{Re}[\chi(\omega')]}{\omega'^2-\omega^2}\mathrm{d}\omega', \tag{3.13}$$

where $\mathcal{P}$ denotes the Cauchy principal-value. The Kramers-Kronig relations show that if the imaginary part of the susceptibility is known, e.g. via transmission measurements of an electromagnetic wave, then it is possible to calculate the phase shift experienced by the wave by calculating the real part of the susceptibility.

3.2.1 *Electric susceptibility & slowly-varying quantities*

Under the slowly-varying envelope approximation (see section 2.2.1) we can write the susceptibility, along with the polarisation density and electric fields, in terms of a slowly-varying part along with a rapidly-oscillating carrier:

$$\chi(t) = \tilde{\chi}(t)\mathrm{e}^{-\mathrm{i}\omega_\mathrm{c}t} + \mathrm{c.c.}, \tag{3.14}$$

$$\mathbf{P}(t) = \tilde{\mathbf{P}}(t)\mathrm{e}^{-\mathrm{i}\omega_\mathrm{c}t} + \mathrm{c.c.}, \tag{3.15}$$

$$\mathbf{E}(t) = \tfrac{1}{2}\tilde{\mathbf{E}}(t)\mathrm{e}^{-\mathrm{i}\omega_\mathrm{c}t} + \mathrm{c.c.}. \tag{3.16}$$

From the wave equation governing the propagation of a forward moving envelope (equation (2.19)), we obtain the following expression for the electric field envelope:

$$\tilde{\mathbf{E}}(z,t) = \frac{1}{\sqrt{2\pi}}\int_{-\infty}^{+\infty} \tilde{\mathbf{E}}(0,\Delta_\omega)\mathrm{e}^{\mathrm{i}\left(\int \Delta_k \mathrm{d}z - \Delta_\omega t\right)}\mathrm{d}\Delta_\omega, \tag{3.17}$$

where the detunings $\Delta_\omega = \omega - \omega_\mathrm{c}$ and $\Delta_k = k - k_\mathrm{c}$ are confined to a small range about the carrier angular frequency ω_c and wavevector k_c, respectively. The carrier wave is a solution of the free-space wave equation, thus its

wavevector is the real-valued $k_\mathrm{c} = \omega_\mathrm{c}/c$. Comparing the dispersion relations of a forward moving wave in both the complete electromagnetic field and its slowly-varying envelope we have

$$ck = \omega\sqrt{1+\chi(z,\omega)}, \tag{3.18}$$

$$c\Delta_k = \Delta_\omega + \tfrac{1}{2}\tilde{\chi}(z,\Delta_\omega). \tag{3.19}$$

In order for these two equations to be consistent (in a similar analysis to that seen in section 2.2.1) it is required that (i) $\omega \approx \omega_\mathrm{c}$, implying that $|\Delta_\omega| \ll 1$; and (ii) $\sqrt{1+\chi} \approx 1+\frac{1}{2}\chi$, implying that $|\chi| \ll 1$. Both of these criteria satisfy general requirements of the slowly-varying envelope approximation: the first criterion satisfies the restriction that the pulse contains only frequencies in a low-bandwidth clustered around the carrier frequency; the second fulfills the requirement that the envelope does not change appreciably over a length scale of the order of the wavelength of the carrier wave. In the limit of small susceptibility, $\chi \equiv \tilde{\chi}$, that is to say close to the carrier angular frequency there is no contribution of the negative-frequency electric field components to the electric susceptibility. After transforming to the frequency domain and only keeping terms close to the carrier angular frequency, $\tilde{\mathbf{P}}(\Delta_\omega) = \frac{1}{2}\epsilon_0\chi(\Delta_\omega)\tilde{\mathbf{E}}(\Delta_\omega)$. Thus for the two-level atom described in section 2.3 we have an electrical susceptibility

$$\chi(\Delta_\omega) = 2\frac{\mathbf{d}_0\mathcal{N}_\mathrm{a}}{\epsilon_0}\frac{\tilde{\rho}_{21}(\Delta_\omega)}{\tilde{\mathbf{E}}(\Delta_\omega)}, \tag{3.20}$$

where $\mathbf{d}_0$ is the dipole matrix element of the transition, and $\tilde{\rho}_{21}$ is the off diagonal matrix element of the dipole operator.

In the steady state (section 2.3.2), we find a susceptibility

$$\chi(\Delta) = \frac{d_0^2\mathcal{N}_\mathrm{a}}{\hbar\epsilon_0}\frac{\mathrm{i}\frac{1}{2}\Gamma - \Delta}{\frac{1}{4}\Gamma^2 + \Delta^2 + \frac{1}{2}|\Omega|^2}, \tag{3.21}$$

where $\Delta = \omega_\mathrm{c} - \omega_0$ is the detuning of the carrier from the resonant angular frequency ω_0. The presence of the square modulus of the Rabi angular frequency Ω tells us that the susceptibility is dependent on intensity I. Its presence in the denominator, however, allows us to expand to arbitrary powers of $|\Omega|^2$:

$$\chi(\Delta) = \frac{\mathbf{d}_0^2\mathcal{N}_\mathrm{a}}{\hbar\epsilon_0}\left(f - \tfrac{1}{2}f|f|^2|\Omega|^2 + \ldots\right), \tag{3.22}$$

where $f = \mathrm{i}/(\frac{1}{2}\Gamma - \mathrm{i}\Delta)$. The zeroth order term is independent of intensity: this is the regime we refer to as 'weak'.

The imaginary component of the susceptibility takes the form of a Lorentzian line-shape, whose FWHM (full-width at half-maximum) of $\Gamma\sqrt{1 + I/I_{\mathrm{sat}}}$ is intensity dependent, a situation known as power broadening [16]. In the limit of low-intensity radiation (where $I \ll I_{\mathrm{sat}}$, the saturation intensity of the transition) χ is independent of intensity, and the decay rate out of the excited state Γ provides the width of the line-shape.

3.3 Weak beam propagation

It is often the case that the electromagnetic wave is weak enough such that it has little effect upon the medium through which it propagates: we arrived at this conclusion in chapter 2. Assuming the atomic system begins in a stable state (i.e. other mechanisms such as spontaneous decay will not significantly alter the system during the time in which the atom-light interaction takes place), the evolution of the atomic ensemble is linearly proportional to the applied electric field. Then only the time-dependence of the field and its coupling to the ensemble need be solved for. The solutions derived in section 3.1 are applicable in the general case irrespective of the intensity of the light. The form of the susceptibility (representing the atom-light coupling) in section 3.2 is applicable to the case of a two-level atom only. Two-level atoms do not exist in reality, though under certain experimental conditions (see for example reference [84]) atomic transitions can effectively be treated as such. Under general experimental conditions there may be many close-lying transitions which can interact with the incident light, and for sufficiently high intensity atomic population can be transfered to multiple excited states. In contrast to saturation, in which population can only return to the state it was excited from, atoms can decay into other states: a process known as optical pumping [85]. Optical pumping has been shown to be a more efficient mechanism of altering the atom-light interaction than saturation [86]. With these considerations in mind, modelling a multilevel system is best done in the weak regime, since in this regime an atom remains in its initial, unexcited state. Thus a collection of multilevel atomic resonances can be effectively

modelled as a collection of independent two-level resonances.

In section 2.4 we calculated numerically the transmission and phase of both monochromatic and pulsed light in the weak regime (see figure 2.10). In figure 3.1 we compare the susceptibility calculated by taking the ratio of the atomic coherence to the electric field spectrum (equation (3.20)), and the susceptibility of the steady-state analytic function (equation (3.21)). We see that both the pulsed and continuous-waved numerical solutions are in excellent agreement with the analytic solution of the susceptibility. Thus in the weak-field regime propagation can be simulated using the equation of the electric field derived in section 3.1. The physical interpretation of this is given in section 2.4.

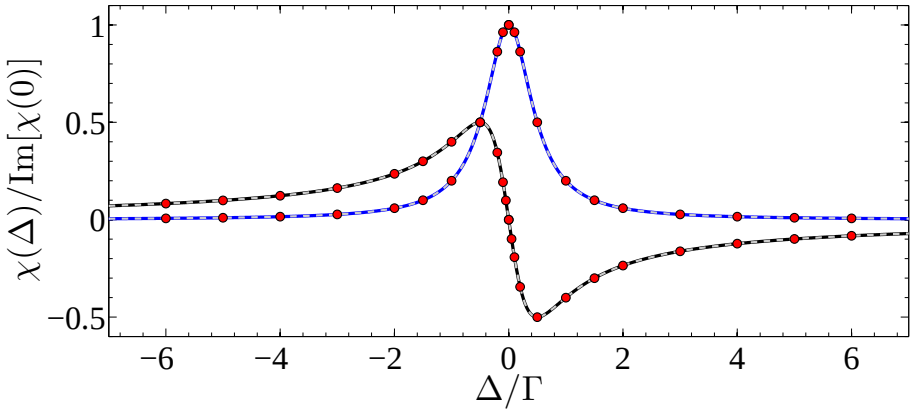

Figure 3.1: Normalised steady-state electric susceptibility in the weak-field regime. The black (blue) curve shows shows the real (imaginary) component of the susceptibility. Dashed grey curves show the values calculated with the numerical scheme (see text) for a pulsed field of $I = 10^{-3} I_{\text{sat}}$; points show the numerical solution for continuous-wave light.

3.4 Particle dynamics

We have so far taken the medium to be a dielectric composed of slices of uniform composition (we have allowed for the possibility of the density changing amongst slices). In a crystalline solid this may well be true, and for amorphous solids averaging over macroscopic distances may result in our treatment of the atom-light being a fair approximation of the actual situa-

tion. We have essentially assumed that the solution for a slice of medium is proportional to the density-matrix solution of the Bloch equations for a single atom. In this section we address the issue of particle dynamics which contribute to the non-uniformity of the atom-light interaction. Nevertheless, under certain experimental conditions some of these factors will be found to cause only slight deviation from the macroscopically-averaged solution.

In an atomic vapour the most important of these factors is particle motion, the effects of which include Doppler shift, transit across the extent of the laser beam, diffusion across medium slices, and collisions between each other and the walls of the container. However, the first factor we will address are the interactions between particles via dipolar electric fields and dipole-radiated electromagnetic fields.

3.4.1 *Local electric field effects*

The polarisability of an atom, α, is defined as a single dipole's receptiveness to the local electric field, thus $\langle \mathbf{d} \rangle = \alpha \mathbf{E}_{\text{local}}$. It is essentially the microscopic equivalent of the electric susceptibility χ. As with the electric susceptibility, α is in general a tensor. The local field seen by a given dipole is the sum of the applied electric field $\mathbf{E}$ and the contributing fields due to neighbouring dipoles. The solution for uniformly distributed dipoles in a cubic lattice is the well-known Clausius-Mossotti relation [87, 88], calculated by replacing the lattice with its point-like dipoles with an equivalent dielectric solid of uniform polarisation; the calculation has also been performed from a microscopic perspective [89]. The Clausius-Mossotti relation gives

$$\alpha \mathcal{N}_{\text{a}} = \frac{3\epsilon_0 \chi}{3 + \chi}. \tag{3.23}$$

For a low density medium, $\chi \ll 1$ and hence $\alpha \mathcal{N}_{\text{a}} \approx \epsilon_0 \chi$. Indeed, the field due to a dipole decreases with the cube of distance, thus for a low density dielectric the local electric field can be assumed to be identical to the applied field. We will see in later chapters that under typical experimental conditions used in this thesis, $\mathcal{N}_{\text{a}} \approx 10^{19}$ m^{-3} with a measured susceptibility $\chi \approx 10^{-4}$.

The foregoing analysis is based on the interaction of stationary dipoles. The trajectory of an atom in motion may take it sufficiently close to an-

other such that the atom-light interaction is altered. Detailed examination of the inter-atomic potentials involved in such encounters (see for example the comprehensive study in reference [90]) predict dipole-dipole interactions whose effect is to broaden the atom's spectral line-width. An examination of the process in Rb vapour cells at high number density ($\mathcal{N}_a$ approximately greater than 10^{19} m^{-3}) is presented in reference [91]: it suffices here to state that the additional broadening mechanism is Lorentzian in nature, and thus we add a density-dependent term to the natural broadened line-width: $\Gamma_{\text{Total}} = \Gamma + \beta\mathcal{N}_a$.

Though the *static* electric field of a dipole is relatively short range, a radiating dipole can give rise to electromagnetic fields which by their very nature can act farther afield. The radiated light which is coherent with the applied field is accounted for in the Maxwell-Bloch equations; the contribution which is incoherent is not. This incoherent light can propagate to other atoms, undergoing repeated cycles of absorption/emission and thus its progression through the medium is impeded, a process known as radiation trapping [92]. For an applied field of low intensity, the radiation emitted by the dipole is mostly coherent (see section 2.3.2), so radiation trapping is unlikely to be of much concern when we look at weak incident fields.

3.4.2 *Particle motion*

Motion is an important process in a thermal vapour as individual particles are typically moving at hundreds of metres per second[2], leading to phenomena such as the Doppler effect (for motion parallel to the light beam axis) and beam-transit effects (for transverse motion). Nevertheless, there are regimes where some or all of these effects can be neglected. For example, if the duration of the atom-light interaction is short (nanoseconds or less for the room temperature Rb), an atom does not move significant distances compared to the size of the beam, so beam-transit effects can be ignored. Recent studies of spectroscopy which take account of particle motion include references [93–95]. For our part, we will neglect all but Doppler broadening in this thesis. Nevertheless, we shall see in chapter 5 that for light with a frequency detuned

[2]For a vapour of ^{87}Rb at room temperature the most probably velocity is 240 ms^{-1}

sufficiently far from resonance the Doppler shift is negligible compared to the frequency range over which a stationary atom would interact.

With the inclusion of the Doppler effect, the susceptibility can be generalised to

$$\chi(\Delta) = \frac{d_0^2 \mathcal{N}_\mathrm{a}}{\hbar \epsilon_0} s(\Delta). \tag{3.24}$$

The line-shape factor $s(\Delta)$ is the convolution of $f(\Delta)$, the homogeneous atomic line-shape derived in section 3.2, and $g(v)$, the distribution of longitudinal velocities v. For an atomic vapour close to thermodynamic equilibrium (which is an excellent assumption for a sample illuminated by low-intensity light) the atomic velocity components are described by the Maxwell-Boltzmann distribution, which is Gaussian in form. This convolution is given by:

$$s(\Delta) = \int_{-\infty}^{+\infty} f(\Delta - kv) \times g(v) \mathrm{d}v, \tag{3.25}$$

where k is the wavenumber of the radiation, and

$$f(\Delta) = \frac{\mathrm{i}}{\Gamma/2 - \mathrm{i}\Delta}, \tag{3.26}$$

$$g(v) = \frac{1}{u\sqrt{\pi}} \mathrm{e}^{-(v/u)^2}. \tag{3.27}$$

Here Γ is the FWHM of the homogeneous broadening, and u is the 1/e half-width of the inhomogeneous broadening mechanism (and the RMS atomic speed). The line-shape $s(\Delta)$ is related to the Faddeeva function (which is discussed in chapter 5). This function, $w(\mathrm{i}z)$, of complex argument z, is related to the line-shape $s(\Delta)$ via

$$s(\Delta) = \frac{\mathrm{i}\sqrt{\pi}}{ku} w(\mathrm{i}z), \tag{3.28}$$

$$w(\mathrm{i}z) = \frac{\mathrm{i}}{\pi} \int_{-\infty}^{+\infty} \frac{\mathrm{e}^{-x^2}}{\mathrm{i}z - x} \mathrm{d}x = \mathrm{e}^{z^2} \mathrm{erfc}(z), \tag{3.29}$$

$$z(\Delta) = \frac{1}{2} \frac{\Gamma}{ku} - \mathrm{i} \frac{\Delta}{ku}, \tag{3.30}$$

where the complementary error function $\mathrm{erfc}(z)$ is defined as

$$\mathrm{erf}(z) = \frac{2}{\sqrt{\pi}} \int_z^\infty \mathrm{e}^{-t^2} \mathrm{d}t. \tag{3.31}$$

We now have a function s which describes the line-shape of atomic resonances in a Doppler broadened medium.

3.5 Discussion

In this chapter we have derived an equation for the electric field of a plane wave propagating through an inhomogeneous dielectric, equation (3.6), along with its slowly-varying envelope, equation (3.17). An equation relating the electric susceptibility of the medium, i.e. the response of the medium to the applied field, has also been derived based on the dynamics of a two-level atom (equation (3.21)). In the regime where the light field is of low intensity the medium remains in its initial state, thus obviating the necessity of solving the dynamics of the atomic system. Only the dynamics of the light needs to be considered, in contrast to the numerical analysis undertaken in chapter 2. Thus we have a set of equations which can be used to solve for light propagation, which we will use in the next chapter to compare a theoretical model of the transmission of light through a vapour of rubidium to experimental measurements.

Chapter 4

Transmission of a weak beam through a Doppler-broadened medium

In this chapter we develop a model that allows us to predict quantitatively the absorptive and dispersive properties of rubidium vapour probed in the vicinity of the D lines (for an alkali metal atom the D_2 transition is $n\,^2S_{1/2} \rightarrow n\,^2P_{3/2}$ (where n is the principal quantum number of the valence electron) and the D_1 transition is $n\,^2S_{1/2} \rightarrow n\,^2P_{1/2}$). We apply the weak beam theory of the two-level atom we have developed in the previous chapters to a multi-level, multi-species atomic system and compare the predictions with an experimental study of the absolute Doppler-broadened absorption spectrum. We begin by describing the process by which the absorption coefficients of an individual transition are calculated before going on to describe the experimental methodology used to measure the transmission spectrum. We then compare our predictions to experimental measurements.

4.1 Calculating absorption coefficients

4.1.1 Atomic absorption cross-section

We calculated in both section 2.3.2 and 3.1.1 that the absorption of monochromatic light as it propagates along the z-direction through a uniform density atomic vapour is given by:

$$I(z) = I_0 \mathrm{e}^{-\alpha z}, \tag{4.1}$$

where $I(z)$ is the intensity of light at position z inside the medium with an absorption coefficient α, and I_0 is the beam intensity at the entrance of the medium. In a dispersive medium the absorption coefficient is dependent on the angular frequency, ω, of incident light. We assume that the probe beam is sufficiently weak that the absorption coefficient is independent of intensity. A full discussion of how weak the light has to be for this simplification to be valid is given in section 4.4.1.

The transmission, $\mathcal{T}$, of a beam through a medium of length L is defined as

$$\mathcal{T} = I(L)/I_0 = \mathrm{e}^{-\alpha L}. \tag{4.2}$$

In general, a medium consists of multiple species, each with multiple transitions. A beam of light will interact with all species, the total absorption coefficient being the sum over all transition for each species.

The macroscopic absorption coefficient of the medium can be written [1] in terms of σ, the microscopic atomic absorption cross-section and $\mathcal{N}_\mathrm{a}$, the number density of the atomic gas, $\alpha = \mathcal{N}_\mathrm{a}\sigma$. There are two reasons why the medium's absorption coefficient is temperature dependent: (i) the atomic cross-section is influenced by the Doppler width, proportional to the square root of the temperature; and (ii) the number density is a strong function of temperature. Doppler broadening of the spectral lines is dealt with in section 4.1.5, and the temperature dependence of the atomic density in appendix D.

We label each hyperfine state of the atom with the usual angular momentum quantum numbers $|F_\mathrm{g}, m_{F_\mathrm{g}}\rangle$ for the $^2\mathrm{S}_{1/2}$ term, and $|F_\mathrm{e}, m_{F_\mathrm{e}}\rangle$ for the $^2\mathrm{P}_{3/2}$ or $^2\mathrm{P}_{1/2}$ term, where the subscript g(e) denotes the ground (excited) state.

For a multi-level atom, such as rubidium, the calculation of the atomic cross-section is in two parts: first, the relative line-strengths among the different $|F_g, m_{F_g}\rangle \rightarrow |F_e, m_{F_e}\rangle$ transitions are calculated, then the absolute value is deduced. These calculations are facilitated by initially assuming the atoms are at rest, with the manifestation of atomic motion (Doppler broadening) incorporated later. In this chapter we neglect pressure broadening. Gorris-Neveux *et al.* measured the Rb-Rb collisional self-broadening to be of the order of 10^{-7} Hz cm^3 [96]; for the temperature range spanned in this work the pressure broadening is at least four orders of magnitude less than the natural broadening. For temperatures greater than approximately 120°C the self-broadening becomes comparable to the natural width and thus needs to be accounted for [91].

4.1.2 Transition frequencies

In order to predict the absorption spectrum the relative spacing of the hyperfine-resolved energy levels for both Rb isotopes (illustrated in Figure 4.1) are needed. The frequency of zero detuning for the D_2 (D_1) line is set to be the centre of mass frequency of the $5^2S_{1/2} \rightarrow 5^2P_{3/2}$ ($5^2S_{1/2} \rightarrow 5^2P_{1/2}$) transition in the absence of hyperfine splitting, taking into account the natural abundance of each isotope. The atomic energy level intervals were obtained for D_2 from [8, 97, 98] and for D_1 from [99]. The positions of the atomic transitions relative to the centre of mass for D_2 (384,230,426.6 MHz) and D_1 (377,107,407.299 MHz) are listed in table 4.1.

4.1.3 Relative line-strength factors

The strength of the interaction between an atom and near-resonant electromagnetic radiation is characterised by the dipole matrix elements. The dipole matrix element of the transition between states $\left|F_g, m_{F_g}\right\rangle$ and $|F_e, m_{F_e}\rangle$ is $\left\langle F_g, m_{F_g}|er_q|F_e, m_{F_e}\right\rangle$. In order to calculate this matrix element, it is possible to factor out the angular dependence and write the matrix element as a product of Wigner $3-j$ and $6-j$ symbols and a reduced matrix element

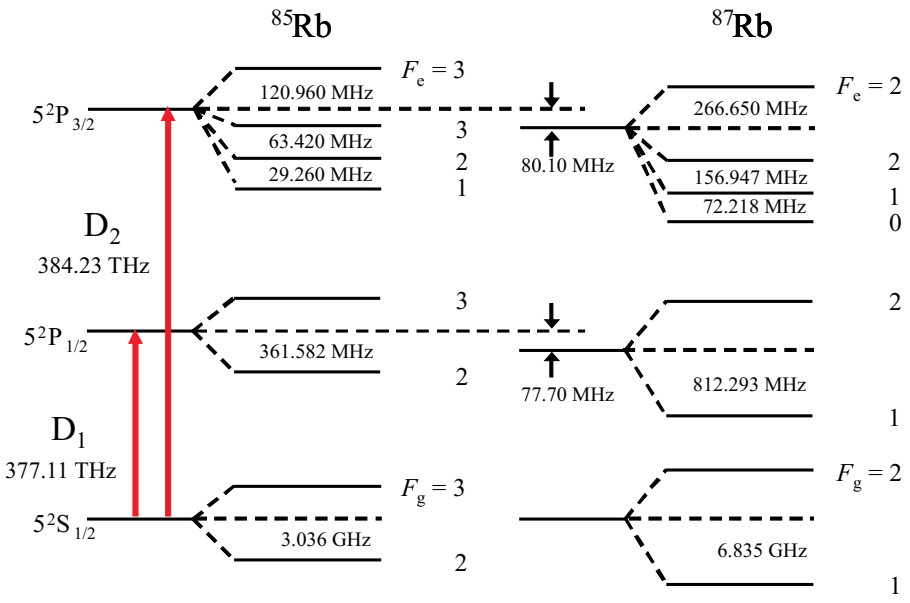

Figure 4.1: A schematic showing the hyperfine structure and intervals of Rb for the D spectroscopic lines. Due to the isotope shift, the $P_{1/2}$ and $P_{3/2}$ states are offset by 77.701 MHz [99] and 80.1 MHz [97], respectively, and has been taken into account for the calculated transition frequencies. Not to scale.

Table 4.1: Transition frequencies for the (a) D_2 line, and (b) D_1.

(a)

Line	Detuning / MHz	F_e
^{87}Rb	−2735.05	1
$F_g = 2 \rightarrow F_e = 1, 2, 3$	−2578.11	2
	−2311.26	3
^{85}Rb	−1371.29	2
$F_g = 3 \rightarrow F_e = 2, 3, 4$	−1307.87	3
	−1186.91	4
^{85}Rb	1635.454	1
$F_g = 2 \rightarrow F_e = 1, 2, 3$	1664.714	2
	1728.134	3
^{87}Rb	4027.403	0
$F_g = 1 \rightarrow F_e = 0, 1, 2$	4099.625	1
	4256.57	2

(b)

Line	Detuning / MHz	F_e
^{87}Rb	−3014.644	1
$F_g = 2 \rightarrow F_e = 1, 2$	−2202.381	2
^{85}Rb	−1497.657	2
$F_g = 3 \rightarrow F_e = 2, 3$	−1135.721	3
^{85}Rb	1538.063	2
$F_g = 2 \rightarrow F_e = 2, 3$	1900.087	3
^{87}Rb	3820.046	1
$F_g = 1 \rightarrow F_e = 1, 2$	4632.339	2

[100, 101]. Thus,

$$\begin{aligned}\langle F_{\rm g}, m_{F_{\rm g}}|er_q|F_{\rm e}, m_{F_{\rm e}}\rangle &= (-1)^{2F_{\rm e}+\mathcal{I}+J_{\rm g}+J_{\rm e}+L_{\rm g}+S+m_{F_{\rm g}}+1}\langle L_{\rm g}||e\mathbf{r}||L_{\rm e}\rangle \\ &\times\sqrt{(2F_{\rm g}+1)(2F_{\rm e}+1)(2J_{\rm g}+1)(2J_{\rm e}+1)(2L_{\rm g}+1)} \\ &\times\begin{pmatrix} F_{\rm e} & 1 & F_{\rm g} \\ m_{F_{\rm e}} & -q & -m_{F_{\rm g}}\end{pmatrix}\begin{Bmatrix} J_{\rm g} & J_{\rm e} & 1 \\ F_{\rm e} & F_{\rm g} & \mathcal{I}\end{Bmatrix}\begin{Bmatrix} L_{\rm g} & L_{\rm e} & 1 \\ J_{\rm e} & J_{\rm g} & S\end{Bmatrix}.\end{aligned} \tag{4.3}$$

Here $F, \mathcal{I}, J, L, S$, and m_F are the angular momentum quantum numbers, and q is the integer change in m_F during the transition. $\mathcal{I}$, the nuclear spin, has the value $\frac{5}{2}$ and $\frac{3}{2}$ for ^{85}Rb and ^{87}Rb respectively. S, the electron spin, has the value $\frac{1}{2}$. The $3-j$ symbol is the term contained in the large round brackets, and the $6-j$ in curly brackets. Note that the $3-j$ symbol is non-zero for $m_{F_{\rm e}} = m_{F_{\rm g}} + q$, according to the usual definition of q. $\langle L_{\rm g}||e\mathbf{r}||L_{\rm e}\rangle$ is the reduced matrix element, and can be expressed in terms of the wavelength of the transition, λ, and the decay rate of the excited state, Γ. By calculating the Wigner coefficients and prefactors, equation (4.3) reduces to

$$\left\langle F_{\rm g}, m_{F_{\rm g}}|er_q|F_{\rm e}, m_{F_{\rm e}}\right\rangle = c_{m_F}\langle L_{\rm g}||e\mathbf{r}||L_{\rm e}\rangle \equiv c_{m_F} d, \tag{4.4}$$

where c_{m_F} is a coefficient that determines the transition strength of a particular transition, and is dependent on the initial and final states of the transition.

The strength of a transition is proportional to the square of the transition matrix element, thus the transition strength is $c_{m_F}^2 d^2$. Each hyperfine transition is degenerate in F (since we are assuming zero magnetic field). The total transition strength of the hyperfine transition $F_{\rm g} \to F_{\rm e}$ is denoted by C_F^2, the sum of transition strengths $c_{m_F}^2$ of each Zeeman transition in the hyperfine manifold. These C_F^2 coefficients have been calculated for linearly polarised light ($q = 0$), and are presented in table 4.2.

Table 4.2: C_F^2 for the D_2 line of (a) ^{85}Rb, and (b) ^{87}Rb; D_1 line of (c) ^{85}Rb, and (d) ^{87}Rb

(a)

F_g \ F_e	1	2	3	4
2	1/3	35/81	28/81	0
3	0	10/81	35/81	1

(b)

F_g \ F_e	0	1	2	3
1	1/9	5/18	5/18	0
2	0	1/18	5/18	7/9

(c)

F_g \ F_e	2	3
2	10/81	35/81
3	35/81	28/81

(d)

F_g \ F_e	1	2
1	1/18	5/18
2	5/18	5/18

4.1.4 Reduced dipole matrix element

The reduced matrix element, d, can be calculated using the expression for the decay rate [1]

$$\Gamma = \frac{\omega_0^3}{3\pi\epsilon_0\hbar c^3}\frac{2J_g+1}{2J_e+1}|\langle J_g||e\mathbf{r}||J_e\rangle|^2. \tag{4.5}$$

$\langle J_g||\mathbf{r}||J_e\rangle$ can be written in terms of $\langle L_g||e\mathbf{r}||L_e\rangle$ via the relation

$$\begin{aligned}\langle J_g||e\mathbf{r}||J_e\rangle = (-1)^{J_e+L_g+S+1}\langle L_g||e\mathbf{r}||L_e\rangle \\ \times\sqrt{(2J_e+1)(2L_g+1)}\begin{Bmatrix} L_g & L_e & 1\\ J_e & J_g & S\end{Bmatrix}.\end{aligned} \tag{4.6}$$

The Wigner $6-j$ coefficient and prefactor, both of which are independent of the F and m_F quantum numbers, can be calculated for the D_2 line. Thus

$$\langle J_g = 1/2||e\mathbf{r}||J_e = 3/2\rangle = \sqrt{\frac{2}{3}}\langle L_g = 0||e\mathbf{r}||L_e = 1\rangle. \tag{4.7}$$

Substituting (4.7) into (4.5) and rearranging,

$$d = \langle L_g = 0||e\mathbf{r}||L_e = 1\rangle = \sqrt{3}\sqrt{\frac{3\epsilon_0\hbar\Gamma\lambda^3}{8\pi^2}}. \tag{4.8}$$

For the D_1 line a similar analysis leads to the same result as equation (4.8). The reduced dipole matrix element for the fine structure splitting should

be identical for the D lines. However, we have used experimentally measured values for the wavelength and decay rates: $\lambda = 780.241$ nm [102] and $\Gamma = 2\pi(6.065$ MHz) [103] for D_2, and $\lambda = 794.979$ nm [104] and $\Gamma = 2\pi(5.746$ MHz) [103] for D_1. This yields $d = 5.177\ ea_0$ for D_2, and $d = 5.182\ ea_0$ for D_1, where a_0 is the Bohr radius.

4.1.5 Including atomic velocity

The thermal velocity of atoms along the axis of the probe beam is given by the well-known Maxwell-Boltzmann distribution. It is Gaussian in nature, with a 1/e width of $u = \sqrt{2k_{\rm B}T/M}$, where T is the temperature, and $k_{\rm B}$ is the Boltzmann constant and M is the atomic mass. It is this longitudinal motion that leads to Doppler broadening of the absorption spectra; on the Rb D line at room temperature this broadening is ~ 0.5 GHz, which is in general larger than the excited state hyperfine splitting. Let the angular frequency of the laser be ω, and that of an atomic resonance be ω_0. The angular detuning, Δ, is defined as $\Delta = \omega - \omega_0$. For an atom moving along the direction of propagation of the probe beam we incorporate the Doppler effect by simply replacing the detuning by $\Delta - kv$, where k is the magnitude of the wavevector of the light, and v is the atomic velocity. We assume that the experiment is conducted in the weak-probe limit, i.e. the laser intensity is sufficiently low that optical pumping processes which redistribute population amongst the hyperfine levels of the ground term do not occur during the transit of an atom across the finite beam width. The transverse motion of atoms can therefore be neglected.

4.2 Electric susceptibility

The electric susceptibility of a medium, χ, describes the medium's absorptive and dispersive properties. For the case of an isolated resonance in a Doppler-broadened atomic medium the susceptibility as a function of detuning from resonance, Δ, is (3.24):

$$\chi(\Delta) \;=\; c^2_{m_F}\frac{d^2\mathcal{N}_{\rm a}}{\hbar\epsilon_0}s(\Delta). \tag{4.9}$$

Here $c^2_{m_F}$ is the transition strength factor for the transition $\left|F_\mathrm{g}, m_{F_\mathrm{g}}\right\rangle \rightarrow |F_\mathrm{e}, m_{F_\mathrm{e}}\rangle$, $d = \langle L_\mathrm{g}||e\mathbf{r}||L_\mathrm{e}\rangle$ is the reduced dipole matrix element of the $|L_\mathrm{g}\rangle \rightarrow |L_\mathrm{e}\rangle$ transition, $\mathcal{N}_\mathrm{a}$ is the atomic number density of state $\left|F_\mathrm{g}, m_{F_\mathrm{g}}\right\rangle$, and $s(\Delta)$ is the line-shape factor. The total susceptibility of the medium is obtained by summing over all transitions which the light is stimulating. The absorption coefficient is proportional to the imaginary part of the susceptibility, χ_I, and has the form of the well-known Voigt profile (which is the convolution of a Lorentzian and Gaussian function). Dispersion results from the real part, χ_R.

4.2.1 Absorption coefficients

The absorption coefficient can be obtained from the imaginary part of the susceptibility, $\chi(\Delta)$, via

$$\alpha(\Delta) = k\chi_\mathrm{I}(\Delta), \tag{4.10}$$

where k is the free-space wavenumber of the probe beam. $\chi_\mathrm{I}(\Delta)$ has the form of a Voigt profile, $s_\mathrm{I}(\Delta)$, multiplied by prefactors which depend on the properties of the resonant transition.

The shape of the Voigt profile is characterised by a single parameter, a: the ratio of the widths of the Lorentzian to the Gaussian profiles. The width of the Lorentzian, Γ, is the full-width at half-maximum (FWHM) of the hyperfine-free atomic transition. Γ is identical for all hyperfine transitions and Zeeman sublevels within the hyperfine-free manifold, and is also equal for different isotopes of an element. The width of the Gaussian profile is proportional to the width of the Maxwell-Boltzmann distribution, u, and is a function of temperature and isotopic mass. Considering all of the above, the width of the absorption profile of every hyperfine transition for a particular isotope is identical.

The height of the Voigt profile depends on two factors: the forms of the Lorentzian and Gaussian functions, which are identical for all transitions for a given isotope; and the transition strength of a particular transition.

All transitions for a particular isotope can be represented by a single Voigt profile, which is then centred on the relevant transition frequencies, and multiplied by the relevant transition strengths. Hence, recalling equa-

tions (4.9) and (4.10), the absorption profile for a particular hyperfine transition $F_g \rightarrow F_e$ is

$$\alpha(\Delta) = kC_F^2 \frac{d^2 \mathcal{N}_a}{\hbar \epsilon_0} \frac{1}{2(2\mathcal{I}+1)} s_I(\Delta). \tag{4.11}$$

Here, $2\,(2\mathcal{I}+1)$ is the degeneracy of the ground state of the particular isotope (12 for ^{85}Rb, 8 for ^{87}Rb). The degeneracy appears as we are assuming that the population is evenly distributed amongst the ground state Zeeman sublevels. The expected transmission profile for the vapour cell can then be calculated as a function of detuning.

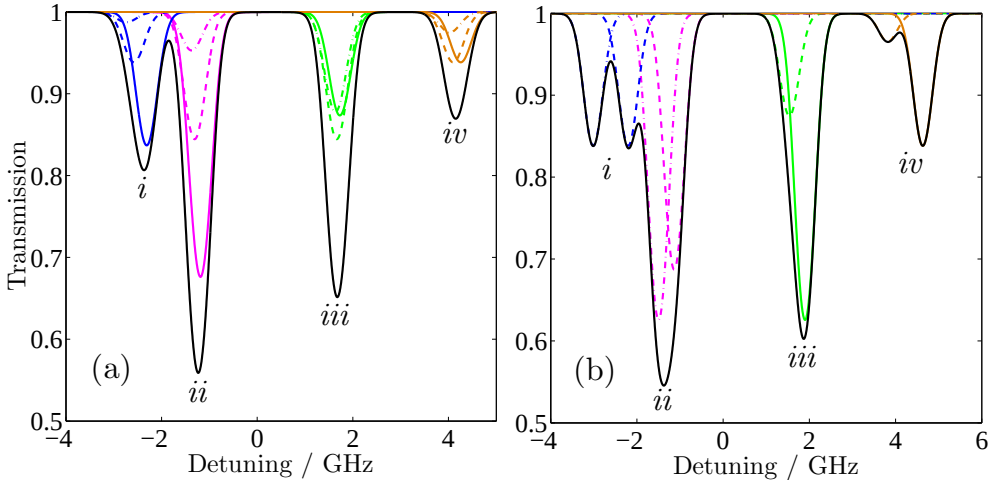

Figure 4.2: Plots of the transmission through a vapour cell of length 75 mm as a function of linear detuning, $\Delta/2\pi$. Plot (a) shows D_2 at 20°C, and (b) shows D_1 at 30°C. The blue curves (*i*) show the transmission for the transitions ^{87}Rb $F_g = 2 \rightarrow F_e$, the magenta (*ii*) ^{85}Rb $F_g = 3 \rightarrow F_e$, the green (*iii*) ^{85}Rb $F_g = 2 \rightarrow F_e$, and the orange (*iv*) ^{87}Rb $F_g = 1 \rightarrow F_e$. The solid curves show the transitions between hyperfine states $F_g \rightarrow F_e = F_g + 1$, dashed $F_g \rightarrow F_e = F_g$, and dot-dash $F_g \rightarrow F_e = F_g - 1$. The black curve shows the total transmission through the cell. Zero detuning corresponds to the weighted centre of the line.

Figure 4.2 shows the predicted transmission spectrum for rubidium vapour in a 75 mm-long cell for (a) D_2 at 20°C, and (b) D_1 at 30°C. The contributions of the individual $F_g \rightarrow F_e$ transitions are shown, in addition to their combined total. For both D lines the ground state hyperfine splitting is larger than the Doppler width of ~ 0.5 GHz. For the D_2 line, the excited hyperfine splitting of both isotopes is smaller than the Doppler width; consequently

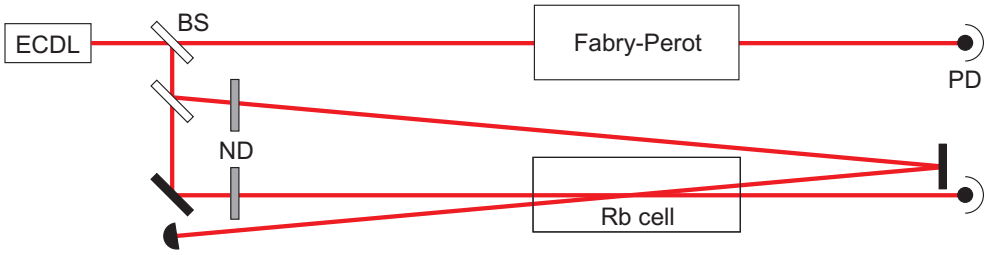

Figure 4.3: Schematic of the experimental apparatus. Light from an external cavity diode laser (ECDL) impinges on a beam splitter (BS). A fraction of the beam passes through a Fabry-Perot etalon onto a photo detector (PD). The beam is further split into pump and probe beams which cross at a small angle in a Rb vapour cell. The probe beam is incident on a photo detector, and neutral density filters (ND) are used to give independent control over the pump and probe beam powers

four composite lines are observed. For the D_1 line, the excited state splitting for ^{85}Rb is smaller than the Doppler width, whereas the splitting for ^{87}Rb is larger; hence six composite lines are seen.

4.3 Experimental methods & results

4.3.1 Experimental apparatus

We now test the accuracy of the prediction experimentally. A schematic of the experiment is shown in figure 4.3. External cavity diode lasers were the source of light (Toptica DL100 at 780.2 nm and 795.0 nm for D_2 and D_1 respectively). A fraction of the output beam was used as a probe beam for rubidium vapour in a 75 mm cell. A portion of the light was also sent into a Fabry-Perot etalon. Before the cell the beam had a $1/e^2$ half-width of (2.00±0.05) mm. The cell could be heated to change the vapour pressure of rubidium and hence the opacity. A thermocouple was used to measure the approximate temperature of the cell. No attempt was made to null the laboratory magnetic field. A pump beam generated sub-Doppler spectral features to provide a frequency reference. The crossing angle between probe and counter-propagating pump within the vapour cell was 6 mrad. Neutral density filters were used to give independent control of the pump and probe

powers. The Fabry-Perot etalon was used to assist with calibrating and linearising the frequency scan. A plane-plane cavity was used, with a separation of the mirrors of 250 mm, with a free-spectral range of 0.6 GHz. The probe beam was incident on a photo detector comprising a simple current-to-voltage circuit designed to output a voltage linearly proportional to the incident power.

4.3.2 Scaling the frequency axis.

For the D_2 line the frequency axis of the laser scans were linearised by use of the etalon transmission peaks. In order to generate atomic frequency markers on a scale narrower than the Doppler-broadened features pump-probe spectroscopy was employed. By counterpropagating a pump beam with the weak probe it is possible to generate sub-Doppler saturated-absorption and hyperfine-pumping spectra [86, 105]. For each isotope ground state F_g, three transitions $F_g \rightarrow F_e = F_g, F_g \pm 1$ are resolved, and so-called cross over resonances are seen halfway between each resonance. In this way it is possible to obtain 24 atomic resonances.

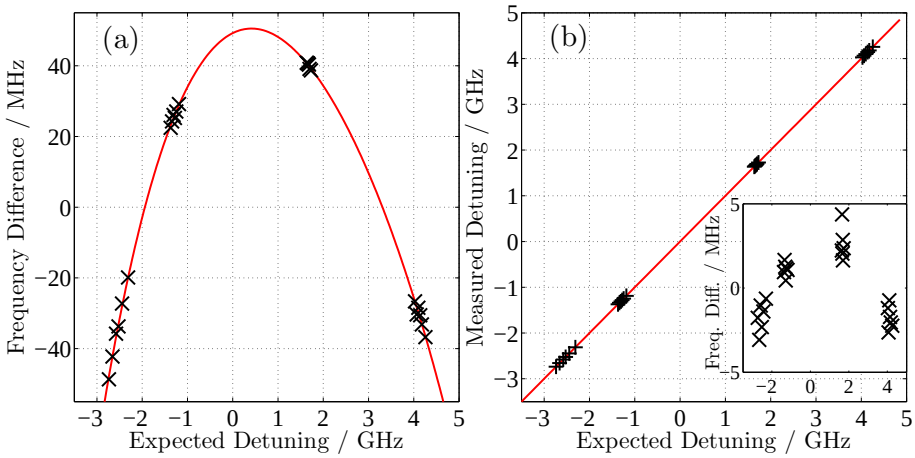

Figure 4.4: (a) Deviation of the measured spectral line frequencies from their expected positions for the D_2 line before linearisation of the laser scan. The black crosses mark the measured positions of the sub-Doppler spectra. (b) Linear fitting of the expected to the measured frequency after linearisation. The red line shows a linear relationship between the two axes, with a gradient of 1 and an intercept of zero. The inset shows the deviation of the measured spectral line frequencies from their expected positions. [*Data taken by Chang Ge*]

Figure 4.4(a) shows a plot of the difference between the measured and expected detunings of the 24 atomic resonances before linearisation. The expected detunings were obtained from table 4.1a. The relatively large deviations from zero are seen to have a polynomial relationship with expected frequency. Figure 4.4(b) shows a plot of measured detuning of the atomic resonances versus the expected detuning after linearisation. The solid line has slope 1 and passes through the origin. The inset shows the deviation between measured and expected frequency. It can be seen that each atomic resonance is within 5 MHz of this ideal fit over a span of 8 GHz. The residual deviations are a consequence of laser drift. If a better frequency fitting were desired additional reference etalons could be used.

Figure 4.5 shows the pump-probe transmission features for the upper hyperfine level for each isotope; six sub-Doppler features are clearly seen, with their positions being in excellent agreement with the predicted values.

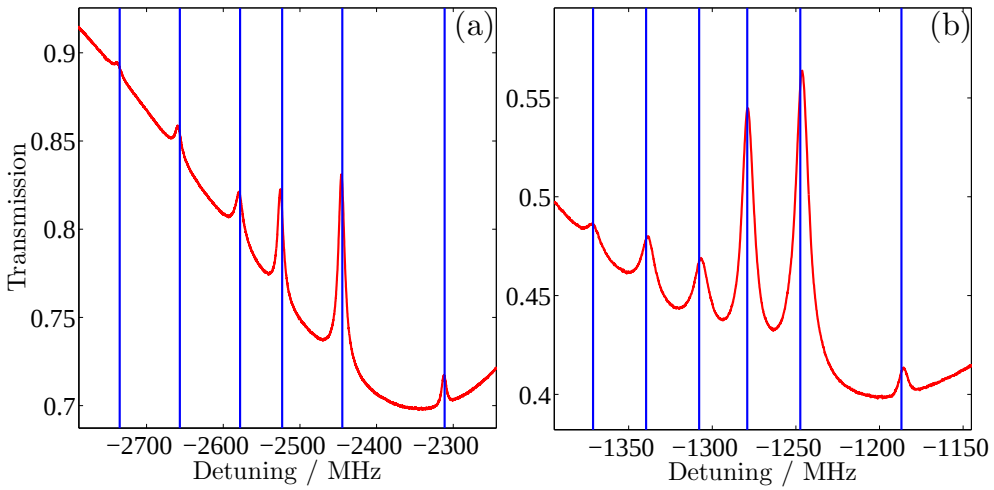

Figure 4.5: Experimentally measured transmission plots for D_2 showing saturated-absorption/hyperfine pumping spectra of (a) the ^{87}Rb $F_g = 2$ line, and (b) the ^{85}Rb $F_g = 3$. The vertical reference lines show the expected peak positions. [*Data taken by Chang Ge*]

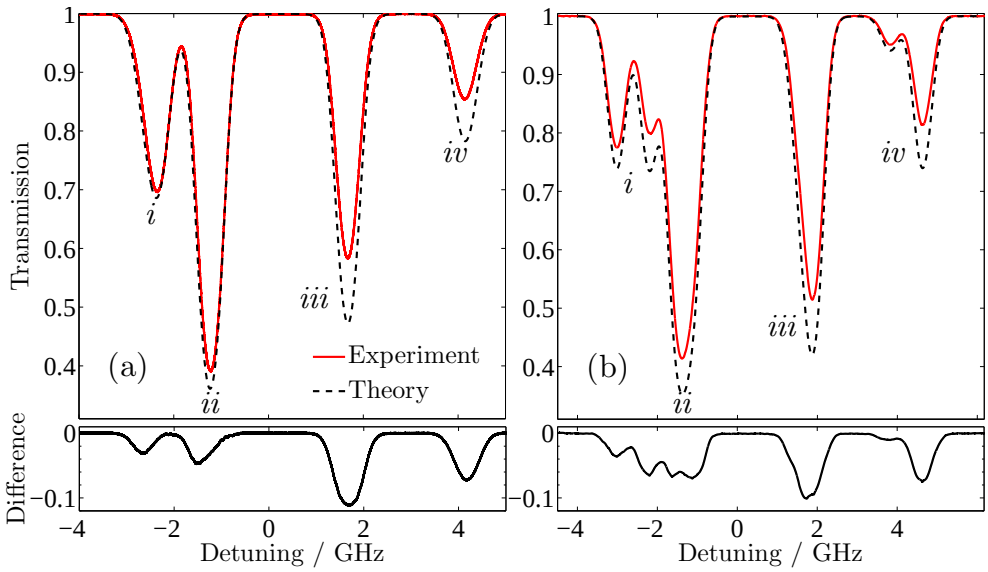

Figure 4.6: Transmission through the vapour cell, showing the role of hyperfine pumping in absorption spectroscopy of (a) the D_2 line at 25.4°C [*Data taken by Chang Ge*] and (b) the D_1 line at 35.6°C. The solid red curve is the experimentally measured transmission and the dashed black the predicted value. Beneath each plot we provide the difference between theory and experiment. Note that the noise in the data is of the order of the line thickness.

4.4 Experimental results

4.4.1 Effects of hyperfine pumping

Figure 4.6 shows transmission, $\mathcal{T}$, versus linear detuning, $\Delta/2\pi$ for (a) D_2 line, for a probe intensity at the centre of the beam of 1.6 μW/mm^2, and (b) D_1 line, 1.5 μW/mm^2. Both intensities correspond to $I/I_{\rm sat} = 0.1$ for that particular line. The expected transmission is also plotted. Although the temperature of the outside of the cell was measured using the thermocouple, the temperature was treated as an adjustable parameter throughout this thesis, representing the fact that there is likely to be a temperature difference between the cell wall and the atomic vapour contained within it. Nevertheless, it was only necessary to adjust the temperature by up to 0.1°C in order to obtain agreement between theory and experiment. For the D_2 line, reasonable agreement is obtained for transitions from the upper hyperfine level of the ground term $F_{\rm g} = \mathcal{I} + 1/2 \rightarrow F_{\rm e}$ (labelled i and ii), often referred

to as the "laser cooling" transitions. Poor agreement is seen for transitions from the lower hyperfine level of the ground term $F_g = \mathcal{I} - 1/2 \rightarrow F_e$ (*iii* and *iv*), often referred to as the "repump" transitions. For the D_1 line, poor agreement is seen across the whole spectrum.

Although the power of the beam is such that the intensity is less than the saturation intensity, the assumption that the atomic population has not been influenced by the propagation of the probe through the medium is obviously invalid. The process by which an atom is excited from one F_g level and is transferred by spontaneous emission into the other F_g level is known as optical, or hyperfine, pumping. Allowing for transfer out of the two-level system is known to modify the absorption process [106, 107].

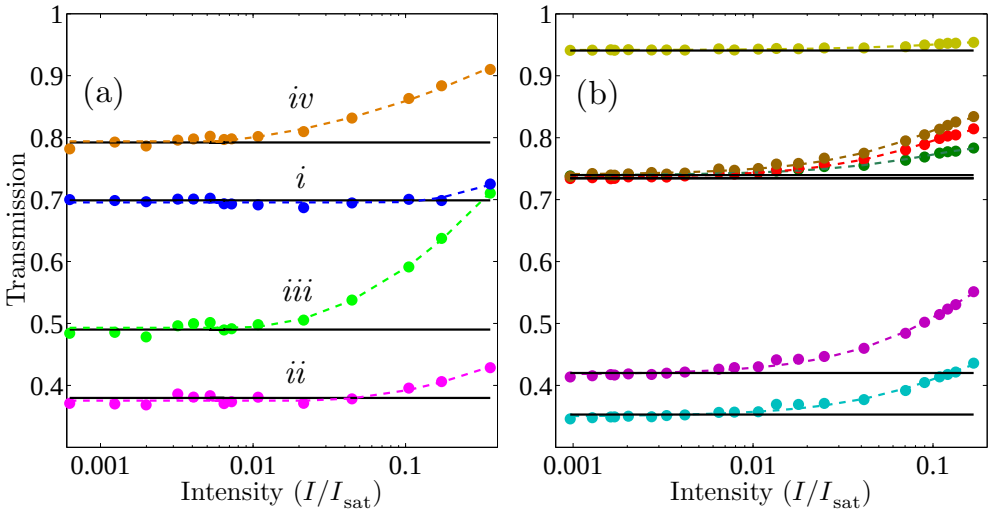

Figure 4.7: (a) The transmission at the centre of the four Doppler-broadened absorption features for D_2 is plotted against laser intensity [*Data taken by Chang Ge*]. The data points correspond to the measured transmission, and the solid lines show the transmission expected. The dotted lines are guides to the eye. The cell was at 25°C. (b) Similar for D_1 where six Doppler-broadened absorption features are observed. Here the cell was at 36°C in order to make the minimum transmission comparable to the D_2 line.

To investigate this further a sequence of spectra were recorded for different probe powers, for both D transitions. Figure 4.7 shows the line-centre transmission for (a) the D_2 transition in a room temperature cell, and (b) the D_1 transition in a cell heated to 36°C. The laser intensity has been normalised in terms of the saturation intensity [15]. Consider the closed

hyperfine-resolved transition D_2 line: $F_g = \mathcal{I} + 1/2 \rightarrow F_e = \mathcal{I} + 3/2$. Owing to the $\Delta F = 0, \pm 1$ selection rule atoms excited into this state have to decay to the ground state from which they started. These transitions have a significantly larger oscillator strength than the two neighbouring transitions $F_g = \mathcal{I} + 1/2 \rightarrow F_e = \mathcal{I} \pm 1/2$, found in the Doppler-broadened transitions ^{87}Rb, $F_g = 2 \rightarrow F_e$ (i) and ^{85}Rb, $F_g = 3 \rightarrow F_e$ (ii). Consequently, the agreement with the theory which neglects transfer into other ground states is good. Notice in Figure 4.6(a) the agreement is excellent on the high-frequency side of the resonance, where the closed transition is located, but poor on the low-frequency side (this is most easily seen in the difference plot). The presence of optical pumping not only reduces the peak absorption but also distorts the line-shape [93]. For the Doppler-broadened transitions ^{85}Rb $F_g = 2 \rightarrow F_e$ (iii) and ^{87}Rb $F_g = 1 \rightarrow F_e$ (iv) there are two closed transitions, $F_g = \mathcal{I} - 1/2 \rightarrow F_e = \mathcal{I} - 3/2$. However these have similar line-strengths to their neighbouring transitions, and hence do not dominate the absorption profile. There are no such closed transitions in the D_1 spectrum. The conclusion therefore is that great care has to be taken to ensure that the probe beam intensity is sufficiently low that hyperfine pumping does not occur during an atom's transit through the beam - this places a far more strict limitation on the upper intensity to be used in contrast to the condition $I < I_{sat}$ valid for two-level atoms [108].

An alternative way to visualise the relative importance of optical pumping is to plot the normalised absorption coefficient $\alpha(I)/\alpha(0)$. This is done in figure 4.8 for the two D_2 repump transitions, and all D_1 transitions. Also included is the theoretical prediction for a Doppler-broadened medium consisting of two-level atoms [15] of the form $1/\sqrt{1 + I/I_{sat}}$. It is apparent that optical pumping reduces the absorption at intensities much weaker than those necessary to saturate the transition. The large error-bars for small intensities are a consequence of the very low light levels and consequently poor signal-to-noise. The data are fit to curves of the form $1/\sqrt{1 + \beta(I/I_{sat})}$, with β being a parameter that characterises the effective reduction in saturation intensity. This is done as a guide to the eye, and care should be taken not to over interpret this parameterisation. In this work the beams had a fixed width and the intensity was varied by changing the probe power. It is pos-

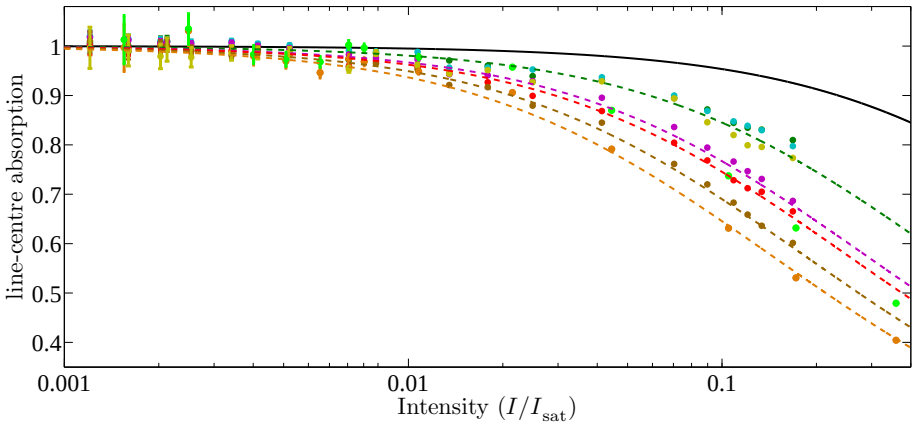

Figure 4.8: Normalised line-centre absorption of the D_2 line showing the effects of hyperfine pumping. The solid curve is the theoretical prediction for a Doppler-broadened medium of two-level atoms. The dotted lines are guides to the eye. Hyperfine pumping on open transitions is seen to be more effective at reducing the line-centre absorption than saturation. [*Data taken by Chang Ge*]

sible to realise the same intensity with different power beams of different radii; in this case the presence of optical pumping means that knowledge of intensity alone is not enough to predict the absorption strength [108].

4.4.2 Comparison of experiment & theory

With knowledge of how weak the probe beam had to be, we performed a series of experiments to test the agreement between our theory for the Doppler-broadened absorption profile of rubidium vapour and experiment. The probe intensity was 32 nW/mm^2, corresponding to $I/I_{sat} = 0.002$. Figure 4.9 shows transmission spectra at three different temperatures (16.5°C, 25.0°C and 36.6°C) for the D_2 line. There is excellent agreement between theory and experiment; the rms discrepancy is at the 0.2% level. Note that the measured absorption is still slightly smaller than the predicted value. This could arise due to the broad frequency pedestal of the emission from the laser, and also the finite laser linewidth which is of the order of 0.1% of the Doppler width.

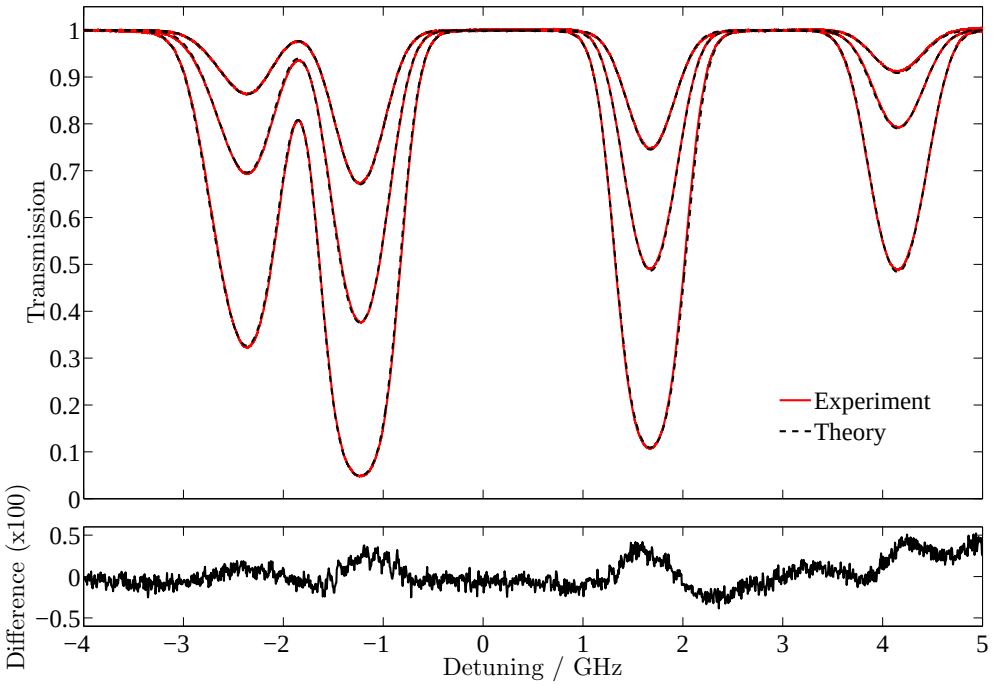

Figure 4.9: D_2 transmission plots for the comparison between experiment and theory, at temperatures of 16.5°C (top), 25.0°C (middle), and 36.6°C (bottom). Red and black curves show measured and expected transmission respectively. Below the main figure is a plot of the difference in transmission between theory and experiment for the 16.5°C measurement. [*Data taken by Chang Ge*]

4.5 Discussion

In summary, we have studied Doppler-broadened spectra for the Rb D lines. A model was developed which allows the absorption profile and refractive index to be evaluated in terms of tabulated functions. Excellent agreement was found between theory and experiment for transmissions ranging from 5 to 95%. We showed that the effect of hyperfine pumping is significant for open transitions, and outlined how to achieve the weak-field limit. The weak-probe limit is only reached for $I/I_{\text{sat}} \approx 0.001$ for a beam width of 2 mm. Our model allowing quantitative predictions of the absorption and dispersion in alkali metal vapour will both aid the burgeoning field of controlled light propagation [29, 30, 36] and in the understanding of the spectra obtained in widely used laser locking schemes [18–24].

Chapter 5

Off-resonant interactions

The motivation behind this chapter is to investigate the relationship between the absorption and dispersion experienced by off-resonant radiation interacting with an inhomogeneously broadened atomic medium. Of particular interest is the dispersive response of the medium when the detuning is larger than the inhomogeneous linewidth. In this region scattering of photons is reduced, but this does not necessarily mean that the dispersive atom-light coupling suffers accordingly. We take the analytic results for the susceptibility developed early in this thesis, and investigate the domain of validity of two approximations which facilitate the analysis of experimental data. These simple analytic expressions allow us to predict where it is best to perform dispersive experiments without having to consider the more numerically intensive full solution to the susceptibility. For detunings larger than twice the inhomogeneous linewidth we demonstrate that inhomogeneous broadening may be neglected for both absorption and dispersion measurements.

The structure of this chapter is as follows. We begin by describing the function which governs the absorption and dispersion of a Doppler-broadened medium, and go on to make approximations to this function. We then use these analytic approximations to compare the absorptive and dispersive characteristics of an atomic resonance. Finally, we compare the theoretical expressions to experimental measurements.

5.1 Electric susceptibility

We have met the electric susceptibility, χ, previously in this thesis (see chapter 3), but we will reiterate the salient features here for ease of reference. Absorption is proportional to the imaginary part of the susceptibility, χ_{I}, and we have shown in chapter 4 that our model of the susceptibility is in excellent agreement with experimental data. Dispersive effects result from the real part, χ_{R}, and it is this quantity (and its relationship to χ_{I}) which is of interest in this chapter. The important expressions relating to the susceptibility are

$$\chi(\Delta) = c_{m_F}^2 \frac{d^2\mathcal{N}}{\hbar\epsilon_0} s(\Delta), \tag{5.1}$$

$$s(\Delta) = f \otimes g = \frac{\mathrm{i}\sqrt{\pi}}{ku} w(\mathrm{i}z), \tag{5.2}$$

$$w(\mathrm{i}z) = \mathrm{e}^{z^2}\mathrm{erfc}(z), \tag{5.3}$$

$$z(\Delta) = \tfrac{1}{2}\frac{\Gamma}{ku} - \mathrm{i}\frac{\Delta}{ku}. \tag{5.4}$$

Here $s(\Delta)$ is derived from convolution of the homogeneous line-shape f and inhomogeneous line-shape g, and is related to the ubiquitous Faddeeva function $w(\mathrm{i}z)$. The associated widths are Γ, the FWHM of the homogeneously broadened line, and ku, the 1/e half-width of the inhomogeneously broadened line (here the inhomogeneous broadening mechanism is assumed to be purely due to the Doppler effect with a Maxwell-Boltzmann velocity distribution).

5.1.1 Approximating the Faddeeva function

The line-shape given by the Faddeeva function appears in a number of areas in the physics community: in atomic spectroscopy [109], magnetic resonance [110], and as the plasma dispersion function [111, 112]. The line-shapes found in these fields are fundamentally related to the complex error function, which was tabulated in 1954 by Faddeeva and Terent'ev [113, 114]. Given the transcendental nature of the complex error function, and its ubiquity in physics, extensive research has been carried out into finding analytic approximations to it [115, 116]. There have also been studies to produce fast algorithms to compute the function numerically [117, 118].

Equation (5.2) is the exact analytic line-shape of the Doppler-broadened susceptibility; unfortunately this exact result can be difficult to use. Although algorithms exist for the Faddeeva and complementary error function $\mathrm{erfc}(z)$, they are not easy to manipulate analytically, and can be time-consuming to evaluate numerically. Also, manipulating numerical expressions makes it difficult to gain any insight into the underlying physical processes [119]. Consequently it is difficult to relate χ to z and the parameters of which they are composed (namely the widths Γ and ku). This in turn makes it difficult to see the relationship between the absorptive and dispersive properties. The preceding reasons motivate our study of approximations to the analytic result by looking at the Faddeeva function in two regimes, named the Gaussian and Lorentzian approximations for reasons that will become apparent.

5.1.2 The Gaussian approximation

We consider the situation where the broadening due to atomic motion is much larger than natural broadening, which is the case for typical room temperature alkali-metal atoms. For this approximation we therefore look at the limit that $\Gamma/ku \to 0$ in the derivation of the Faddeeva function. Approximating the imaginary part of the homogeneous line-shape $f = \mathrm{i}/kuz$ to a Dirac delta function,

$$f(z) \approx -\frac{ku}{\Delta} + \mathrm{i}\pi\delta\left(\frac{\Delta}{ku}\right), \tag{5.5}$$

where the real part has been calculated using the Kramers-Kronig relations (see section 3.2). With this expression substituted into the convolution integral of equation (5.2), the real and imaginary parts of the susceptibility are, respectively

$$s_{\mathrm{R}} = -\frac{\sqrt{\pi}}{ku}\,\mathrm{e}^{-(\Delta/ku)^2}\mathrm{erfi}(\Delta/ku), \tag{5.6}$$

$$s_{\mathrm{I}} = \frac{\sqrt{\pi}}{ku}\,\mathrm{e}^{-(\Delta/ku)^2}. \tag{5.7}$$

The real part contains the imaginary error function $\mathrm{erfi}(z)$ which is similar to the Faddeeva function in that it needs to be evaluated numerically. The imaginary term is the convolution of a Gaussian and a Dirac delta function,

and as expected evaluates to the Gaussian function responsible for Doppler-broadening, with the FWHM Doppler width $\Delta\omega_{\mathrm{D}} = 2\sqrt{\ln 2}\, ku$.

In this approximation both s_{R} and s_{I} have a Gaussian detuning dependence, whose exponential decrease means that it decays rapidly away from resonance. The real part s_{R} has an additional imaginary error function dependence which increases rapidly with detuning; hence dispersion contains the long-range characteristics associated with the Faddeeva function.

5.1.3 The Lorentzian approximation

In the Gaussian approximation we made the assumption that homogeneous broadening was negligible compared to inhomogeneous broadening, based on the ratio of their frequency widths. We will see that this is not true far from resonance. In this section we will find regimes under which homogeneous broadening dominates the susceptibility. We begin by noting that the complementary error function can be written in the form of a continued fraction [120, 121]

$$\sqrt{\pi}\,\mathrm{erfc}(z) = 2\int_z^\infty \mathrm{e}^{-t^2}\mathrm{d}t = \frac{2\mathrm{e}^{-z^2}}{2z + \cfrac{2}{2z + \cfrac{4}{2z + \cfrac{6}{2z + \cdots}}}}. \tag{5.8}$$

For $|z| \gg 1$ the continued fraction can be approximated to e^{-z^2}/z. This requires either of the following conditions to be fulfilled:

(i) $\quad |\Delta| \gg \Delta\omega_{\mathrm{D}}$

(ii) $\quad \Gamma \gg \Delta\omega_{\mathrm{D}}$

The first condition is that the laser is detuned from resonance further than the Doppler width and is essentially a property of the light source; the second is that natural broadening dominates over Doppler broadening and is a property of the medium. The Doppler width can be reduced by, for example, using cold atoms at sub-milliKelvin temperatures [4–6]. Many experiments, including the ones considered in this thesis, are conducted with alkali-metal atoms on the D lines at room temperature (or hotter); the parameters of interest are then $\Gamma \sim 2\pi(5\text{ MHz})$, and $\Delta\omega_{\mathrm{D}} \sim 2\pi(0.5\text{ GHz})$, thus $\Gamma/\Delta\omega_{\mathrm{D}} \sim 10^{-2}$. Therefore, for the limit $|z| \gg 1$ to be valid, it is necessary to be detuned far from resonance, $|\Delta| \gg \Delta\omega_{\mathrm{D}}$.

Substituting the approximated erfc(z) into (5.2) we get the result

$$s = \frac{\mathrm{i}}{kuz} = \frac{\mathrm{i}}{\Gamma/2 - \mathrm{i}\Delta}. \tag{5.9}$$

Note that this is identical to the case for homogeneous broadening, e.g. an ensemble of stationary atoms, or atoms at ultra-low temperatures for which Doppler broadening is negligible [122]. The real part of the susceptibility gives the dispersion function, and the imaginary part the Lorentzian function; specifically

$$s_{\mathrm{R}} = -\frac{\Delta}{(\Gamma/2)^2 + \Delta^2}, \tag{5.10}$$

$$s_{\mathrm{I}} = \frac{\Gamma/2}{(\Gamma/2)^2 + \Delta^2}. \tag{5.11}$$

Furthermore, since $|\Delta| \gg \Delta\omega_{\mathrm{D}} \gg \Gamma$, these relations simplify further to $s_{\mathrm{R}} = -1/\Delta$, and $s_{\mathrm{I}} = \Gamma/2\Delta^2$ respectively. These detuning dependences are discussed further in section 5.1.5.

The physical interpretation of the Lorentzian approximation is that the Gaussian line-shape responsible for inhomogeneous broadening decreases exponentially with detuning, whereas the homogeneous line-shape decreases much more slowly in the wings. Hence the contribution to the overall line-shape far from resonance is dominated by the Lorentzian function, and both absorption and dispersion will be well approximated.

5.1.4 Validity of the approximations

Figure 5.1 shows the line-shape, s, of the Faddeeva function and its Gaussian and Lorentzian approximations, for a typical room temperature alkali-metal atomic ensemble where the Doppler-broadening is two orders of magnitude larger than natural broadening. It can be seen in figure 5.1(a) that for $|\Delta| < 1.5 \times \Delta\omega_{\mathrm{D}}$ the imaginary part of the Faddeeva function is adequately described by the Gaussian approximation, and for $|\Delta| > 2\Delta\omega_{\mathrm{D}}$ the Lorentzian approximation holds. Therefore, close to resonance, Doppler-broadening dominates the absorptive interaction; whereas natural broadening dominates at large detuning. A similar situation for the real part of the Lorentzian approximation is seen in figure 5.1(b), i.e. it is valid for

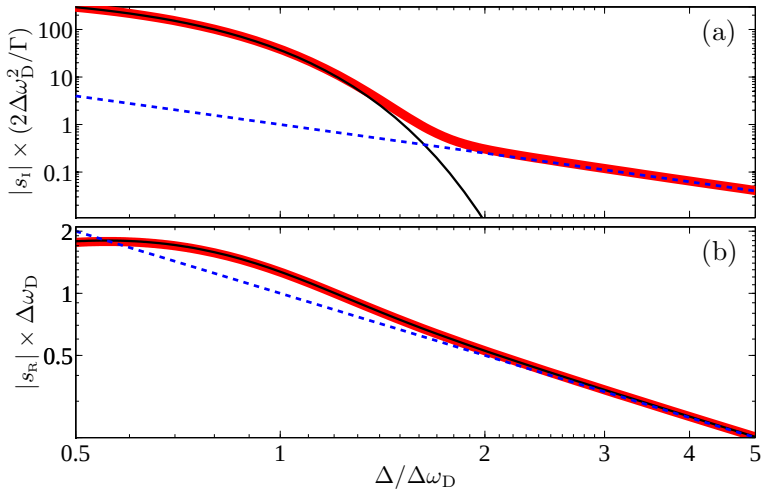

Figure 5.1: Comparison of the Faddeeva function and its approximations. The imaginary and real parts of the susceptibility line-shape, s, are shown in parts (a) and (b), respectively. The horizontal axis is detuning, Δ, in terms of the Doppler width, $\Delta\omega_D$. The thick solid red curve shows s calculated using the Faddeeva function (with $\Gamma/\Delta\omega_D = 10^{-2}$), whilst the Gaussian and Lorentzian approximations are shown as solid black and dashed blue curves, respectively.

$|\Delta| > 2\Delta\omega_D$. However, the Gaussian approximation is in good agreement with the Faddeeva function over the whole spectral range. In appendix E we investigate the Faddeeva function over a wider range of z values and show the relative difference between it and its approximations.

5.1.5 Comparing absorption & dispersion

Figure 5.2 shows the ratio $|\chi_R/\chi_I|$, calculated using the Faddeeva function and its Gaussian and Lorentzian approximations. It shows that the ratio between dispersion and absorption continually increases with detuning, with the asymptotic limit $2|\Delta|/\Gamma$ from the Lorentzian approximation (see equations (5.10) & (5.11)). Note, however, that dispersion also varies inversely with detuning in this limit. Hence, any dispersive effects which require low absorption are best performed far from resonance under conditions which increase the atom-light interaction e.g. high atomic density [40] or stronger coupling [57].

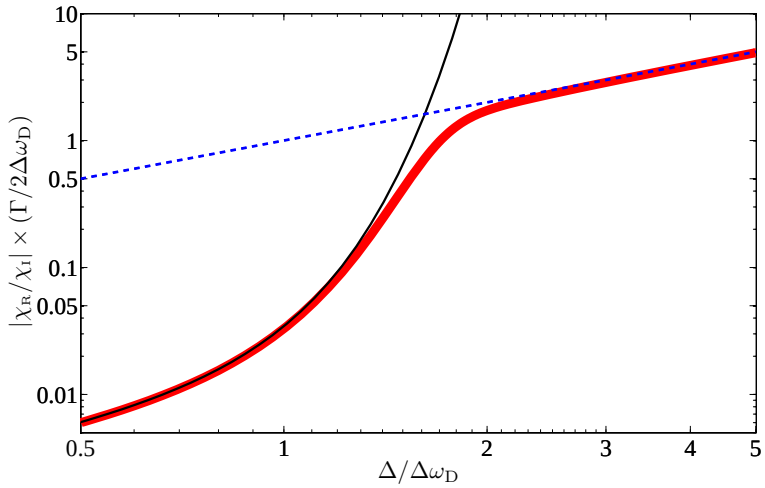

Figure 5.2: The relative importance of dispersive and absorptive properties of a Doppler-broadened atomic medium. The ratio $|\chi^R/\chi^I|$ for a single transition is shown as a function of detuning, Δ, in terms of the Doppler width, $\Delta\omega_D$. The thick solid red curve shows χ calculated using the Faddeeva function (with $\Gamma/\Delta\omega_D = 10^{-2}$), whilst the Gaussian and Lorentzian approximations to χ are shown as solid black and dashed blue curves, respectively.

5.1.6 Hyperfine structure

We have shown that Doppler-broadening can effectively be ignored for detunings $|\Delta| > 2\Delta\omega_D$. However, this situation is somewhat complicated due to the presence of hyperfine structure. For alkali-metal atoms the hyperfine structure is such that the ground state splitting, $\Delta\omega_{hfs}$, is much larger than the room temperature Doppler width. This is not the case for the excited states, which tend to have intervals of comparable size to $\Delta\omega_D$. Hence, in order to calculate χ near to the line-centre, each individual hyperfine transition needs to be modelled individually, although for some purposes excited state splitting can be ignored (for example, on the D_2 lines of Rb [36] and Cs [29]). Far from line-centre, at detunings larger than the ground state hyperfine splitting, it is possible to approximate all hyperfine transitions to a single Lorentzian function. By performing this calculation we find that there is a less than 5% error for $|\Delta| > 3.5 \times \Delta\omega_{hfs}$ for the Rb D lines.

5.2 Comparing theory & experiment

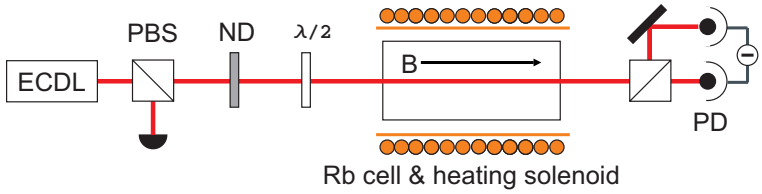

Figure 5.3: Schematic of the experimental apparatus. The output of an external cavity diode laser (ECDL) is passed through a polarisation beam splitter (PBS), providing linearly polarised light. The beam is attenuated with a neutral density filter (ND) before passing through a heated vapour cell. A half-wave plate ($\lambda/2$) is used to control the polarisation angle of the light before it is analysed with a PBS and collected on a differencing photodiode (PD).

In order to test experimentally the validity of the approximations to the Faddeeva function, the transmission of a probe beam on the D_1 line of rubidium was recorded. The experimental apparatus is shown in figure 5.3. The source of laser light was an external cavity diode laser at 795 nm. The laser output polarisation was made linear using a polarisation beam splitting cube, and then attenuated to be less than 1 μW such that it is in the weak probe limit (see reference [108]). The beam had a $1/e^2$ half-width of 2 mm. After passing through a half-wave plate the beam was sent through a heated vapour cell, based on the design of [18]. A solenoid[1]provided the heating and magnetic field, when required (it was briefly switched off for measurements with zero magnetic field). Upon transmission through the cell, the two orthogonal linear polarisations of the beam where separated with a PBS cube and sent to the two ports of a differencing photodiode. For transmission measurements under zero applied magnetic field the half-wave plate was rotated to maximise the signal incident upon a single detector port; for balanced detection of beam rotation the wave plate axis was set such that equal amounts of light were transmitted from the two PBS cube ports. The vapour cell used was a 75 mm ^{87}Rb cell containing the Rb isotopes according to the ratio ^{87}Rb:^{85}Rb of 99:1.

[1]Built and tested by Yifei Cai.

5.2.1 Absorption

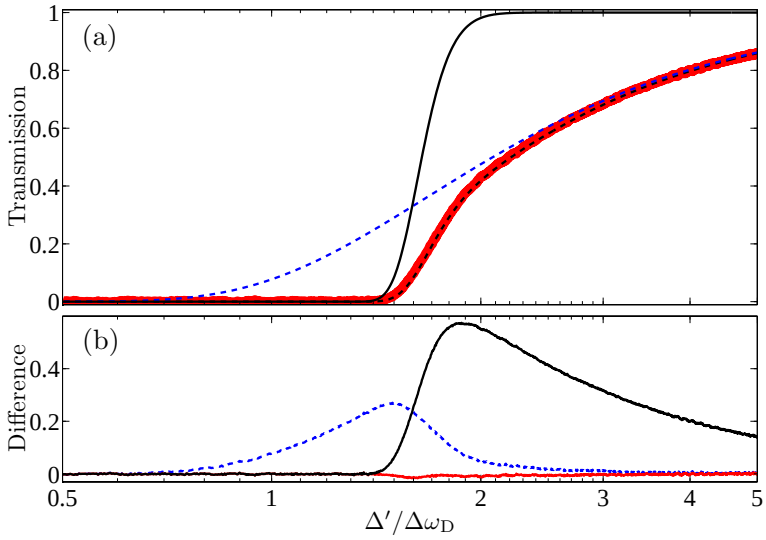

Figure 5.4: Comparison between experiment and theory for the transmission of a weak probe beam through a vapour cell (a) Experimental data are shown in red, whilst the dashed black curve shows the transmission calculated using the Voigt function. The Gaussian and Lorentzian approximations to the Voigt function are shown as solid black and dashed blue curves, respectively. (b) The difference in transmission between theoretical and measured data. The experimental data were obtained with red-detuned light, but plotted against $\Delta' = -\Delta$. The origin of the detuning axis is from the ^{87}Rb $F_g = 2 \rightarrow F_e = 1$ transition.

The solid curve in figure 5.4(a) shows the transmission measured at 132°C as a function of detuning from the weighted line-centre in units of Doppler width, $\Delta\omega_D = 2\pi(584\text{ MHz})$. Absorption in the region shown is due to the ^{87}Rb $F_g = 2 \rightarrow F_e = 1, 2$ transitions. Theoretical transmission (dashed curves) was calculated using equations (5.2), (5.7) and (5.11) to model each hyperfine transition involved. The transmission difference between theory and experiment is shown in figure 5.4(b). It can be seen that the Faddeeva function agrees with the measured data to within the noise level; any discrepancy beyond this is due to the fitting of the frequency axis. Both the Gaussian and Lorentzian approximations agree on resonance. This is because the transition is optically thick so any variation between the two approximations is obscured. At a detuning of about one Doppler width the Lorentzian is no longer at zero transmission and only matches with measured data again

for detunings greater than two Doppler widths. Conversely, the Gaussian approximation matches the experiment up to about 1.5 Doppler widths before differing significantly for larger detunings. It was stated in the derivation of the Gaussian and Lorentzian approximations that Doppler broadening dominates close to resonance, whilst natural broadening dominates far from resonance. It can be seen that at around two Doppler widths absorption due to the Gaussian line-shape rapidly decreases, and it is from this point that the Lorentzian function becomes the dominant broadening mechanism.

The situation with the two approximations is similar to that seen in previous experiments, where Gaussian fits to data are used when the line-centre is of interest, e.g. in reference [93], and Lorentzian fits for off resonant behaviour, e.g. in reference [29]. However, we have derived these line-shapes *ab initio* and quantified their regime of validity.

5.2.2 Dispersion

Dispersion is more difficult to measure than the absorption of a medium and, as such, most experimental studies have concentrated on absorptive measurements. Absolute dispersive measurements generally require actively-stabilised interferometry [123, 124] or beam deflection measurements [125]. However, the *differential* dispersion of a medium is easily probed via the Faraday effect [40, 53]. We will give a more detailed explanation of the Faraday effect later in this thesis (see chapter 7), suffice it to say here that the Faraday effect produces a difference in the dispersion between left and right circularly polarised light. This leads to rotation of the polarisation plane for incident linearly polarised light. In a heated vapour this rotation can be as large as tens of radians over a frequency range of many Doppler widths. Using the technique described later in this thesis we measured the rotation of light polarisation using a differencing signal in a balanced polarimeter. Light transmitted through the vapour is sent through a polarisation beam splitter and the resulting vertical and horizontal polarisations directed to a differencing photodiode, where the intensities I_x and I_y are subtracted. An important feature of this signal is that the positions of the zero crossings are solely due to dispersion. These zero crossings correspond to a rotation angle,

θ, of integer multiples of $\pi/2$.

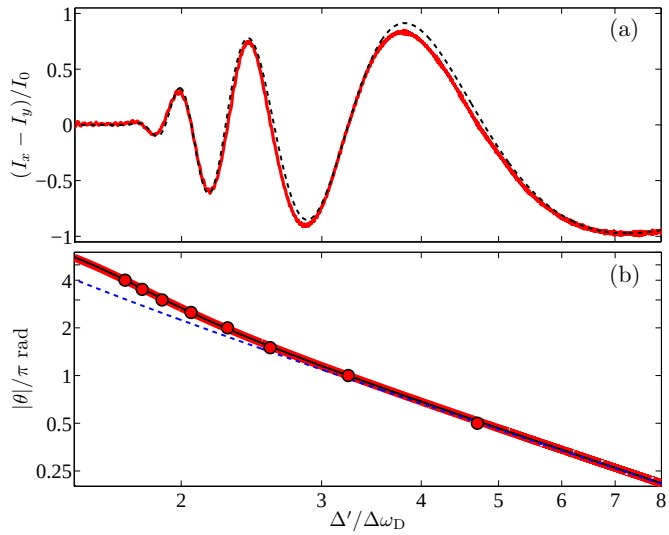

Figure 5.5: Comparison between experiment and theory for the polarisation rotation of a weak probe beam through a vapour cell. (a) Balanced differencing signal. Experimental data are shown in red, whilst the dashed black curve shows the theoretical signal calculated using the Faddeeva function. (b) The rotation angle of the beam's plane of polarisation: red points are from the zero crossings of the measured data, curves are calculated using the Faddeeva (thick solid red), Gaussian (solid black) and Lorentzian (dashed blue) functions. The Doppler width is $\Delta\omega_D = 2\pi(569\text{ MHz})$.

Figure 5.5(a) shows the differencing signal for a temperature of 112°C and applied field of 200 G. The signal is normalised to the maximum intensity, I_0, received by one of the photodiodes in the absence of a magnetic field. Also shown is the signal calculated by solving the complete Hamiltonian of the system, with a Faddeeva line-shape. There is good agreement between the two curves, the main difference being in the amplitude, which is due in part to the differencing photodiodes not being perfectly balanced. Figure 5.5(b) compares the Faddeeva function and its approximations to the rotation angle experienced by the linearly polarised probe beam. Data points are taken from zero crossings in figure 5.5(a). Excellent agreement is seen between measured data and both the Faddeeva function and Gaussian approximation over the whole spectral range, whilst the Lorentzian approximation only holds far from resonance, in agreement with the conclusion of sections 5.1.2 and 5.1.3.

5.3 Discussion

We have seen in the previous two sections that the Faddeeva function gives a good fit to data over the whole frequency range, whereas the Lorentzian approximation is only valid far from resonance. The Gaussian approximation, however, shows contrasting behaviour in its absorptive and dispersive properties. With regard to absorption it is valid close to resonance only, whilst the dispersive properties are accounted for over all detuning. The differing nature of the two approximations stems from the fact that only in the Lorentzian approximation did we assume that $|\Delta| \gg \Delta\omega_{\mathrm{D}}$.

The approximations to the electric susceptibility we have described facilitate (i) the analytic manipulation of χ, allowing a comparison between the dispersive and absorptive properties of atomic media; and (ii) ease of computation of properties of interest. In particular, we have seen that for a detuning greater than two Doppler-broadened linewidths the fully analytic Lorentzian approximation is valid. From this we have shown that off resonance dispersion increasingly dominates over absorption. Quantitative predictions of dispersion were made and were found to be in excellent agreement with measured data.

Chapter 6

The slow-light effect

In chapter 4 our main concern was the development of a theoretical model which could predict the transmission of a weak, continuous-wave beam through an atomic vapour. Due to the inextricable link between absorption and dispersion (epitomised in the Kramers-Kronig relations, see section 3.2), our model also gives us some insight into the dispersion experienced by interacting light. We briefly came across dispersion in chapter 5 when we compared theoretical and experimental polarisation rotation of off-resonant light, finding that our model accounts well for absorption and dispersion. In this chapter we investigate another manifestation of dispersion, that of slow light. This phenomenon is most readily observable in the propagation of optical pulses through a hot atomic vapour.

6.1 Optical pulses & Fourier optics

So far in this thesis we have mostly concerned ourselves with monochromatic waves. The electric field of these single frequency waves is of infinite temporal and spatial extent and as such they are not physically realisable. The loophole we used to justify our continued use of these waves is that after a sufficiently long time under constant illumination a state of equilibrium of the atom-light interaction is achieved[1]. We saw in sections 2.4 and 3.3 that

[1] We saw in chapter 2 that typically several excited state lifetimes is long enough for the medium to 'forget' about its past state.

even over short timescales a low-intensity wave will be in quasi-static equilibrium with the medium through which it propagates, and in section 3.1 we calculated the electric field of these weak waves. In this chapter we limit discussion to atom-light interactions in which the medium is unaffected by the passage of light, allowing us to use the weak-field solutions to model pulse propagation.

A superposition of many monochromatic waves can be formed such that the resultant pulse is localised (either as a single disturbance, or many sequential disturbances in the form of a 'pulse train'). Consider the sum of N forward-traveling plane waves all polarised in the same direction:

$$E(z,t) = \sum_{j}^{N} E_{0j} \mathrm{e}^{\mathrm{i}(k_j z - \omega_j t)}. \tag{6.1}$$

The waves interfere constructively and destructively due to relative phase differences. For a sum of closely spaced frequencies, the resulting superposition is the product of two components: a rapid temporal variation enclosed by a slower, amplitude modulated envelope (cf. acoustic beats). As the number of individual waves is increased in this sum, the distance between regions of constructive interference (i.e. individual pulses) increases. In order to create a single, well-defined pulse the discrete sum of wave frequencies above must be replaced by a continuum of frequencies. This is then a Fourier integral:

$$E(z,t) = \frac{1}{\sqrt{2\pi}} \int_{-\infty}^{+\infty} E(z,\omega) \mathrm{e}^{-\mathrm{i}\omega t} \mathrm{d}\omega, \tag{6.2}$$

where $E(z,\omega) = E(0,\omega)\exp[\mathrm{i}k(\omega)z]$ is the angular-frequency spectrum of the pulse, where the initial spectrum is given by the inverse Fourier transform of the electric field at $z = 0$,

$$E(0,\omega) = \frac{1}{\sqrt{2\pi}} \int_{-\infty}^{+\infty} E(0,t) \mathrm{e}^{\mathrm{i}\omega t} \mathrm{d}t. \tag{6.3}$$

The angular-frequency spectrum is a measure of how much each angular frequency contributes to the pulse. It is important to the propagation of pulses through dispersive media because the wavevector k is frequency dependent: each monochromatic wave comprising the pulse will behave differently inside the medium. This will lead to distortion and attenuation of the pulse as each angular-frequency component has its own velocity and absorption coefficient.

For a sufficiently weak pulse, these single-frequency, or monochromatic, wave components propagate unaffected by each other (via the superposition principle of linear systems), at a phase velocity $v_\mathrm{p} = c/n$. In a non-dispersive medium, where the refractive (or phase) index n is identical for all frequencies, each phase element of a pulse is travelling at the same velocity and is being attenuated by the same amount. The pulse velocity v_g will be identical to this. However, in media where n is frequency dependent phase elements propagate with a range of velocities, and the superposition of these elements give rise to a pulse which can travel at a vastly different speed.

As we did in section 3.2.1 we can make the slowly-varying envelope approximation. The pulse envelope that will be considered in this investigation is Gaussian, since it is easy to manipulate analytically and to a fair degree it can be reproduced experimentally. The envelope has the property that its angular-frequency spectrum is also Gaussian. For an envelope of unit amplitude and zero phase at the entrance to the medium, $\tilde{E}(z = 0, t)$, the relationship between it and its initial spectrum $\tilde{E}(0, \omega)$ is

$$\tilde{E}(0, t) = \exp[-\tfrac{1}{2}(t/\tau)^2], \tag{6.4}$$

$$\tilde{E}(0, \omega) = \tau \exp[-\tfrac{1}{2}\tau^2(\omega - \omega_\mathrm{c})^2], \tag{6.5}$$

where the spectrum is centred at the carrier angular frequency ω_c, and τ is the half-width of the envelope's intensity profile at $|\tilde{E}(0, t)|^2 = 1/\mathrm{e}$. τ is related to the full-width at half-maximum (FWHM) of the intensity profile, Δt, and intensity spectrum, $\Delta\omega$, via

$$\Delta t/\tau = \tau\Delta\omega = 2\sqrt{\ln 2} \approx 1.665. \tag{6.6}$$

Hence the relationship between the FWHM of the profile and spectrum is $\Delta t\Delta\nu = 2\ln 2/\pi \approx 0.441$, where $\Delta\omega = 2\pi\Delta\nu$. Another useful quantity describing the pulse is the bandwidth $\Delta\omega_\mathrm{band} = 2\pi\Delta\nu_\mathrm{band} = 6/\tau$. This describes the (angular-)frequency range in which the majority (99%) of the pulse is contained.

To simulate weak pulse propagation through homogeneous media we first calculate the spectrum at the entrance to the medium, $\tilde{E}(0, \omega)$, and then multiply by the frequency dependent phase factor $\exp[\mathrm{i}k(\omega)z]$ to get the spectrum at a point z inside the medium. The temporal electric field inside

the medium, $E(z,t)$, can then be calculated by taking the Fourier transform of the spectrum.

6.2 Narrowband approximation

According to the previous section, calculating the electric field at a point in space requires a Fourier integral to be performed, and given the complexity of the wavevector k a numerical method is usually required to obtain solutions (but see reference [64] for analytic solutions to some restricted cases of the wavevector). In this section we make the *narrowband approximation*, that is, we assume that the variation of the dispersive and absorptive properties of the medium over the bandwidth of the pulse is small. This approximation allows the use of a simplified wavevector, leading to analytic solutions of pulse propagation for a Gaussian envelope. It is often the case in experiments that we require the pulse to be transmitted with little distortion and only moderate absorption, and in this regime the narrowband approximation is perfectly justifiable.

A Taylor-series expansion of the wavevector (here assumed to be real-valued) about the pulse carrier angular frequency, ω_c, yields [10]

$$k(\omega) = k(\omega_\mathrm{c}) + (\omega - \omega_\mathrm{c})\frac{\mathrm{d}k}{\mathrm{d}\omega}\bigg|_{\omega=\omega_\mathrm{c}} + \frac{1}{2!}(\omega - \omega_\mathrm{c})^2\frac{\mathrm{d}^2k}{\mathrm{d}\omega^2}\bigg|_{\omega=\omega_\mathrm{c}} + \ldots . \tag{6.7}$$

The zeroth-order coefficient $k = \omega_\mathrm{c}/v_\mathrm{p}$ is inversely proportional to the phase velocity of the carrier wave; the first-order coefficient is proportional to $\mathrm{d}k/\mathrm{d}\omega = 1/v_\mathrm{g}$, which is the inverse of the group velocity. The group velocity is given by the well-known expression [64]

$$v_\mathrm{g} = \frac{c}{n(\omega) + \omega\frac{\mathrm{d}n(\omega)}{\mathrm{d}\omega}}\bigg|_{\omega=\omega_\mathrm{c}} = \frac{c}{n_\mathrm{g}}, \tag{6.8}$$

where n_g is the group refractive index. The time it takes for a pulse to traverse a medium of length L is the transit time $t_\mathrm{transit} = L/v_\mathrm{g} = Ln_\mathrm{g}/c$. The second-order coefficient depends on the term

$$\frac{\mathrm{d}^2k}{\mathrm{d}\omega^2} = \frac{1}{c}\frac{\mathrm{d}n_\mathrm{g}}{\mathrm{d}\omega}, \tag{6.9}$$

which describes the dispersion of the group velocity. For non-zero group velocity dispersion (GVD), points on the pulse profile move at different velocities through a dispersive medium, and there will therefore be a spread in transit times across the pulse. This spread, $\delta t_{\text{transit}}$, can be approximated to $\delta t_{\text{transit}} = \delta\omega(L/c)(\mathrm{d}n_{\text{g}}/\mathrm{d}\omega)$, where $\delta\omega$ is a measure of the angular frequency extent of the pulse.

If a pulse's bandwidth is large, higher-order terms in (6.7) need to be considered. These higher-order dispersive terms cause the pulse to distort and hence such a pulse will no longer bear much resemblance to its initial temporal profile. For a pulse to propagate through a dispersive medium and remain close to its initial profile, it is necessary that the transit time spread be much less than the initial temporal duration. This limits the pulse bandwidth, as its frequency components must be within a spectral region where third-order and higher terms in (6.7) vanish.

We will consider the analytic case of a Gaussian pulse propagating through a medium in which dispersion leads to only group delay and broadening, in addition to constant absorption over the pulse bandwidth. Thus the envelope travels at the group velocity. For the pulse to remain essentially unbroadened (and thus retain its initial width τ), the propagation distance must be less than the dispersion length [126]

$$L_{\text{GVD}} = c\tau^2 \left| \frac{\mathrm{d}n_{\text{g}}}{\mathrm{d}\omega} \right|^{-1}. \tag{6.10}$$

The temporal pulse width increases with propagation distance through the medium, z, by a factor [126]

$$\eta = \sqrt{1 + (z/L_{\text{GVD}})^2}. \tag{6.11}$$

Hence the dispersion length is the propagation distance at which the pulse width is a factor $\sqrt{2}$ of the initial value. For propagation distances comparable to or longer than L_{GVD}, or shorter initial temporal width (and hence larger frequency extent), the pulse broadens but retains its Gaussian profile (in the absence of terms higher than second order in (6.7)).

The intensity of the Gaussian envelope as a function of distance is

$$I(z,t) = I_0 \frac{\mathrm{e}^{-\alpha z}}{\eta} \exp\left[-\frac{(t - z/v_{\text{g}})^2}{(\eta\tau)^2} \right], \tag{6.12}$$

which is the input intensity profile shifted in time to a position z/v_g and broadened by a factor η. Loss of amplitude is the result of two factors. The first, $1/\eta$, represents the fact that the energy of the pulse (and hence area under the intensity envelope) is conserved by the dispersive effect of GVD. The second, $\exp[-\alpha z]$, is the Beer-Lambert law transmission calculated with the absorption coefficient α of the carrier wave, and taken to be the transmission of the pulse as a whole.

6.3 Predicted delay & absorption of pulsed light

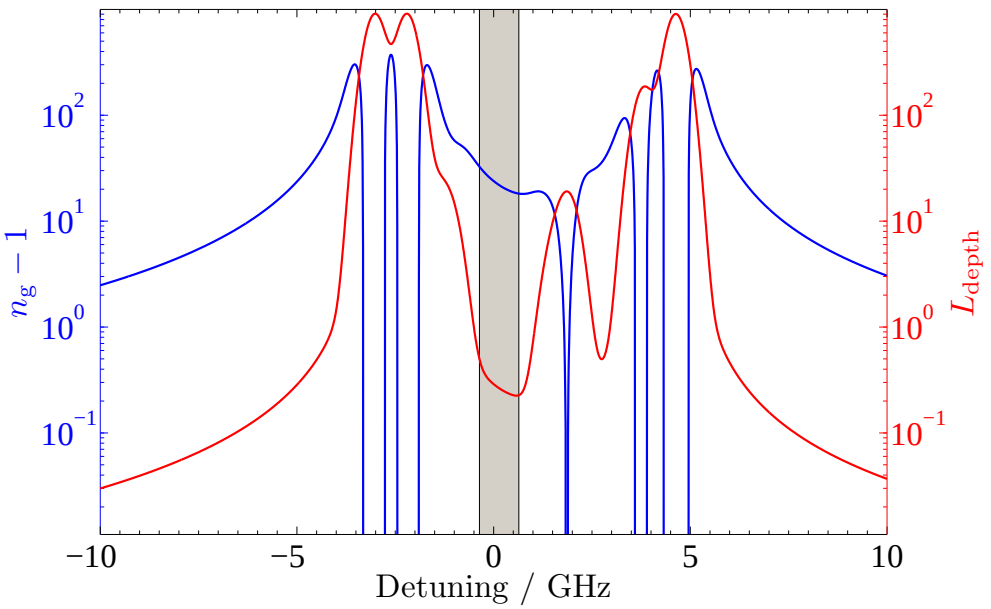

Figure 6.1: Theoretical group index (blue) and optical depth (red) in a 75 mm long, 125°C, 99% isotopically-pure ^{87}Rb vapour cell. The grey region shows the 1 GHz bandwidth of a 1.5 ns Gaussian pulse, centred at a detuning of 0.14 GHz. Detuning is with respect to the weighted line-centre (see chapter 4).

The time difference between a pulse traversing a medium and travelling in free-space (or a medium with $n_g = 1$) of equal length gives a convenient measure of the slow-light effect, and is given by

$$t_{\text{delay}} = \frac{L}{c}(n_g - 1). \tag{6.13}$$

Delaying a pulse by a time greater than its duration whilst experiencing little in the way of absorption or distortion is the goal of many areas of research [32, 127]. From the weak-field model we developed in chapter 4 we are able to calculate the real and imaginary parts of the refractive index, and thus able to predict the delay experienced by the pulse and optical depth, L_{depth}, of the medium (related to the Beer-Lambert law derived transmission $\mathcal{T} = \exp[-L_{\text{depth}}]$). Since we are interested in observing a pulse delayed by more than its width, we look for regions in the spectrum which have high group index, in order to provide large time delay and low absorption, so that the pulse is not attenuated to such an extent that it is of no use to us. Another consideration is how rapidly the group index and absorption vary in the region of interest: a slow variation means we can have a greater bandwidth within which to work and thus larger fractional time delays are possible, i.e., delaying a pulse by many times its duration. A variation of dispersion and absorption across the bandwidth may cause distortion of the pulse.

Figure 6.1 shows the theoretical group index and optical depth experienced by a D_1-resonant beam travelling through a hot vapour cell[2]. A high temperature is required so that there is sufficient vapour pressure (and hence atomic density) so that $n_g \gg 1$. In the figure we can see that the requirement for slow light is met away from atomic resonance. Also, for large detunings, both quantities are approximately constant over hundreds of MHz, the bandwidth of a pulse of around 1-10 ns. Of particular interest is the 1 GHz window around zero detuning (highlighted in grey) in which the delay and optical depth have a relatively constant frequency dependence. For a pulse whose carrier wave is at 0.14 GHz detuning, we see a group index of 23 and an optical depth of 0.26. From the narrowband approximation, a 1.5 ns Gaussian pulse has a dispersion length of $L_{\text{GVD}} = 122$ mm (compared to a propagation distance $L = 75$ mm), so we expect a small degree of broadening of the pulse by a factor $\eta = 1.2$. Hence the peak delay and transmission are predicted to be around 5.5 ns and 64%, respectively.

[2]Note that on resonance, in addition to massive attenuation, a pulse will experience a *negative* group index. This is the phenomenon of fast or superluminal light, which we shall tacitly draw a veil over. For discussion on this topic see references [64, 128].

6.4 Pulse propagation

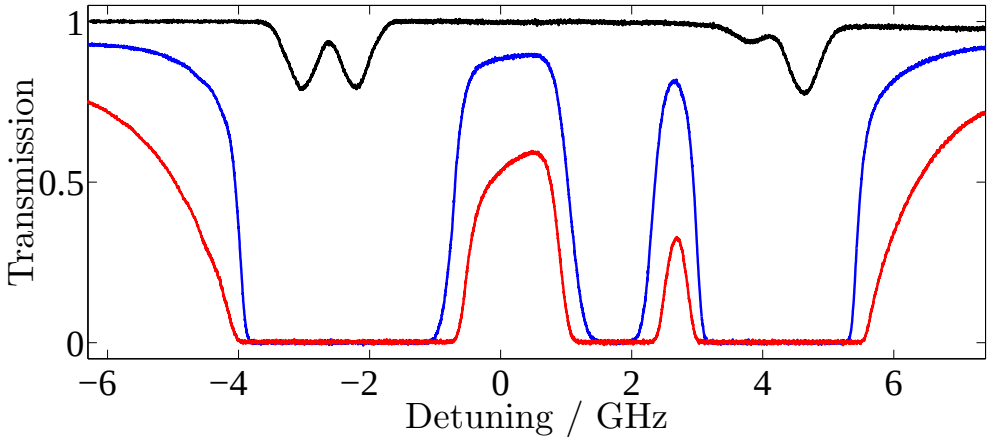

Figure 6.2: Transmission of a continuous-wave beam as a function of detuning from the D_1 line-centre, through a vapour cell at room temperature (black curve), $\sim 115°C$ (blue), and $\sim 135°C$ (red).

The experimental setup used to demonstrate the slow-light effect is almost identical to the apparatus required to measure transmission spectroscopy (see chapter 4, for example), except we now include a Pockels cell to produce pulsed light. This device is based on the Pockels effect (after Friedrich Pockels, 1893 [129, 130]), in which an applied electric field produces birefringence in a material. Application of a time-varying electric field can modulate the polarisation of an incident optical field, and placing the Pockels cell between two crossed polarisers can produce amplitude modulated optical pulses. We use an EM508-TT Pockels cell with an applied voltage supplied by an FID FDS 7-1NM driver (sold by Leysop Ltd). This apparatus produces optical pulses with FWHM 1.5 ± 0.2 ns at a rate of 50 Hz. We begin by showing the continuous-wave transmission spectrum through a 75 mm long, 99% ^{87}Rb vapour cell for a few temperatures in figure 6.2(a). In contrast to the D_1 spectra seen in chapter 4 (where both naturally occuring isotopes were present), at room temperature four absorption lines are seen, compared to the six seen in a natural-abundance cell. Due to Doppler-broadening, at higher temperature each pair of lines merge into one. The additional line appearing between them is due to the presence of ^{85}Rb in the cell; at a concentration of 1% it is much weaker than the ^{87}Rb transitions and hence not visible at room temperature. Another important point to make about such high tem-

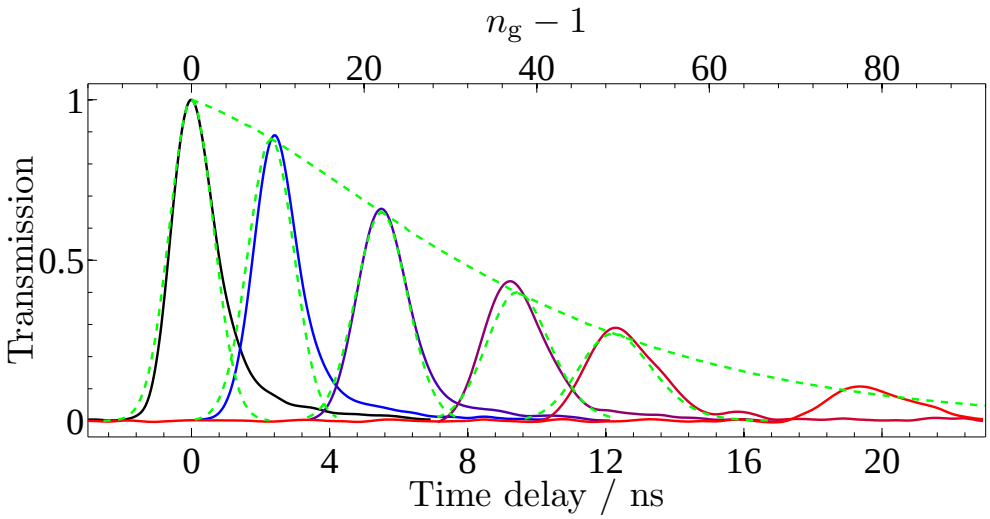

Figure 6.3: Measured pulse propagation through a vapour cell at various temperatures. The black curve is a non-interacting reference pulse from which transmission and time delay are measured; group index is calculated using equation (6.13). The subsequent curves (blue to red) show transmission for 110, 125, 135, 140, and 160°C. Dashed curves show theoretical pulses calculated by solving the Fourier integral (6.2), along with the line traced out by the theoretical pulse peaks.

peratures is that we are now in a regime at which the density of atoms is sufficiently large that dipole-dipole interactions act to broaden the atom's spectral line-width. The additional broadening mechanism is Lorentzian in nature, and thus we add a density-dependent term to the natural broadening line-width $\Gamma_{\text{Total}} = \Gamma + \beta\mathcal{N}_{\text{a}}$ [91].

The slow-light effect is measured in figure 6.3, where a pulse centred between the two absorption lines (close to zero detuning) is delayed by more than its width, as observed in previous work [28–30]. Commensurate with increased absorption is increased delay and broadening of the pulse. Note also the distortion of the pulse (most readily seen in figure 6.3 at temperatures ≥ 140°C) which is a result of higher-order dispersive effects. Theory curves are a result of solving the Fourier integral from section 6.1. Good agreement is seen between experiment and theory (bearing in mind the measured input pulse is not Gaussian) up to temperatures of 140°C. The trend is most easily seen if we plot the transmission and delay of the pulse peak versus temperature, as is done in figure 6.4. The discrepancy between theory and experiment becomes noticeable at 150°C, and there is a marked difference at

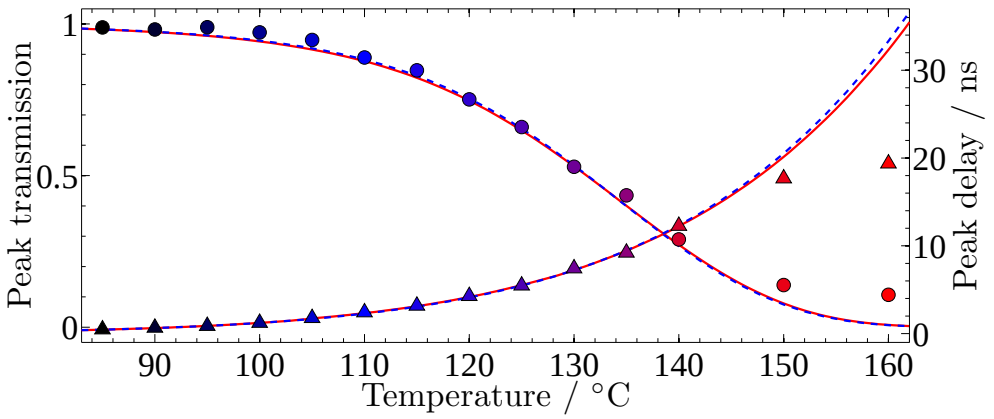

Figure 6.4: Measured temperature dependence on the transmission (circles) and time delay (triangles) of the pulse peak. Solid red curves show the result of solving the Fourier integral, whilst dashed blue curves show the narrowband approximation to this theory (see text). Measurement errors are of the order of the point size.

160°C where the time delay of the pulse is half of what is expected by theory, with four times the expected transmission. The likely explanation for this disagreement is that the theoretical model assumes that the pulse is sufficiently weak that it does not affect the medium as it propagates. However, to get a good signal-to-noise ratio in detecting the pulse it was necessary to use a light intensity of 3.82 mW/mm^2. This high intensity results in the pulse having an area of order unity, which we will see in chapter 10 means there is high probability of the pulse affecting the medium. This likely causes pumping of the atoms, particularly at higher temperatures when the atomic density is sufficient large that a significant proportion of the atoms are close to resonance with the pulse beam.[3] Figure 6.4 also shows there is little difference between the numerical solution to the Fourier integral (6.2) and its approximation (6.12), showing that the assumptions of small variation of the dispersive and absorptive properties of the medium over the bandwidth of the pulse are justified. In particular the predictions made for the 125°C medium in section 6.3 are borne out.

[3]Since the pulse is several gigahertz from an atomic resonance, it is unlikely to cause optical pumping of atoms with zero longitudinal velocity. However it is possible to cause pumping of sufficiently high velocity atoms which have been shifted into resonance via the Doppler effect.

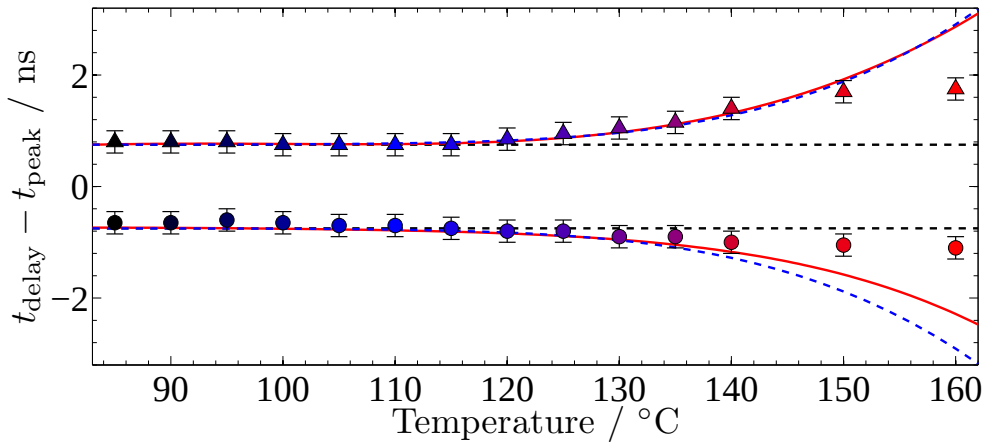

Figure 6.5: Positions of the pulse front and back relative to the peak delay, t_{peak}. Curves show theoretical broadening calculated from solving the Fourier integral (solid red) and broadening by GVD (dashed blue). The horizontal dashed line represents the width of the reference pulse.

The broadening and distortion of the pulse are investigated in figure 6.5. Here we show the half-width at half-maximum of the front (negative values) and back (positive values) of the pulse relative to the peak delay. Again experiment and the numerical solution to the Fourier integral agree well below 140°C. The approximate theory, calculated using equation (6.11), assumes that the pulse envelope remains Gaussian and thus is symmetric around t_{peak}. Comparing the two theory curves we see that the back broadens as expected, but the front broadens to a lesser degree. This asymmetry in the Fourier integral (and experimental data) demonstrate a deviation from the initial Gaussian envelope, due to distortion by higher-order dispersive terms than GVD.

6.5 Spectral sensitivity of slow-light media

The large group refractive index responsible for the delay of pulsed light is also of relevance to continuous-wave propagation. Here we derive an expression for the spectral sensitivity of the slow-light effect, i.e. the rate of change of dispersion with frequency. We begin with a well-known result from the interference of waves. If two waves (a and b) of angular frequency ω travel along separate paths, upon meeting up they experience a phase shift $\Delta\phi$ which is proportional to the difference in length ΔL between the two paths. This assumes that both waves are travelling at equal speed, i.e. in the case of optical waves, the refractive index of the medium n is identical for both paths. If we now consider paths of the same length L, the phase shift between two co-propagating waves is produced by a differing optical path length $L(n^a - n^b) = L\Delta n$, where n^i is the phase index experienced by wave i, and Δn is the relative refractive index. The phase shift between the two waves is given by [78]

$$\Delta\phi = \frac{\omega}{c} L(n^a - n^b) = L(k^a - k^b), \tag{6.14}$$

The wavenumber, $k = \omega n/c$, is introduced to simplify calculations later on. As a further simplification, here both n and k are taken to be real.

In dispersive media, n is a function of ω. Changing the angular frequency by an amount $\delta\omega$ produces a change in relative phase $\delta\Delta\phi$ given by

$$\begin{aligned}
\delta\Delta\phi(\omega, L) &= \Delta\phi(\omega + \delta\omega, L) - \Delta\phi(\omega, L) = L[\Delta k(\omega + \delta\omega) - \Delta k(\omega)] \\
&= L[\Delta k(\omega) + \frac{\mathrm{d}\Delta k(\omega)}{\mathrm{d}\omega}\delta\omega + \frac{1}{2!}\frac{\mathrm{d}^2\Delta k(\omega)}{\mathrm{d}\omega^2}\delta\omega^2 + \ldots - \Delta k(\omega)] \\
&= \frac{L}{c}[\Delta n_\mathrm{g}(\omega) + \frac{1}{2!}\frac{\mathrm{d}\Delta n_\mathrm{g}(\omega)}{\mathrm{d}\omega}\delta\omega + \ldots]\delta\omega.
\end{aligned} \tag{6.15}$$

Here $\Delta n_\mathrm{g} = n_\mathrm{g}^a - n_\mathrm{g}^b$ is the relative group refractive index, and $\mathrm{d}\Delta n_\mathrm{g}/\mathrm{d}\omega$ is the relative group velocity dispersion.

In the limit that $\delta\omega \to 0$, equation (6.15) becomes

$$\frac{\mathrm{d}(\Delta\phi)}{\mathrm{d}\omega} = \frac{L}{c}\Delta n_\mathrm{g}. \tag{6.16}$$

A small change in angular-frequency thus produces a change in relative phase proportional to the relative group refractive index. Thus the larger the difference in n_g, the higher the spectral sensitivity.

6.6 Discussion

We have shown that in a hot atomic vapour a pulse can be delayed by more than its duration, and that the wavevector calculated for weak, monochromatic light in earlier chapters can be applied successfully to pulse propagation. In particular the narrowband approximation, in which we model propagation of a weak Gaussian pulse analytically, is shown to be accurate, despite being a simple extension of the continuous-wave transmission model developed in chapter 4.

In the second part of this thesis, we concern ourselves with the Faraday effect. The Faraday effect arises due to the medium's differing response to the two orthogonal circular components of a linearly (or in general, elliptically) polarised wave. Instead of two separate waves following different paths as in the foregoing example (section 6.5), the two polarisation components co-propagate through the medium. The relative phase between them manifests itself as a rotation of the composite wave. Therefore, whilst Δn determines the magnitude of the rotation, Δn_{g} describes the spectral dependence of this rotation. These quantities can vary by several orders of magnitude in a slow-light medium, thus Faraday rotation is extremely sensitive to a variation in frequency.

Part II

The Faraday effect

Chapter 7

Faraday rotation of continuous-wave light

The resonant Faraday effect and magneto-optical effects have been studied extensively over the past century [52], but in line with chapter 5 we are here more interested in the off-resonant characteristics of the interaction where absorption is negligible with respect to dispersive effects. While the off-resonant Faraday effect has been used to probe semiconductor spin ensembles [131] and quantum dots [132], in atomic systems it has mainly been studied in the context of narrowband filtering [53]. In this chapter we develop techniques that have found applications as a tunable Faraday dichroic beam splitter [39] and as a laser frequency-stabilisation device [133].

7.1 Birefringence in an atomic medium

An isotropic medium responds identically to an applied electric field regardless of the field's polarisation direction. Thus the interaction has one associated refractive index used to describe the propagation of light. However, there exist materials for which the interaction is anisotropic. First described in Iceland spar by Erasmus Bartholin in 1669 [134, 135], the effect of birefringence decomposes light into two components with separate indices of refraction. This is most easily understood in solid state systems with crystalline structure, in which case spatial symmetry of the crystal structure can

lead to a difference in refraction for light polarised parallel or perpendicular to the crystal axis [77]. Commensurate with birefringence is dichroism, that is, differing absorption between polarisation components.

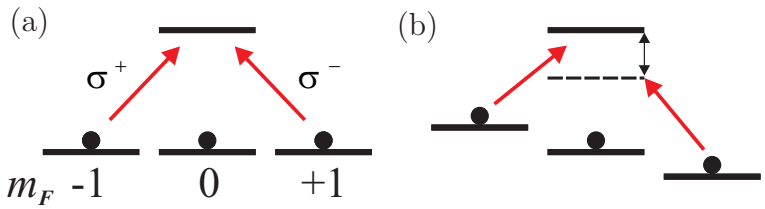

Figure 7.1: An illustration of energy level configurations leading to circular birefringence. (a) The energies of the σ transitions are degenerate, and the states are equally populated: no asymmetry is seen for circularly polarised light. (b) An applied magnetic field lifts the degeneracy to such an extent that whilst the σ^+ transition is close to resonance, the σ^- is detuned farther away.

The Faraday effect, (after Michael Faraday, 1846 [136]) is a well-known magneto-optical phenomenon in which a magnetic field applied parallel to the direction of light propagation induces the medium to respond differently to left and right circularly polarised light - an instance of *circular* birefringence. Circular birefringence produces a relative phase shift between circular field components. In an atomic medium left (right) circularly polarised light stimulates σ^+ (σ^-) optical transitions when the axis of quantisation is taken to be in the direction of light propagation [137]. In the absence of a magnetic field, no birefringence is seen, as illustrated in figure 7.1(a). The effect of a magnetic field applied along the quantisation axis is to shift the energy levels such that, for a particular frequency of light, the σ transitions are shifted from resonance. If one of the σ transitions is closer to resonance than the other, the probability of a σ^+ or σ^- transition happening are now different. This is illustrated in figure 7.1(b). For incident linearly polarised light (equal amounts of left and right circular polarisations), an asymmetry in the refractive indices of the σ transitions results in a rotation of the plane of polarisation, which is illustrated in 7.2.

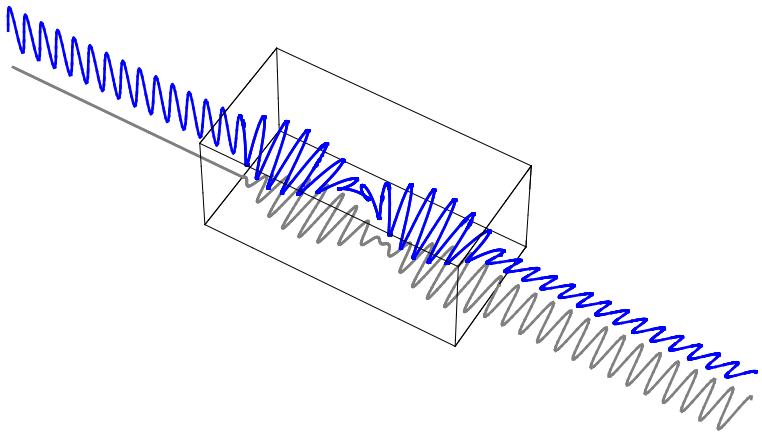

Figure 7.2: A representation of a linearly polarised electric field, propagating from left to right along the z-axis. The other axes show the electric field magnitudes E_x and E_y. The box marks the position of the vapour cell where the magneto-optical effect occurs. The beam remains linearly polarised throughout the interaction, as its polarisation angle rotates by almost 2π rad.

7.2 The effect of Faraday rotation on vapour cell transmission

The transmission of a near-resonant, weak continuous-wave laser beam was investigated earlier in this thesis. No attempt was made to shield those experiments from the geomagnetic field which is, nevertheless, too weak to produce energy-level shifts which are observable by the equipment used. However, the effect produced by applying a modest magnetic field of tens to hundreds of Gauss is dramatic. In addition to the light source (which produces a beam with a $1/e^2$ half-width of (2.00 ± 0.05) mm of wavelength 795.0 nm) and vapour cell (75 mm long, containing a mixture of the two naturally occurring isotopes of Rb according to the ratio ^{87}Rb:^{85}Rb 99:1), we add two new elements to the experimental set-up: polarisation-sensitive optics and a heating solenoid (figure 7.3). The polarisation beam splitter separates input light into two orthogonal, linearly-polarised components. We work in the local coordinate system (see appendix F) with the beam propagation direction and quantisation axis along the z-direction. The output ports of a polarisation beam splitter define the x- and y-axes, allowing us to identify the orthogonal components as E_x and E_y. The intensity $I_{x(y)} \propto |E_{x(y)}|^2$ of each component

is detected on separate photodetectors. The half-wave plate ($\lambda/2$) allows the polarisation plane of linearly polarised light to be adjusted, controlling the relative amount of light in each polarisation component. The solenoid heating unit (based on the design of reference [18]) produces both the magnetic field and Joule heating required for the experiment[1]. The variation in magnetic field along the cell is about 10%.

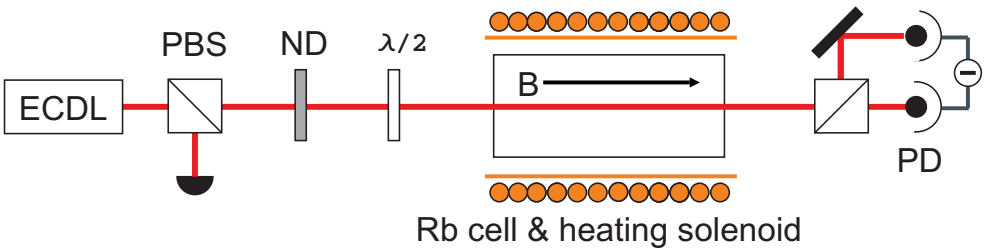

Figure 7.3: The output of an external cavity diode laser (ECDL) is sent through a polarisation beam splitter (PBS) in order to purify its initial polarisation, and is then attenuated with a neutral density (ND) filter. The waveplate ($\lambda/2$) controls the polarisation entering the vapour cell. The two orthogonal linear components of the beam are collected on a differencing photodiode (PD).

In figure 7.4(a) conventional Doppler-broadened transmission spectroscopy is shown, with a beam attenuated to 30 nW/mm^2 such that it was in the weak-probe limit (see chapter 4). Application of a magnetic field causes an energy shift between the σ transitions. The total transmission, which includes all polarisation components, is relatively unchanged by the field[2]. However, the rotation between the x- and y-components is clearly visible, with the signals oscillating between zero and a maximum value, here given by the total field transmission. Even at detunings of many GHz the difference between the transmissions of the x- and y-components is noticeable. The experimental data are compared to predictions of the theoretical model (introduced in chapter 4) in figure 7.4(b). The theoretical model assumes that the energy shift between the σ transitions is proportional to the magnitude of the applied magnetic field. In this regime the model predicts both the Doppler-broadened line-shape, and the number and positions of the oscillations.

[1] Built and tested by Yifei Cai.

[2] The energy shift is too small to be resolved here: for the ^{87}Rb ground states the shift per field is ~ 1 MHz/Gauss.

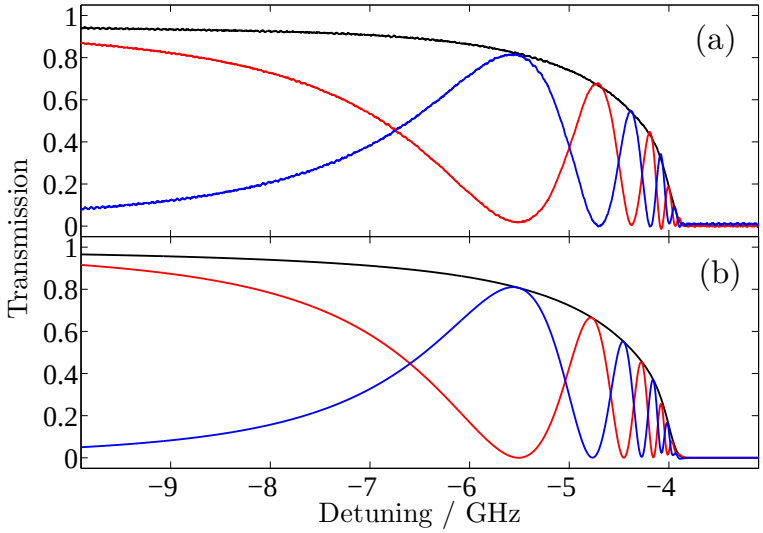

Figure 7.4: Transmission of a continuous-wave beam through a 75 mm vapour cell at 136°C. Plotted are the transmissions of the x-component (red), y-component (blue), and the total intensity of the light (black). The applied magnetic field is ~ 50 G. (a) Experimentally measured data and (b) theoretical model. Detuning is with respect to the D_1 line-centre (see chapter 4).

7.3 Measuring the polarisation rotation

In this section we detail the method by which the angular rotation due to the Faraday effect, θ, of the polarisation plane of probe light is measured. In appendix G we give a more general account of the transmission signals measurable in a circularly anisotropic medium; here we choose to present the differencing signal, which is proportional to $(I_x - I_y)$, as it conveys both the birefringent and dichroic characteristics of the medium. The rotation angle can then be extracted from this signal by looking at the zero crossings and/or extrema.

For an input beam of linearly polarised light set at an angle of $-\pi/4$ rad to the x-axis, of total intensity I_0, the differencing and total signals are, respectively,

$$(I_x - I_y)/I_0 = \sin(2\theta)\mathrm{e}^{-\frac{1}{2}(\alpha^+ + \alpha^-)L}, \tag{7.1}$$

$$(I_x + I_y)/I_0 = \tfrac{1}{2}(\mathrm{e}^{-\alpha^+ L} + \mathrm{e}^{-\alpha^- L}), \tag{7.2}$$

where L is the length of the medium, and $\alpha^\pm$ are the absorption coefficients of the $\sigma^\pm$ transitions. The magnetically induced birefringence responsible for

polarisation rotation thus also causes circular dichroism (polarisation dependent absorption), both effects being strongest close to resonance. We saw in chapter 5 that absorptive effects dominate the interaction close to resonance, whilst far from resonance dispersive effects are more important. Hence at large detunings the incident light retains its linear polarisation whilst being rotated; near-resonant light experiences greater rotation at the expense of becoming highly elliptical. The differencing signal of equation (7.1) is a sinusoidal function delineated by the transmission due to the average absorption coefficient, whilst the total intensity signal of equation (7.2) is the average transmission of the two circular polarisations.

Figure 7.5(a) shows a differencing signal produced by a hot vapour under the influence of a large magnetic field, shown versus red detuning Δ' from the D_1 ^{87}Rb $F_g = 2 \rightarrow F_e = 1$ transition in units of Doppler width $\Delta\omega_D = 2\pi(585\text{ MHz})$. We use this variable to emphasise the data close to resonance, by way of a logarithmic scale. Many oscillations are seen in the signal, the peaks of which become increasingly close together at smaller detunings. The large number of oscillations observed arises from the same phenomenon that enhances the spectral response in a slow-light interferometer [36]. A powerful property of the polarimetry signal is that it allows a direct read-out of the rotation angle experienced by the incident light. The signal tends to zero at large detuning (not shown) and each subsequent zero corresponds to a $\pi/2$ rad rotation. This rotation, θ, is plotted in figure 7.5(b). Note that the first zero crossing (corresponding to a $\pi/2$ rad rotation) occurs at $\Delta = 12 \times \Delta\omega_D$ (that is, ~ -10 GHz from the D_1 line-centre) where the absorption is less than 1%. At temperatures of order 200°C, the first zero shifts out to beyond -50 GHz.

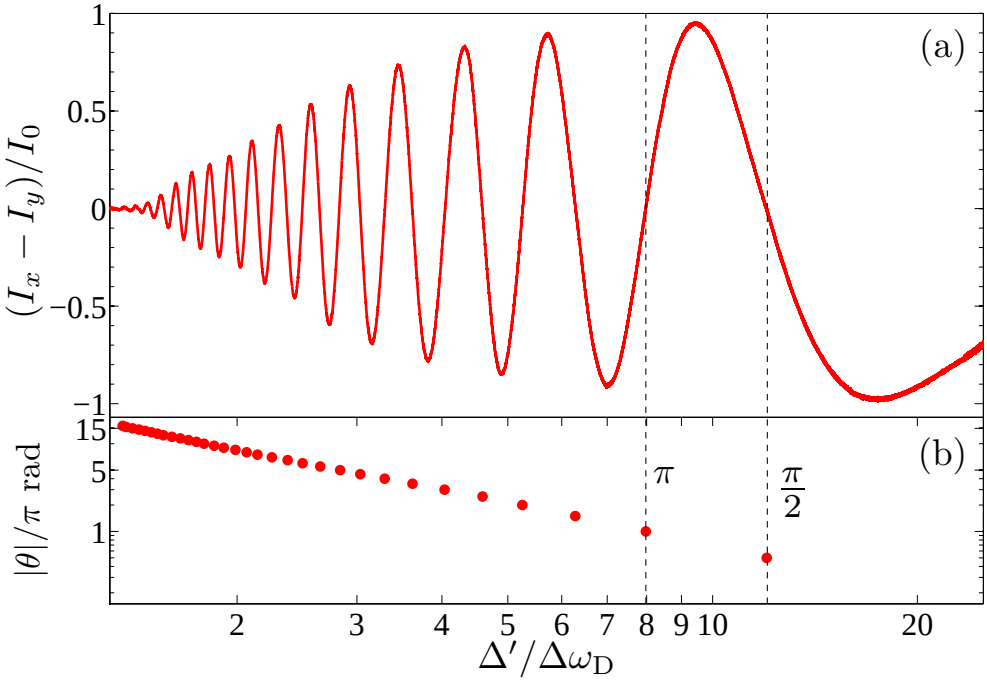

Figure 7.5: (a) The differencing signal for a 75 mm long vapour cell at a temperature of 135°C and applied magnetic field of 230 G. The signal is normalised to the total intensity of the input. (b) The rotation angle determined from the zero crossing of the differencing signal. [*Data taken by Nia C. Bell*]

7.4 Discussion

For linearly polarised continuous-wave light the rotation plane of polarisation is highly frequency dependent and hence of interest in the fields of interferometry and polarimetry. The Faraday rotation angle was seen to increase from zero at large detunings to 15π rad close to resonance, over a frequency range of ~ 20 GHz. This rotation corresponds to a Verdet constant of 3×10^{-2} rad G^{-1} cm^{-1}, three orders of magnitude larger than in typical commercial Faraday rotators [52]. Large rotations are also seen in thin magneto-optical photonic crystals [138], but the effect in such a system cannot be varied dynamically. The rotation in the atomic vapour is temperature, magnetic-field and frequency dependent, therefore the effect can be used as a tunable polarisation switch. In addition, we recall that polarimetry provides a useful spectroscopic tool with applications in, e.g., laser frequency stabilisation [20, 133]. The large bandwidth of off-resonant polarimetry could provide a useful technique to probe fast dynamics of Rydberg states in a thermal vapour [14, 139] or atomic beam [140] in the high density regime where interactions and hence novel non-linear optical effects are significant.

Chapter 8

The slow-light Faraday effect

In chapter 6 we demonstrated the transmission of pulsed light through an atomic vapour. Then in chapter 7 we investigated the Faraday effect and its application to continuous-wave light. In this chapter we marry the two concepts, showing increased spectral sensitivity of the Faraday effect due to the slow-light effect, and demonstrate rotation of a nanosecond pulse.

8.1 Slow-light & relative dispersion

In this section we explore the effect that an applied magnetic field has on media in which the group refractive index is large. We will assume that the laser detuning, $\Delta = \omega - \omega_0$ (laser angular frequency minus resonant angular frequency), is greater than the Doppler-broadened linewidth $\Delta\omega_{\mathrm{D}}$. In this case, as we have seem in chapter 5 the atomic resonance can be approximated by a Lorentzian shaped distribution, with a natural linewidth Γ. Then for $\Delta > 2 \times \Delta\omega_{\mathrm{D}} > \Gamma$ the phase and group indices, can be approximated by

$$n - 1 = -C\frac{1}{\Delta}, \tag{8.1}$$

$$n_{\mathrm{g}} - 1 = C\frac{\omega_0}{\Delta^2}, \tag{8.2}$$

where the constant $C = \mathcal{N}d^2/2\hbar\epsilon_0$ (see chapter 4 for discussion of these parameters). In (8.2), the resonant angular frequency $\omega_0 \sim 2 \times 10^{15}$ rad s^{-1} for visible and near visible light. Consequently $n_{\mathrm{g}} - 1$ and $n - 1$ can differ by several orders of magnitude.

On application of a magnetic field, the degeneracy between σ^+ and σ^- transitions is broken and there is now an asymmetry in the interaction between the medium and the two helical components of light (+ and −). The energy states of the transitions are shifted away from each other. If we assume that this shift is small such that it acts with equal magnitude, a, but opposite sign on the σ transitions, we replace $\Delta \rightarrow \Delta \pm a$. The relative refractive indices can then be approximated as

$$n^- - n^+ = -2C\frac{a}{\Delta^2}, \tag{8.3}$$

$$n_\mathrm{g}^- - n_\mathrm{g}^+ = 4C\frac{a\omega_0}{\Delta^3}. \tag{8.4}$$

Inspection of equations (8.2) and (8.4) shows that the ratio of the relative group index to the group index is approximately $4a/\Delta$; the energy-level shift is typically hundreds of MHz for a field of hundreds of Gauss, so for a detuning of a few GHz this ratio is > 0.1. Hence in a slow-light medium where n_g is large the relative group index can also be large.

We saw the effect that the relative phase index has on light propagation in chapter 7: it is responsible for Faraday rotation. Essentially, the refractive index of the individual helical components controls the velocity at which they travel through the medium. After travelling through a distance L, the light, which has a free-space wavevector k_0, experiences a phase shift $\Delta\phi = k_0 L(n^- - n^+)$. This results in a rotation of the plane in which the linearly polarised light oscillates by an angle $\theta = \Delta\phi/2$. This speed of propagation phenomenon is mirrored in the relative group index, in which case a temporal shift leads to a separation of the pulse envelope of the helical components. The effects of the slow-light Faraday effect on pulse propagation are illustrated in figure 8.1. For a small relative group index the pulse retains its shape, with its linear polarisation rotated by an amount dependent on the relative phase index. If the relative group index is larger, the pulse splits into two spatially (and temporally) separated circular components of opposite chirality. By varying the relative refractive indices it is possible to switch dynamically between split or rotated pulses (and also control the magnitude of this rotation). We will show that this is possible by changing a single experimental parameter.

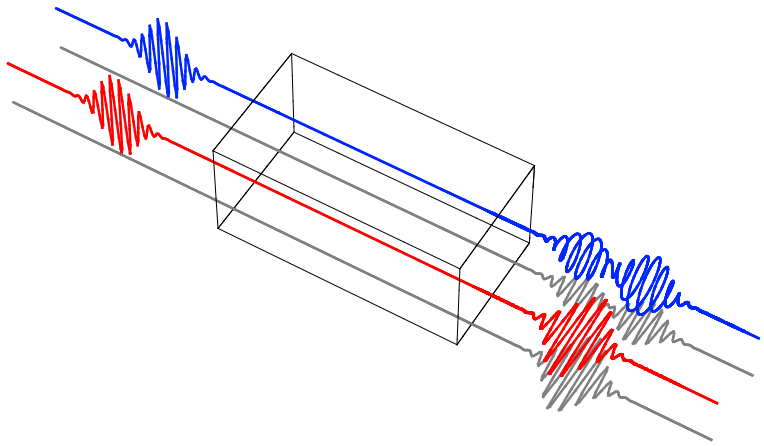

Figure 8.1: A representation of two pulsed electric fields, propagating from left to right along the z-axis. The other axes show the electric field magnitudes E_x and E_y. The box marks the position of the vapour cell where the magneto-optical effect occurs. Both input beams are linearly polarised along the vertical axis. The two cases correspond to different values of either the detuning, magnetic field or atomic density. The red beam remains linear as its polarisation angle is rotated on exiting the medium, whilst the blue beam is split into two pulses of left and right circular polarisation.

8.2 Measuring the relative refractive indices

In chapter 7 we made a measurement of the rotation θ experienced by a monochromatic probe beam in a hot atomic vapour. The relative phase shift between the two circular components of light $\Delta\phi$ is equal to 2θ, and from section 8.1 we see that by measuring the rotation angle we have also made a measurement of the relative phase index $n^- - n^+$. The relative phase shift and index are plotted in figure 8.2(a), where we have used the rotation measured in section 7.5. Similarly, the relative group index is determined by the derivative of $\Delta\phi$ and is shown in figure 8.2(b). The relative phase and group indices are seen to differ by six orders of magnitude. Thus a small difference in refractive index can still lead to a large difference in group index. In section 6.5 we showed that the spectral sensitivity of dispersion, characterised by the frequency dependence of the phase shifted, is related to the relative group index.

In pulse propagation the light has a finite bandwidth. For example, the

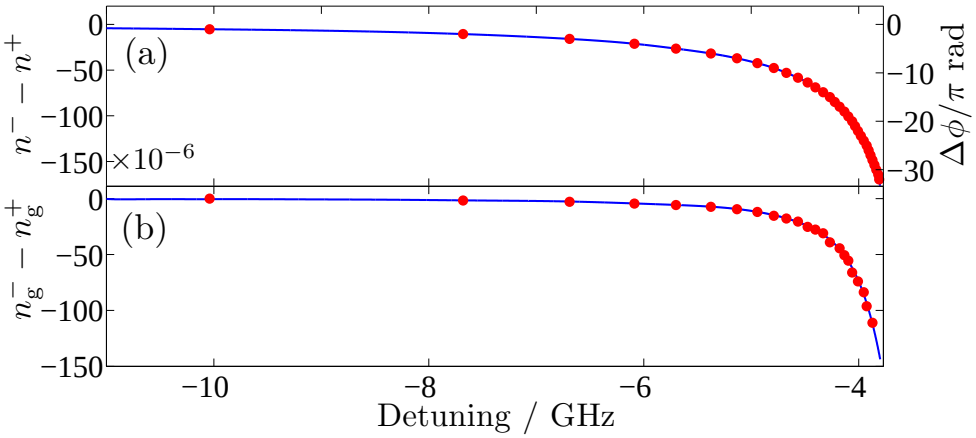

Figure 8.2: (a) Relative refractive index (left) calculated from the measured phase (right). (b) The relative group index calculated from the gradient of the phase. Points show measured data; curves are guides to the eye. Experimental parameters are identical to those in 7.5, viz. 75 mm long vapour cell of 99% ^{87}Rb at a temperature of 135°C under an applied magnetic field of 230 G.

one nanosecond (or thereabouts) pulse used throughout this thesis has a bandwidth of one gigahertz. Recalling our simple illustration in figure 8.1, it is obvious that close to resonance where the variation of phase is changing rapidly with respect to frequency the slow-light Faraday effect will manifest itself as pulse splitting because there is a large variation in phase over the bandwidth of the pulse. In contrast, farther away from resonance where the phase changes more slowly we will observe pulse rotation.

8.3 Propagation of optical pulses

The experimental setup used to demonstrate the slow-light Faraday effect is almost identical to the apparatus described in chapter 7, except we now include a Pockels cell placed between two crossed polarisers to produce pulsed light. An off-resonant pulse being delayed in slow-light medium is shown in 8.3(a). In figure 8.3(b), we show the effect of applying a magnetic field along the propagation direction. In this case the pulse is split into a double pulse. By using a $\lambda/4$ waveplate it is possible to observe the magneto-optic effect on the $\sigma^{\pm}$ transitions individually, shown in 8.3(c). Comparison of these last two plots shows that the linearly polarised pulse is split into its

two circular component as illustrated schematically in figure 8.1. This effect was first observed by Grischkowsky (in reference [141]) in a 1 m long cell at 140°C with an 8.5 kG pulsed magnetic field, who recorded a time separation of 26 ns, with the slowest pulse having a velocity of $c/9$ (compared to our observations of 3.5 ns and $c/37$, respectively). Although Grischkowsky achieved significant pulse separation (using a much longer cell and higher field than our experiment) he did not investigate Faraday rotation of pulses. In the next section we demonstrate that the large bandwidth available to the off-resonant Faraday effect enables the rotation of broadband pulses (as illustrated by the red beam in figure 8.1).

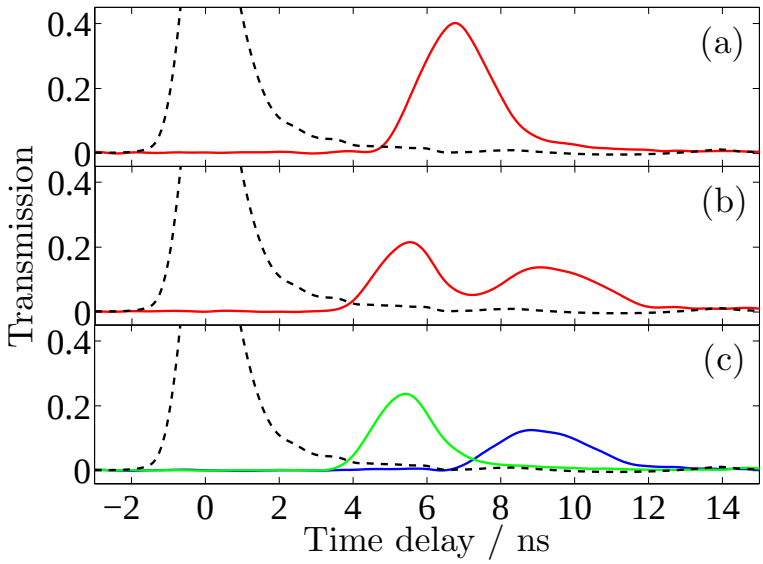

Figure 8.3: Propagation of an input 1.5 ns pulse through a slow-light medium. Transmission/delay are relative to a non-interacting reference pulse (dashed curve). Pulse detuned to ~ -6 GHz at a temperature of $\sim$ 165°C. A magnetic field of $\sim$ 360 G is applied to the linearly polarised pulse in plot (b), resulting in pulse splitting. In (c) we analyse the split pulse with a $\lambda/4$ waveplate, distinguishing between light facilitating the σ^- transition (green curve) and σ^+ transition (blue). Noise in the data is reflected by the line thickness.

8.4 Broadband pulse rotation

We saw in figure 8.2 that far from resonance the relative index evolves slowly with detuning, in particular for detunings greater than −8 GHz, where $|\Delta\phi| < 2\pi$. For a linearly polarised pulse centred in this region with GHz bandwidth, the phase variation across its spectrum is sufficiently low that the polarisation of the pulse as a whole can be rotated by a large angle. Experimental measurements of broadband rotation are seen in figure 8.4, where a 1 GHz bandwidth pulse polarised in the x-direction is rotated into the y-direction by increasing an applied magnetic field from zero to 230 G. This high-fidelity $\pi/2$ rotation is accompanied by low absorption (less than 2%) and negligible distortion since the pulse is detuned by many Doppler-broadened linewidths from resonance.

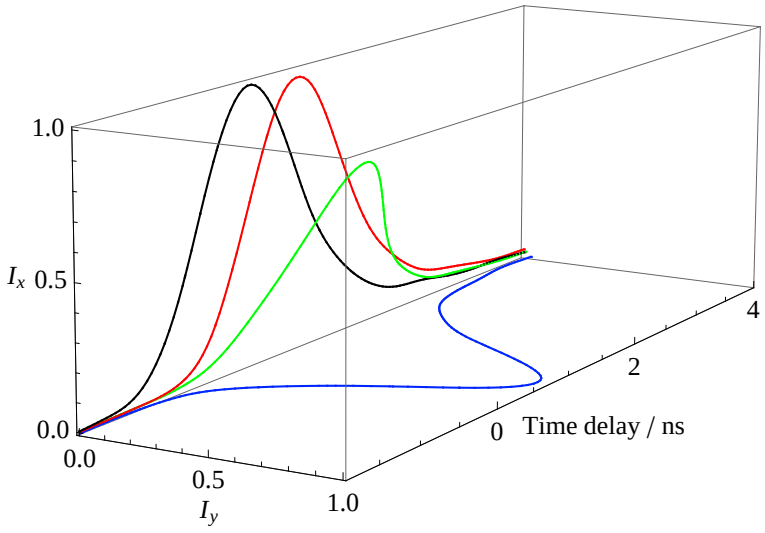

Figure 8.4: An input 1.5 ns pulse initial linearly polarised in the x-direction (red) is delayed by 0.6 ns with respect to a non-interacting reference pulse (black), in the absence of an applied magnetic field. The pulse is red-detuned from the weighted D_1 transition centre by ∼10 GHz. For a temperature of 135°C and a field of 80 G (green) or 230 G (blue) the pulse is rotated into the y-direction whilst retaining its linear polarisation and intensity.

In figure 8.5 we demonstrate the magnetic field dependence of polarisation rotation angle θ for the pulse. The data points are taken by measuring the I_x and I_y components of peak of the transmitted pulse and calculating the rotation angle using $\cos^2\theta = I_x/(I_y + I_x) = \mathcal{T}_x$, where $\mathcal{T}_x$ is the

transmission of the x-component of the pulse. The curves are the result of theoretical modelling with the Faddeeva function and Lorentzian approximation (see chapter 5). It can be seen that theory and experiment agree well for the range of magnetic field considered (and in particular the Faddeeva function and its approximation are indistinguishable). The experimental pulse rotation as a function of magnetic field is a measurement of the Verdet constant, $V = \theta/BL$ (where L is the length of the cell), for the medium at a specific temperature and detuning. A linear fit to the data results in $V = (9.44 \pm 0.08) \times 10^{-4}$ rad G^{-1} cm^{-1}, in excellent agreement with the theoretical value of 9.45×10^{-4} rad G^{-1} cm^{-1}.

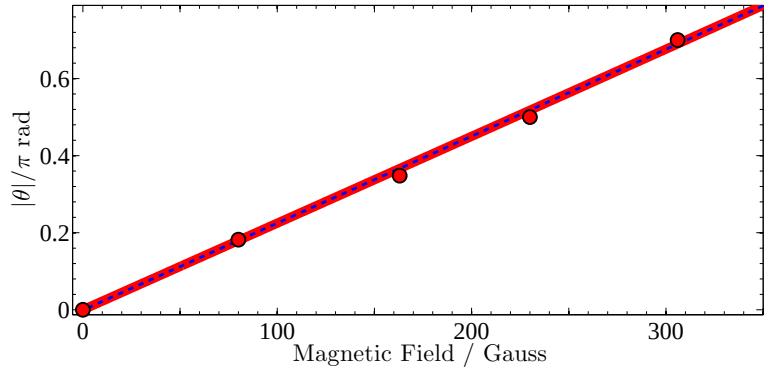

Figure 8.5: Comparison between experiment and theory for the polarisation rotation of a 1.5 ns pulse through a vapour cell at a temperature of ~ 135°C. The measured rotation angle of the pulse as a function of applied magnetic field is shown (red points) along with the theoretical rotation calculated using the Faddeeva function (thick solid red) and Lorentzian approximation (dashed blue). The pulse is red-detuned from the ^{87}Rb $F_g = 2 \rightarrow F_e = 1$ transition by $\sim 12\Delta\omega_D$, where $\Delta\omega_D = 2\pi(585$ MHz). Experimental uncertainty is of the order of the point size.

8.5 Discussion

For broadband pulses, with spectral widths of hundreds of MHz to GHz, in the wings of a resonance the Faraday effect manifests itself as an asymmetry in the propagation of left/right circularly polarised light. If the linearly polarised pulse's bandwidth is narrow enough such that the relative phase shift across it is essentially constant, the polarisation angle is rotated in the same way as for cw light. Far from resonance, a GHz bandwidth pulse can be rotated by $\pi/2$ rad with less than 2% loss and negligible distortion. Light switching with such large bandwidth and with low loss/distortion has not been observed previously using atomic ensembles. Pulses as short as 5 ns have previously been rotated using self-induced transparency (SIT) [142]. However, this resonant technique requires intensities above saturation and the near-resonant character of the process leads to higher-order dispersive terms, resulting in considerable pulse distortion.

Increasing the phase variation across the pulse, e.g. by changing the applied field or carrier detuning, changes a single rotated linear pulse to split circular pulses in a dynamic way. Splitting a pulse into two components separated by more than their temporal widths could be used for pump-probe experiments; or for photon switching or atomic ensemble entanglement [56] in quantum information applications. The time separation of the two pulses can be controlled by varying the cell temperature or applied magnetic field.

At higher temperatures and magnetic fields, the available bandwidth of many GHz make it possible for pulses of hundreds of picosecond duration to be delayed and rotated with high transmission. Appropriate choice of atomic species and laser wavelength opens up the possibility of communications at the large bit rates required for rapid data transfer.

Chapter 9

Optical control of Faraday rotation

We saw in chapter 7 that large polarisation rotations are possible in an atomic vapour. This was achieved by application of a static magnetic field in order to break the degeneracy of the σ^+ and σ^- transitions, thereby inducing birefringence which manifests itself as a rotation of the plane of polarisation of linearly polarised light. In this chapter we make a move towards light switching i.e. temporal control over the polarisation state of light, here demonstrating high fidelity modulation of a probe field using *optical* control. By application of an optical control field we open up the possibility of switching at shorter timescales than would be feasible using a magnetic field.

To achieve a large induced rotation with low loss, i.e., a high value of the figure of merit, $\Delta\chi_{\mathrm{R}}/\chi_{\mathrm{I}}$, we bias the rotation of the probe using the off-resonant Faraday effect and employ a control beam to induce population transfer to modulate around this bias. We demonstrate optical control of the Faraday rotation due to both changes in the total number of atoms and due to their spin distribution. For the probe field detuned by more than 5 times the inhomogeneous atomic linewidth we observe a phase shift of $\pi/2$ radians with a loss of less than 5%, corresponding to $\Delta\chi_{\mathrm{R}}/\chi_{\mathrm{I}} = 40\pi$. This combination of large dispersion and low loss is interesting in the context of all-optical manipulation of light pulses. As a large rotation is achieved off-resonance the process potentially can be operated at high bandwidth of

order GHz [40]. In addition, by combining this technique with the dispersive filtering properties of the Faraday effect [39, 53, 143] one could realise an optically tunable narrowband filter.

9.1 Controlling birefringence in an atomic medium

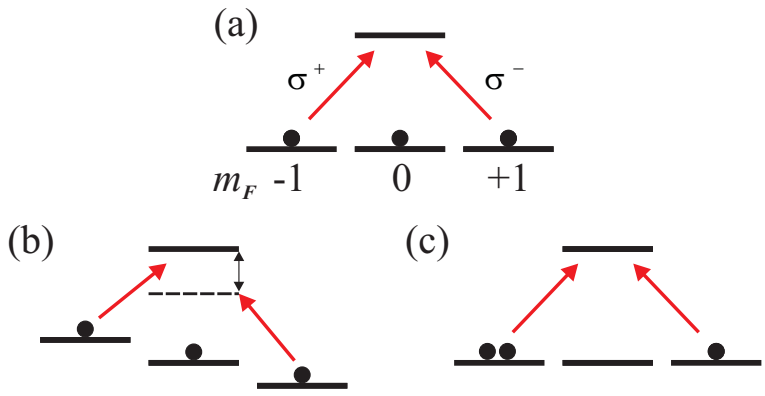

Figure 9.1: An illustration of energy level configurations leading to circular birefringence. (a) The energies of the σ transitions are degenerate, and the states are equally populated: no asymmetry is seen for circularly polarised light. (b) An applied magnetic field lifts the degeneracy to such an extent that whilst the σ^+ transition is close to resonance, the σ^- is detuned farther away. (c) Whilst both transitions have the same detuning from resonance, a population difference is present, leading to birefringence.

We briefly alluded to the underlying cause of birefringence in chapter 7, defining it as a medium's tendency to discriminate between two orthogonal polarisation states of light and responding accordingly. The Faraday effect was held up as an example of circular birefringence, a process in which left and right circularly polarised light are the eigenmodes of the atom-light interaction. Here, a longitudinal magnetic field (i.e. parallel to the light propagation direction) splits the degeneracy of the σ^+ and σ^- angular momentum transitions, which are affected by left and right circularly polarised light, respectively (see appendix F). This is illustrated in figures 9.1(a) and (b). Any method of altering the optical properties of a medium can induce

birefringence. One such example is illustrated in figure 9.1(c). Here, the populations of the transition ground states are altered, which causes birefringence by changing the relative probability of a σ^+ or σ^- transition happening. The redistribution of population among angular momentum states gives a net spin polarisation to the medium, hence the name 'paramagnetic Faraday effect', though strictly speaking it is unrelated to the magneto-optic Faraday effect since an applied magnetic field is not required. The spin polarisation is achieved via optical pumping [56, 85]. Thus the polarisation of a probe beam can be controlled by a pumping field.

9.2 Optical pumping

Although optical-induced birefringence has its advantages, as far as we are aware rotations of the $\pi/2$ radians necessary to realise orthogonal polarisation channels have not been observed. However, magnetically induced birefringence easily produces the required channels [39]. Optical control can be introduced to the Faraday effect via optical driving. By transferring population among ground states coupled and uncoupled by the probe field, the strength of the Faraday effect can be controlled. Here the static applied magnetic field produces a rotation offset to the probe beam around which the polarisation angle can be tuned via the optical control field.

In order to achieve and record optical control, we add another light field to the experimental lay out used to measure polarisation rotation (see chapters 5 and 7). Figure 9.2 shows a schematic of the experimental apparatus along with the energy level scheme used to observe the optically controlled Faraday effect on the D_1 transition of rubidium. As in early parts of this thesis, the source of probe light was an external cavity diode laser (ECDL) at 795 nm, the output beam having a $1/e^2$ half-width of 0.8 mm and a power less than 1 μW. The beam was sent through a 75 mm vapour cell containing the Rb isotopes according to the ratio ^{87}Rb:^{85}Rb of 99:1, the heating of which was provided by a solenoid (which also provided a magnetic field). The counter-propagating control field is resonant with the D_2 line at 780 nm. The control beam was linearly polarised with a spot size of 2 mm ($1/e^2$ half-width).

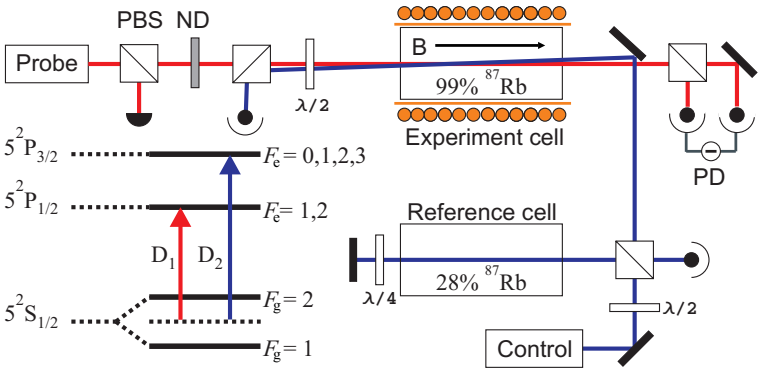

Figure 9.2: Schematic of the experimental apparatus. A probe beam passes through a polarisation beam splitter (PBS), providing linearly polarised light. The beam is attenuated with a neutral density filter (ND) before passing through a heated vapour cell. A half-wave plate ($\lambda/2$) is used to control the polarisation angle of the light before it is analysed with a PBS and collected on a differencing photodiode (PD). A control beam is linearly polarised and counter-propagated at a crossing angle of ~ 5 mrad. A small fraction of the beam is used to perform sub-Doppler spectroscopy in a reference cell.

In figure 9.3 we demonstrate optical pumping to uncoupled, or 'dark' states. Plotted is the transmission of a probe beam through a medium subjected to a 9 mW counter-propagating control field tuned to a frequency between the D_2 $F_g = 2 \rightarrow F_e = 1$ and 2 resonances. At the low-frequency side of the plot (close to resonance with the D_1 $F_g = 2 \rightarrow F_e$ transition) we see spikes of increased transmission of probe laser light. Conversely, on the high-frequency side of the plot (D_1 $F_g = 1 \rightarrow F_e$) enhanced absorption is seen. The pumping scheme is illustrated in the inset to figure 9.3(a), which also helps to explain the structure of the transmission spikes. In a thermal vapour there are a distribution of velocities which each atom can have, the velocity component along the axis of the laser beam being responsible for the Doppler effect. An intense pumping field interacts strongly with those atoms Doppler-shifted close to resonance. Of the three transitions allowed by the dipole selection rules, pumping on the two open transitions D_2 $F_g = 2 \rightarrow F_e = 1$ and 2 results in population classes with a large fraction of population in the dark state $F_g = 1$. However, the $F_g = 2 \rightarrow F_e = 3$ transition is closed, so that population transfered into the excited state can only decay back into $F_g = 2$. When the probe and control beams are resonant with the same

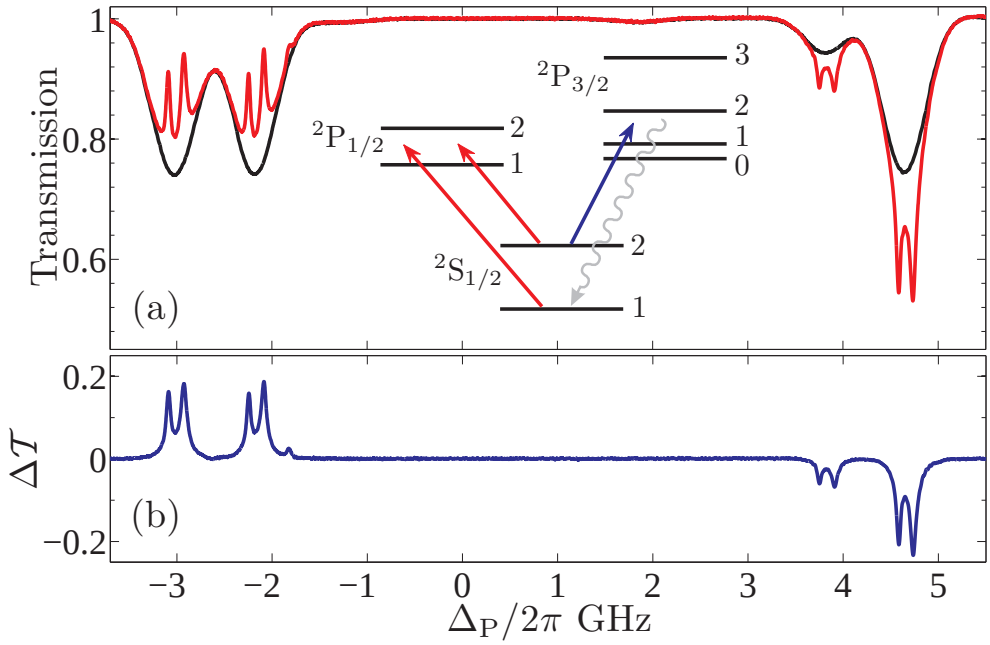

Figure 9.3: (a) Transmission of the probe beam in the vicinity of the D_1 line versus blue detuning Δ_P, with (red curve) and without (black) the control beam tuned to the ^{87}Rb D_2 $F_g = 2 \rightarrow F_e$ transition. The inset shows a schematic of the laser coupling scheme (not to scale). (b) The difference in transmission, $\Delta\mathcal{T}$, between two curves in part (a). The 99% ^{87}Rb cell is held at a temperature of 20°C.

velocity classes, modification to probe transmission is seen. Hence in each Doppler-broadened line-shape of the probe beam two prominent spikes are seen, due to a combination of hyperfine pumping and saturation of the open transitions, with only a small contribution due to saturation of the closed transition[1]. The probe transitions with $F_g = 2$ as the ground state are less populated and thus produce less absorption, and vice versa for $F_g = 1$.

[1]The fact that the $F_g = 2 \rightarrow F_e = 3$ transition is farther detuned from the pump laser frequency than $F_g = 2 \rightarrow F_e = 1$ and 2 also affects its relative amplitude. For completeness, appendix H shows the effect of pump detuning on the probe transmission spectrum.

9.3 Measuring the polarisation rotation

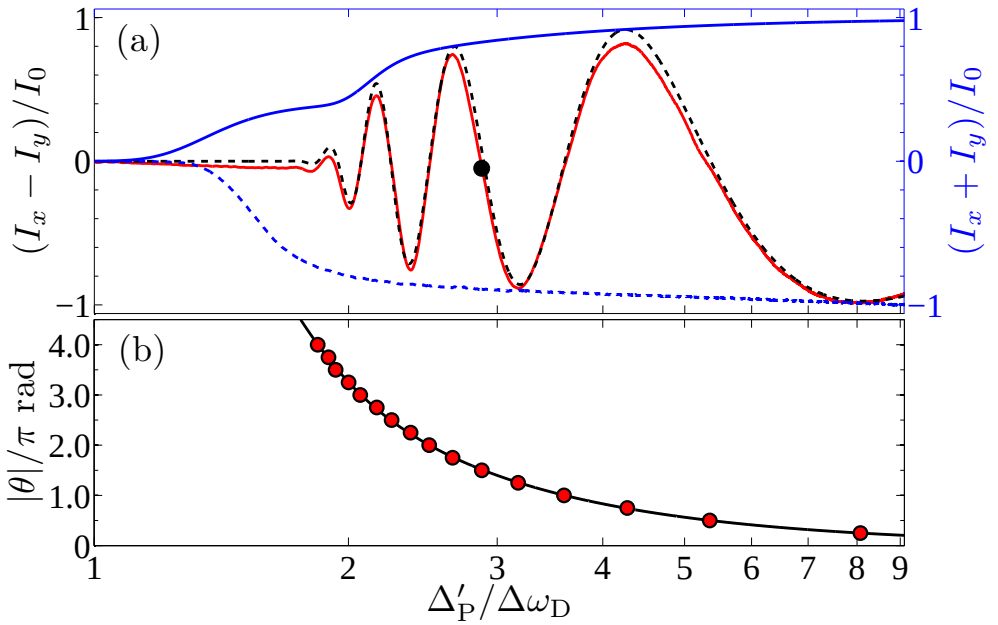

Figure 9.4: (a) Probe signal produced by scanning the probe versus red detuning, $\Delta'_{\rm p}$, from the D_1 ^{87}Rb $F_{\rm g} = 2 \rightarrow F_{\rm e} = 1$ transition in units of Doppler width $\Delta\omega_{\rm D} = 2\pi(571$ MHz). On the left axis, the red and dashed black curves show, respectively, the measured and theoretical differencing signal. On the right axis, the solid blue curve shows the theoretical total transmission through the cell in the presence of the magnetic field, whilst the dashed blue curve shows the measured total transmission in the absence of the magnetic field (flipped vertically for clarity). (b) The measured rotation angle (data points) and theoretical rotation (curve). The temperature of the cell is 115°C and the applied magnetic field is 204 G.

To observe the Faraday effect, only the probe beam and the applied magnetic field need be present. Figure 9.4(a) shows a typical differencing signal in rubidium vapour and the calculated theoretical signal obtained by diagonalising the complete Hamiltonian (including the magnetic field interaction) of the system. Good agreement with experimental data is seen: any discrepancy is due to the different detectors used in the measurement of I_x and I_y. For the differencing signal, as the probe detuning is increased, $\theta \rightarrow 0$ and thus the signal tends to zero. As the light nears resonance, the rotation increases from zero, and due to the signal's sinusoidal dependence on θ oscillations in the

differencing signal are observed. As can be seen by comparing figure 9.4(a) and (b), zero crossings correspond to rotations of integer multiples of $\pi/2$ radians to the incident beam; extrema correspond to $\pm\pi/4$ rad.

The familiar Doppler-broadened line-shape in the absence of magnetic field is seen in figure 9.4(a). The total intensity signal in the presence of the magnetic field is also shown, and is related to the dichroism of the medium. The total intensity is unity far from resonance where there is little absorption, and zero on resonance due to the large optical depth at the parameters for which the signal is calculated. At detunings of greater than two Doppler widths, the peaks of the differencing signal lie close to the total intensity signal. At detunings closer to resonance circular dichroism becomes important, with the shoulder indicating where one circular polarisation is absorbed significantly more than the other. The light polarisation here is almost circular, hence the differencing signal is zero. See appendix G for a more complete description of circular birefringence/dichroism.

9.4 Spectral dependence of Faraday rotation on the optical control field

In section 9.2 we saw that at room temperature optical pumping was highly efficient close to resonance. Perversely, Faraday rotation requires a hot vapour, which is likely to absorb the resonant pumping beam completely as it enters the medium, leaving the remainder of the atoms unperturbed from their original state. In this section we investigate the effect of scanning the control field across the whole D_2 spectrum. We fix the detuning of the probe laser at a frequency where the polarimeter signal is close to zero (indicated by the dot (•) in figure 9.4, at a red detuning of ~ 2.9 Doppler widths, or 1.7 GHz). Hence any effect caused by the control field will be seen in the measurement of the probe differencing signal as a deviation from zero. In figure 9.5 we show the response of the Faraday rotation signal as a function of the blue detuning of the control field, Δ_C. Figure 9.5(a) shows the probe differencing signal for the same temperature and magnetic field as figure 9.4, whilst figure 9.5(b) shows the transmission of the control beam through the

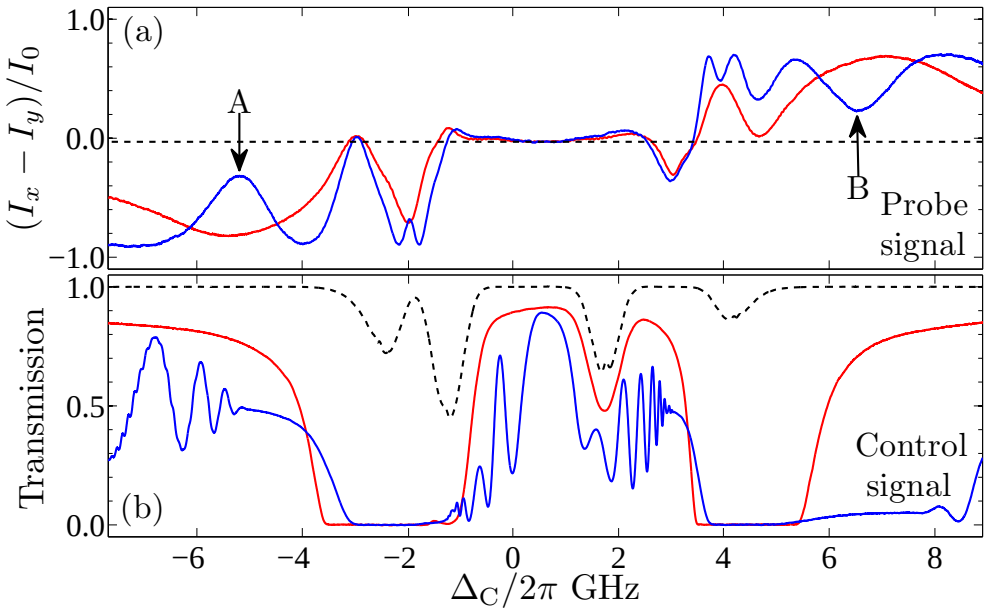

Figure 9.5: (a) Differencing signal of the D_1 probe versus D_2 control field blue detuning, Δ_C. The power of the control field is 9 mW (red) and 30 mW (blue). The experiment cell is at a temperature of $\sim 115°C$, with a 204 G applied magnetic field. In the absence of the control field, the differencing signal is given by the dashed black line. (b) Transmission of the control field light through the room temperature natural abundance reference cell (dashed black) and the ^{87}Rb experiment cell with (blue) and without (red) the magnetic field. Control detuning is with respect to the weighted D_2 line-center (see chapter 4).

experiment cell and a weaker beam through the reference cell. Between the two ^{87}Rb absorption lines the control field appears to have little effect on the difference signal, but close to resonance and at greater detunings the effect of optical control is significant. The maximum/minimum signal corresponds to alignment with the x/y axis before folding back upon itself for greater rotation angles. Increasing the control power increases the rotation angle whilst retaining similar spectral dependence, hence the dips seen in the 30 mW curve in figure 9.5(a) correspond to rotations beyond $\pm\pi/4$ rad to the input beam, most noticeable at points A and B. Repeating the experiment with a circularly polarised control field (stimulating the σ transitions) changes the differencing signal by $\sim \pm 30\%$ over the whole D_2 spectrum.

From figure 9.5(b) it can be seen that the control beam also experiences Faraday rotation (in tandem with dichroic absorption, which cannot be gleaned

from this plot). This has implications for the optical pumping process as both the intensity and polarisation state of the control beam vary over the length of the cell, resulting in an inhomogeneously prepared medium. The measured rotation of the probe is the average rotation it experiences upon traversing the cell, so ideally the medium should be homogeneous.

9.5 Optical control of the probe differencing signal

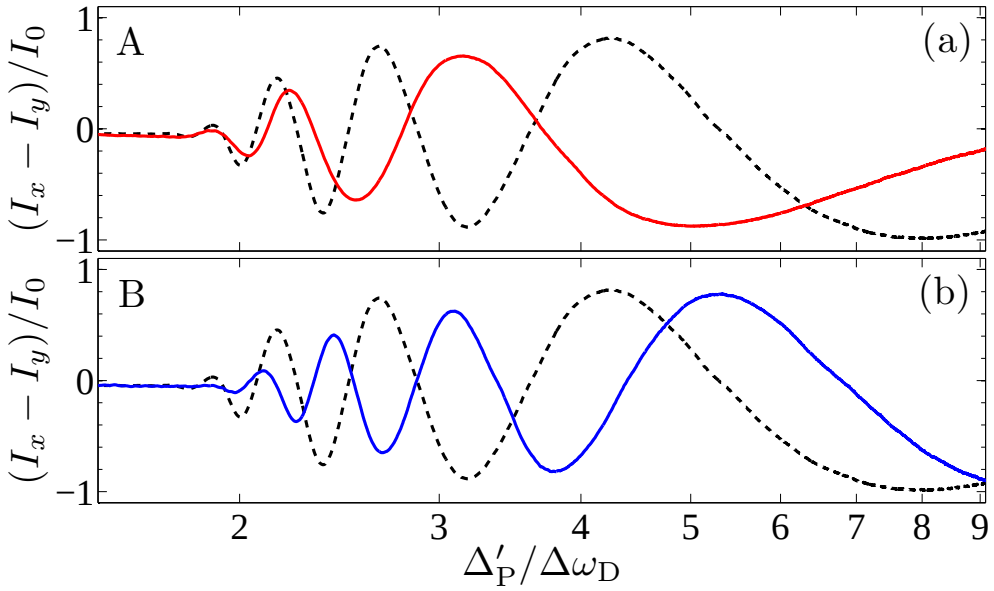

Figure 9.6: D_1 Probe differencing signal versus red detuning, Δ'_P. The dashed black curve shows the experimentally measured signal in the absence of the D_2 control field (from figure 9.4). Plots (a) and (b) illustrate the effect of optical pumping on the probe signal when the 38 mW control field is fixed at detunings A and B given in figure 9.5. Temperature and applied magnetic field are the same as figure 9.4.

In section 9.4 we observed that the largest change to the birefringence of the medium was at control detunings either side of the D_2 transition. We now wish to find the spectral dependence of birefringence for the probe beam by scanning its frequency in a region red detuned from the D_1 line. Figure 9.6 shows the resulting difference signal produced in the presence of the D_2 control field. Plots (a) and (b) show the influence of the applied control field

with its frequency fixed at the two points of maximum rotation shown in figure 9.5. From these plots we are able to take the absolute angular rotation, θ, of the probe using the zero-crossings and extrema (which are independent of absorption or dichroism). The measured rotations are shown in figure 9.7. It can be seen that rotations of many π radians are possible with the Faraday effect, as observed in previous studies [40, 60]. For the rotation angle of $\pi/2$ rad induced by the applied magnetic and optical fields, the change in refractive index $\Delta n = 5 \times 10^{-6}$.

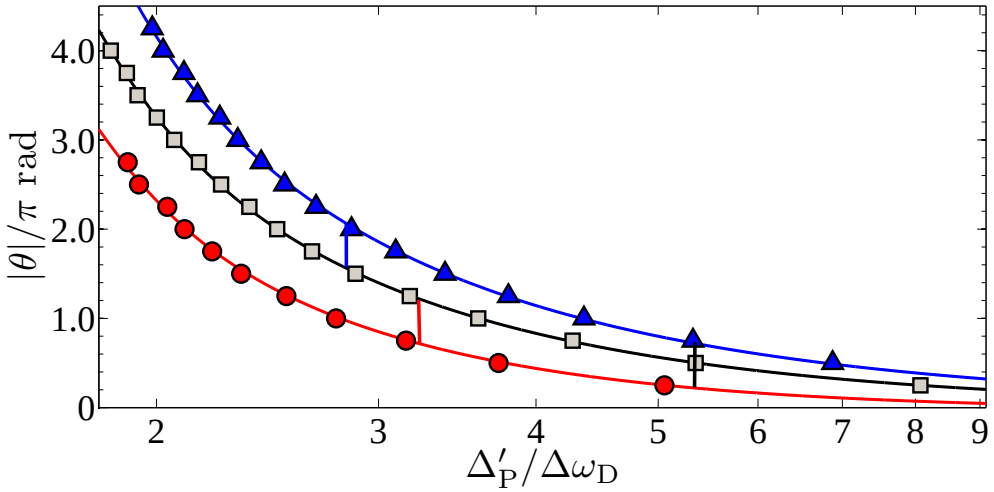

Figure 9.7: The measured rotation angles, θ, versus red detuning, $\Delta'_{\rm P}$, of the D_1 probe. The angles are calculated from the zero crossings/extrema of figure 9.6 for no optical control (squares), a red-detuned control field (circles), and a blue-detuned control field (triangles). The curves are from theory. Vertical bars show the detunings at which $\pi/2$ rotations are possible by switching amongst the three curves.

By taking the difference of the curves in figure 9.7 we can get an idea of rotation attainable by switching amongst the three cases of no control field, and red/blue detuned control. For $\pi/2$ rotation caused by switching between control field on and off the transmission is $\sim$ 90%. The red- and blue-detuned cases have opposite sign, so that the difference between these two has a greater magnitude, achieving $\pi/2$ at $\sim$ 95% transmission. The figure of merit, $\Delta\chi_{\rm R}/\chi_{\rm I}$, is conveniently equal to the ratio of measurable quantities $2\Delta\phi$ (twice the relative phase shift) and $L_{\rm depth}$ (the optical depth). The figure of merit is $> 40\pi$ for probe detunings up to $5 \times \Delta\omega_{\rm D}$. This is more than an

order of magnitude larger than previous work e.g. 1.4π in reference [58], and $\pi \times 10^{-2}$ to $\pi \times 10^{-1}$ for other experiments [144–146]. The figure of merit is essentially constant beyond two Doppler widths from resonance. This is ideal for broadband light where large differential dispersion over the spectrum of the pulse can lead to distortion [40].

In order to calculate the optically induced rotations we extended our steady-state model used to generate the theory curve in figure 9.4 by setting the populations of the atomic states as independent parameters. This model quantitatively imitates the behaviour of the optical pumping which induces the controlled Faraday rotation. Population transfer via a π polarised pump (zero angular momentum transfer) is modeled as a change in the F_g state populations; transfer by $\sigma^{\pm}$ pumping is modeled as an anisotropy in the m_{F_g} state populations, i.e. the paramagnetic Faraday effect. For the case of no pumping, an equilibrium population produces an excellent fit to data (black curve, figure 9.7). Decreasing the population of the ^{87}Rb $F_g = 2$ by 2.5%, with an m_{F_g} anisotropy such that there is an increased occupation of the $m_{F_g} = -2, -1$ states, reproduces the effect of a red-detuned control field; increasing the population by 16%, with an m_{F_g} anisotropy which increases the occupation of the $m_{F_g} = 2, 1$ states, reproduces the blue-detuned control field effect. The parameters used here on an *ad hoc* basis agree with the expected pumping behaviour: the red-detuned beam pumps depletes the population of the ground state being probed. As such the rotation is decreased with respect to the equilibrium case. The opposite is true for the blue-detuned beam. The m_{F_g} anisotropy is due to the pump polarisation changing from its initially linear state to being highly elliptical as it propagates through the medium.

Unlike the paramagnetic Faraday scheme in which a large spin polarisation in the population of m_{F_g} states is created, thereby inducing birefringence, the dominant effect in the measured data is the optical pumping of population into or out of the F_g state. Nevertheless, simulations show that only a small amount of anisotropy need be created amongst the magnetic sublevels to produce rotations of the order seen for the pure Faraday effect. Tighter control of the pumping scheme, such as σ-pumping on an isolated closed transition, should allow true paramagnetic Faraday rotation without the magnetic field.

9.6 Discussion

In summary, we have demonstrated controlled Faraday rotation of one optical field due to the presence of another, with high transmission of both beams. A continuous-wave field was used to incoherently pump atoms into a dark ground state, a process which typically takes $0.1 - 1$ μs [20]. Hence this process could allow rapid switching, and has applications as a dynamic half-wave plate.

There are a number of issues with the approach taken in this chapter. Firstly, the required magnetic field to bias the Faraday signal has a large effect on the control field, a situation which is not ideal. It is preferable to fix the control field polarisation to limit the number of variables in the system. Another issue is the inhomogeneity of the medium, brought about as a result of the probe and control beams sharing the same propagation axis. This can be rectified by setting the axes at right angles to each other and changing the control beam's aspect ratio such the medium is prepared homogeneously along the probe axis (see figure 9.8).

In the experiment described in this chapter, a continuous-wave control field was used to bring the medium into a steady-state whilst a weak continuous-wave probe field simultaneously propagates through it. In the next chapter, we will consider a pulsed control field coherently driving population into the excited state, in a time less than the excited state lifetime.

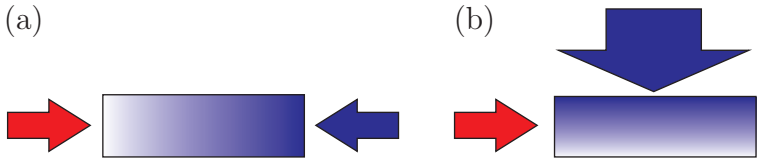

Figure 9.8: An illustration of preparation schemes. (a) Co-axial counter-propagation (b) Orthogonal propagation. The gradient shading of the medium represents the preparation efficiency of the control beam.

Chapter 10

Atom-light interactions in the nonlinear regime

Throughout this thesis we have considered light propagation phenomena in the regime where the atom-light interaction is linearly dependent on the applied electric field. In this weak regime, illuminated atoms effectively remain in the ground state and are unaffected by the passage of light. In this chapter we investigate the regime where the light has a significant effect on the medium.

10.1 Population transfer & pulse area

We begin with a well-known concept of resonant interactions, the *area* of a light field [147, 148]. In the Bloch equations of a two-level atom, the Rabi angular-frequency Ω is the rate at which population is coherently transfered between the ground and excited state. If the atom is initially in the ground state, after a time $\tau = \pi/\Omega$ the probability of finding the atom in the excited state is equal to unity: the population is said to be inverted[1]. After a further period τ the atom is now found back in its initial state. However, if the Rabi angular-frequency is now taken to be dependent on time it no longer has a clear physical significance. The concept of population transfer can be

[1] Assuming τ is much shorter than the excited state lifetime $1/\Gamma$, in which case the probability of spontaneous emission happening in this time is small.

generalised to a time-dependent field via the envelope area, which is given by

$$\mho(t) = \int_{-\infty}^{t} \Omega(t')\mathrm{d}t'. \tag{10.1}$$

Here we assume that the Rabi angular-frequency has a constant phase (for the effect of phase and frequency modulation see reference [2]). As a physical pulse has a finite duration, by extending the integration limits over the whole pulse we can assign an area to the pulse as a whole. For a pulse which has an area of $\mho(+\infty) = \pi$ rad, i.e. a *π-pulse*, the population is inverted in the same manner as for constant illumination over a time τ (indeed the constant field can be thought of as a sequence of adjoining square pulses of area π rad). A 2π-pulse returns the atom to its initial state.

For a Gaussian intensity envelope (for which see chapter 6) which has a full-width at half-maximum (FWHM) Δt and an initial peak Rabi angular-frequency Ω_0 the initial area of the pulse is

$$\mho(t) = \Omega_0 \Delta t \sqrt{\frac{\pi}{2\ln 2}} \left[\frac{1}{2}\mathrm{erf}\left(\sqrt{2\ln 2}\,(\mathrm{t}/\Delta\mathrm{t})\right) + \frac{1}{2}\right], \tag{10.2}$$

where $\mathrm{erf}(x)$ is the error function[2]. Taken over the extent of the pulse we find an area of $\mho(+\infty) = \Omega_0 \Delta t \sqrt{\pi/(2\ln 2)}$.

Of course, when we consider the full Maxwell-Bloch equations we must take account of how population transfer affects the pulse as it propagates through an extended medium. Population transfer must be balanced by a transfer of energy between the pulse and the medium. Consider the following heuristic argument. The electromagnetic field contains a number of photons, of energy $\hbar\omega_\mathrm{c}$, at a density $\mathcal{N}_\gamma$ traversing a medium composed of atoms at a density $\mathcal{N}_\mathrm{a}$. For a photon energy approximately equal to the energy of the atomic excited state $\hbar\omega_0$, each atom has the capacity to store one photon (we are assuming a two-level atom so we'll ignore such effects as multiple photon absorption).

In the limit $\mathcal{N}_\gamma \ll \mathcal{N}_\mathrm{a}$, the medium can in principle remove all photons

[2]The error function is the integral of the Gaussian function:

$$\mathrm{erf}(x) = \frac{2}{\sqrt{\pi}} \int_0^x \mathrm{e}^{-t^2}\mathrm{d}t. \tag{10.3}$$

from the field with only a small probability of a given atom being excited. In the opposite limit $\mathcal{N}_\gamma \gg \mathcal{N}_\mathrm{a}$, many photons can be removed from the field without significantly altering it. In this limit however the medium can experience large excitations, with an increased probability for a larger density of photons.

10.2 Large-area pulse propagation

We will consider the cases of a π- and 2π-pulse propagating in a Doppler-free medium of two-level atoms identical to the one considered in chapter 2. We take an atomic density of $\mathcal{N}_\mathrm{a} = 1.5\times10^{16}$ m^{-3}. Such a medium has a resonant optical depth[3] of $L_\mathrm{depth} = 1.4 \times 10^4$ in the limit of weak incident light, and as such we would expect a weak continuous-wave light to be absorbed in the first millimetre.

The initial pulse envelope has a FWHM of $\Delta t = 0.71$ ns (short in comparison to the excited state lifetime of 27.7 ns) and thus a frequency of FWHM $\Delta\nu = 624$ MHz. For such an envelope, an $n\pi$-pulse requires a peak Rabi angular-frequency of $\Omega_0 = n\ 2\pi(470\text{ MHz})$, corresponding to a peak average photon density[4] $\mathcal{N}_\gamma = n^2\ 8.9 \times 10^{14}$ m^{-3}. We are therefore in the regime $\mathcal{N}_\gamma \sim \mathcal{N}_\mathrm{a}$.

From figures 10.1 and 10.2 it can be seen that the π-pulse is absorbed heavily as it enters the dense medium, accompanied by excitation of the atoms. The pulse frequency width is much greater than the 5.75 MHz FWHM of the resonance. Thus a significant proportion of the field is beyond the frequency range of absorption; however, this portion is still within the range over which dispersion acts. Thus much of the energy of the pulse survives, though the envelope is heavily distorted. The pulse loses its identity and becomes an oscillation alternating between negative and positive values (as we saw in section 2.3.1). The resonant portion of the pulse is absorbed at the entrance, leading to an excitation that remains after the pulse has passed (decaying away with a lifetime of 27.7 ns). The excitation on the interior is transient,

[3] The optical depth is defined via $I/I_0 = \exp[-L_\mathrm{depth}]$, where I and I_0 are the transmitted and incident intensity, respectively. See section 3.1.1.

[4] $I = \frac{1}{2}c\epsilon_0|\tilde{E}|^2 = c\hbar\omega_\mathrm{c}\mathcal{N}_\gamma$

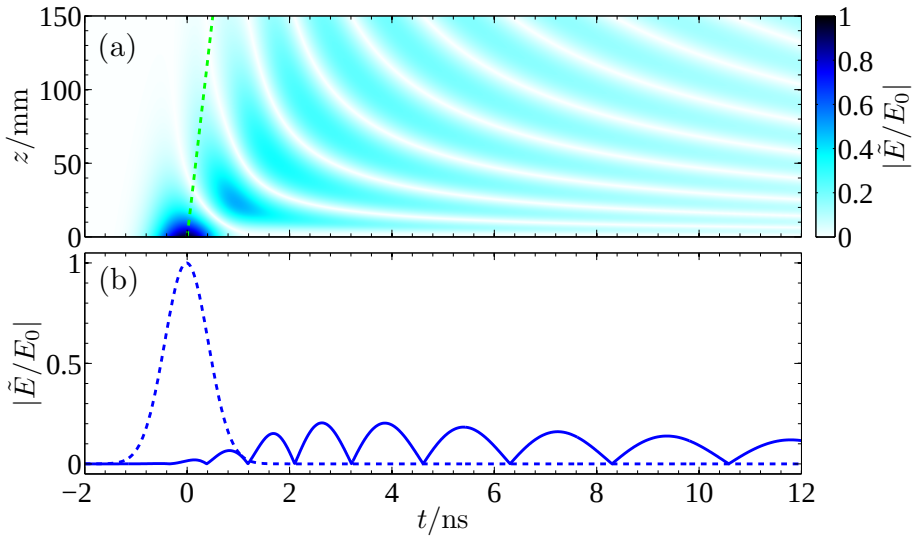

Figure 10.1: Propagation of a resonant π-pulse. (a) The magnitude of the pulse envelope versus time and propagation distance. The green dashed curve shows the trajectory a pulse in free-space would take. (b) The temporal envelope of the incident pulse (dashed curve) and outgoing pulse (solid).

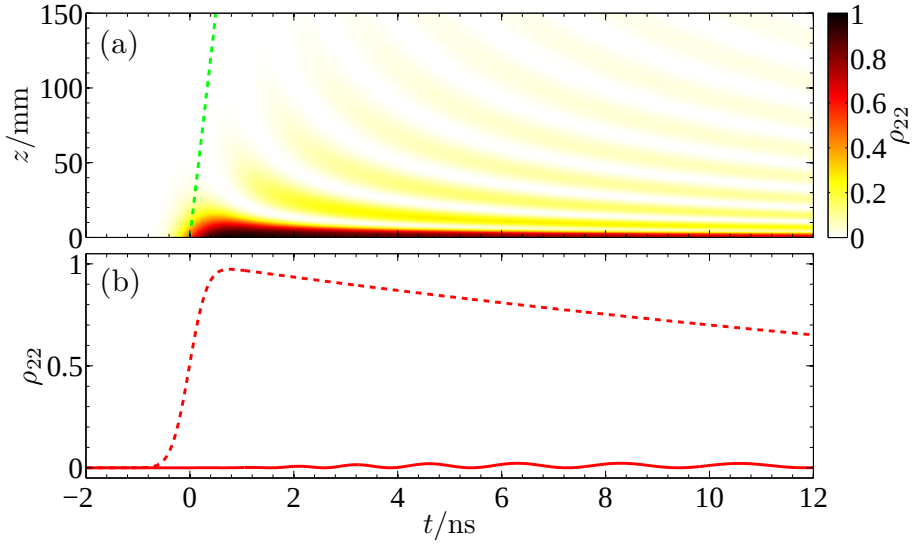

Figure 10.2: Excitation by a resonant π-pulse. (a) The excited state population against time and propagation distance. The green dashed curve shows the trajectory a pulse in free-space would take. (b) Time dependence of the population at the entrance (dashed curve) and exit (solid) of the medium.

the energy stored in the atoms is repeatedly exchanged between the medium and off-resonant light.

In contrast to the lower area pulse, the 2π-pulse is able to travel deeper inside the medium (figures 10.3 and 10.4). The first half of the pulse acts to transfer population to the excited state, becoming absorbed in the process. The second half of the pulse gains this energy via stimulated emission, which can have the effect of increasing the peak electric field (typified by the envelope at 35 mm). The cycle of absorption-emission successively holds the pulse back from its expected trajectory, a demonstration of resonant slow-light with an average velocity corresponding to a group refractive index of $n_g = 4.8$. This is due to the electromagnetic energy spending a significant amount of time as an excitation in the immobile medium. The net transfer of energy to the medium is close to zero and thus the pulse effectively 'sees' a transparent medium, a transparency caused by the light itself in a process known as self-induced transparency (SIT) [147, 148].

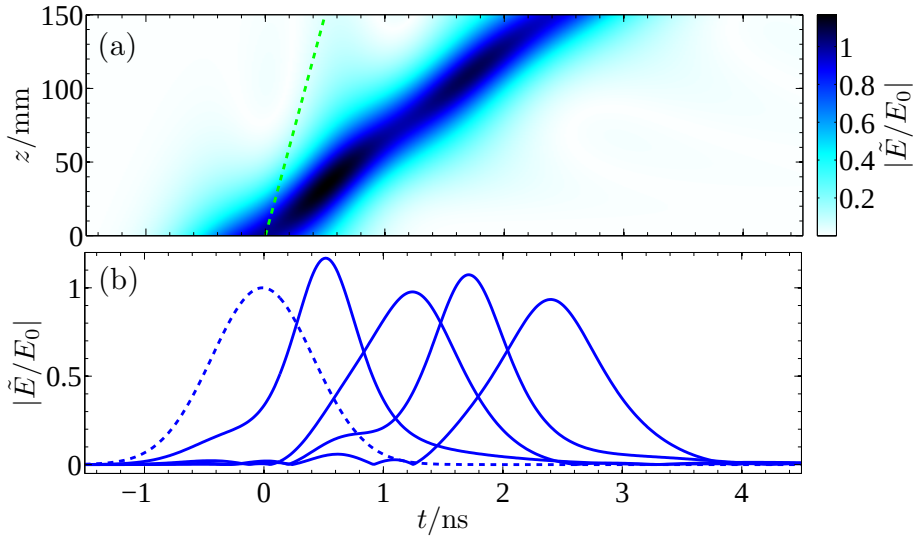

Figure 10.3: Propagation of a resonant 2π-pulse. (a) The magnitude of the pulse envelope versus time and propagation distance. The green dashed curve shows the trajectory a pulse in free-space would take. (b) The temporal envelope of the incident pulse (dashed curve) and successive pulses (solid) at displacements 35, 80, 110 and 150 mm inside the medium.

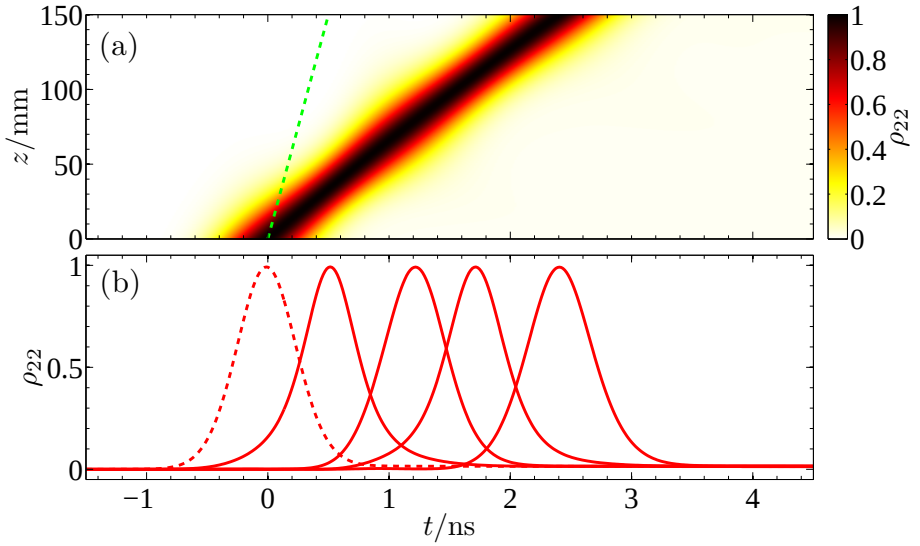

Figure 10.4: Excitation by a resonant 2π-pulse. (a) The excited state population against time and propagation distance. The green dashed curve shows the trajectory a pulse in free-space would take. (b) Time dependence of the population at the medium entrance (dashed curve) and at displacements 35, 80, 110 and 150 mm inside the medium (solid).

10.3 Energy transfer & Poynting's theorem

The interaction between atoms and light inevitably leads to an exchange of energy between the two systems. In considering the energy of the system, we must balance the energy flowing into a volume with the energy being stored and dissipated within this volume. We begin by providing a completely general expression of the rate of change of energy which can be applied equally to the electromagnetic and atomic excitation (or indeed other forms of energy such as thermal or mechanical) [149]:

$$-\oint_A \mathbf{S}\cdot \mathrm{d}\mathbf{A} = \partial_t \int_V U \mathrm{d}V + \int_V R \mathrm{d}V. \tag{10.4}$$

The energy energy per unit time passing through a surface enclosing an arbitrary volume V is given by the surface integral of the energy flux $\mathbf{S}$ (having dimensions of energy per unit time per unit area). This is balanced by the change in the energy density U (energy per unit volume) stored inside the volume, and the rate at which energy dissipates R (energy per unit time per unit volume). By dissipation we mean a process which transforms energy from one form to another: of particular interest to us is the transformation of electromagnetic energy to atomic excitation. A more convenient form of the above equation can be derived by making use of the divergence theorem to transform the surface integral into a volume integral, and by noting that the volume is arbitrary. Thus we can move to a picture in which we consider quantities at spatial points rather then over entire volumes. This leaves us with the general statement of energy conservation in differential form

$$\nabla\cdot\mathbf{S} + \partial_t U + R = 0. \tag{10.5}$$

We will now look for equations having the form of this energy conservation expression for the electromagnetic field and the medium through which it propagates. Poynting's theorem [150] provides the energy continuity equation for electromagnetic fields [149]:

$$\nabla\cdot(\mathbf{E}\times\mathbf{H}) + \partial_t(\tfrac{1}{2}\epsilon_0\mathbf{E}\cdot\mathbf{E} + \tfrac{1}{2}\mu_0\mathbf{H}\cdot\mathbf{H}) + \mathbf{E}\cdot\partial_t\mathbf{P} + \mu_0\mathbf{H}\cdot\partial_t\mathbf{M} + \mathbf{E}\cdot\mathbf{J} = 0, \tag{10.6}$$

where $\mathbf{H}$ is related to the magnetic field via $\mathbf{B} = \mu_0(\mathbf{H}+\mathbf{M})$. In a non-magnetic medium we can neglect the magnetisation $\mathbf{M}$, and if free charge

carriers are absent then the free current density $\mathbf{J} = 0$. The theory of electromagnetism is underpinned by the fact that the electric and magnetic fields are inextricably linked. For plane waves propagating in the z direction, we can simplify things by inserting the electric field calculated in section 3.1 into the Maxwell equation III, i.e. $\nabla \times \mathbf{E} = -\partial_t \mathbf{B}$. We find $n\hat{\mathbf{k}} \times \mathbf{E} = c\mathbf{B}$ [62], where $\hat{\mathbf{k}}$ is a unit vector in the direction of propagation, and n is the refractive index[5]. Equation (10.6) then simplifies to

$$\partial_z(nc\epsilon_0 E^2) + \tfrac{1}{2}\partial_t\left(\epsilon_0\left(1+n^2\right)E^2\right) + \mathbf{E}\cdot\partial_t\mathbf{P} = 0 \tag{10.7}$$

Comparing this to the general statement of energy conservation (10.5), we can identify that the flux of electromagnetic radiation S, the energy density U_{em}, and rate of dissipation R_{em}:

$$S = nc\epsilon_0 E^2, \tag{10.8}$$

$$U_{\mathrm{em}} = \tfrac{1}{2}\epsilon_0\left(1+n^2\right)E^2, \tag{10.9}$$

$$R_{\mathrm{em}} = \mathbf{E}\cdot\partial_t\mathbf{P}. \tag{10.10}$$

Averaging over an oscillation period we obtain the following in terms of slowly-varying quantities (noting that the total electric field is in general composed of multiple envelopes $\tilde{\mathbf{E}}_j$ centred at carrier angular frequencies ω_{c_j}, for which see section 2.2.1):

$$\langle S\rangle = \sum_j \tfrac{1}{2}c\epsilon_0|\tilde{E}_j|^2, \tag{10.11}$$

$$\langle U_{\mathrm{em}}\rangle = \sum_j \tfrac{1}{2}\epsilon_0|\tilde{E}_j|^2, \tag{10.12}$$

$$\langle R_{\mathrm{em}}\rangle = \sum_j \omega_{\mathrm{c}_j}\mathrm{Im}[\tilde{\mathbf{E}}_j^*\cdot\tilde{\mathbf{P}}_j], \tag{10.13}$$

where we have used the fact that under the slowly-varying envelope approximation $|n-1| \ll 1$. We have met the time-averaged flux previously in this thesis, where we referred to it as the intensity I, being the average power per unit area incident upon a surface.

An energy-conservation equation for the medium also needs to be derived. Assuming the medium is stationary, there is no flow of particles and hence

[5]Note this relationship between the electric and magnetic fields is only strictly true for an approximately monochromatic field. Fortunately the slowly-varying envelope approximation ensures this is the case.

no flux of atomic energy out of the volume (we also exclude particle-particle interactions). The rate of change of energy density in the atoms, $\partial_t U_\mathrm{a}$, can be found by considering the rate of change of population amongst the atomic energy levels: this is provided by the Bloch equations. With $\mathcal{N}_\mathrm{a}\rho_{mm}$ as the number density of atoms in the state $|m\rangle$ of energy $\mathcal{E}_m$, the total rate of change of the internal energy of the ensemble (assuming the energy of each state remains constant) is

$$\partial_t U_\mathrm{a} = \mathcal{N}_\mathrm{a} \sum_m \mathcal{E}_m \partial_t \rho_{mm}. \tag{10.14}$$

As we saw in section 2.3 for the case of the two-level atom, the expression for $\partial_t \rho_{mm}$ has terms that contain the coherent interaction with the light field $\sim \mathbf{d}\cdot\mathbf{E}$ and incoherent decay/repopulation terms $\sim \Gamma$. Needless to say the full dynamics of the ensemble is specific to the particular system under consideration, but we can derive some general results using heuristic arguments (the following is based on the discussion found in [63]). Energy is supplied via the electric field of the electromagnetic wave, which interacts with the electron of each atom. Between t and $t+\delta t$ the electron moves from $\mathbf{r}$ to $\mathbf{r}+\delta\mathbf{r}$, the field supplying an energy of $\delta W = q\mathbf{E}\cdot\delta\mathbf{r}$ in the process. The power absorbed by the atom thus equals $\partial_t W = \mathbf{E}\cdot\partial_t\mathbf{d}$, using the definition of the electric dipole $\mathbf{d} = q\mathbf{r}$. On the assumption that the medium is composed of $\mathcal{N}_\mathrm{a}$ atoms per unit volume which do not interact with each other, we may look at the macroscopic power density by taking the average $\partial_t U_\mathrm{a} = \mathbf{E}\cdot\partial_t\mathbf{P}$. Unsurprisingly, this happens to be the rate at which electromagnetic energy is dissipated we found earlier (10.10). Hence the negative of this is the rate at which atomic energy is delivered to the electromagnetic wave.

The only other way for the medium to lose energy we consider is via radiative decay to lower internal energy states, a process which transfers energy into electromagnetic field modes distinct from the field leading to excitation. These modes partake in no further interacting and hence energy dissipated in this manner is removed from the atom-light system. The average rate at which dissipation happens is

$$\langle R_\Gamma \rangle = \mathcal{N}_\mathrm{a} \sum_{n,m<n} \mathcal{A}_{nm}\Gamma_n\rho_{nn}\left(\mathcal{E}_n - \mathcal{E}_m\right). \tag{10.15}$$

Here the outer sum represents the rate of energy dissipation from the state

$|n\rangle$, with the inner sum taken over $m < n$ representing the fact that some of the energy of decay is gained by states of lower energy $|m\rangle$. The coefficient $\mathcal{A}_{nm}$ is the branching ratio of decay for the spontaneous transition $|n\rangle \to |m\rangle$; population is conserved via the condition $\sum_m \mathcal{A}_{nm} = 1$.

We can then write the conservation equations

$$\langle \nabla \cdot \mathbf{S}_{\mathrm{em}} \rangle + \langle \partial_t U_{\mathrm{em}} \rangle + \langle R_{\mathrm{em}} \rangle = 0, \tag{10.16}$$

$$\langle \partial_t U_{\mathrm{a}} \rangle - \langle R_{\mathrm{em}} \rangle + \langle R_{\Gamma} \rangle = 0. \tag{10.17}$$

Thus we have arrived at our objective of this section, to describe the flow of energy between the atomic and electromagnetic systems. One of the important implications is that energy can be stored in the medium, the ulterior motive of our discussion of conservation equations.

10.3.1 *Energy velocity*

Transient storage of electromagnetic energy as atomic energy can lead to an apparent slowing down of a light pulse. The energy per unit area passing through a slice of medium of length δz in a time δt is $\delta t S$. The energy per unit area contained in the medium during this time is $\delta z U$, where $U = U_{\mathrm{em}} + U_{\mathrm{a}}$ is the sum of atomic and electromagnetic energy. As energy is conserved we can equate the two to give $S = U \delta z / \delta t$. In the limit that the slice length tends to zero, $\delta z / \delta t \to v_{\mathcal{E}}$. This is the velocity at which energy propagates through the medium, and is given by [65]

$$v_{\mathcal{E}} = \frac{S}{U} = \frac{c/n}{1 + U_{\mathrm{a}}/U_{\mathrm{em}}}. \tag{10.18}$$

For the examples of the π-pulse seen in section 10.1, the speed of the pulse rapidly decelerates from the speed of light *in vacuo* to close to zero. Indeed, it is almost entirely absorbed by the medium: the resonant portion of the pulse thus has zero velocity (since it is stored in the stationary medium), whilst the off-resonant light is sufficiently weakly-interacting that it travels close to the speed of light in free-space. The 2π-pulse behaves more ballistically and hence the concept of a velocity is more meaningful in this case. Even so, due to pulse reshaping the speed of the pulse varies between $\sim c/4$ to

$\sim c/5.5$, resulting in an average group index of $n_g = 4.8$, in agreement with the 'time-of-flight' method used in section 10.1.

In the limit of low intensity light and hence low excitation, we were able to calculate an analytic form for the expected group velocity of pulse propagation as detailed in chapter 6. In fact, the concept of energy velocity and group velocity are identical in the limit of low excitation/absorption [65].

10.4 Energy storage

In light of our considerations into the transfer of energy between atoms and optical fields, we will look at the feasibility of coherently storing and retrieving energy. We look at the simplest case of the two-level atom, sending two π-pulses into the medium one after another. The energy of the first pulse will be stored as an atomic excitation, and during the interaction with the second pulse this energy should be retrieved (though due to spontaneous emission the energy available diminishes with time).

Figure 10.5 shows the electric field of two pulses separated by a time of two nanoseconds. The first pulse is absorbed in the same manner as the single π-pulse we saw in section 10.1, transferring population into the excited state in the process (as seen in figure 10.6). When the second pulse arrives it experiences a medium which is almost completely inverted and is able to gain the energy stored inside the medium. The new pulse created in this way has an area close to 2π rad and is thus able to burn a hole through the medium, reaching deep into the interior. Note that it travels much more slowly than the 2π-pulse considered previously, having a speed of $\sim c/50$. This is due to the pulse having a longer duration (the FWHM of the intensity profile $\Delta t \approx 2$ ns) and thus lower energy density; we saw in the previous section that the relative energy densities of the atoms and medium determine the energy velocity.

In figure 10.7 we examine the transfer of energy between the light and medium, here expressed as the average dissipation rate of photon density $\langle R_\gamma \rangle = \langle R_{\mathrm{em}} \rangle / \hbar\omega_c$. At the entrance to the medium the large positive rate of dissipation marks the absorption of the first pulse. During the time between

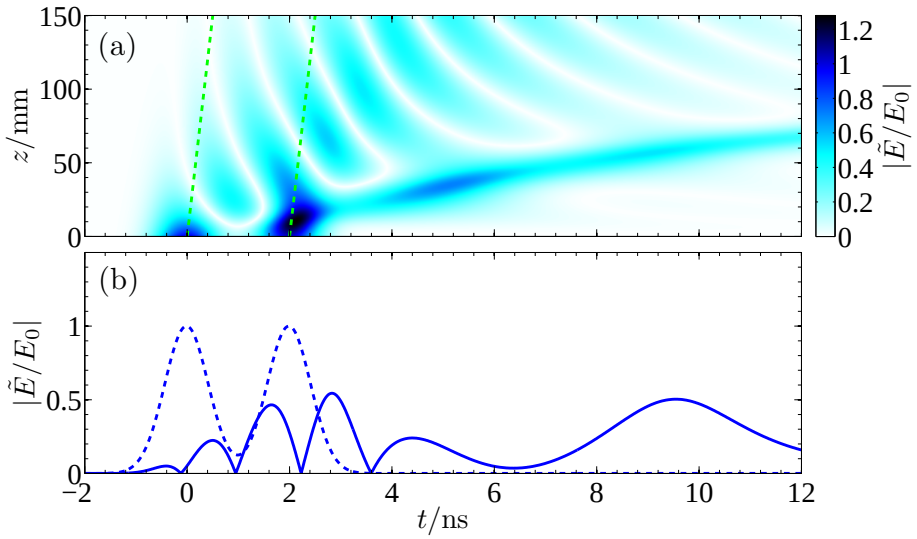

Figure 10.5: Storage and retrieval of a π-pulse. (a) The magnitude of the electric field envelope versus time and propagation distance. The green dashed curves show the trajectory both pulses would take in free-space. (b) The temporal envelope of the incident pulses (dashed curve) and the resultant field 60 mm into the medium (solid): note the field after 6 ns is the envelope of the created pulse.

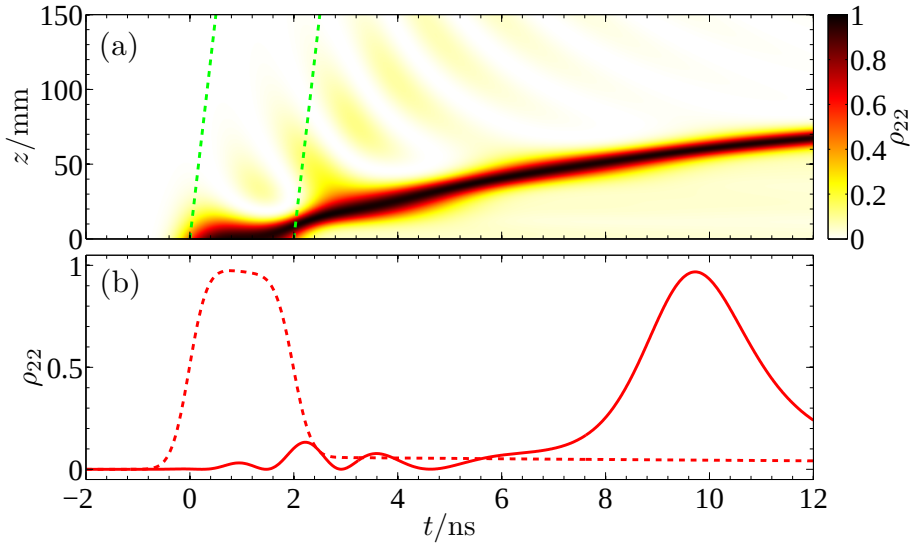

Figure 10.6: Atomic excitation during light storage and retrieval. (a) The excited state population against time and propagation distance. The green dashed curves show the trajectory both pulses would take in free-space. (b) Time dependence of the population at the medium entrance (dashed curve) and at a displacement 60 mm inside the medium (solid).

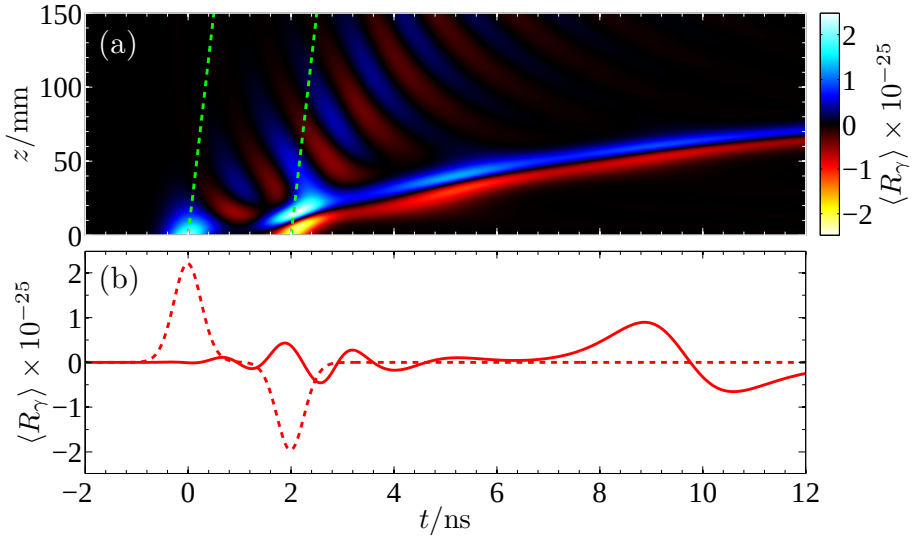

Figure 10.7: The average rate of photon transfer between the field and atoms during light storage and retrieval. (a) Transfer rate versus time and propagation distance. Blue tones represent transfer of energy *from* the light *into* the medium, i.e. absorption; red tones represent transfer of energy *into* the light *from* the medium, i.e. emission. The green dashed curves show the trajectory both pulses would take in free-space. (b) Time dependence of the transfer rate at the medium entrance (dashed curve) and at a displacement 60 mm inside the medium (solid). A positive rate indicates absorption, a negative rate emission.

the two pulses only the field of the off-resonant fraction of the first pulse is able to propagate and, due to its off-resonant nature, it is able to travel deep into the medium. The cyclical positive-negative dissipation rate shows energy is absorbed but soon returned to the light (though a small fraction is lost due to spontaneous emission); this is the mechanism by which the off-resonant frequency components of the pulse acquire shifted phase. The arrival of the second pulse inside the medium is marked by a negative rate of dissipation as stimulated emission puts energy back into the resonant optical field. With its newly-acquired energy the second pulse is now able to burn a hole through the medium. This process is clearly visible by the adjacent bands of positive and negative dissipation leading away from the time at which the second π-pulse entered.

In figure 10.8 we show the electric field envelope for several time separations between the two π-pulses. The inherent complexity of pulse propagation

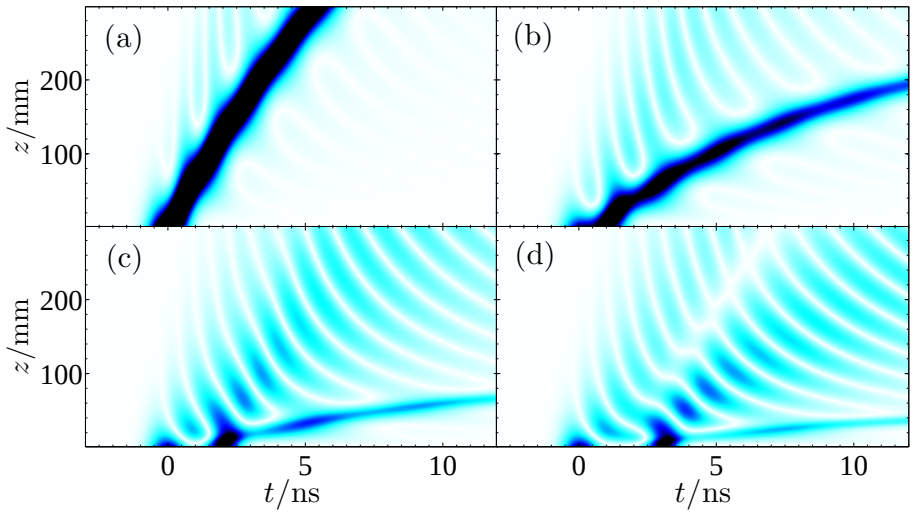

Figure 10.8: Storage and retrieval of a π-pulse for various initial time separations. The magnitude of the electric field envelope for a separation of (a) 0 ns, (b) 1 ns, (c) 2 ns, and (d) 3 ns. The field is normalised to the peak field of an individual π-pulse.

in the high density medium makes it difficult to compare individual cases, but some general trends are obvious. Clearly a separation of zero gives an envelope indistinguishable from a single Gaussian 2π-pulse; a separation of less than the pulse width is essentially a slightly deformed 2π-pulse. The greater the initial separation the greater the amount of energy that is lost due to spontaneous emission and dipolar radiation of off-resonant light (the field of this off-resonant fraction has the same striated pattern as seen for the single π-pulse in figure 10.1). The situation is made more complicated by the fact that the second pulse leads to stimulated emission of both resonant and off-resonant light which may propagate independently. Nevertheless, it it clear that the created pulse is increasingly slower, broader and of a lower amplitude with increasing time separation.

We have seen in this section that transfer of energy between pulses is possible in a quick and dirty manner: the second pulse doesn't actually take all of the energy available to it, quite apart from the energy that has been lost due to off-resonant interactions and excited state decay. Also the pulse loses its original envelope, and due to distortion decelerates and may actually become trapped inside the medium.

10.5 Optically induced birefringence

In chapter 9 we saw that it is possible to alter the Faraday rotation experienced by a weak beam via the application of an additional, higher-intensity field. This additional field acts to drive ground state population into an excited state from where it can decay into a multiplicity of lower-lying energy levels, in addition to the ground state from whence it came. We found in the experiment that preparing a high-density medium with a field close to resonance is inherently flawed as the pumping beam is heavily absorbed during the procedure. Preparation schemes normally rely on specific field amplitude and phase, and if these conditions are not maintained throughout the medium, an inhomogeneous sample will be produced. Another disadvantage of preparation schemes based on spontaneous emission is that it takes many excited state lifetimes for a medium to reach its final state, which substantially limits the speed of the operation. The preparation scheme simulated in section 10.4 does not rely upon spontaneous emission (indeed, in the simulation decay from the excited state was positively avoided), but due to the resonant nature of the field the scheme nevertheless suffers the same problems as the experiment.

Taking stock of the situation, we want to control the polarisation state of a weak probe beam using a medium which has been prepared optically in such a way that the deleterious effects of spontaneous emission have minimal influence. Ideally the medium should also be relatively homogeneous. We have already extolled the virtues of working with an off-resonant probe field (chapter 5), namely that dispersion dominates over absorption far off resonance and that Doppler broadening can be neglected. We now note that it is possible to work away from resonance with pumping fields as well. Stimulated Raman adiabatic passage (STIRAP) is one such technique for the highly efficient transfer of population between two non-degenerate metastable states, facilitated via a stimulated two-photon transition involving an unstable intermediate state. We will not go over the details of STIRAP in this thesis as it is a well-known phenomenon: for a review of previous studies see reference [151]. Our interest in it is purely as a technique for altering the birefringent properties of the medium by removing population from a subset

of atomic states which is in turn probed by a weak field. STIRAP has been investigated in situations were back action on the light from the medium is taken into consideration, e.g. for optically thick media [152, 153]. Here evolution of the fields as they propagate through the medium can result in the break down of the conditions required for STIRAP, resulting in incomplete or non-adiabatic population transfer. This is of particular concern for us as we are required to work in the high-density regime to maximise the interaction of the weak probe.

In chapter 9 the effect of pumping was to transfer population out of (or into) one of the hyperfine F states of the Rb $^2S_{1/2}$ state. This rather crudely alters the dispersive properties of the medium by effectively reducing the density of atoms interacting with the probing field. Ideally we should alter the population distributed amongst the magnetic sublevels of the F state, thereby inducing birefringence in the medium. STIRAP has been further generalised to include the possibility of some or all of the three principal energy levels being degenerate manifolds [154]. In this case adiabatic transfer for any arbitrary pure or mixed initial ground state can be achieved under certain conditions (for definitions of pure and mixed states see appendix A). In this thesis we are not interested in complete transfer out of the ground-state manifold, but rather removal of population from certain states of an incoherent mixture which will lead to an increase in the coherence of the ground state. By judicious choice of pumping fields an anisotropy can be created in the medium which alters the polarisation state of a probe beam in a predictable way. Thus, an initially isotropic medium can be made anisotropic to a probe, and this anisotropy measured, on timescales which are not limited by the rate at which population decays from intermediate states.

10.5.1 *Atom-light system for observing birefringent control*

We consider the energy level scheme shown in figure 10.9(a). This consists of $|\mathrm{g}\rangle$, a $J_\mathrm{g} = 1$ ground state which is a manifold of degenerate magnetic sublevels $\{|-\rangle, |0\rangle, |+\rangle\}$, an intermediate state $|\mathrm{f}\rangle$ with $J_\mathrm{f} = 0$, and an excited state $|\mathrm{e}\rangle$. This three-level system is referred to as a ladder or cascade system, in which the levels successively increase in energy. For simplicity

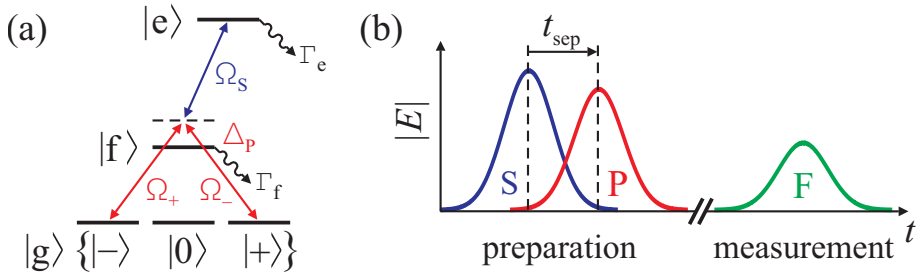

Figure 10.9: (a) Energy level scheme. (b) Pulse sequence: the mutual interaction of the Stokes (S) and pump (P) pulses with the medium constitute the preparation stage. The two pulses are separated in time by $t_{\rm sep}$, which may be negative. The preparation stage is succeeded by the measurement stage, achieved via a relatively weak Faraday pulse.

we do not consider the degeneracy of the excited state. The excited state population decays at a rate $\Gamma_{\rm e}$, a fraction of which reaches the intermediate state. Similarly, the intermediate state population decays at a rate $\Gamma_{\rm f}$, where it is distributed equally among the ground state sublevels. As is typical for the STIRAP process, the excited state population is relatively long-lived. The ground-intermediate state coupling is via the pump electric field $\mathbf{E}_{\rm P}$, with associated slowly-varying envelope $\tilde{\mathbf{E}}_{\rm P} = \tilde{E}_+\boldsymbol{\epsilon}_+ + \tilde{E}_-\boldsymbol{\epsilon}_-$. Here we have written the polarisation state in the helical basis (see appendix F), where the components $\tilde{E}_+$ and $\tilde{E}_-$ stimulate the $|-\rangle \leftrightarrow |{\rm f}\rangle$ and $|+\rangle \leftrightarrow |{\rm f}\rangle$ transitions, respectively. The Faraday field $\mathbf{E}_{\rm F}$ stimulates the same transitions as the pump, but is of much lower intensity. Note that the remaining ground-state sublevel $|0\rangle$ is only coupled to the other states via incoherent decay processes. Intermediate-excited state coupling is via the Stokes field $\mathbf{E}_{\rm S}$. The strength of a particular pump/Faraday-mediated transition is defined via the Rabi angular-frequency $\Omega_\pm = c_{m_J}\mathbf{d}_{\rm gf}\cdot\tilde{\mathbf{E}}_\pm/\hbar$. Here $\mathbf{d}_{\rm gf}$ is a reduced dipole matrix element (for the definition of which see chapter 4) describing the dipole coupling strength of a particular $|L\rangle \rightarrow |L'\rangle$ transition; the coefficients c_{m_J} are factors governing the strength of specific $|J, m_J\rangle \rightarrow |J', m'_J\rangle$ transitions. Likewise, the Stokes-mediated transition has a Rabi angular-frequency $\Omega_{\rm S} = c_{m_J}\mathbf{d}_{\rm fe}\cdot\tilde{\mathbf{E}}_{\rm S}/\hbar$. The pump (Faraday) fields are detuned from resonance by $\Delta_{\rm P(F)} = \omega_{\rm P(F)} - \omega_{\rm fg}$; the Stokes field is detuned from resonance by $\Delta_{\rm S} = \omega_{\rm S} - \omega_{\rm ef}$.

Having described how energy levels are linked via the applied fields, we obtain the resultant atomic Hamiltonian, under the rotating-wave approximation, of

$$\mathscr{H}_{\mathrm{RWA}} = -\tfrac{1}{2}\hbar\Big(\Omega_+|\mathrm{f}\rangle\langle -| + \Omega_-|\mathrm{f}\rangle\langle +| + \Omega_\mathrm{S}|\mathrm{e}\rangle\langle \mathrm{f}| + 2\Delta_\mathrm{P}|\mathrm{f}\rangle\langle \mathrm{f}| + 2(\Delta_\mathrm{S}+\Delta_\mathrm{P})|\mathrm{e}\rangle\langle \mathrm{e}|\Big) + \mathrm{H.c.} \quad (10.19)$$

Once combined with the operators describing atomic-state decay, we can form the master equation of population dynamics (for which see chapter 2), represented by the time-dependence of the density operator $\hat{\rho}$, in exactly the same manner as for the two-level system. We then use this master equation in the Maxwell-Bloch equations to describe the evolution of the three applied fields, the pulse sequence of which is shown in figure 10.9(b).

To give an explicit example, we choose to model the $5\mathrm{S}_{1/2}(F=1) \rightarrow 5\mathrm{P}_{3/2}(F=0) \rightarrow 5\mathrm{D}_{5/2}$ transition found in ^{87}Rb. This system has an intermediate-state decay rate of $\Gamma_\mathrm{f} = 2\pi(6.065\mathrm{MHz})$, all of the atoms decaying out of state $|\mathrm{f}\rangle$ ends up in the ground state. The excited state decays at the rate $\Gamma_\mathrm{e} = 2\pi(0.66\mathrm{MHz})$; only a fraction (0.65) of the population decaying from $|\mathrm{e}\rangle$ ends up in $|\mathrm{f}\rangle$, the remaining fraction decays to other states not included in our five-level system. The reduced dipole matrix element of the pump transition $d_\mathrm{gf} = 5.177ea_0$ (appendix C), with transition coefficients $c_{m_J} = 1/3$ for the three transitions $\{|-\rangle, |0\rangle, |+\rangle\} \leftrightarrow |\mathrm{f}\rangle$; for the Stokes transition the reduced dipole element and transition coefficient are $d_\mathrm{fe} = 1.262ea_0$ [155] and $c_{m_J} = -\sqrt{3/10}$ (here e is the magnitude of the charge of an electron, a_0 is the Bohr radius). The Gaussian pulses have a full-width at half-maximum (FWHM[6]) $\delta t = 1$ ns, with a 15π area for both components of the pump pulse and the Stokes pulse. The pump is initially linearly polarised at $-\pi/4$ rad to the x-axis, and has a detuning $\Delta_\mathrm{P} = 2\pi(10\ \mathrm{GHz})$ from resonance. We assume two-photon resonance between the Stokes and pump fields, requiring that $\Delta_\mathrm{P} + \Delta_\mathrm{S} = 0$. The Faraday pulse has an area of $10^{-3}\pi$, is initially right-circularly polarised and is 5 GHz detuned from resonance. The medium has an atomic density of $\mathcal{N}_\mathrm{a} = 10^{20}\ \mathrm{m}^{-3}$ (corresponding to a vapour temperature of $\sim 150^\circ$C).

[6]Note this is the FWHM of the electric field envelope, which is related to the FWHM of the intensity profile, Δt, via $\delta t = \Delta t\sqrt{2}$

10.5.2 *Preparation of the medium*

Before simulating the preparation stage of the atom-light interaction, we first examine the effect of quantum interference [156] in the system. The two competing paths to the excited state $|-\rangle \rightarrow |\mathrm{f}\rangle \rightarrow |\mathrm{e}\rangle$ and $|+\rangle \rightarrow |\mathrm{f}\rangle \rightarrow |\mathrm{e}\rangle$ lead to quantum interference: a well-known phenomena in the interaction of multi-state systems with coherent light, see for example the review article [11]. It is instructive to transform the bare-atom set of basis states in to a new set which takes into account the interaction with the light fields. We reformulate the ground state manifold $\{|-\rangle, |0\rangle, |+\rangle\}$ using the Morris-Shore (MS) transformation [157] to $\{|\mathrm{b}\rangle, |0\rangle, |\mathrm{d}\rangle\}$. The new basis states (the so-called dressed-atom states [63])

$$|\mathrm{b}\rangle = \frac{1}{\Omega_{\mathrm{P}}^{*}}(\Omega_{+}^{*}|-\rangle + \Omega_{-}^{*}|+\rangle), \tag{10.20}$$

$$|\mathrm{d}\rangle = \frac{1}{\Omega_{\mathrm{P}}}(\Omega_{-}|-\rangle - \Omega_{+}|+\rangle), \tag{10.21}$$

are, respectively, coupled and uncoupled from the state $|\mathrm{f}\rangle$; the magnetic sublevel $|0\rangle$ remains uncoupled. For simplicity we take the polarisation state of the pump to be fixed throughout the experiment, and thus the dressed states also remain fixed. The Hamiltonian of the transformed system

$$\mathscr{H}'_{\mathrm{RWA}} = -\tfrac{1}{2}\hbar\Big(\Omega_{\mathrm{P}}|\mathrm{f}\rangle\langle\mathrm{b}| + \Omega_{\mathrm{S}}|\mathrm{e}\rangle\langle\mathrm{f}| + 2\Delta_{\mathrm{P}}|\mathrm{f}\rangle\langle\mathrm{f}| + 2(\Delta_{\mathrm{S}} + \Delta_{\mathrm{P}})|\mathrm{e}\rangle\langle\mathrm{e}|\Big) + \mathrm{H.c.}, \tag{10.22}$$

shows that the transition $|\mathrm{b}\rangle \leftrightarrow |\mathrm{f}\rangle$ is mediated by the Rabi angular-frequency $|\Omega_{\mathrm{P}}| = \sqrt{|\Omega_{+}|^2 + |\Omega_{-}|^2}$. This tells us that the atomic state $|\mathrm{b}\rangle$ is associated with the polarisation state of the pump field $\mathbf{E}_{\mathrm{P}}$; similarly, the uncoupled state $|\mathrm{d}\rangle$ is associated with a field orthogonal to $\mathbf{E}_{\mathrm{P}}$, the magnitude of which is zero in the preparation stage. We discuss the implications of this later.

If we begin with an atomic ensemble in a mixed state, the initial ground state density operator in the MS transformed basis is $\hat{\rho}_{\mathrm{initial}} = \frac{1}{3}(|\mathrm{d}\rangle\langle\mathrm{d}| + |0\rangle\langle 0| + |\mathrm{b}\rangle\langle\mathrm{b}|)$, i.e. the three possible states are evenly populated and there is no coherence amongst them. The effect of the preparation fields is to affect a two-photon transition between the states $|\mathrm{b}\rangle$ and $|\mathrm{e}\rangle$. The final ground state density operator is then $\hat{\rho}_{\mathrm{final}} = \frac{1}{3}(|\mathrm{d}\rangle\langle\mathrm{d}| + |0\rangle\langle 0| + \delta|\mathrm{b}\rangle\langle\mathrm{b}|)$, where $\delta \rightarrow 0$ for complete population transfer. Examining the form of the dressed-atom

states in equations 10.20 and 10.21 we see that they are orthogonal and are coherent superpositions of the bare-atom states $|-\rangle$ and $|+\rangle$. Therefore asymmetry in the populations of the dressed states leads to an increase in the coherence of the ground-state subsystem $\{|-\rangle, |+\rangle\}$. The aim of the preparation process is to create a partially coherent ground state and the efficiency of the preparation stage can be parameterised as the degree of coherence $p_{+-} = |\rho_{+-}|/\sqrt{\rho_{++}\rho_{--}}$, which takes a value from zero (an incoherent mixture) to the maximum allowed value of unity (a pure state).

Figure 10.10 shows the results of pulse propagation in the preparation stage. In parts (a)-(d) the field envelopes are plotted. The peak of the Stokes pulse enters the medium at $t = 0$ ns, followed by the pump at $t = 0.6$ ns. This pulse spacing amounts to a time separation of one 1/e width, which is the optimal separation for STIRAP using Gaussian envelope functions [151]. The front of the Stokes pulse is seen to traverse the medium at close to the speed of light without distortion, due to there initially being no population on the Stokes transition. As the pump arrives, the two-photon transition can now be affected, leading to strong coupling of the Stokes and pump fields to each other and to the atoms. Back action on the light distorts the coupled fields as they travel deeper inside the medium. The initial field parameters were chosen based on the naive assumption that the relationship between the envelopes of the two preparation pulses remains (relatively) stable. Unless the atom-light interaction is balanced to maintain the required conditions, the consequence of heavy field distortion is that the STIRAP process is likely disrupted, which is indeed what is seen in figure 10.10(e). Here we show the coherence of the subsystem $\{|+\rangle, |-\rangle\}$. In the first 2 mm the STIRAP process is carried out with high preparation efficiency, and after the beams have gone ($t > 1.5$ ns) the coherent state is of high purity ($p_{+-} > 0.95$). Deeper into the medium, the efficiency is steadily reduced (ignoring the transient 'ridge' which is influenced by pulse distortion). Despite the limited range, STIRAP fares better than preparation via resonant processes (such as inversion via π-pulses). Simulations show that during resonant processes the preparation fields are absorbed in the first few tens of microns inside the medium.

Preparation of a ground-state coherence in optically thick media has been studied previously in reference [153]. There, a non-degenerate lambda system

was used, i.e. the final state $|e\rangle$ is lower in energy than state $|f\rangle$, in which case the Stokes transition is formally a gain resonance. Thus in an optically thick medium where back action on the light is significant, energy is transfered from the pump into the Stokes field; this is in contrast to the results of the cascade system seen in this thesis where both pump and Stokes fields are absorbed.

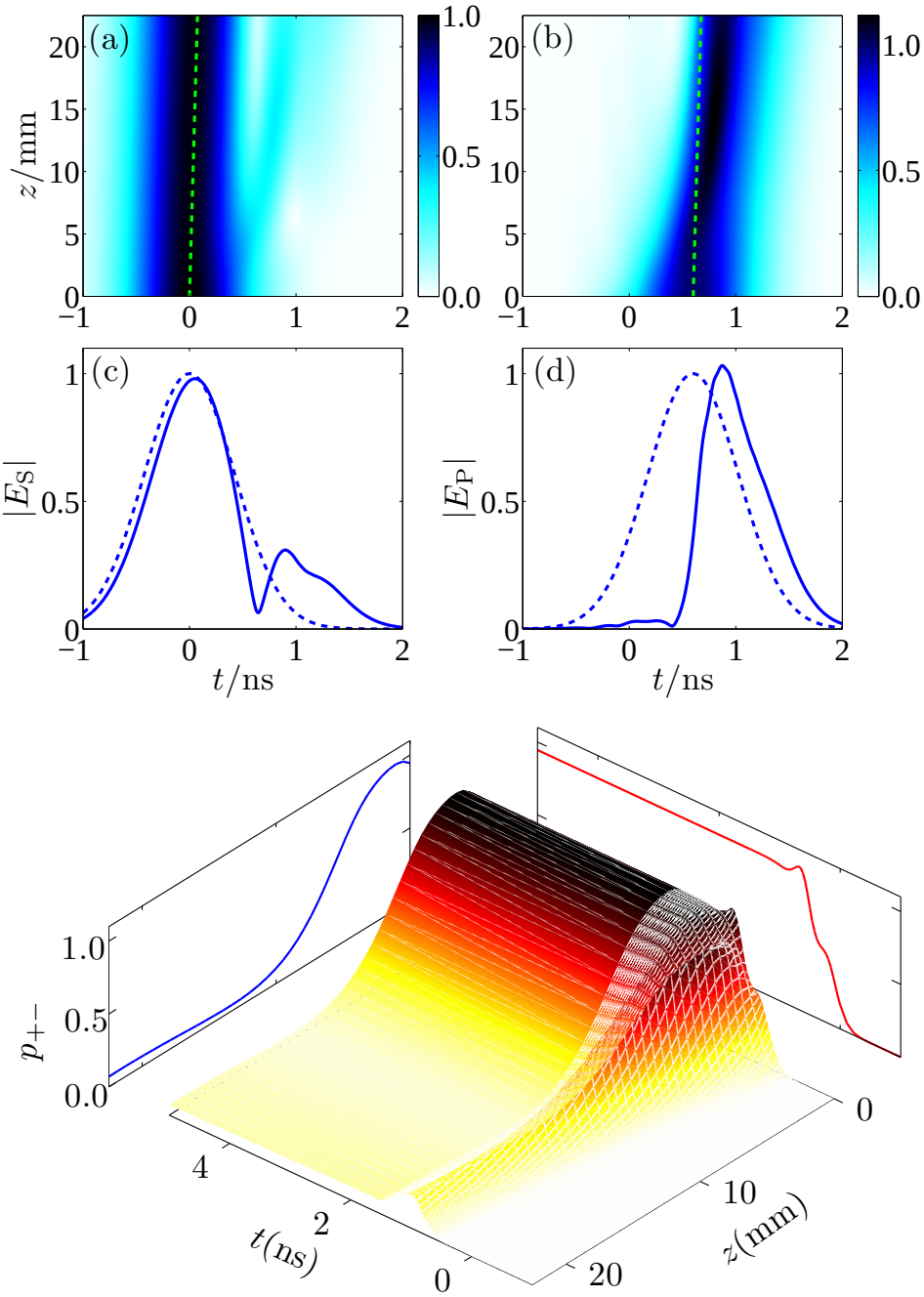

Figure 10.10: Preparation of the medium. The normalised magnitude of (a) the Stokes and (b) the pump electric field envelopes versus time and displacement inside the medium. The dashed green line shows the hypothetical position of the peak if the pulse were propagating at the speed of light *in vacuo*. (c) The Stokes field magnitude versus t, at $z = 0$ (dashed curve) and $z = 22.5$ mm (solid curve); (d) shows the same information for the pump field. (e) The degree of coherence p_{+-} between the ground state sublevels $|-\rangle$ and $|+\rangle$, including its projections at $t = 5$ ns (blue curve) and $z = 0$ mm (red).

10.5.3 *A simple model of polarisation rotation*

After the STIRAP preparation stage we are left with a medium possessing a ground-state subsystem prepared to a high degree of coherence which is stable against decay (we ignore particle-particle interactions such as collisions which may serve to dephase the partially coherent state). The rest of the atomic population is found in the metastable excited state from where it will eventually filter back to the ground state, but only over a timescale longer than the duration of the experiment. To a fair degree of accuracy we can then treat the medium as if it were in a stable state. In the measurement stage, we apply a weak probing field to the medium. We know from chapters 3 and 4 that for a weak enough probe beam the medium is unaffected by the passage of the field, which leaves us free to assume quasi-static conditions.

Working in the frequency domain we have a polarisation density of $\tilde{\mathbf{P}} = \frac{1}{2}\epsilon_0\hat{\chi}\tilde{\mathbf{E}} = \mathcal{N}_\mathrm{a}\langle\tilde{\mathbf{d}}\rangle$, where $\hat{\chi}$ is the susceptibility tensor. We can write the field and expectation value of the dipole operator as column vectors, giving the expression

$$\hat{\chi}\begin{pmatrix}\tilde{E}_+\\ \tilde{E}_-\end{pmatrix} = 2\frac{\mathcal{N}_\mathrm{a}d_0}{\epsilon_0}\begin{pmatrix}\tilde{\rho}^{\mathrm{st}}_{\mathrm{f}-}\\ \tilde{\rho}^{\mathrm{st}}_{\mathrm{f}+}\end{pmatrix}. \tag{10.23}$$

Here the dipole matrix element d_0 is equal to the reduced dipole matrix element d_{gf} multiplied by c_{m_J}, the relative coefficient of the $\{|-\rangle, |+\rangle\} \rightarrow |\mathrm{f}\rangle$ transitions. Note that the magnitude of c_{m_J} is equal for both transtions (due to the symmetry of the electronic wavefunction [100]). The steady-state values of the coherence terms can be derived from the Bloch equations, and are found to be

$$\tilde{\rho}^{\mathrm{st}}_{\mathrm{f}-} = \frac{\mathrm{i}d_0}{2\hbar}\frac{\tilde{E}_+\rho^{\mathrm{st}}_{--} + \tilde{E}_-\tilde{\rho}^{\mathrm{st}}_{+-}}{\Gamma_\mathrm{f}/2 - \mathrm{i}\Delta_\mathrm{F}} \tag{10.24}$$

$$\tilde{\rho}^{\mathrm{st}}_{\mathrm{f}+} = \frac{\mathrm{i}d_0}{2\hbar}\frac{\tilde{E}_+\tilde{\rho}^{\mathrm{st}}_{-+} + \tilde{E}_-\rho^{\mathrm{st}}_{++}}{\Gamma_\mathrm{f}/2 - \mathrm{i}\Delta_\mathrm{F}}, \tag{10.25}$$

assuming that the population of the intermediate state $\rho^{\mathrm{st}}_{\mathrm{ff}} \approx 0$. Substituting these steady-state solutions of the coherence into equation (10.23), we can express the susceptibility tensor as

$$\hat{\chi} = \frac{\mathcal{N}_\mathrm{a}d_0^2}{\hbar\epsilon_0}\frac{\mathrm{i}}{\Gamma_\mathrm{f}/2 - \mathrm{i}\Delta_\mathrm{F}}\begin{pmatrix}\rho^{\mathrm{st}}_{--} & \tilde{\rho}^{\mathrm{st}}_{+-}\\ \tilde{\rho}^{\mathrm{st}}_{-+} & \rho^{\mathrm{st}}_{++}\end{pmatrix}. \tag{10.26}$$

In the absence of a coherence between states $|-\rangle$ and $|+\rangle$, the susceptibility tensor is diagonal and thus the field components $\tilde{E}_-$ and $\tilde{E}_+$ propagate independently of one other. However, in the presence of a coherence this is not the case and there will be interference between the two field components. The normal modes of the field, i.e. the field polarisations that propagate independently of each other, can be found by diagonalising $\hat{\chi}$. However, we noted in section 10.5.2 that during the STIRAP process the polarisation state of the pump field defines the coupled dressed state $|\mathrm{b}\rangle$ (and the orthogonality condition determines the uncoupled state $|\mathrm{d}\rangle$). The fields associated with the states $|\mathrm{b}\rangle$ and $|\mathrm{d}\rangle$ are the normal modes of the medium.

A convenient visual representation of light polarisation is the Poincaré sphere (appendix I). Points in this three-dimensional space correspond to the column vector[7], $\mathbf{S} = (S_1 \; S_2 \; S_3)^{\mathrm{T}}$, the components of which are, respectively, the intensity difference between linearly polarised light in the x and y directions, the intensity difference between linearly polarised light at an angle $+\pi/4$ and $-\pi/4$ rad to the x-axis, and the intensity difference between left and right circularly polarised light. Note that orthogonality is represented by antipodal points. A light field with temporally and spatially varying polarisation is generally described by a surface. The vector/surface is often normalised by the total light intensity, and for fully polarised light each point lies on a sphere of unit radius. The evolution of the polarisation vector is implicit in the Maxwell-Bloch equations, but to aid the interpretation of the numerical solution to theses equations, we note that the torque equation of motion provides a simple analogy of birefringence [79, 158]. The equation describes the spatial evolution of the polarisation vector $\mathbf{S}$ in response to the anisotropy of the medium, represented by the birefringence vector $\mathbf{a}$:

$$\frac{\mathrm{d}\mathbf{S}}{\mathrm{d}z} = \mathbf{a} \times \mathbf{S}. \tag{10.27}$$

The geometric interpretation on the Poincaré sphere is that $\mathbf{a}$ provides the instantaneous rotation axis and rotary power for the evolution of $\mathbf{S}$. Note the limitations of this simple picture, however, in that it assumes monochromatic waves in a time-independent medium with zero losses.

The birefringence vector points in the direction of the preponderance of atoms

[7] Here T denotes the transpose operation.

in the $|\mathrm{d}\rangle$ state. The Stokes parameters of the anisotropy vector can be related to the density matrix elements of the ground-state subsystem via the expression [159]

$$\mathbf{a} = \left(-2\mathrm{Re}\left[\tilde{\rho}^{\mathrm{st}}_{+-}\right] \quad 2\mathrm{Im}\left[\tilde{\rho}^{\mathrm{st}}_{+-}\right] \quad \rho^{\mathrm{st}}_{--} - \rho^{\mathrm{st}}_{++}\right)^{\mathrm{T}}. \tag{10.28}$$

Note the third element in this vector which is due to an imbalance in the populations of the states $|-\rangle$ and $|+\rangle$. This is the cause of the traditional paramagnetic Faraday effect, which is described in chapter 9, and is a manifestation of circular birefringence. If the populations are equal and a ground-state coherence exists, the medium will be linearly birefringent i.e. will respond differently to two orthogonal linearly polarised field components. In the general case the medium is elliptically birefringent.

We compare the results of the numerical simulation and torque equation in the next section.

10.5.4 *Results of polarisation rotation*

In consideration of the complications of the STIRAP process seen in figure 10.10, a 2 mm long medium will be used to ensure a relatively homogeneous sample for the measurement stage. In this stage, the Faraday pulse interacts with the medium after the preparation fields have exited: this is to avoid further coherent field coupling. The pulse is sufficiently weak that it does not perturb the medium as it propagates. As the pulse is detuned far off resonance, it suffers little attenuation/distortion but does experience dispersion, leading to polarisation rotation. Rotation of the Faraday pulse for different medium parameters is seen in figure 10.11. In figure 10.11(a) the medium is prepared under the same conditions as used in figure 10.10. The Faraday pulse is initially right-circularly polarised, having a polarisation vector $(0\ 0\ -1)^{\mathrm{T}}$. As it propagates through the medium it becomes linearly polarised as it crosses the equator of the Poincaré sphere, before becoming left-elliptically polarised. The polarisation rotates anticlockwise around an axis in the $(0\ 1\ 0)^{\mathrm{T}}$ direction, which is to be expected because the medium has population balanced in favour of the state $|\mathrm{d}\rangle$, which is associated with the field polarised at $\pi/4$ rad. However, the pulse doesn't rotate as a single entity, rather the variation of dispersion over its bandwidth leads to differential

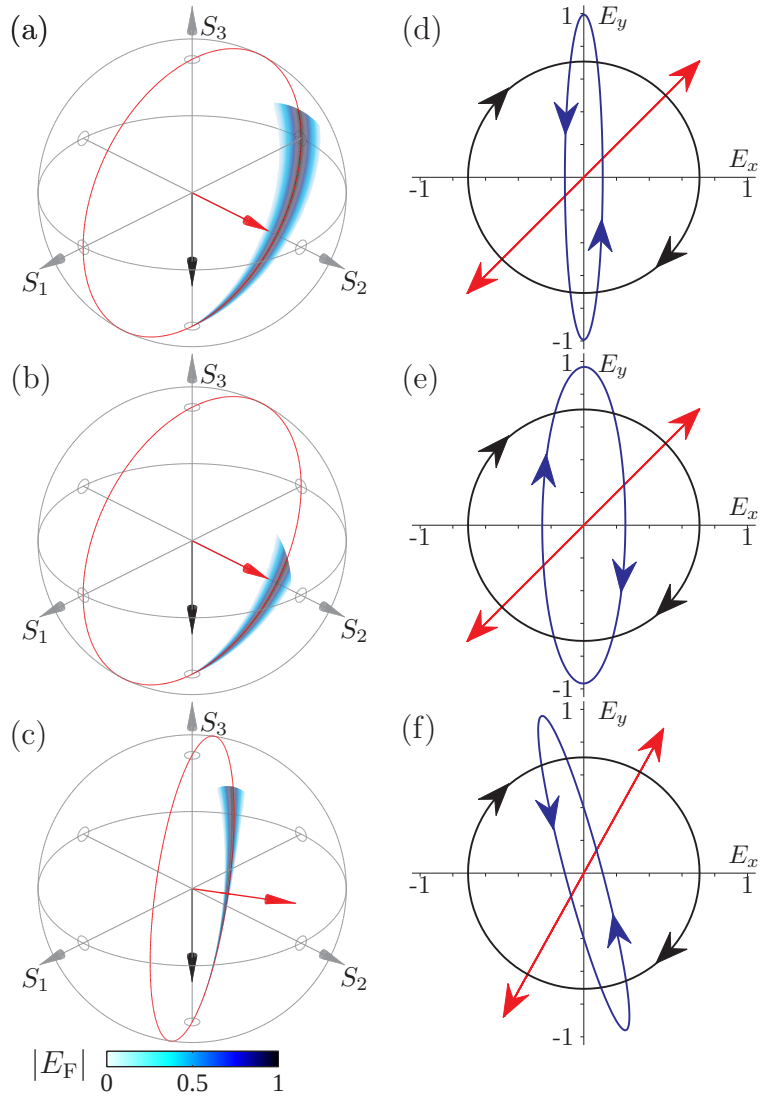

Figure 10.11: Birefringence induced by atomic coherence. (a)-(c) Poincaré sphere representation of the Faraday pulse polarisation state, showing the magnitude of the electric field envelope, $|\tilde{\mathbf{E}}_\mathrm{F}|$, as the surface on a unit sphere. The black arrow represents the initial polarisation state (right-circularly polarised); the red arrow represents the birefringence vector of the medium; the red circle is the path the polarisation state would trace according to the torque model. (d)-(f) polarisation ellipse representation of polarisation, showing the x and y components of $\tilde{\mathbf{E}}_\mathrm{F}$ at the entrance (black circle) and exit (blue ellipse) of the medium. The red line shows one of the normal modes of birefringence. Arrows represent the circulation of the electric field over one optical period.

rotation. Thus for each position inside the medium the Stokes vector varies in time. This manifests itself upon the Poincaré sphere as the spreading out from a single point. Figure 10.11(d) shows the field on the polarisation ellipse. Here the polarisation state corresponding to the peak of the pulse is shown at the entrance and exit of the medium, along with one of the normal modes of the medium (the other mode is orthogonal to this).

We have previously considered the regime in which the ground state is stable against dephasing mechanisms which have the tendency to lessen the degree of coherence of the atomic subsystem we are interested in. To model the effects of dephasing we now add a 27 MHz dephasing term to the master equation (this rate is chosen so as to significantly affect the coherence during the few nanoseconds that is the duration of the simulation). Dephasing causes the sublevel coherence to decay towards an incoherent mixture and thus the rotary power of the birefingent medium decreases with time, though the axis of rotation remains pointing in the same direction of the Poincaré sphere. The Faraday pulse thus rotates to a lesser degree than the case where dephasing mechanisms are ignored, as seen in figure 10.11 parts (b) and (e).

Finally, we consider the effect of an energy difference between the two sublevels involved in the coherence. This simulates an applied magnetic field used in Faraday rotation. The energy difference causes precession of the atomic spin, analogous to the Larmor precession of magnetic moments around an applied magnetic field [160]. The degeneracy of the levels is broken to such an extent that the partially coherent state precesses at a rate of 27 MHz. By the time the Faraday pulse enters the medium, the birefringence vector has rotated to a new direction, as observed in figure 10.11(c) and (f).

10.5.5 *Effect of varying the pump-Stokes pulse separation time*

It is well known that the overlap of the Stokes and pump envelopes plays a part in the efficiency of the STIRAP process [151]. Figure 10.12(a) shows the population transfered to the excited state versus the separation time between the peaks of the incident Stokes and pump pulses. For positive t_{sep}, the Stokes pulse precedes the pump, which is the correct order for adiabatic

population transfer. This can be seen from the trough in figure 10.12(b), where transfer to the intermediate state is at a minimum. Note that due to the pump beam being detuned off resonance, the intermediate state is only transiently populated during the preparation stage. The asymmetry isn't mirrored in figure 10.12(a) because by carrying out the transfer faster than the decay rate we are less harshly punished for going on an excursion to the intermediate state. Figure 10.12(c) shows both the rotation experienced by the peak of the Faraday pulse, and the length of the birefringence vector **a**, the two of which are clearly linked.

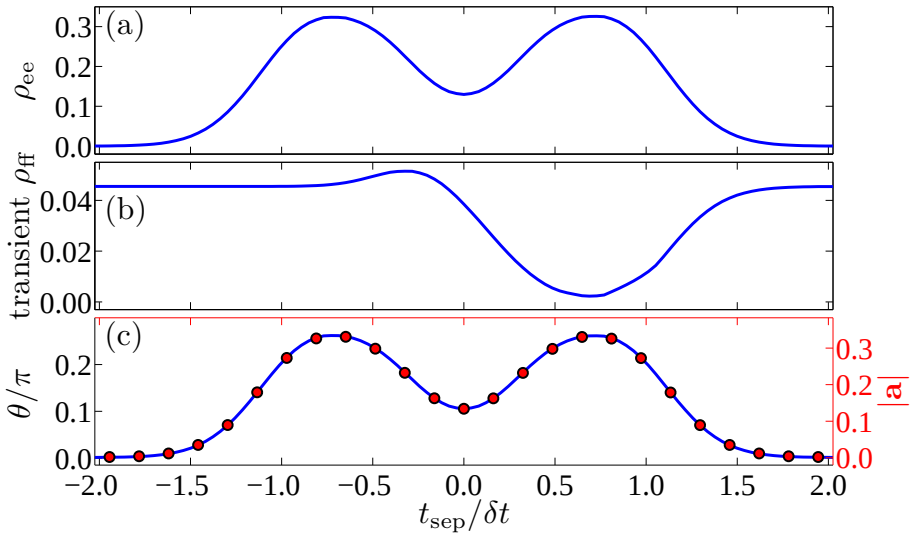

Figure 10.12: Effect of time-separation of the pump & Stokes pulses on the STIRAP process. (a) Population of the excited state upon completion of the preparation stage, shown against the separation time between the Stokes and pump pulses. (b) The maximum population seen in the intermediate state. The asymmetry around $t_{sep} = 0$ and the trough on the positive side is the signature of the STIRAP process. (c) Rotation of the Faraday pulse is show (left axis, solid line), overlaid with the magnitude of the birefringence vector (right axis, data points, the number of which has been reduced for clarity).

10.6 Discussion

We have investigated the nonlinear interactions of short pulses in optically thick media, showing the storage and retrieval of energy. We have demonstrated a theoretical method for the preparation and measurement of a ground-state coherence, using gigahertz bandwidth pulses. With the use of realistic parameters, our method is readily amenable to experimental investigation.

Chapter 11

Conclusions & outlook

Here we provided a brief summary of the work investigated in this thesis, and look to the future of the project. Our main concern throughout this thesis was the comparison of experimental data with theoretical calculations. Our *sine qua non* of the investigation, the rubidium vapour cell, provided both an oft-used ingredient in many atomic experiments, and a system to which a number of gross approximations can be made which nevertheless result in an accurate theoretical representation. A model of the Doppler-broadened spectrum of the Rb D lines was developed which allows the absorption profile and refractive index to be calculated. Excellent agreement was found between theory and experiment. Our model allows quantitative predictions of the absorption and dispersion in alkali metal vapour, both under illumination by continuous-wave and pulsed light.

The Faraday effect and related birefringent phenomena were studied. The rotation of the plane of polarisation was shown to be highly frequency-dependent in hot atomic vapour, and thus of interest to the fields of interferometry and polarimetry. The Faraday rotation angles measured were seen to be many π radians over a frequency range much farther-reaching than the absorptive properties of the medium. The rotation in atomic vapour is temperature, magnetic-field and frequency dependent, therefore the effect can be used as a tunable polarisation switch. Our work has already provided a useful spectroscopic tool with applications in laser frequency stabilisation [133] and as a tunable Faraday dichroic beam splitter [39].

Controlled Faraday rotation of one optical field due to the presence of another was experimentally demonstrated, with high transmission of both beams. One of the as yet unrealised goals of this thesis is the rotation of nanosecond pulsed light by other similarly short-duration control fields. This was shown to be feasible in Doppler-free atomic vapour via theoretical calculations, so it is reasonable to assume that a future experimental investigation will observe such large-bandwidth high-speed phenomena[1].

[1]The assumption of a Doppler-free medium is valid provided that the experiment is carried out with off-resonant light.

Appendix A

The density operator

In quantum mechanics, a particle is described by a wavefunction $|\psi\rangle$ in a orthonormal basis set given by

$$|\psi\rangle = \sum_m a_m |m\rangle, \tag{A.1}$$

with the complex amplitudes a_m following the probability conservation rule $\sum |a_m|^2 = 1$. An equivalent representation of the system is provided by the density matrix picture. The density operator is defined as the projection of the wavefunction on itself:

$$\hat{\rho} = |\psi\rangle\langle\psi| = \sum_{m,n} \rho_{mn} |m\rangle\langle n|, \tag{A.2}$$

where the density operator matrix elements $\rho_{mn} = \langle m|\hat{\rho}|n\rangle$. The diagonal matrix elements $\rho_{mm} = |a_m|^2$, and hence give the probability of the particle occupying a particular state. Conservation of probability requires that $\mathrm{Tr}[\hat{\rho}] = 1$. Consider the expectation value of an operator $\hat{\mathrm{A}}$ for the state $|\psi\rangle = a_\downarrow|\downarrow\rangle + a_\uparrow|\uparrow\rangle$, viz. $\langle\hat{\mathrm{A}}\rangle = |a_\downarrow|^2 A_{\downarrow\downarrow} + |a_\uparrow|^2 A_{\uparrow\uparrow} + 2\mathrm{Re}[a_\downarrow^* a_\uparrow A_{\downarrow\uparrow}]$. The first two terms are the product of the probability of the particle occupying the state in question and the respective expectation value. The third term containing the cross term represents the extent to which the two states can interfere, in the parlance of wave mechanics the degree of coherence. Hence the off-diagonal terms in (A.2) $\rho_{mn} = a_m a_n^*$ are known as the coherence terms. They represent the degree to which the individual probabilities of finding a particle in either the state $|m\rangle$ or $|n\rangle$ are linked. A useful definition

in the density matrix formalism is that the expectation of an operator A is $\langle\hat{\mathrm{A}}\rangle = \mathrm{Tr}[\hat{\rho}\hat{\mathrm{A}}]$.

The advantage of density operator formalism over wavefunction formalism is that it allows one to treat an ensemble of many particles statistically. If the number density of particles in state $|\psi_i\rangle$ is $\mathcal{N}_i$, with the total density of particles $\mathcal{N}_\mathrm{a}$, the density operator of the statistical mixture is

$$\hat{\rho} = \sum_i p_i |\psi_i\rangle\langle\psi_i|, \tag{A.3}$$

where $p_i = \mathcal{N}_i/\mathcal{N}_\mathrm{a}$ is the classical probability of a particle being in the state $|\psi_i\rangle$. If all particles are in the same state, the system is fully determined by a single wavefunction and is said to be in a pure state. Else the system is described as a mixed state, which cannot be represented by a single wavefunction.

Consider the following problem: what is the difference between a pure ensemble represented via the wavefunction $|\psi\rangle = \frac{1}{\sqrt{2}}(|\uparrow\rangle + |\downarrow\rangle)$, in which all atoms are simultaneously half up and half down, and mixed ensemble represented by the density operator $\hat{\rho}_\mathrm{mixed} = \frac{1}{2}(|\uparrow\rangle\langle\uparrow| + |\downarrow\rangle\langle\downarrow|)$, where half the atoms are in the up state and the other half are in the down state? Both have populations $\rho_{\uparrow\uparrow} = \frac{1}{2}$, $\rho_{\downarrow\downarrow} = \frac{1}{2}$, and so in this respect they are indistinguishable. However, by inspecting the ensembles' respective density matrices

$$\hat{\rho}_\mathrm{pure} = \tfrac{1}{2}\begin{pmatrix} 1 & 1 \\ 1 & 1 \end{pmatrix} \qquad \text{and} \qquad \hat{\rho}_\mathrm{mixed} = \tfrac{1}{2}\begin{pmatrix} 1 & 0 \\ 0 & 1 \end{pmatrix},$$

it can be seen that the off-diagonal terms, the coherences, give a means of discriminating between mixed and pure ensembles. The mixed state has zero coherence because there is no relationship between the probability of a particle being found in its up state and the probability of being in its down state.

In general, a mixed ensemble may contain some degree of coherence. A new mixed state can be produced by combining the two ensembles considered above, which has a density operator $\hat{\rho}_\mathrm{new} = \frac{1}{2}(\hat{\rho}_\mathrm{pure} + \hat{\rho}_\mathrm{mixed})$. Here it is assumed that the process doesn't result in any changes of state. The new

density matrix is

$$\hat{\rho}_{\text{new}} = \tfrac{1}{4}\begin{pmatrix} 2 & 1 \\ 1 & 2 \end{pmatrix}$$

which clearly shows a diminished degree of coherence compared to that of the pure ensemble, and is never the less none zero. It is possible to distinguish between the new ensemble and the pure ensemble via the inequality $|\rho_{\downarrow\uparrow}|^2 \leq \rho_{\downarrow\downarrow}\rho_{\uparrow\uparrow}$ (and, equivalently, $\text{Tr}[\hat{\rho}^2] \leq 1$), with the equality holding for a state of maximal coherence i.e. a pure state.

Appendix B

Numerical methods

In order to solve the Maxwell-Bloch equations we need to find a way of representing the coupled atom-light system in such a way that it is amenable to a numerical scheme. The atomic system is represented by the density operator $\hat{\rho}(z,t)$; the electromagnetic system is represented by the envelope of the electric field $\tilde{\mathbf{E}}(z,t)$. We have the set of coupled equations $\partial_t\tilde{\mathbf{E}}(z,t) = g(z,t,\tilde{\mathbf{E}},\partial_z\tilde{\mathbf{E}},\hat{\rho})$ and $\partial_t\hat{\rho}(z,t) = h(z,t,\tilde{\mathbf{E}},\hat{\rho})$. The aim of this appendix is to describe a way of solving first-order partial differential equations of the form $\partial_t f(z,t) = g(z,t,f,\partial_z f)$.

The numerical scheme involves the discretisation of z, t and f, and the finding of approximations to the derivatives $\partial_z f$ and $\partial_t f$. Physically, we can consider an extended medium to be composed of many adjacent slabs of thickness δz (which is large compared to the wavelength of incident radiation in line with the dipole approximation made in section 2.2.2). The Bloch equations (the solutions of which are the matrix elements of the density operator $\hat{\rho}(z,t)$) depend only upon local quantities i.e. values at the slab position z. Therefore each slab evolves independently of each other. However, the electric field contained in the slab depends on the field in the adjacent slabs at $z - \frac{1}{2}\delta z$ and $z + \frac{1}{2}\delta z$, this being evident from the presence of the spatial derivative of the field.

In numerical analysis, a function $f(z,t)$ needs be defined by a finite number of elements along some interval in the variables $z \in [z_0, z_L]$ and $t \in [t_0, t_M]$. This is achieved by discretising the variables z_ℓ, t_m, where ℓ, m are the indices. In

this work the time variable is decomposed into evenly spaced elements with a separation δt, giving $t_m = t_0 + m\delta t$, for $m = 0, 1, 2, \ldots, M$. For reasons that with becomes clear subsequently, the spatial variable is unevenly spaced.

The numerical scheme we utilise is a pseudo-spectral time-domain (PSTD) method [161, 162] which is, in a sentence, a method that uses the spatial frequency spectrum of f at a time t to calculate the function at a later time $t + \delta t$. A function can be approximated by the sum of $L + 1$ basis functions $\phi_\ell(z)$:

$$f(z) \approx \sum_{\ell=0}^{L} F_\ell \phi_\ell(z), \tag{B.1}$$

which of course will ultimately need to be discretised. The coefficients F_ℓ make up the discrete spectrum of the function. Calculating these coefficients is the heart of the pseudo-spectral method. The reason for using this method is that it can be straightforward to evaluate a derivative in the spatial frequency domain if there is a simple relationship between $\phi_\ell(z)$ and $\partial_z \phi_\ell(z)$. As an example, consider the Fourier transform of a function, $\mathcal{F}[f(z)] = F(k)$. This transformation gives the spectrum $F(k)$ of orthogonal sinusoidal basis functions $\mathrm{e}^{\mathrm{i}kz}$ required to reconstruct $f(z)$ in the space domain:

$$F(k) = \frac{1}{\sqrt{2\pi}} \int_{-\infty}^{+\infty} f(z) \mathrm{e}^{-\mathrm{i}kz} \mathrm{d}z, \tag{B.2}$$

$$f(z) = \frac{1}{\sqrt{2\pi}} \int_{-\infty}^{+\infty} F(k) \mathrm{e}^{\mathrm{i}kz} \mathrm{d}k, \tag{B.3}$$

where k is the spatial frequency. Due to the simple relation between the Fourier basis functions and their derivatives (namely $\partial_z \mathrm{e}^{\mathrm{i}kz} = \mathrm{i}k\mathrm{e}^{\mathrm{i}kz}$), the derivative property of the Fourier transform can be defined:

$$\mathcal{F}[f^{(n)}(z)] = (\mathrm{i}k)^n F(k), \tag{B.4}$$

where $f^{(n)}$ denotes the nth spatial derivative of f. Hence a derivative of f is readily calculated by finding its spectrum and then taking the inverse transform of (B.4).

The Fourier transform is the most often used spectral transform, but the related Chebyshev transform is used in this work. The main reason for this is that the Fourier transform is periodic, whereas the domain over which the

spectrum is required to be taken is not. The Chebyshev basis functions are

$$\phi_\ell(\cos\theta) = \cos \ell\theta. \tag{B.5}$$

From this, the relationship with the Fourier transform can be gleaned by noting that the complex exponential of the Fourier transform basis functions can be expressed in terms of sines and cosines. Hence with the co-ordinate transform $z = \cos\theta$ the Chebyshev transform is the Fourier transform containing only cosine functions, in which case the derivative can be dealt with accordingly. This Chebyshev basis functions exist in the interval [-1,1] (which can be scaled so that $z \in [z_0, z_L]$) and the variable θ is discretised as an evenly spaced grid according to $\theta_\ell = \pi\ell/L$, for $\ell = 0, 1, 2, \ldots, L$. Note that this results in an unevenly spaced z_ℓ variable.

The spatial derivatives has been disposed of, leaving the temporal derivative which can, in principle, be solved in exactly the same manner. However, it is more efficient computationally to treat this derivative by time-marching the variable in even steps. The partial derivative of a function $f(z,t)$ with respect to variable t is defined as the limit

$$\partial_t f(z,t) = \lim_{\delta t \to 0} \frac{f(z, t+\delta t) - f(z,t)}{\delta t}. \tag{B.6}$$

It is clear from this definition that the differential is readily amenable to discretisation. The derivative at a time t is proportional to the difference between the function evaluated at this point and a time δt later. By treating δt not as an infinitesimal but as a small, finite quantity, we obtain the finite difference method. At a time $t + \delta t$ the function can be approximated by

$$f^\ell_{m+1} = f^\ell_m + \delta t\, g(z_\ell, t_m, f^\ell_m, \partial_z f^\ell_m). \tag{B.7}$$

Equation (B.7) is known as the explicit forward Euler equation [163], as the function at $t + \delta t$ is determined using expressions at earlier times which have already been calculated. Given $f(z,t)$ and $g(z,t,f,\partial_z f)$ at the time $t = t_0$, it is possibly to calculate $f(z,t)$ at successive times by time-stepping at intervals of δt. It turns out that this simple treatment of the derivative is not used often due to its inaccuracy, the error at each step is proportional to the step size δt. In addition to this error, a global error is accumulated between during each successive iteration [163].

A scheme which is more accurate than the Euler equation described above is the widely used fourth-order Runge-Kutta (RK4) method [163], which accumulates an error proportional to $(\delta t)^4$. It is similar to the explicit forward Euler in that it uses the function and derivative at a point to estimate the function at a later time. However, it averages several of these estimates to reduce errors associated the Euler method. Thus

$$f^{\ell}_{m+1} = f^{\ell}_{m} + \tfrac{1}{6}\delta t(h_1 + 2h_2 + 2h_3 + h_4), \tag{B.8}$$

where

$$h_1 = g(z_\ell, t_m, f^{\ell}_{m}, \partial_z f^{\ell}_{m}), \tag{B.9}$$

$$h_2 = g(z_\ell, t_m + \tfrac{1}{2}\delta t, f^{\ell}_{m} + \tfrac{1}{2}\delta t\, h_1, \partial_z(f^{\ell}_{m} + \tfrac{1}{2}\delta t\, h_1)), \tag{B.10}$$

$$h_3 = g(z_\ell, t_m + \tfrac{1}{2}\delta t, f^{\ell}_{m} + \tfrac{1}{2}\delta t\, h_2, \partial_z(f^{\ell}_{m} + \tfrac{1}{2}\delta t\, h_2)), \tag{B.11}$$

$$h_4 = g(z_\ell, t_m + \delta t, f^{\ell}_{m} + \delta t\, h_3, \partial_z(f^{\ell}_{m} + \delta t\, h_3)). \tag{B.12}$$

The discretisation of the spatial variable onto an unevenly spaced grid in the interval $[z_0, z_L]$ means that spacing around the edges $\delta z \sim \pi^2 \Delta z/4L^2$, whilst towards the centre the grid points are less closely spaced at $\delta z \sim \pi\Delta z/2L$ (here $\Delta z = z_L - z_0$). This implies that the most rapidly varying spatial function that can be represented on the grid is limited by the spacing at the grid centre, the maximum spatial frequency in this case being $k_{\max} = \pi L/\Delta z$. For reasons of numerical stability (see references [161, 162]), it is required that the spacing along the temporal grid is approximately $\delta t < \pi^2\Delta z/4cL^2$ (where c is the speed of light in free-space), hence we have a relation between the indices M and L of

$$M = \frac{4}{\pi^2}\left(\frac{c\Delta t}{\Delta z}\right) L^2, \tag{B.13}$$

where $\Delta t = t_M - t_0 = M\delta t$. The number of points along the temporal grid $M+1$ is thus related to the square of the number of points on the spatial grid $L+1$. From the factor in parentheses, more temporal points are required to solve for a grid such that $\Delta z < c\Delta t$, hence the scheme is computationally more intensive (in terms of memory usage and computation time) in this regime. Physically this means studying the evolution of the Maxwell-Bloch equations for a small length of medium over a long duration is more intensive than the opposite case of a long medium observed over a small timescale.

In summary, we have outlined a numerical scheme which can be used to solve for the coupled evolution of the electric field and density operator, describing possible limits of the scheme including possible sources of uncertainty and computational complexity. This scheme was used extensively to obtain the results found in chapters 2 and 10.

Appendix C

Rubidium atomic & spectroscopic data

Table C.1: Atomic data for (a) ^{85}Rb, and (b) ^{87}Rb.

(a)

Atomic Number	Z	37	[164]
Atomic Mass	M	84.911 789 732 (14) u	[165]
Nuclear Spin	$\mathcal{I}$	5/2	
Relative Natural Abundance	NA	72.17(2)%	[165]
Groundstate Degeneracy	$2(2\mathcal{I}+1)$	12	

(b)

Atomic Number	Z	37	[164]
Atomic Mass	M	86.909 180 520(15) u	[165]
Nuclear Spin	$\mathcal{I}$	3/2	
Relative Natural Abundance	NA	27.83(2)%	[165]
Groundstate Degeneracy	$2(2\mathcal{I}+1)$	8	

Table C.2: Spectroscopic data for (a) D_2, and (b) D_1.

(a)

Wavelength (vacuum)	λ	780.241 368 271(27) nm	[102]
Frequency	ν	384.230 406 373(14) THz	[102]
Decay Rate	Γ	2π(6.066 66(18) MHz)	[103]
Reduced Dipole Matrix Element	d	5.177 ea_0	(4.8)

(b)

Wavelength (vacuum)	λ	794.979 014 933(96) nm	[104]
Frequency	ν	377.107 385 690(46) THz	[104]
Decay Rate	Γ	2π(5.750 0(56) MHz)	[103]
Reduced Dipole Matrix Element	d	5.182 ea_0	(4.8)

Appendix D

Vapour Pressure and Number Density

Naturally occuring rubidium exists in two isotopes: ^{85}Rb (relative atomic mass $M_{85} = 84.911789732(14)\ u$) and ^{87}Rb ($M_{87} = 86.909180520(15)\ u$), with a natural abundances of 72.17(2)% and 27.83(2)% respectively [165]. The vapour pressure (in Torr), p, for solid rubidium is given by the following equation [166]:

$$\log_{10} p = 2.881 + 4.857 - \frac{4215}{T}, \tag{D.1}$$

and for liquid rubidium is given by

$$\log_{10} p = 2.881 + 4.312 - \frac{4040}{T}. \tag{D.2}$$

Using this vapour pressure the number density $\mathcal{N}_\mathrm{a}$ of rubidium atoms can be calculated,

$$\mathcal{N}_\mathrm{a} = \frac{133.323 \times p}{k_\mathrm{B} T}, \tag{D.3}$$

and is plotted in figure D.1. This model is quoted as having an accuracy of better than 5% in a temperature range 298-550 K. The melting point of rubidium is 39.31°C. The factor of 133.323 converts the vapour pressure from Torr to Pa. Since there are two isotopes present in a vapour cell, the number densities need to be calculated separately according to their abundance.

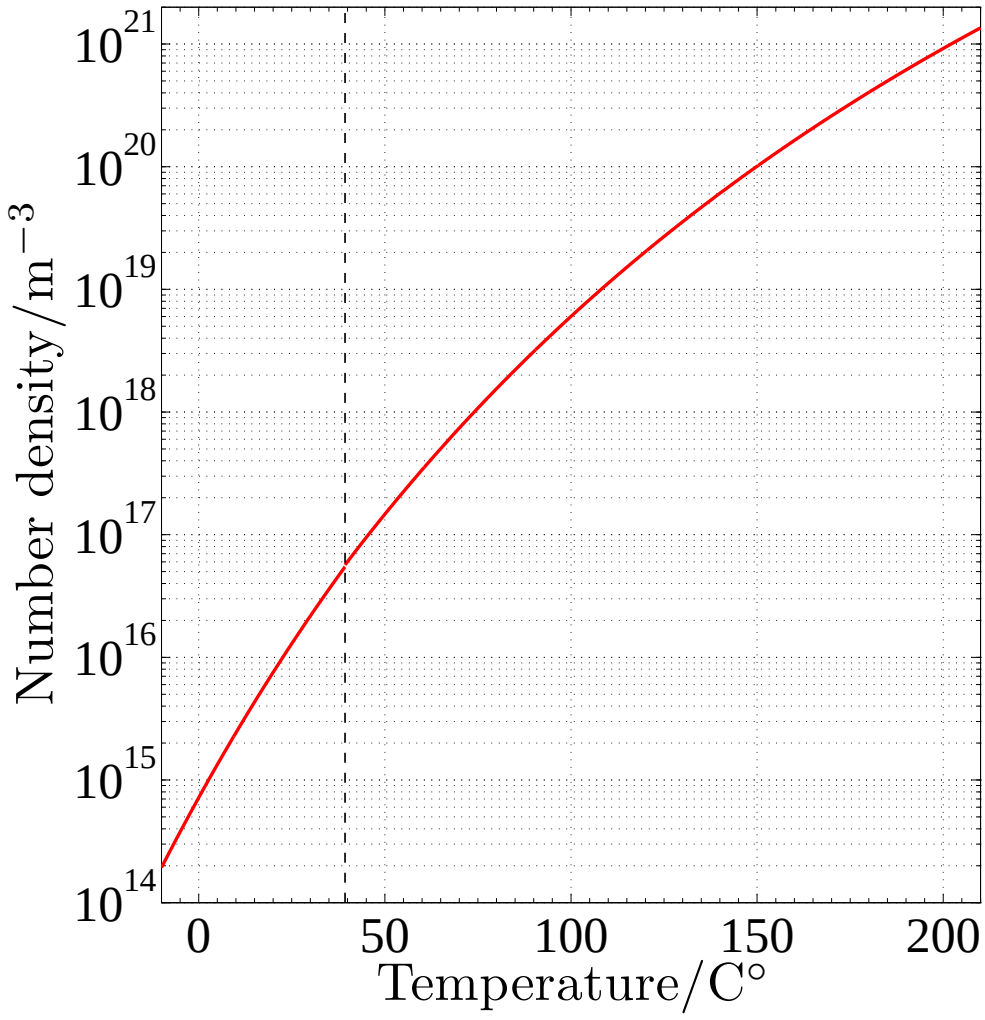

Figure D.1: Rubidium number density versus temperature. The vertical dashed line at 39.31°C marks the transition between solid and liquid phases.

Appendix E

Approximating the Faddeeva function

Here we generalise our analysis of the Faddeeva function by accounting for the ratio of the widths of the Lorentzian and Gaussian functions which comprise the Faddeeva line-shape. The natural broadening mechanism provides a Lorentzian-profiled resonance, of full-width at half-maximum (FWHM) Γ. For a thermal vapour with a Maxwell-Boltzmann distribution of atomic velocities, the Doppler effect leads to an additional broadening line-shape in the form of a Gaussian profile with a FWHM of $\Delta\omega_{\mathrm{D}}$. For alkali metals, $\Gamma/2\pi$ is 10^0 to 10^1 MHz, and for temperatures in the region of 20 to 200°C $\Delta\omega_{\mathrm{D}}/2\pi$ is 10^2 to 10^3 MHz (see reference [7]). Thus $\Gamma/\Delta\omega_{\mathrm{D}} \sim 10^{-2}$ in the experiments performed in this thesis. However, mechanisms exist which can be used to alter this ration by several orders of magnitude. The Doppler width can be reduced by cooling to extremely low temperatures [4–6], essentially nullifying the atomic motion responsible for the Doppler effect. Additional, Lorentzian-like broadening mechanisms can increase γ such as dipole-dipole interactions and collisions [91].

Both the Faddeeva and complex Lorenztian functions are functions of the complex variable $z = 2\sqrt{\ln 2}\,[(\Gamma/2\Delta\omega_{\mathrm{D}}) - \mathrm{i}\,(\Delta/\Delta\omega_{\mathrm{D}})]$, hence in the complex plane

$$\text{Relative difference} = \left| \frac{\text{Faddeeva} - \text{Approximation}}{\text{Faddeeva}} \right|, \tag{E.1}$$

where we have taken the modulus so that it can be displayed on a logarithmic scale.

Figure E.1 shows the relative difference between the Faddeeva function and its approximations. Figure E.1(a) and (b) are, respectively, the relative difference for the real and imaginary parts of the Lorentzian; Figure E.1(c) and (d) are the same quantities for the Gaussian function. From inspection of the colour scale, red denotes a relative difference of >1 (the values plotted have been capped at just above 1 for clarity), thus representing regions of poor approximation. Yellow denotes values from roughly 0.07 to 0.11, demarcating regions of fair approximation, whilst errors of <0.05 are seen from green to white. Thus the Lorentzian approximation is excellent many Doppler widths from resonance or when it dominates the Faddeeva function, i.e., for $|z| \gg 1$. The Gaussian approximation is preferable close to resonance so long as the Lorentzian width is comparatively small. Note the real part of either is a good estimate sufficiently far from resonance. By multiplying the relative difference for the Lorentzian and Gaussian approximations together, we have a rough guide to the regions in which neither of the approximations are adequate, as shown in Figure E.2.

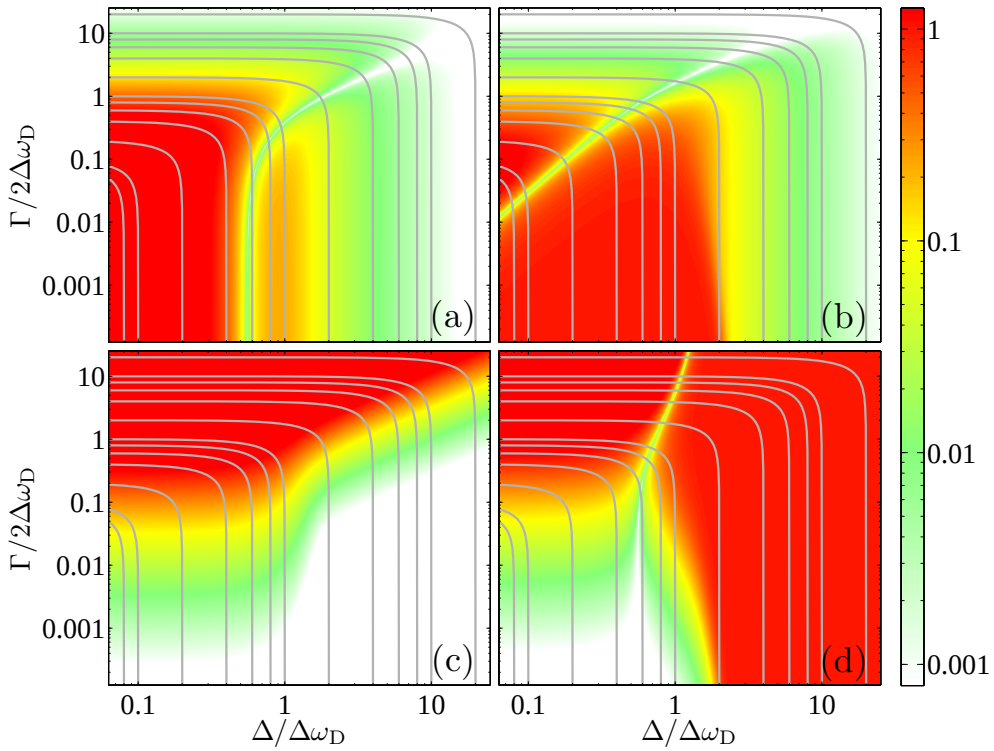

Figure E.1: Relative difference of the Faddeeva function and its approximations, shown versus detuning Δ and Lorentzian HWHM $\Gamma/2$ scaled by the Doppler width $\Delta\omega_{\mathrm{D}}$. Comparison to the Lorentzian approximation's real and imaginary components are shown in (a) and (b) respectively; comparison to the Gaussian approximation's real and imaginary components are shown in (c) and (d). The grid-lines are concentric circles of constant $|z|$ (appearing square due to the logarithmic scale used on both axes).

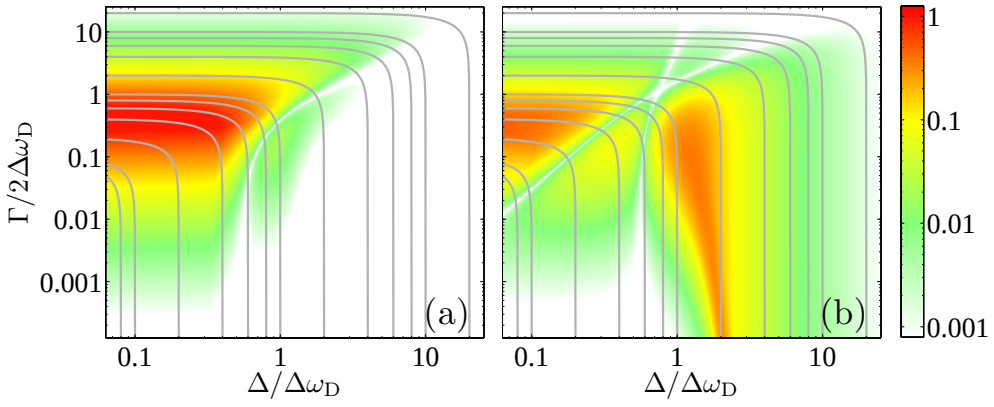

Figure E.2: The region over which either of the Lorentzian or Gaussian approximations leads to a good estimate of the Faddeeva function, for (a) the real and (b) the imaginary component.

Appendix F

Vector bases & polarisation states of plane waves

Various algebraic basis are used in this thesis, in reference to the vectorial nature of light polarisation, in addition to properties such as spin and polarisation density associated with atomic media. In line with the rest of this thesis, we treat the light as a classical plane wave (see for example references [62, 77]). An electromagnetic plane wave has an electric field vector $\mathbf{E}$ confined to infinite parallel planes, orthogonal to the direction in which the field propagates. Hence the polarisation can be described by two orthogonal vectors such that $\boldsymbol{\epsilon}_1 \times \boldsymbol{\epsilon}_2 = \hat{\mathbf{k}}$, where $\hat{\mathbf{k}}$ is a unit vector in the direction of propagation. Making the slowly-varying envelope approximation (see chapter 2), the electric field is the real part of the product of an envelope, $\tilde{\mathbf{E}}$, and a scalar carrier wave, E_c. In terms of unit vectors, the envelope is given by

$$\tilde{\mathbf{E}} = \tilde{E}_1\boldsymbol{\epsilon}_1 + \tilde{E}_2\boldsymbol{\epsilon}_2 = |\tilde{E}|\boldsymbol{\epsilon} \tag{F.1}$$

$$\boldsymbol{\epsilon} = \cos(\theta_0)\mathrm{e}^{\mathrm{i}\phi_1}\boldsymbol{\epsilon}_1 + \sin(\theta_0)\mathrm{e}^{\mathrm{i}\phi_2}\boldsymbol{\epsilon}_2. \tag{F.2}$$

Here, $\boldsymbol{\epsilon}$ is a unit vector in the direction of the electric field, the relative amounts of its two components expressed by the angle $\theta_0 = \arctan(|\tilde{\mathrm{E}}_2|/|\tilde{\mathrm{E}}_1|)$. The phase of each component, ϕ_1 and ϕ_2, allows for the fact that the envelope is, in general, complex. The carrier wave varies sinusoidally in time and space. The implication of a complex envelope is that the electric field generally oscillates out of phase with the carrier. As for a phase difference between the vectorial component of the envelope, this implies that the component are

oscillating out of phase with one another.

Table F.1: Vectorial bases.

system	*basis*	$\boldsymbol{\epsilon}_1$	$\boldsymbol{\epsilon}_2$	$\boldsymbol{\epsilon}_3$
optical	linear	$\boldsymbol{\epsilon}_{\mathrm{H}}$	$\boldsymbol{\epsilon}_{\mathrm{V}}$	$\hat{\mathbf{k}}$
	rotated linear	$\boldsymbol{\epsilon}_{+\frac{\pi}{4}}$	$\boldsymbol{\epsilon}_{-\frac{\pi}{4}}$	$\hat{\mathbf{k}}$
	circular	$\boldsymbol{\epsilon}_{\mathrm{L}}$	$\boldsymbol{\epsilon}_{\mathrm{R}}$	$\hat{\mathbf{k}}$
	helical	$\boldsymbol{\epsilon}_{+}$	$\boldsymbol{\epsilon}_{-}$	$\hat{\mathbf{k}}$
atomic	spin	$\boldsymbol{\epsilon}_{+}$	$\boldsymbol{\epsilon}_{-}$	$\boldsymbol{\epsilon}_0$
common	local	$\boldsymbol{\epsilon}_x$	$\boldsymbol{\epsilon}_y$	$\boldsymbol{\epsilon}_z$

A table of bases used in this thesis is provided in table F.1. A basis in the optical system refers to a two-state plane-wave basis used to describe the light polarisation (bearing in mind that for a plane wave there is no electric field component in the direction of propagation). The linear basis has components in the horizontal (H) and vertical (V) planes. The rotated linear basis has components at $+\pi/4$ and $-\pi/4$ rad to the horizontal plane. The circular basis has basis vectors which rotate (as a function of time) around the direction of propagation. By convention [77], a left (L) polarised wave rotates anticlockwise around the axis, looking towards the source; a right (R) polarised wave rotates clockwise. In addition to linear momentum, related to the wavevector $\mathbf{k}$, plane waves have associated angular momentum. This is represented in the helical basis, which has angular momentum parallel (+) and antiparallel (−) to the direction of propagation[1]. The atomic system refers to bases associated with atomic quantities e.g. projection of quantum numbers, polarisation density, electric dipole vector etc. The spin basis has as its basis vectors the projection of spin parallel (+), antiparallel (−), and orthogonal (0) to the quantisation axis. The direction of the local magnetic field is the natural choice of quantisation axis (the projection quantum numbers are defined relative to a magnetic field, and as such choosing the quantisation axis to be parallel to the field makes the maths easier). In the absence of a magnetic field, any arbitrary direction can be taken as the

[1]The helical basis is formally equivalent to the circular basis, i.e. $\boldsymbol{\epsilon}_{\mathrm{L}} \equiv \boldsymbol{\epsilon}_{+}$, $\boldsymbol{\epsilon}_{\mathrm{R}} \equiv \boldsymbol{\epsilon}_{-}$ but unambiguously provides the sign of the angular momentum carried by the wave.

quantisation axis as the system is degenerate. The system common to both light and atoms is a local, linear basis using the cartesian basis vectors x, y and z. Typically the z-direction is chosen to coincide with the quantisation axis of the atomic system.

Given that both optical and atomic systems are described in terms of their own bases which are characterised by a propagation direction and quantisation axis, respectively, it is important that we use the correct basis for each separate atom-light interaction. For example, left circularly polarised light can stimulate both σ^+ and σ^- transitions, depending on the relative orientation of the light propagation direction and atomic quantisation axis [137]. This is clear if we remember that a $\sigma^\pm$ transition is characterised by a transfer of ± 1 unit of angular momentum (measured in units of $\hbar$) *along the direction of the quantisation*, and that left circularly polarised light has $+1$ unit of angular momentum *in the direction of propagation*.

In order to transform between linear and circular optical bases, apply the following transformation:

$$\begin{pmatrix} \tilde{E}_\mathrm{L} \\ \tilde{E}_\mathrm{R} \end{pmatrix} = \frac{1}{\sqrt{2}} \begin{pmatrix} -1 & \mathrm{i} \\ 1 & \mathrm{i} \end{pmatrix} \begin{pmatrix} \tilde{E}_\mathrm{H} \\ \tilde{E}_\mathrm{V} \end{pmatrix}, \tag{F.3}$$

$$\begin{pmatrix} \tilde{E}_\mathrm{H} \\ \tilde{E}_\mathrm{V} \end{pmatrix} = \frac{1}{\sqrt{2}} \begin{pmatrix} 1 & -1 \\ 1 & 1 \end{pmatrix} \begin{pmatrix} \tilde{E}_{+\frac{\pi}{4}} \\ \tilde{E}_{-\frac{\pi}{4}} \end{pmatrix}, \tag{F.4}$$

$$\begin{pmatrix} \tilde{E}_{+\frac{\pi}{4}} \\ \tilde{E}_{-\frac{\pi}{4}} \end{pmatrix} = \frac{1}{\sqrt{2}} \begin{pmatrix} \mathrm{e}^{-\mathrm{i}\frac{3\pi}{4}} & \mathrm{e}^{-\mathrm{i}\frac{\pi}{4}} \\ \mathrm{e}^{-\mathrm{i}\frac{\pi}{4}} & \mathrm{e}^{-\mathrm{i}\frac{3\pi}{4}} \end{pmatrix} \begin{pmatrix} \tilde{E}_\mathrm{L} \\ \tilde{E}_\mathrm{R} \end{pmatrix}. \tag{F.5}$$

Bearing in mind the circular basis vectors are complex, take note that $\boldsymbol{\epsilon}_\mathrm{L} \cdot \boldsymbol{\epsilon}_\mathrm{L}^* = 1$ and $\boldsymbol{\epsilon}_\mathrm{L} \cdot \boldsymbol{\epsilon}_\mathrm{R}^* = 0$. Transforming between circular and helical bases is straightforward: $\boldsymbol{\epsilon}_\mathrm{L} \to \boldsymbol{\epsilon}_+$, $\boldsymbol{\epsilon}_\mathrm{R} \to \boldsymbol{\epsilon}_-$.

Appendix G

Circularly anisotropic media

A circularly anisotropic medium interacts with light via the circularly-polarised components of the electromagnetic field. Here we work in the local coordinate system (see appendix F), with the quantisation axis in the z-direction. Thus a field linearly polarised at an angle θ_0 to the x-axis can be described by the components $\tilde{E}_{x_0} = \tilde{E}_0 \cos(\theta_0)$ and $\tilde{E}_{y_0} = \tilde{E}_0 \sin(\theta_0)$. After propagation through a medium of length L, the helical components $\tilde{E}_+$ and $\tilde{E}_-$ experience a phase shift of $\phi^\pm = k_0 n^\pm L$ and transmission $\mathrm{e}^{-\frac{1}{2}\alpha^\pm L}$, where n^i (α^i) is the refractive index (absorption coefficient) of the particular transition, and k_0 is the free-space wavevector. We are working towards the Stokes parameters of the system (see appendix I), so we use the transformations given in appendix F to find the output electric field in the three relevant bases, which are:

$$\begin{pmatrix} \tilde{E}_+ \\ \tilde{E}_- \end{pmatrix} = \frac{\tilde{E}_0}{\sqrt{2}} \begin{pmatrix} -\mathrm{e}^{\mathrm{i}(\phi^+ - \theta_0) - \frac{1}{2}\alpha^+ L} \\ \mathrm{e}^{\mathrm{i}(\phi^- + \theta_0) - \frac{1}{2}\alpha^- L} \end{pmatrix}, \tag{G.1}$$

$$\begin{pmatrix} \tilde{E}_x \\ \tilde{E}_y \end{pmatrix} = \frac{\tilde{E}_0}{2} \begin{pmatrix} \mathrm{e}^{\mathrm{i}(\phi^+ - \theta_0) - \frac{1}{2}\alpha^+ L} + \mathrm{e}^{\mathrm{i}(\phi^- + \theta_0) - \frac{1}{2}\alpha^- L} \\ \mathrm{e}^{\mathrm{i}(\phi^+ - \theta_0 + \frac{\pi}{2}) - \frac{1}{2}\alpha^+ L} - \mathrm{e}^{\mathrm{i}(\phi^- + \theta_0 + \frac{\pi}{2}) - \frac{1}{2}\alpha^- L} \end{pmatrix}, \tag{G.2}$$

$$\begin{pmatrix} \tilde{E}_{+\frac{\pi}{4}} \\ \tilde{E}_{-\frac{\pi}{4}} \end{pmatrix} = \frac{\tilde{E}_0}{2} \begin{pmatrix} -\mathrm{e}^{\mathrm{i}(\phi^+ - \theta_0 - \frac{3\pi}{4}) - \frac{1}{2}\alpha^+ L} + \mathrm{e}^{\mathrm{i}(\phi^- + \theta_0 - \frac{\pi}{4}) - \frac{1}{2}\alpha^- L} \\ -\mathrm{e}^{\mathrm{i}(\phi^+ - \theta_0 - \frac{\pi}{4}) - \frac{1}{2}\alpha^+ L} + \mathrm{e}^{\mathrm{i}(\phi^- + \theta_0 - \frac{3\pi}{4}) - \frac{1}{2}\alpha^- L} \end{pmatrix}. \tag{G.3}$$

Using the definition of the intensity $I = \frac{1}{2}c\epsilon_0|\tilde{E}|^2$, the output intensities are

$$\begin{pmatrix} I_+ \\ I_- \end{pmatrix} = \frac{I_0}{2}\begin{pmatrix} \mathrm{e}^{-\alpha^+ L} \\ \mathrm{e}^{-\alpha^- L} \end{pmatrix}, \tag{G.4}$$

$$\begin{pmatrix} I_x \\ I_y \end{pmatrix} = \frac{I_0}{4}\begin{pmatrix} \mathrm{e}^{-\alpha^+ L} + \mathrm{e}^{-\alpha^- L} + 2\cos(2\varphi)\mathrm{e}^{-\frac{1}{2}(\alpha^+ + \alpha^-)L} \\ \mathrm{e}^{-\alpha^+ L} + \mathrm{e}^{-\alpha^- L} - 2\cos(2\varphi)\mathrm{e}^{-\frac{1}{2}(\alpha^+ + \alpha^-)L} \end{pmatrix}, \tag{G.5}$$

$$\begin{pmatrix} I_{+\frac{\pi}{4}} \\ I_{-\frac{\pi}{4}} \end{pmatrix} = \frac{I_0}{4}\begin{pmatrix} \mathrm{e}^{-\alpha^+ L} + \mathrm{e}^{-\alpha^- L} + 2\sin(2\varphi)\mathrm{e}^{-\frac{1}{2}(\alpha^+ + \alpha^-)L} \\ \mathrm{e}^{-\alpha^+ L} + \mathrm{e}^{-\alpha^- L} - 2\sin(2\varphi)\mathrm{e}^{-\frac{1}{2}(\alpha^+ + \alpha^-)L} \end{pmatrix}. \tag{G.6}$$

Hence we arrive at the Stokes parameters of the transmitted light:

$$S_0 = I_+ + I_- \quad = I_0\tfrac{1}{2}(\mathrm{e}^{-\alpha^+ L} + \mathrm{e}^{-\alpha^- L}), \tag{G.7}$$

$$S_1 = I_x - I_y \quad = I_0\cos(2\varphi)\mathrm{e}^{-\frac{1}{2}(\alpha^+ + \alpha^-)L}, \tag{G.8}$$

$$S_2 = I_{+\frac{\pi}{4}} - I_{-\frac{\pi}{4}} = I_0\sin(2\varphi)\mathrm{e}^{-\frac{1}{2}(\alpha^+ + \alpha^-)L}, \tag{G.9}$$

$$S_3 = I_+ - I_- \quad = I_0\tfrac{1}{2}(\mathrm{e}^{-\alpha^+ L} - \mathrm{e}^{-\alpha^- L}), \tag{G.10}$$

Here the light is assumed to be completely polarised (hence the total intensity S_0 can be taken to be the sum of the intensity components in any of the three bases) with initial intensity $I_0 = \frac{1}{2}c\epsilon_0|\tilde{E}_0|^2$. The angle $\varphi = \frac{1}{2}(\phi^- - \phi^+) + \theta_0 = \theta + \theta_0$ is the angle at which the plain of polarisation of the light is rotated with respect to the x-axis. For balanced polarimetry our convention is to take the initial rotation angle θ_0 equal to $-\pi/4$ rad, such that $S_1 \to 0$ when $\theta \to 0$.

Figure G.1(a) shows the Stokes parameters calculated for a Doppler-broadened medium of hot ^{87}Rb atoms in a magnetic field. Far from resonance absorption and dispersion are negligible. As the light comes closer to resonance dispersion is the dominant interaction mechanism, leading to birefringence. S_1 and S_2 begin to vary. At around 2.3 Doppler line-widths from resonance absorption begins to increase. Dichroism also starts to express itself here resulting in a change in S_3, the Stokes parameter sensitive to dichroism, which peaks around 1.8 Doppler widths. From figure G.1(b), which shows the absorption coefficients of the interaction, it is clear that the σ^+ transition is at a higher red-detuning than the σ^- transition. Thus the circular component of positive helicity is almost completely absorbed 1.6 Doppler widths from resonance. S_1 and S_2 cease to vary as there is little

linear characteristic to the polarisation. The medium is optically thick to both polarisations around one Doppler width from resonance.

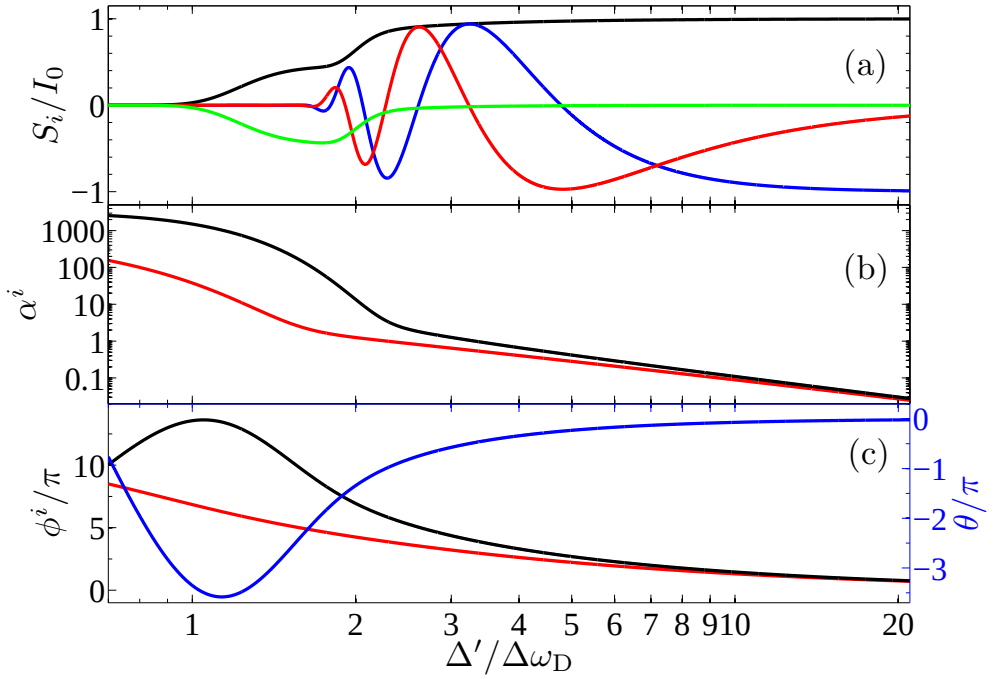

Figure G.1: (a) Theoretical Stokes parameters for a typical experimental, showing S_0 (black curve), S_1 (red), S_2 (blue), S_3 (green). (b) The absorption coefficients α^- (red) and α^+ (black). (c) The rotation due to birefringence θ (blue), along with phases ϕ^- (red) and ϕ^+ (black). The 75 mm long medium contains ^{87}Rb atoms at a temperature of 100°C, subjected to a 200 G magnetic field. Red detuning Δ' from the D_1 ^{87}Rb $F_g = 2 \rightarrow F_e = 1$ transition is in units of the Doppler width $\Delta\omega_D = 2\pi(560)$ MHz.

Figure G.1(c) shows the birefringence-induced rotation experienced by the incident light, which is proportional to the difference between the phase shifts experienced by the individual helical components. A measurement of the rotation angle which is independent of dichroism can be made via the ratio $S_2/S_1 = \tan(2\varphi)$, requiring the simultaneous measurement of the x- and y-components along with the $+\pi/4$- and $-\pi/4$-components. This can be achieved by first splitting the beam with a polarisation-conserving optical device. One of the output beams is sent through a polarisation beam splitter, separating the x- and y-components which are then sent to the two ports of a differencing photodiobe. The other output beam is sent through a half-wave plate followed by a polarisation beam splitter. This creates the necessary

$\pi/4$ rad rotation required to separate the $+\pi/4$- and $-\pi/4$-components. In practice, however, noise will be introduced at each optical element, adding to the experimental uncertainty of the rotation angle. In this thesis we choose to present S_1 (which is referred to throughout as the differencing signal) as it conveys both the birefringent and dichroic characteristics of the medium. The rotation angle is extracted from this signal by looking at the zero crossings and extrema, whose positions are independent of the magnitude of the measured signals.

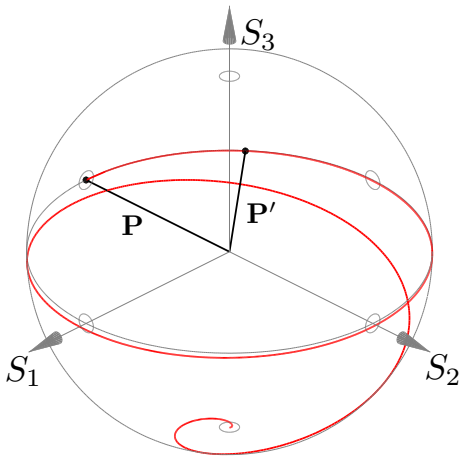

Figure G.2: Poincaré representation of the light polarisation. The initial polarisation $\mathbf{P} = (0, -1, 0)$ follows the red path as the light comes into resonance.

Figure G.2 considers the same situation seen in figure G.1, this time in the Poincaré representation (for which see appendix I). We have normalised the Poincaré vector to emphasise the rotation and ellipticity angles, losing information about the total transmission in the process. $\mathbf{P}$ shows the initial polarisation state, namely linearly-polarised at an angle $-\pi/4$ rad to the horizontal. As the light comes into resonance its polarisation initially remains linear whilst experiencing rotation (vector $\mathbf{P}'$). Closer to resonance the light becomes highly elliptical, becoming almost purely circularly polarised (with negative helicity) before being completely absorbed by the medium.

Appendix H

Optical pumping of D-line transmission spectroscopy

Here we present companion plots to figure 9.3, where we investigate pump-probe spectroscopy of the D line in a 99% ^{87}Rb vapour cell. We restrict ourselves to pump and probe transitions from the $5S_{1/2}$ $F_g = 2$ ground state. In figure H.1 we show the transmission difference of the D_1 probe, the frequency range is such that it encompases transitions to the $5P_{1/2}$ $F_e = 1$ and 2 states separated by 812 MHz. Both of these transitions contain a substructure of three spikes due to optical pumping by the D_2 control beam. These are (from left to right) transitions to the $5P_{3/2}$ $F_e = 1, 2$ and 3 states, having spacings of 157 MHz and 267 MHz, respectively. The effect of changing the detuning of the control beam is seen in figure H.2.

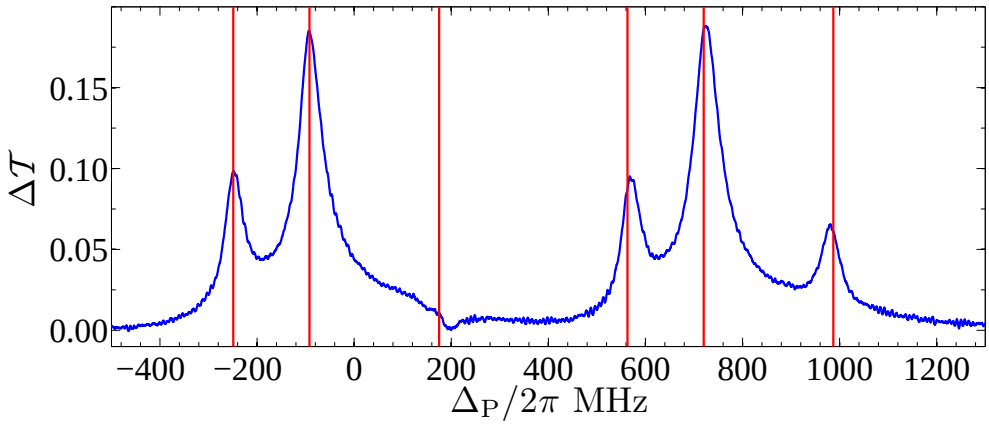

Figure H.1: Change in transmission $\Delta\mathcal{T}$ of a probe beam in the presence of an intense control beam, shown versus probe detuning Δ_P from the D_1 $F_g = 2 \rightarrow F_e = 1$ transition. Vertical lines show the expected positions of the D_2 transitions (see text). For experimental parameters see chapter 9.

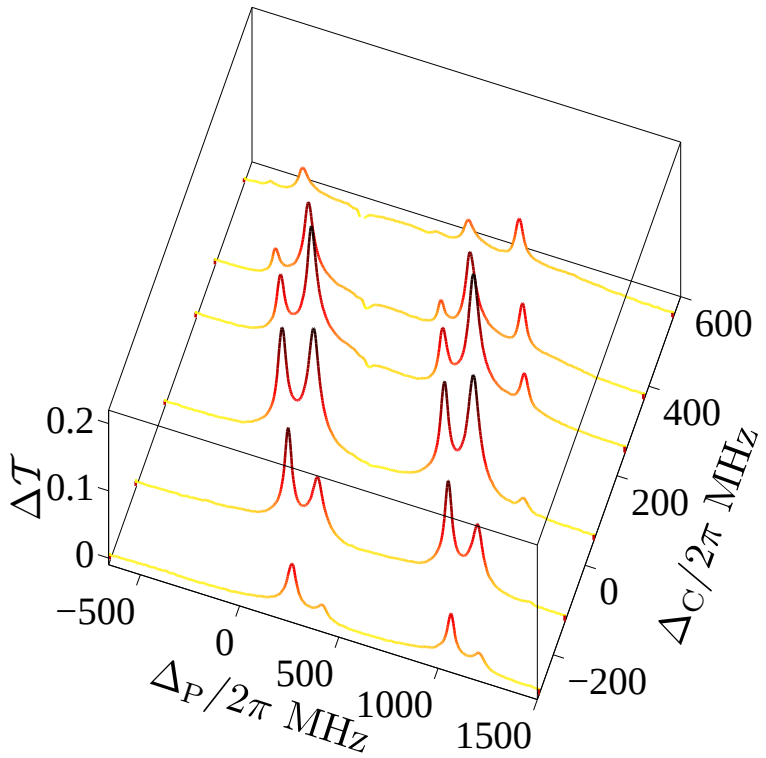

Figure H.2: Change in transmission versus probe detuning Δ_P from the D_1 $F_g = 2 \rightarrow F_e = 1$ transition and control detuning Δ_C from the D_2 $F_g = 2 \rightarrow F_e = 1$ transition.

Appendix I

Stokes parameters & Poincaré representation

The polarisation state of light can be fully represented via the Stokes parameters (after George Stokes, 1852 [167]), which are based on combinations of the intensities of various polarisation components. As the intensity is an observable quantity, they are readily measured [168]. The Stokes parameters are

S_0;	total intensity of the light field,
$S_1 = I_{\mathrm{H}} - I_{\mathrm{V}}$;	intensity difference between linearly polarised light in the horizontal and vertical directions,
$S_2 = I_{+\frac{\pi}{4}} - I_{-\frac{\pi}{4}}$;	intensity difference between linearly polarised light at an angle $+\pi/4$ rad and $-\pi/4$ rad to the horizontal axis,
$S_3 = I_{\mathrm{L}} - I_{\mathrm{R}}$;	intensity difference between left- and right-circularly polarised light.

The total intensity of light reaching the detector, S_0, includes both polarised and unpolarised light. Since we are only interested in the polarised light, we define the Poincaré vector $\mathbf{P} = (S_1, S_2, S_3)$, the magnitude of which is the total intensity of polarised light. Conveniently this vector can be represented in three-dimensional space, as shown in figure I.1, where we present a general normalised Poincaré vector $(\sin 2\vartheta \cos 2\varphi, \sin 2\vartheta \sin 2\varphi, \cos 2\vartheta)$. When normalised like this, the vector connects the origin to a point on what is known as the Poincaré sphere. The angle ϑ is a measure of the ellipticity and chirality of the polarisation: the north ($\vartheta = 0$) and south ($\vartheta = \pi/2$) poles denote left- and right-circularly polarised light, respectively, whilst the

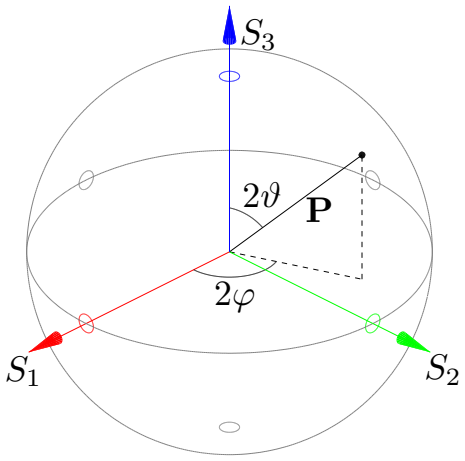

Figure I.1: Illustration of the Poincaré sphere

equator ($\vartheta = \pi/4$) denotes linear polarisation. Between these values the light is elliptically polarised with the chirality of the hemisphere it resides in. φ denotes the angle between the major axis of the ellipse and the horizontal axis; for linearly polarised light this is simply the rotation angle. Note that in this vector space orthogonality is represented by antipodal points, i.e., $\mathbf{P}$ is orthogonal to $-\mathbf{P}$.

Bibliography

[1] R. Loudon, *The Quantum Theory of Light*, 3rd ed. (Oxford University Press, 2000). 1, 12, 22, 53, 57

[2] L. Allen and J. H. Eberly, *Optical Resonance and Two-Level Atoms* (Wiley, 1975). 2, 11, 22, 23, 124

[3] P. R. Berman and V. S. Malinovsky, *Principles of Laser Spectroscopy and Quantum Optics* (Princeton University Press, 2010). 2, 11

[4] S. Chu, *Nobel Lecture: The manipulation of neutral particles*, Rev. Mod. Phys. **70**, 685 (1998), 10.1103/RevModPhys.70.685. 3, 72, 166

[5] C. N. Cohen-Tannoudji, *Nobel Lecture: Manipulating atoms with photons*, Rev. Mod. Phys. **70**, 707 (1998), 10.1103/RevModPhys.70.707.

[6] W. D. Phillips, *Nobel Lecture: Laser cooling and trapping of neutral atoms*, Rev. Mod. Phys. **70**, 721 (1998), 10.1103/RevModPhys.70.721. 72, 166

[7] C. S. Adams and E. Riis, *Laser cooling and trapping of neutral atoms*, Prog. Quantum Electron. **21**, 1 (1997), 10.1016/S0079-6727(96)00006-7. 3, 166

[8] E. Arimondo, *Coherent Population Trapping in Laser Spectroscopy*, Prog. Opt. **35**, 257 (1996), 10.1016/S0079-6638(08)70531-6. 3, 54

[9] P. D. D. Schwindt *et al.*, *Chip-scale atomic magnetometer*, Appl. Phys. Lett. **85**, 6409 (2004), 10.1063/1.1839274. 4

[10] R. W. Boyd and D. J. Gauthier, *"Slow" and "fast" light*, Prog. Opt. **43**, 497 (2002), 10.1016/S0079-6638(02)80030-0. 4, 84

[11] M. Fleischhauer, A. Imamoglu, and J. P. Marangos, *Electromagnetically induced transparency: Optics in coherent media*, Rev. Mod. Phys. **77**, 633 (2005), 10.1103/RevModPhys.77.633. 141

[12] P. W. Milonni, *Controlling the speed of light pulses*, J. Phys. B: At. Mol. Opt. Phys. **35**, R31 (2002), 10.1088/0953-4075/35/6/201. 4

[13] S. D. Badger, I. G. Hughes, and C. S. Adams, *Hyperfine effects in electromagnetically induced transparency*, J. Phys. B: At. Mol. Opt. Phys. **34**, L749 (2001), 10.1088/0953-4075/34/22/107. 4

[14] A. K. Mohapatra, T. R. Jackson, and C. S. Adams, *Coherent Optical Detection of Highly Excited Rydberg States Using Electromagnetically Induced Transparency*, Phys. Rev. Lett. **98**, 113003 (2007), 10.1103/PhysRevLett.98.113003. 4, 102

[15] A. Corney, *Atomic and Laser Spectroscopy* (Oxford University Press, 1977). 4, 65, 66

[16] W. Demtröder, *Laser Spectroscopy: Basic Concepts and Instrumentation*, 2nd ed. (Springer-Verlag, 1996). 4, 29, 46

[17] A. C. Eckbreth, *Laser Diagnostics for Combustion Temperature and Species* (Overseas Publishers Association, 1996). 4

[18] D. J. McCarron, I. G. Hughes, P. Tierney, and S. L. Cornish, *A heated vapor cell unit for dichroic atomic vapor laser lock in atomic rubidium*, Rev. Sci. Instrum. **78**, 093106 (2007), 10.1063/1.2785157. 4, 68, 76, 98

[19] C. Wieman and T. W. Hänsch, *Doppler-Free Laser Polarization Spectroscopy*, Phys. Rev. Lett. **36**, 1170 (1976), 10.1103/PhysRevLett.36.1170. 4, 7

[20] C. P. Pearman *et al.*, *Polarization spectroscopy of a closed atomic transition: applications to laser frequency locking*, J. Phys. B: At. Mol. Opt. Phys. **35**, 5141 (2002), 10.1088/0953-4075/35/24/315. 102, 122

[21] M. L. Harris *et al.*, *Polarization spectroscopy in rubidium and cesium*, Phys. Rev. **73**, 062509 (2006), 10.1103/PhysRevA.73.062509. 4

[22] B. Chéron, H. Gilles, J. Hamel, O. Moreau, and H. Sorel, *Laser frequency stabilization using Zeeman effect*, J. Physique III **4**, 401 (1994), 10.1051/jp3:1994136. 4

[23] K. L. Corwin, Z.-T. Lu, C. F. Hand, R. J. Epstein, and C. E. Wieman, *Frequency-Stabilized Diode Laser with the Zeeman Shift in an Atomic Vapor*, Appl. Opt. **37**, 3295 (1998), 10.1364/AO.37.003295.

[24] A. Millett-Sikking, I. G. Hughes, P. Tierney, and S. L. Cornish, *DAVLL lineshapes in atomic rubidium*, J. Phys. B: At. Mol. Opt. Phys. **40**, 187 (2007), 10.1088/0953-4075/40/1/017. 4, 68

[25] T. F. Krauss, *Why do we need slow light?*, Nature Photon. **2**, 448 (2008), 10.1038/nphoton.2008.139. 4

[26] R. W. Boyd *et al.*, *Slow Light and Its Applications*, J. Opt. Soc. Am. **25**, SL1 (2008), 10.1364/JOSAB.25.000SL1. 4

[27] L. V. Hau, S. E. Harris, Z. Dutton, and C. H. Behroozi, *Light speed reduction to 17 metres per second in an ultracold atomic gas*, Nature **397**, 594 (1999), 10.1038/17561. 4

[28] H. Tanaka *et al.*, *Propagation of optical pulses in a resonantly absorbing medium: observation of negative velocity in Rb vapor*, Phys. Rev. A **68**, 053801 (2003), 10.1103/PhysRevA.68.053801. 5, 89

[29] R. M. Camacho, M. V. Pack, J. C. Howell, A. Schweinsberg, and R. W. Boyd, *Wide-Bandwidth, Tunable, Multiple-Pulse-Width Optical Delays Using Slow Light in Cesium Vapor*, Phys. Rev. Lett. **98**, 153601 (2007), 10.1103/PhysRevLett.98.153601. 5, 68, 75, 78

[30] M. R. Vanner, R. J. McLean, P. Hannaford, and A. M. Akulshin, *Broadband optical delay with a large dynamic range using atomic dispersion*, J. Phys. B: At. Mol. Opt. Phys. **41**, 051004 (2008), 10.1088/0953-4075/41/5/051004. 5, 68, 89

[31] R. N. Shakhmuratov and J. Odeurs, *Off-resonance slow light*, Phys. Rev. **78**, 063836 (2008), 10.1103/PhysRevA.78.063836. 5

[32] D. J. Gauthier, A. L. Gaeta, and R. W. Boyd, *Slow light: from basics to future prospects*, Photon. Spectra **40**, 44 (2006). 5, 87

[33] M. Fleischhauer and M. D. Lukin, *Dark-state polaritons in electromagnetically induced transparency*, Phys. Rev. Lett. **84**, 5094 (2000), 10.1103/PhysRevLett.84.5094. 5

[34] C. Liu, Z. Dutton, C. H. Behroozi, and L. V. Hau, *Observation of coherent optical information storage in an atomic medium using halted light pulses*, Nature **409**, 490 (2001), 10.1038/35054017.

[35] D. F. Phillips, A. Fleischhauer, A. Mair, R. L. Walsworth, and M. D. Lukin, *Storage of light in atomic vapor*, Phys. Rev. Lett. **86**, 783 (2001), 10.1103/PhysRevLett.86.783. 5

[36] Z. Shi, R. W. Boyd, R. M. Camacho, P. K. Vudyasetu, and J. C. Howell, *Slow-Light Fourier Transform Interferometer*, Phys. Rev. Lett. **99**, 240801 (2007), 10.1103/PhysRevLett.99.240801. 5, 68, 75, 100

[37] G. T. Purves, C. S. Adams, and I. G. Hughes, *Sagnac interferometry in a slow-light medium*, Phys. Rev. A **74**, 023805 (2006), 10.1103/PhysRevA.74.023805. 5

[38] Z. Shi, R. W. Boyd, D. J. Gauthier, and C. C. Dudley, *Enhancing the spectral sensitivity of interferometers using slow-light media*, Opt. Lett. **32**, 915 (2007), 10.1364/OL.32.000915. 5

[39] R. P. Abel, U. Krohn, P. Siddons, I. G. Hughes, and C. S. Adams, *Faraday dichroic beam splitter for Raman light using an isotopically pure alkali-metal-vapor cell*, Opt. Lett. **34**, 3071 (2009), 10.1364/OL.34.003071. 6, 95, 112, 113, 152

[40] P. Siddons, N. C. Bell, Y. Cai, C. S. Adams, and I. G. Hughes, *A gigahertz-bandwidth atomic probe based on the slow-light Faraday effect*, Nature Photon. **3**, 225 (2009), 10.1038/nphoton.2009.27. 6, 7, 8, 74, 78, 112, 120, 121

[41] R. Löw and T. Pfau, *Magneto-optics: Hot atoms rotate light rapidly*, Nat. Photon. **3**, 197 (2009), 10.1038/nphoton.2009.41. 6

[42] B. Dayan and Y. Silberberg, *Optical switching: Atoms and photons share quarters*, Nature Photon. **3**, 429 (2009), 10.1038/nphoton.2009.125. 6

[43] I. Glesk, B. C. Wang, L. Xu, V. Baby, and P. R. Prucnal, *Ultrafast all-optical switching in optical networks*, Prog. Opt. **45**, 53 (2003), 10.1016/S0079-6638(03)80004-5. 6

[44] S. E. Harris and Y. Yamamoto, *Photon Switching by Quantum Interference*, Phys. Rev. Lett. **81**, 3611 (1998), 10.1103/PhysRevLett.81.3611. 6

[45] M. Yan, E. G. Rickey, and Y. Zhu, *Observation of absorptive photon switching by quantum interference*, Phys. Rev. A **64**, 041801(R) (2001), 10.1103/PhysRevA.64.041801. 6

[46] M. O. Scully, *Enhancement of the index of refraction via quantum coherence*, Phys. Rev. Lett. **67**, 1855 (1991), 10.1103/PhysRevLett.67.1855. 6

[47] M. O. Scully and M. Fleischhauer, *High-sensitivity magnetometer based on index-enhanced media*, Phys. Rev. Lett. **69**, 1360 (1992), 10.1103/PhysRevLett.69.1360.

[48] N. A. Proite, B. E. Unks, J. T. Green, and D. D. Yavuz, *Refractive Index Enhancement with Vanishing Absorption in an Atomic Vapor*, Phys. Rev. Lett. **101**, 147401 (2008), 10.1103/PhysRevLett.101.147401. 6

[49] D. Bouwmeester, A. K. Ekert, and A. Zeilinger, *The Physics of Quantum Information* (Springer, 2000). 6

[50] J. Zhang, G. Hernandez, and Y. Zhu, *All-optical switching at ultralow light levels*, Opt. Lett. **32**, 1317 (2007), 10.1364/OL.32.001317. 6

[51] A. M. C. Dawes, L. Illing, J. A. Greenberg, and D. J. Gauthier, *All-optical switching with transverse optical patterns*, Phys. Rev. A **77**, 013833 (2008), 10.1103/PhysRevA.77.013833. 6

[52] D. Budker *et al.*, *Resonant nonlinear magneto-optical effects in atoms*, Rev. Mod. Phys **74**, 1153 (2002), 10.1103/RevModPhys.74.1153. 7, 95, 102

[53] J. Menders, K. Benson, S. H. Bloom, C. S. Liu, and E. Korevaar, *Ultranarrow line filtering using a Cs Faraday filter at 852 nm*, Opt. Lett. **16**, 846 (1991), 10.1364/OL.16.000846. 7, 78, 95, 112

[54] Z. K. Lee *et al.*, *Faraday-Stark optoelectronic effect*, Appl. Phys. Lett. **69**, 3731 (1996), 10.1063/1.117204. 7

[55] W. Happer and B. S. Mathur, *Off-Resonant Light as a Probe of Optically Pumped Alkali Vapors*, Phys. Rev. Lett. **18**, 577 (1967), 10.1103/PhysRevLett.18.577. 7

[56] K. Hammerer, A. S. Sørensen, and E. S. Polzik, *Quantum interface between light and atomic ensembles*, Rev. Mod. Phys. **82**, 1041 (2010), 10.1103/RevModPhys.82.1041. 110, 113

[57] M. Kubasik *et al.*, *Polarization-based light-atom quantum interface with an all-optical trap*, Phys. Rev. A **79**, 043815 (2009), 10.1103/PhysRevA.79.043815. 7, 74

[58] S. Li *et al.*, *Controlled polarization rotation of an optical field in multi-Zeeman-sublevel atoms*, Phys. Rev. A **74**, 033821 (2006), 10.1103/PhysRevA.74.033821. 7, 121

[59] P. Siddons, C. S. Adams, C. Ge, and I. G. Hughes, *Absolute absorption on rubidium D lines: comparison between theory and experiment*, J. Phys. B: At. Mol. Opt. Phys. **41**, 155004 (2008), 10.1088/0953-4075/41/15/155004. 7

[60] P. Siddons, C. S. Adams, and I. G. Hughes, *Off-resonance absorption and dispersion in vapours of hot alkali-metal atoms*, J. Phys. B: At. Mol. Opt. Phys. **42**, 175004 (2009), 10.1088/0953-4075/42/17/175004. 7, 120

[61] P. Siddons, C. S. Adams, and I. G. Hughes, *Optical control of Faraday rotation in hot Rb vapor*, Phys. Rev. A **81**, 043838 (2010), 10.1103/PhysRevA.81.043838. 8

[62] J. D. Jackson, *Classical Electrodynamics*, 3rd ed. (Wiley, 1999). 11, 44, 130, 169

[63] C. Cohen-Tannoudji, J. Dupont-Roc, and G. Grynberg, *Atom-photon interactions: basic processes and applications* (Wiley, 1998). 11, 16, 28, 31, 131, 141

[64] L. Brillouin, *Wave Propagation and Group Velocity* (Academic Press, 1960). 14, 84, 87

[65] G. Diener, *Energy transport in dispersive media and superluminal group velocities*, Phys. Lett. A **235**, 118 (1997), 10.1016/S0375-9601(97)00600-2. 15, 132, 133

[66] U. Leonhardt and H. Paul, *Measuring the quantum state of light*, Prog. Optics **19**, 89 (1995), 10.1016/0079-6727(94)00007-L. 15

[67] H. C. Torrey, *Transient Nutations in Nuclear Magnetic Resonance*, Phys. Rev. **76**, 1059 (1949), 10.1103/PhysRev.76.1059. 15

[68] H.-R. Noh and W. Jhe, *Analytic solutions of the optical Bloch equations*, Opt. Commun. **283**, 2353 (2010), 10.1016/j.optcom.2010.01.069. 15

[69] G. Lindblad, *On the generators of quantum dynamical semigroups*, Commun. Math. Phys. **48**, 119 (1976), 10.1007/BF01608499. 17

[70] P. N. Butcher and D. Cotter, *The elements of nonlinear optics* (Cambridge University Press, 1991), p. 216. 20

[71] J. C. Eilbeck, *Reflection of short pulses in linear optics*, J. Phys. A: Gen. Phys. **5**, 1355 (1972), 10.1088/0305-4470/5/9/008. 21

[72] J. Z. Sanborn, C. Hellings, and T. D. Donnelly, *Breakdown of the slowly-varying-amplitude approximation: generation of backward-traveling, second-harmonic light*, J. Opt. Soc. Am. B **20**, 152 (2003), 10.1364/JOSAB.20.000152. 21

[73] I. I. Rabi, *Space Quantization in a Gyrating Magnetic Field*, Phys. Rev. **51**, 652 (1937), 10.1103/PhysRev.51.652. 24, 27

[74] A. V. Durrant, *Some basic properties of stimulated and spontaneous emission: A semiclassical approach*, Prog. Optics **44**, 630 (1976), dx.doi.org/10.1119/1.10322. 27

[75] D. C. Burnham and R. Y. Chiao, *Coherent Resonance Fluorescence Excited by Short Light Pulses*, Phys. Rev. **188**, 667 (1969), 10.1103/PhysRev.188.667. 32

[76] M. D. Crisp, *Propagation of Small-Area Pulses of Coherent Light through a Resonant Medium*, Phys. Rev. A **1**, 1604 (1970), 10.1103/PhysRevA.1.1604. 32

[77] E. Hecht, *Optics*, 4th ed. (Addison-Wesley, 2003). 34, 96, 169, 170

[78] R. W. Boyd., *Nonlinear Optics*, 3rd ed. (Academic Press, 2008). 40, 92

[79] S. Huard, *Polarization of Light* (Wiley, 1997). 40, 146

[80] J. S. Toll, *Causality and the Dispersion Relation: Logical Foundations*, Phys. Rev. **104**, 1760 (1956), 10.1103/PhysRev.104.1760. 43

[81] H. M. Nussenzveig, *Causality and Dispersion Relations* (Academic Press, 1972). 43

[82] H. Kramers, *La diffusion de la lumiere par les atomes*, in *Atti Cong. Intern. Fisica, (Transactions of Volta Centenary Congress)*, volume 2, pp. 545–557, 1927. 44

[83] R. de L. Kronig, *On the theory of the dispersion of X-rays*, J. Opt. Soc. Am. **12**, 547 (1926), 10.1364/JOSA.12.000547. 44

[84] M. L. Citron, H. R. Gray, C. W. Gabel, and C. R. Stroud, Jr., *Experimental study of power broadening in a two-level atom*, Phys. Rev. A **16**, 1507 (1977), 10.1103/PhysRevA.16.1507. 46

[85] W. Happer, *Optical Pumping*, Rev. Mod. Phys. **44**, 169 (1972), 10.1103/RevModPhys.44.169. 46, 113

[86] D. A. Smith and I. G. Hughes, *The role of hyperfine pumping in multilevel systems exhibiting saturated absorption*, Am. J. Phys. **72**, 631 (2004), 10.1119/1.1652039. 46, 62

[87] C. Kittel, *Introduction to Solid State Physics*, 8th ed. (Wiley, 1995). 48

[88] R. P. Feynman, R. B. Leighton, and M. Sands, *Feynman Lectures on Physics* volume 2 (Addison Wesley, 1989), chap. 32 (Refractive Index of Dense Materials). 48

[89] D. E. Aspnes, *Local-field effects and effective-medium theory: A microscopic perspective*, Am. J. Phys. **50**, 704 (1982), 10.1119/1.12734. 48

[90] E. L. Lewis, *Collisional relaxation of atomic excited states, line broadening and interatomic interactions*, Phys. Rep. **58**, 1 (1980), 10.1016/0370-1573(80)90056-3. 49

[91] L. Weller, R. J. Bettles, P. Siddons, C. S. Adams, and I. G. Hughes, *Absolute absorption on the rubidium D_1 line including resonant dipole-dipole interactions*, J. Phys. B: At. Mol. Opt. Phys. **44**, 195006 (2011), 10.1088/0953-4075/44/19/195006. 49, 54, 89, 166

[92] A. F. Molisch and B. P. Oehry, *Radiation trapping in atomic vapours* (Oxford University Press, 1998). 49

[93] T. Lindvall and I. Tittonen, *Effect of optical pumping on alkali-atom Doppler-limited spectra*, J. Mod. Opt. **54**, 2779 (2007), 10.1080/09500340701243566. 49, 66, 78

[94] S. R. Shin and H.-R. Noh, *Calculation and Measurement of Absolute Transmission in Rubidium*, J. Phys. Soc. Jpn. **78**, 084302 (2009), 10.1143/JPSJ.78.084302.

[95] T. M. Stace and A. N. Luiten, *Theory of spectroscopy in an optically pumped effusive vapor*, Phys. Rev. A **81**, 033848 (2009), 10.1103/PhysRevA.81.033848. 49

[96] M. Gorris-Neveux *et al.*, *Doppler-free reflection spectroscopy of rubidium D_1 line in optically dense vapour*, Opt. Commun. **134**, 85 (1997), 10.1016/S0030-4018(96)00559-7. 54

[97] J. Gustafsson, D. Rojas, and O. Axner, *The influence of hyperfine structure and isotope shift on the detection of Rb atoms in atmospheric pressure atomizers by the 2f-wavelength modulation technique*, Spectrochim. Acta **52**, 1937 (1997), 10.1016/S0584-8547(97)00087-6. 54, 55

[98] U. Rapol, A. Krishna, and V. Natarajan, *Precise measurement of hyperfine structure in the state of Rb*, Eur. Phys. J. **23**, 185 (2003), 10.1140/epjd/e2003-00069-9. 54

[99] A. Banerjee, D. Das, and V. Natarajan, *Absolute frequency measurements of the D_1 lines in ^{39}K, ^{85}Rb, and ^{87}Rb with ∼0.1 ppb uncertainty*, Europhys. Lett. **65**, 172 (2004), 10.1209/epl/i2003-10069-3. 54, 55

[100] A. R. Edmonds, *Angular Momentum in Quantum Mechanics*, 2nd ed. (Princeton University Press, 1960). 56, 145

[101] W. J. Thompson, *Angular Momentum: An Illustrated Guide to Rotational Symmetries for Physical Systems* (Wiley, 1994), 10.1002/9783527617821. 56

[102] J. Ye, S. Swartz, P. Jungner, and J. L. Hall, *Hyperfine structure and absolute frequency of the ^{87}Rb $5P_{3/2}$ state*, Opt. Lett. **21**, 1280 (1996), 10.1364/OL.21.001280. 58, 163

[103] U. Volz and H. Schmoranzer, *Precision lifetime measurements on alkali atoms and on helium by beam-gas-laser spectroscopy*, Phys. Scr. **t65**, 48 (1996), 10.1088/0031-8949/1996/T65/007. 58, 163

[104] G. P. Barwood, P. Gill, and W. R. C. Rowley, *Frequency measurements on optically narrowed Rb-stabilised laser diodes at 780 nm and 795 nm*, Appl. Phys. **53**, 142 (1991), 10.1007/BF00330229. 58, 163

[105] K. B. MacAdam, A. Steinbach, and C. Wieman, *A narrow-band tunable diode laser system with grating feedback, and a saturated absorption spectrometer for Cs and Rb*, Am. J. Phys. **60**, 1098 (1992), 10.1119/1.16955. 62

[106] P. G. Pappas, M. M. Burns, D. D. Hinshelwood, M. S. Feld, and D. E. Murnick, *Saturation spectroscopy with laser optical pumping in atomic barium*, Phys. Rev. A. **21**, 1955 (1980), 10.1103/PhysRevA.21.1955. 65

[107] J. Sagle, R. K. Namiotka, and J. Huennekens, *Measurement and modelling of intensity dependent absorption and transit relaxation on the cesium D_1 line*, J. Phys. B: At. Mol. Opt. Phys. **29**, 2629 (1996), 10.1088/0953-4075/29/12/023. 65

[108] B. E. Sherlock and I. G. Hughes, *How weak is a weak probe in laser spectroscopy?*, Am. J. Phys. **77**, 111 (2009), 10.1119/1.3013197. 66, 67, 76

[109] A. C. G. Mitchell and M. W. Zamansky, *Resonance Radiation and Excited Atoms* (Cambridge University Press, 1934), p. 160. 70

[110] A. M. Portis, *Electronic Structure of F Centers: Saturation of the Electron Spin Resonance*, Phys. Rev. **91**, 1071 (1953), 10.1103/PhysRev.91.1071. 70

[111] B. D. Fried and S. D. Conte, *The Plasma Dispersion Function* (Academic Press, 1961). 70

[112] R. Salomaa and S. Stenholm, *Gas Laser with Saturable Absorber. I. Single-Mode Characteristics*, Phys. Rev. **8**, 2695 (1973), 10.1103/PhysRevA.8.2695. 70

[113] V. N. Faddeeva and N. M. Terent'ev, *Tables of Values of the Error Function with a Complex Argument* (Gostekhizdat, 1954), (in russian). 70

[114] V. N. Faddeeva and N. M. Terent'ev, *Tables of Values of the Error Function with a Complex Argument* (Pergamon, 1961), (english translation). 70

[115] J. F. Kielkopf, *New approximation to the Voigt function with applications to spectral-line profile analysis*, J. Opt. Soc. Am. **63**, 987 (1973), 10.1364/JOSA.63.000987. 70

[116] P. Martin and J. Puerta, *Generalized Lorentzian approximations for the Voigt line shape*, Appl. Opt. **20**, 259 (1981), 10.1364/AO.20.000259. 70

[117] W. J. Thompson, *Numerous Neat Algorithms for the Voigt Profile Function*, Comput. Phys. **7**, 627 (1993). 70

[118] R. Wells, *Rapid approximation to the Voigt/Faddeeva function and its derivatives*, J. Quant. Spectrosc. Radiat. Transfer **62**, 29 (1999), 10.1016/S0022-4073(97)00231-8. 70

[119] M. R. Zaghloul, *Comment on "a fast method of modeling spectral line"*, J. Quant. Spectrosc. Radiat. Transfer **109**, 2895 (2008), 10.1016/j.jqsrt.2008.07.014. 71

[120] C. D. Olds, *Continued Fractions* (Random House, 1963), p. 139. 72

[121] L. Lorentzen and H. Waadeland, *Continued Fractions with Applications* (Elsevier, 1992), p. 576. 72

[122] B. E. Schultz, H. Ming, G. A. Noble, and W. A. van Wijngaarden, *Measurement of the Rb D_2 transition linewidth at ultralow temperature*, Eur. Phys. J. **48**, 171 (2008), 10.1140/epjd/e2008-00109-0. 73

[123] M. Xiao, Y.-Q. Li, S.-Z. Jin, and J. Gea-Banacloche, *Measurement of Dispersive Properties of Electromagnetically Induced Transparency in Rubidium Atoms*, Phys. Rev. Lett. **74**, 666 (1995), 10.1103/PhysRevLett.74.666. 78

[124] A. Wicht, M. Müller, R.-H. Rinkleff, A. Rocco, and K. Danzmann, *Experimental demonstration of negative dispersion without absorption*, Opt. Commun. **179**, 107 (2000), 10.1016/S0030-4018(99)00528-3. 78

[125] G. Purves, G. Jundt, C. Adams, and I. Hughes, *Refractive index measurements by probe-beam deflection*, Eur. Phys. J. D **29**, 433 (2004), 10.1140/epjd/e2004-00056-8. 78

[126] G. P. Agrawal, *Nonlinear Fibre Optics*, 2nd ed. (Academic Press, 1995). 85

[127] R. W. Boyd, *Slow light now and then*, Nat. Photon. **2**, 454 (2008), 10.1038/nphoton.2008.148. 87

[128] P. W. Milonni, *Fast light, slow light and left-handed light* (Taylor & Francis, 2004). 87

[129] F. C. A. Pockels, Abhandl. Gesell. Wiss. Göttingen **39** (1893), (in german). 88

[130] F. C. A. Pockels, *Lehrbuch Der Kristalloptik* (Teubner, 1906), (in german). 88

[131] D. D. Awschalom and J. M. Kikkawa, *Electron spin and optical coherence in semiconductors*, Phys. Today **52**, 33 (1999), 10.1063/1.882695. 95

[132] M. Atatüre, J. Dreiser, A. Badolato, and A. Imamoglu, *Observation of Faraday rotation from a single confined spin*, Nature Phys. **3**, 101 (2007), 10.1038/nphys521. 95

[133] A. L. Marchant *et al.*, *Off-resonance laser frequency stabilization using the Faraday effect*, Optics Letters **36**, 64 (2011), 10.1364/OL.36.000064. 95, 102, 152

[134] E. Bartholin, *Experimenta Crystalli Islandici disdiaclastici, quibus mira et insolita refractio detegitur*, 1669, (in latin). 95

[135] E. Bartholin, *Experiments on birefringent Icelandic crystal* (Danish National Library of Science and Medicine, 1991), (translation by T. Archibald; introduction by J. Z. Buchwald and K. M. Pedersen; contains a facsimile of the original 1669 publication). 95

[136] M. Faraday, *Experimental Researches in Electricity. Nineteenth Series*, Philos. Trans. R. Soc. London **136**, 1 (1846), http://www.jstor.org/stable/108303. 96

[137] B. H. Bransden and C. J. Joachain, *Physics of Atoms and Molecules*, 2nd ed. (Benjamin Cummings, 2003). 96, 171

[138] S. Kahla and A. M. Grishin, *Enhanced Faraday rotation in all-garnet magneto-optical photonic crystal*, Appl. Phys. Lett. **84**, 1438 (2004), 10.1063/1.1651324. 102

[139] A. K. Mohapatra, M. G. Bason, B. Butscher, K. J. Weatherill, and C. S. Adams, *A giant electro-optic effect using polarizable dark states*, Nature Phys. **4**, 890 (2008), 10.1038/nphys1091. 102

[140] S. Mauger, J. Millen, and M. P. A. Jones, *Spectroscopy of strontium Rydberg states using electromagnetically induced transparency*, J. Phys. B: At. Mol. Opt. Phys. **40**, F319 (2007), 10.1088/0953-4075/40/22/F03. 102

[141] D. Grischkowsky, *Adiabatic following and slow optical pulse propagation in rubidium vapor*, Phys. Rev. A **7**, 2096 (1973), 10.1103/PhysRevA.7.2096. 107

[142] H. M. Gibbs, G. G. Churchill, and G. J. Salamo, *Faraday rotation under cw saturation and self-induced transparency conditions*, Opt. Commun. **12**, 396 (1974), 10.1016/0030-4018(74)90129-1. 110

[143] H. Chen, C. Y. She, P. Searcy, and E. Korevaar, *Sodium-vapor dispersive Faraday filter*, Opt. Lett. **18**, 1019 (1993), 10.1364/OL.18.001019. 112

[144] V. M. Entin, I. I. Ryabtsev, A. E. Boguslavsky, and Y. V. Brzhazovsky, *Laser spectroscopy of spontaneous coherence transfer and optically induced polarization rotation in* ^{87}Rb, Opt. Commun. **2007**, 201 (2002), 10.1016/S0030-4018(02)01485-2. 121

[145] J. M. Choi, J. M. Kim, and D. Cho, *Faraday rotation assisted by linearly polarized light*, Phys. Rev. A **76**, 053802 (2007), 10.1103/PhysRevA.76.053802.

[146] X. Yang, S. Li, X. Cao, and H. Wang, *Light switching at low light level based on changes in light polarization*, J. Phys. B: At. Mol. Opt. Phys. **41**, 085403 (2008), 10.1088/0953-4075/41/8/085403. 121

[147] S. L. McCall and E. L. Hahn, *Self-Induced Transparency by Pulsed Coherent Light*, Phys. Rev. Lett. **18**, 908 (1967), 10.1103/PhysRevLett.18.908. 123, 127

[148] S. L. McCall and E. L. Hahn, *Self-Induced Transparency*, Phys. Rev. **183**, 457 (1969), 10.1103/PhysRev.183.457. 123, 127

[149] H. A. Haus and J. R. Melcher, *Electromagnetic Fields and Energy* (Prentice-Hall, 1989). 129

[150] J. H. Poynting, *On the Transfer of Energy in the Electromagnetic Field*, Phil. Trans. R. Soc. Lond. **175**, 343 (1884), 10.1098/rstl.1884.0016. 129

[151] K. Bergmann, H. Theuer, and B. W. Shore, *Coherent population transfer among quantum states of atoms and molecules*, Rev. Mod. Phys. **70**, 1003 (1998), 10.1103/RevModPhys.70.1003. 137, 142, 149

[152] M. Fleischhauer, *Electromagnetically induced transparencyand coherent-state preparation in optically thick media*, Opt. Express **4**, 107 (1999), 10.1364/OE.4.000107. 138

[153] V. V. Kozlov and E. B. Kozlova, *Adiabatic and nonadiabatic preparation of a ground-state coherence in an optically thick lambda medium*, Optics Communications **282**, 892 (2009), 10.1016/j.optcom.2008.11.059. 138, 142

[154] Z. Kis, A. Karpati, B. W. Shore, and N. V. Vitanov, *Stimulated Raman adiabatic passage among degenerate-level manifolds*, Phys. Rev. A **70**, 053405 (2004), 10.1103/PhysRevA.70.053405. 138

[155] O. S. Heavens, *Radiative Transition Probabilities of the Lower Excited States of the Alkali Metals*, J. Opt. Soc. Am. **51**, 1058 (1961), 10.1364/JOSA.51.001058. 140

[156] Z. Ficek and S. Swain, *Quantum interference and coherence: theory and experiments* (Springer, 2005). 141

[157] J. R. Morris and B. W. Shore, *Reduction of degenerate two-level excitation to independent two-state systems*, Phys. Rev. A **27**, 906 (1983), 10.1103/PhysRevA.27.906. 141

[158] G. Genov, A. Rangelov, and N. Vitanov, *Propagation of light polarization in a birefringent medium: Exact analytic models*, Opt. Commun. **284**, 2642 (2011), 10.1016/j.optcom.2011.01.073. 146

[159] M. Auzinsh, D. Budker, and S. M. Rochester, *Optically polarized atoms: understanding light-atom interactions* (Oxford University Press, 2010). 147

[160] D. Budker, D. F. Kimball, and D. P. DeMille, *Atomic physics: an exploration through problems and solutions* (Oxford University Press, 2004). 149

[161] J. P. Boyd, *Chebyshev and Fourier spectral methods*, 2nd ed. (Dover, 2001). 158, 160

[162] L. N. Trefethen, *Spectral methods in MATLAB* (SIAM, 2000). 158, 160

[163] R. J. LeVeque, *Finite difference methods for ordinary and partial differential equations* (SIAM, 2007). 159, 160

[164] R. Bunsen, *Ueber Cäsium und Rubidium*, Ann. der Chem. **119**, 107 (1861), 10.1002/jlac.18611190110, (in german). 162

[165] D. R. Lide, *CRC Handbook of Chemistry and Physics*, 82nd ed. (CRC Press, 2001-2002). 162, 164

[166] C. B. Alcock, V. P. Itkin, and M. K. Horrigan, *Vapor Pressure Equations for the Metallic Elements: 298-2500 K*, Can. Metall. Quart. **23**, 309 (1984). 164

[167] G. G. Stokes, *Composition and resolution of streams of polarized light from multiple sources*, Trans. Cambridge Philos. Soc. **9**, 399 (1852), Reprinted in Mathematical and Physical Papers, Cambridge Books Online (Cambridge University Press, 2009),10.1017/CBO9780511702266.010. 178

[168] B. Schaefer, E. Collett, R. Smyth, D. Barrett, and B. Fraher, *Measuring the Stokes polarization parameters*, Am. J. Phys. **75**, 163 (2007), 10.1119/1.2386162. 178